Optical Spectroscopy of Orbital and Magnetic Excitations in Vanadates and Cuprates

Eva Benckiser

Optical Spectroscopy of Orbital and Magnetic Excitations in Vanadates and Cuprates

Optical Spectroscopy of Orbital and Magnetic Excitations in Vanadates and Cuprates

Inaugural - Dissertation

zur

Erlangung des Doktorgrades

der Mathematisch-Naturwissenschaftlichen Fakultät

der Universität zu Köln

vorgelegt von

Eva Vera Benckiser

aus Stuttgart

Köln, im Oktober 2007

'The ability to reduce everything
to simple fundamental laws
does not imply the ability
to start from those laws
and reconstruct the universe.'

(P. W. Anderson [1])

for my parents

Contents

1. Introduction

In many transition-metal (TM) oxides the strong electron-electron correlations play a crucial role giving rise to fascinating physics and a rich variety of novel phenomena. Because of their partly filled d shells many TM oxides are expected to be metals, but found experimentally to be insulators [2]. To account for both, the energy gain due to delocalization of the electrons and the Coulomb repulsion between two electrons on the same site, the Hubbard model was introduced [3, 4]. The most important difference to a conventional band insulator is that the atomic degrees of freedom, spin and orbital, still survive in such Mott insulators [5]. The degrees of freedom for electrons, localized on a specific atomic site, give rise to versatile order phenomena, like charge, spin, and orbital order. In particular, these order phenomena offer the possibility of new collective excitations, like charge-density waves, spin waves (magnons), and orbital waves (orbitons). The investigation of these low-energy excitations in undoped Mott insulators is the subject of this thesis.

First, we focus on orbital excitations in orbitally ordered vanadates RVO$_3$ with R = rare-earth ion. The undoped RVO$_3$ compounds are Mott-Hubbard insulators with a pseudo-cubic structure. The octahedrally coordinated V^{3+} ions exhibit two electrons occupying the open $3d$ shell. Due to the crystal field, the five atomic $3d$ levels are split into a low-lying triply degenerate t_{2g} level and a high-lying doubly degenerate e_g level. In the ground state both electrons occupy the t_{2g} orbitals. Two mechanisms are discussed in the literature which give rise to a lifting of the orbital degeneracy of partly filled t_{2g} levels. First, the orbital degeneracy may be lifted by a coupling to phonons, i.e. due to the so-called (collective) Jahn-Teller (JT) effect [6]. Second, a lifting of the degeneracy by superexchange processes has been suggested [7]. In real crystals one may expect that both mechanisms are present, but with different strength. Independent from the respective mechanism, the formation of an orbitally ordered ground state is expected. However, a dominant superexchange may also give rise to exotic ground states. For instance, an orbital liquid state in LaTiO$_3$ [8] and an orbital Peierls state in YVO$_3$ [9, 10] have been predicted. The latter is of particular interest, because the excitations of a dimerized orbital ground state may show some peculiarities.

From the ground state properties it is impossible to decide which mechanism is the most relevant one. However, when concerning the elementary excitations of such an orbitally-ordered system, the coupling to the lattice plays a crucial role. If the JT effect is dominant, the orbital excitations are local crystal-field excitations, i.e. transitions of electrons between local crystal-field levels. Such local orbital excitations have been investigated in detail in many TM compounds over the last decades and

are well described by crystal-field theory. In the case of dominant superexchange interactions the orbital excitations are collective modes (orbitons) which may be visualized by a modulation of the relative shape of orbitals in an orbitally ordered state. Orbitons exhibit a significant dispersion. Because the orbital degree of freedom does not show continuous rotational symmetry, the dispersion of orbitons exhibits a gap, in contrast to the analogue spin waves. First evidence for an experimental observation of orbitons has been reported from Raman scattering studies on $LaMnO_3$, a $3d^4$ compound which exhibits one electron in the e_g orbitals [11]. However, later an explanation of the observed features in terms of multi-phonon scattering has been suggested [12]. In $YTiO_3$ and $LaTiO_3$ a Raman peak at $0.25\,eV$ has been interpreted in terms of a two-orbiton excitation based on its dependence on temperature, polarization, and on the frequency of the incoming photons [13, 14]. However, it cannot be fully excluded that this feature corresponds to a local crystal-field excitation [15]. The compounds RVO_3 are also promising candidates for the observation of orbitons [16, 17], because the t_{2g} orbitals are expected to be less strongly coupled to the lattice, compared to e_g orbitals. Orbital ordering in RVO_3 has been theoretically predicted [18, 19] and subsequently confirmed by experiments [20–23]. In particular, depending on the R ion, the compounds undergo a series of temperature-induced phase transitions accompanied by a change of orbital and magnetic order [19, 24–32]. This diversity of differently ordered orbital and magnetic phases gives the possibility to verify the theoretical predictions in detail. In fact, also in RVO_3 two-orbiton Raman scattering has been reported recently [10, 32, 33]. However, also here the relevant features are observed in the region of phonon, magnon, and multi-phonon scattering which hinders an unambiguous experimental proof of orbitons.

In this thesis we use optical spectroscopy to study the orbital excitations in the undoped Mott-Hubbard insulators RVO_3 with $R = Y$, Ho, and Ce. Optical spectroscopy is a powerful tool to investigate such systems. Particularly in the energy range below the insulating gap, a very accurate determination of the optical conductivity by a combined analysis of reflectance *and* transmittance allows the investigation of very small absorption features. The energy and line shape is characteristic and in many cases well describable by theory. In addition, the selection rules give clear predictions, e.g. for the polarization dependence. Our aim to study the orbital excitations of RVO_3 is to give experimental insight whether the coupling to the lattice or the superexchange interaction is the driving force for orbital order. Local crystal-field excitations can be well investigated by optical spectroscopy, and clear predictions can be made from crystal-field theory. Therefore, we analyze the spectra in comparison with the results of cluster calculations. Additionally we consider $VOCl$ and $Dy(V,Sc)O_3$, which serve as reference materials. The spectra of these compounds ought to demonstrate the local crystal-field excitations of V^{3+} $(3d^2)$ in a predominantly octahedral environment. The investigation of orbitons by means of optical spectroscopy is new [15]. Predictions for the observation of two-orbiton excitations have been derived for inelastic neutron scattering and Raman scattering [34]. Both Raman and optical spectroscopy are in general restricted to the observa-

tion of excitations with momentum $k = 0$. However, by exciting two orbitons with momenta $k_1 = -k_2$, it is, in principle, possible to probe the orbiton dispersion (or, more precisely, the two-orbiton continuum) throughout the entire Brillouin zone, since only $k_1 + k_2 = 0$ is required. In optical spectroscopy the selection rules for local crystal-field transitions and orbitons are expected to be equal. We will point out that in the case of RVO$_3$, the specific orbital and magnetic order in the intermediate monoclinic phase provides a basis for the *direct* observation of two-orbiton excitations, which show a pronounced polarization and temperature dependence.

The second part of this thesis is concerned with magnetic excitations in the low-dimensional quantum spin systems (Sr,Ca)CuO$_2$ and La$_8$Cu$_7$O$_{19}$. The discovery of high-T_c superconductivity in cuprates [35] has attracted renewed interest in the investigation of low-dimensional spin systems because an intimate relationship between magnetism and high-T_c superconductivity has been suggested [36]. A common characteristic of these cuprate superconductors is the presence of CuO$_2$ planes stacked on top of each other. It is widely believed that the relevant low-energy physics are described by the degrees of freedom of these CuO$_2$ planes. In the undoped case, each CuO$_2$ plane corresponds to an antiferromagnetic 2D square lattice with nearest-neighbor coupling of the Cu^{2+} S $= 1/2$ spins, whereas adjacent planes are magnetically nearly decoupled. Aiming for a full understanding of high-T_c superconductivity, the magnetism of the CuO$_2$ planes has been investigated comprehensively in the last twenty years, both theoretically and experimentally. For theoreticians, the investigation of low-dimensional spin systems is an interesting field of activity, also in former times. For instance, H. Bethe worked out the excitation spectrum of a one-dimensional $S = 1/2$ chain already in 1931 [37]. In contrast to higher dimensions, in 1D the quantum fluctuations are so strong that long-range order is suppressed down to zero temperature, i.e., these systems are so-called spin liquids. Accordingly, the excitation spectrum of the $S = 1/2$ chain is very different. While in 2D the excitations are well described by spin waves with $S^z = 1$, the excitations of the spin chain have been identified with incoherent excitations with fractional spin $S = 1/2$, called spinons [38]. In this regard, the crossover from the 2D square lattice to the 1D chain is of particular interest. This crossover is realized by n-leg ladders, i.e. n chains coupled by a perpendicular coupling. It has been predicted by numerical calculations that the crossover from one to two dimensions is not smooth [39]. While ladders with an even number of legs are gapped spin liquids, ladders with an odd number of legs exhibit no energy gap to the lowest magnetic excitations [40, 41]. The excitations of the two-leg ladder have been successfully explained in terms of triplets with $S = 1$ [42]. However, the investigation of magnetic excitations in low-dimensional spin systems is still a hot topic in modern solid-state physics.

In this thesis we study the magnetic excitations of the $S = 1/2$ double chain (Sr,Ca)CuO$_2$ and of the five-leg ladder compound La$_8$Cu$_7$O$_{19}$.

Optical spectroscopy is a powerful tool to investigate low-dimensional spin systems (see e.g. [43]) by means of phonon-assisted magnetic absorption proposed by Lorenzana and Sawatzky [44, 45]. Especially low-dimensional cuprates with com-

paratively large exchange couplings around $\sim 100\,\text{meV}$ are well suited, because the phonon-assisted magnetic absorption is well separated from other excitations, i.e. phonons or electronic excitations. As mentioned above, the determination of $\sigma(\omega)$ in the energy range below the insulating gap is very sensitive to small absorption features, when considering a combined analysis of reflectance *and* transmittance. The energy and line shape of the magnetic contribution is characteristic, which gives the possibility for an unambiguous proof of theoretical predictions.

Our aim to investigate the double chains in $(\text{Sr},\text{Ca})\text{CuO}_2$ is manifold. From optical spectroscopy, only one result for the two-spinon-plus-phonon absorption in the $S = 1/2$ chain Sr_2CuO_3 has been reported [46]. In this closely related compound the determination of J by different experimental techniques is controversial. From the temperature dependence of the magnetic susceptibility a value of $181(17)\,\text{meV}$ has been estimated [47], while mid-infrared absorption data yield a $\sim 37\,\%$ larger value of $260\,\text{meV}$ [46]. Therefore, one motivation was to determine the important parameter J for SrCuO_2 by analyzing the mid-infrared absorption spectra. Additionally, the double chains in SrCuO_2 give the possibility to study the influence of weak perpendicular couplings on the excitation spectrum, also earlier investigated in our group [43, 48]. The investigation of the Ca-substituted compound $(\text{Sr},\text{Ca})\text{CuO}_2$ has been initiated by recent thermal conductivity measurements [49]. Upon substitution of Sr by iso-valent Ca, the thermal conductivity due to acoustic phonons is effectively suppressed, while it is suggested that the magnetic contribution is not strongly affected [49]. Therefore we determine J also for $\text{Sr}_{0.9}\text{Ca}_{0.1}\text{CuO}_2$ by analyzing the mid-infrared absorption spectra.

The successful preparation of large single crystals of $\text{La}_8\text{Cu}_7\text{O}_{19}$ offers the possibility for the first study on a five-leg ladder.

Scope of this Thesis

The structure of this thesis is as follows. In Chapter 2 we give a brief introduction on optical spectroscopy and the therewith associated selection rules. Optical spectroscopy is a very well established method, and a lot of good text books are available (e.g. [50]). Therefore, we mainly focus on selective topics with regard to the scope of this thesis, i.e. the optical spectroscopy of low-energy excitations in TM oxides.

In order to determine $\sigma(\omega)$, we performed measurements using a Fourier transform spectrometer. The experimental setup and the sample preparation are briefly summarized in Chapter 3. Since the development of high-performance computers, Fourier transform spectroscopy has become a powerful and fast method to measure the reflectance and transmittance of solids. Commercial setups are available and the field of application covers medical engineering, sensor technology, as well as chemical analysis in food and pharmaceutical industry. However, we used a specific setup which is equipped with a cryostat, enabling measurements down to liquid helium temperature. This is essential to study the excitations of solids in the limit $T \to 0$.

The orbital excitations in orbitally ordered vanadates are the subject of Chapter 4. After giving a detailed introduction to the up-to-now known structural and physical

properties of $R(V,Sc)O_3$, we present the experimental details, i.e. the resistivity of YVO_3 and the transmittance and reflectance measurements of RVO_3 with $R = Y$, Ho, and Ce. We also present data of VOCl and $Dy(Sc,V)O_3$ which serve as reference systems in the context of local crystal-field excitations.

Due to this comparison and in combination with the results obtained from a cluster calculation, we discuss the observation of collective orbital excitations around $0.4\,\mathrm{eV}$ for $E \parallel c$ in the monoclinic phase of RVO_3.

In Chapter 5, we present the results on the magnetic excitations of the double (zig-zag) chain $(Sr,Ca)CuO_2$ and the five-leg $S = 1/2$ ladder $La_8Cu_7O_{19}$. For $(Sr,Ca)CuO_2$ we will present the detailed analysis of the two-spinon-plus-phonon contribution in chain polarization, which allows us to determine a very exact value of J. Furthermore we sketch a new mechanism which gives rise to a dipole moment *perpendicular* to the chains when two spins are exchanged *along* the chain. Subsequently, we present the first result from a five-leg $S = 1/2$ ladder.

In Chapter 6 we summarize the main results.

2. Optical Spectroscopy

Optical spectroscopy is a powerful technique to study the excitations of solids. The complex optical conductivity $\sigma(\omega)$ can be obtained by measuring the transmittance and/or reflectance of a material as a function of frequency. The real part of $\sigma(\omega)$ is a direct probe of the absorption and reflects the excitation spectrum of the solid.

The chapter on hand is organized as follows. As a start some basics are introduced in order to deduce the formulas used to analyze the experimental data. Afterwards the selection rules for electric-dipole transitions are briefly discussed. Finally, we focus on contributions to $\sigma(\omega)$ in Mott insulators, in particular on orbital and magnetic excitations.

2.1. Some Basics

In most cases the interaction of a solid with an electromagnetic wave can be described within the scope of linear-response theory [51]. Within the series of electric- and magnetic-multipole excitations the electric-dipole excitation is the strongest process.[1] Therefore we will focus on the electric-dipole component of the radiation in the following.

The fundamental linear-response functions which relates the electric field $\mathbf{E}$ to the displacement field $\mathbf{D}$ is the dielectric function $\varepsilon(\mathbf{k}, \omega)$ which in general depends on the wave-vector $\mathbf{k}$ and frequency ω. Since the considered wave lengths (magnitude of microns in the mid-infrared range) are big compared with typical lattice constants in solids (a few Ångstrøm), the electric-field vector of light hardly varies within one unit cell. Therefore the wave-vector dependence of the Fourier-transformed fields is negligible: $|\mathbf{k}| \propto 1/\lambda \approx 0$. Thus we write

$$\mathbf{D}(\omega) = \varepsilon(\omega)\mathbf{E}(\omega). \tag{2.1}$$

More general $\hat{\varepsilon} = \varepsilon_{ij}$ is a second-rank tensor (to be discussed in Sec. 2.1.1). The dielectric function is a complex quantity $\varepsilon = \varepsilon_1 + i\varepsilon_2$, which can be expressed by the complex index of refraction $N = \sqrt{\varepsilon(\omega)} = n(\omega) + i\kappa(\omega)$:

$$\varepsilon_1 = n^2(\omega) - \kappa^2(\omega); \quad \varepsilon_2 = 2n(\omega)\kappa(\omega). \tag{2.2}$$

---

[1] In general the transition probability is proportional to ω^{2l+1} with the frequency ω and the multipole order l [52]. The atomic radiative rate for magnetic-dipole transitions is five orders of magnitude smaller, compared with electric-dipole transitions [50, 53]. The rate for electric-quadrupole transitions is still even less [52].

Another related quantity is the optical conductivity $\sigma(\omega)$, which is used e.g. in the frequency-dependent form of Ohm's law

$$\mathbf{j}(\omega) = \sigma(\omega)\mathbf{E}(\omega). \tag{2.3}$$

The optical conductivity $\sigma = \sigma_1 + i\sigma_2$ can be expressed by the dielectric function ε and consequently by n and κ:

$$\sigma_1(\omega) = \frac{\omega}{4\pi}\varepsilon_2(\omega) = \frac{\omega}{2\pi}n(\omega)\kappa(\omega) \tag{2.4}$$

$$\sigma_2(\omega) = \frac{\omega}{4\pi}\left(1 - \varepsilon_1(\omega)\right) = \frac{\omega}{4\pi}\left(1 - n^2(\omega) + \kappa^2(\omega)\right). \tag{2.5}$$

By measuring the transmittance $T(\omega)$ of a sample with thickness d and the reflectance $R(\omega)$ at normal incidence, $n(\omega)$ and $\kappa(\omega)$ are determined solving the following linear system of equations [54]:

$$
\begin{aligned}
R(\omega) &= \frac{(n-1)^2 + \kappa^2}{(n+1)^2 + \kappa^2} \\
T(\omega) &= \frac{(1-R)^2\Phi}{1 - (R\Phi)^2} \\
\Phi(\omega) &= \exp\left(-2\omega\kappa d/c\right).
\end{aligned}
\tag{2.6}
$$

These equations are solely valid for a sample with plane-parallel surfaces in vacuum and unresolved interference fringes [54]. Using equations 2.4 and 2.5, the complex optical conductivity can be calculated.

In the case of very small sample dimensions a measurement of the reflectance is difficult and inaccurate. Because the main interest of this work is the analysis of weak, often dipole-forbidden features in the mid-infrared range, an estimate of the absorption is often very useful. Because the reflectance of an semiconductor in this energy range, above vibrational lattice modes and below the band gap, is small and nearly constant, the transmittance is approximately [55]

$$T \approx (1 - R)^2 \exp\left(-\alpha(\omega)d\right), \tag{2.7}$$

with the linear absorption coefficient $\alpha = 2\omega\kappa/c$. Then the absorption of a sample is described qualitatively by

$$\alpha(\omega) \approx -\ln T/d + 2\ln\left(1 - R\right)/d \approx -\ln T/d + \text{const.} \tag{2.8}$$

2.1.1. Anisotropic Samples: the Dielectric Tensor

The formulas given in the last section are solely valid for non-magnetic isotropic or cubic materials. Then the tensor $\hat{\varepsilon} = \varepsilon_{ij}$ has just one entry and reduces to the dielectric function mentioned above. In general, the electric field $\mathbf{E}$ and the displacement field $\mathbf{D}$ point in different directions in an anisotropic medium, i.e. are

not parallel vectors. In this case the dielectric function has to be replaced by the complex dielectric tensor

$$\hat{\varepsilon}(\omega) = \begin{pmatrix} \varepsilon_{xx}(\omega) & \varepsilon_{xy}(\omega) & \varepsilon_{xz}(\omega) \\ \varepsilon_{yx}(\omega) & \varepsilon_{yy}(\omega) & \varepsilon_{yz}(\omega) \\ \varepsilon_{zx}(\omega) & \varepsilon_{zy}(\omega) & \varepsilon_{zz}(\omega) \end{pmatrix}. \tag{2.9}$$

For non-magnetic materials ($\mu_r = 1$) the $\hat{\varepsilon}(\omega)$ tensor is symmetric, i.e. $\varepsilon_{ij} = \varepsilon_{ji}$, even for anisotropic materials. Therefore it is always possible to find a set of axes (a basis $\{x, y, z\}$) such that the real as well as the imaginary part of $\hat{\varepsilon}$ have diagonal form. The direction of the principal axes of the real and imaginary part are not necessarily the same, but for crystal symmetries at least as high as orthorhombic the two sets of axes coincide. Confining ourselves at first to these materials the complex dielectric tensor can be written as

$$\hat{\varepsilon}_{\mathrm{orthorhombic}} = \begin{pmatrix} \varepsilon_{xx}(\omega) & 0 & 0 \\ 0 & \varepsilon_{yy}(\omega) & 0 \\ 0 & 0 & \varepsilon_{zz}(\omega) \end{pmatrix} \tag{2.10}$$

with $\varepsilon_{ii} = \varepsilon_{ii}^1 + i\varepsilon_{ii}^2$ ($i = x, y, z$). The chosen basis is clearly related to the crystal structure, i.e $\{x, y, z\} = \{a, b, c\}$, where the latter are the crystallographic axes. Therefore all optical constants (all entries of $\hat{\varepsilon}$) for an orthorhombic crystal can be determined experimentally using linearly polarized light parallel to the three crystallographic axes. Then the formulas given in the former section can be used component-wise, e.g. $E_i = \varepsilon_{ii} D_i$ with $i = a, b, c$ and complex functions $\varepsilon_{ii}(\omega)$. Accordingly, the real part of the optical conductivity, mostly given in this work in the form 'σ_1 for $E \parallel i$' is determined by the imaginary part of ε_{ii} (see Eq. 2.4). However, in this work we also consider compounds which exhibit a monoclinic space group. The linear dielectric response of a monoclinic compound is described by the tensor [56–58]

$$\hat{\varepsilon}_{\mathrm{monoclinic}} = \begin{pmatrix} \varepsilon_{xx}(\omega) & 0 & \varepsilon_{xz}(\omega) \\ 0 & \varepsilon_{yy}(\omega) & 0 \\ \varepsilon_{xz}(\omega) & 0 & \varepsilon_{zz}(\omega) \end{pmatrix} \tag{2.11}$$

with the monoclinic angle being β (standard notation), $y \parallel b$, $z \parallel c$, and $x \perp c$ lying in the ac plane.[2] The tensor 2.11 can be decomposed into a scalar ε_b along the b axis and a two-dimensional tensor

$$\hat{\varepsilon}_{ac} = \begin{pmatrix} \varepsilon_{aa} & \varepsilon_{ac} \\ \varepsilon_{ac} & \varepsilon_{cc} \end{pmatrix} \tag{2.12}$$

describing the optical response within the ac plane. Due to the monoclinic angle $\beta \neq 90°$, the direction of the principal axes of $\hat{\varepsilon}_{ac}$ depends on the frequency and do not coincide for the real and imaginary part.

---

[2]Equivalent, the coordinate system can be chosen $y \parallel b$, $z \parallel a$, and $x \perp a$ within the ac plane.

On of the most famous models of the dielectric function is the Drude-Lorentz (DL) model, which we will use particularly when analyzing phonon spectra. In terms of DL oscillators the components of $\hat{\varepsilon}$ $(i, j = x, y, z)$ can be expressed through [56]

$$\varepsilon_{ij}(\omega) = \varepsilon_{ij}^{\infty} + \sum_{k=1}^{N} \frac{M_{ki} M_{kj}}{\omega_{0k}^2 - \omega^2 - i\gamma_k \omega} \tag{2.13}$$

where $\omega_{0k}, \gamma_k, M_{ki} M_{kj}$ are the frequency, damping coefficient, and effective dipole moment corresponding to the kth of N infrared-active modes. The constant $\varepsilon_{ij}^{\infty}$ reflects the contribution from high-frequency electronic excitations. Often the DL dielectric function (diagonal entries of $\hat{\varepsilon}$ for at least orthorhombic symmetry) is also rewritten with the plasma frequency ω_p [54]:

$$\varepsilon(\omega) = \varepsilon^{\infty} + \sum_{k=1}^{N} \frac{\omega_{pk}^2}{\omega_{0k}^2 - \omega^2 - i\gamma_k \omega}. \tag{2.14}$$

2.2. Electric-Dipole Transitions and Selection Rules

As stated in the beginning of this chapter, the optical conductivity allows to study the excitations of a solid. This section will give a brief overview of contributions to the optical conductivity in Mott insulators and the corresponding absorption mechanisms. In particular, we will focus on orbital and magnetic excitations which are the subject of the present thesis. As a start, the quantum-mechanical description of an absorption process is explained and helpful selection rules are discussed.

Electric-dipole transitions are the quantum-mechanical equivalent to the classical dipole oscillator. An electric-dipole transition between two states, an initial state Ψ_i (ground state) and a final state Ψ_f (excited state), is allowed if it is accompanied by a change of the dipole moment. This means that an incident electric field can induce a transition from Ψ_i to Ψ_f if the expectation value M_{if} of the dipole operator $\hat{p} = \{\hat{x}, \hat{y}, \hat{z}\}$ is non-vanishing:

$$M_{if} = \langle \Psi_f | \hat{p} | \Psi_i \rangle = \int \Psi_f^* \, \hat{p} \, \Psi_i \, d\mathbf{r} \neq 0. \tag{2.15}$$

The strength of the transition, i.e. the transition rate, is proportional to M_{if}^2 and the density of states ρ_f of the final state (Fermi's golden rule):

$$W_{if} = \frac{2\pi}{\hbar} |M_{if}|^2 \rho_f. \tag{2.16}$$

From the properties of the wave functions Ψ_i and Ψ_f, the selection rules for electric-dipole transitions can be deduced [59]. They are summarized in Tab. 2.1 and justified as follows:

Table 2.1.: Selection rules for electric-dipole transitions [59].

	Quantum number	Selection rule	comment
Rigorous rules	parity	$P_i \cdot P_f = -1$	parity changes
	J	$\Delta J = 0, \pm 1$	except $0 \leftrightarrow 0$
	M	$\Delta M = 0, \pm 1$	except $0 \leftrightarrow 0$ for $\Delta J = 0$
Negligible configuration interaction	l	$\Delta l = \pm 1$	
LS coupling only	S	$\Delta S = 0$	spin state does not change
	L	$\Delta L = 0, \pm 1$	except $0 \leftrightarrow 0$

- **Parity:** Because the dipole operator $\hat{p} = \{\hat{x}, \hat{y}, \hat{z}\}$ is odd, the wave functions of the initial and final states must have opposite parity (assuming that parity is a good quantum number).

- **Orbital quantum number:** The parity of the spherical harmonics is equal to $(-1)^l$. Hence the parity selection rule implies that Δl must be an odd number. A detailed evaluation of the overlap integrals yields $\Delta l = \pm 1$. In the case of LS coupling the selection rule reads $\Delta L = 0, \pm 1$, except from transitions from initial states with $L = 0$ to final states with $L = 0$. In the case of J is a good quantum number $\Delta J = 0, \pm 1$ ($0 \not\leftrightarrow 0$) has to be applied.

- **Spin quantum number:** An optical transition must not change the spin, stated by the spin selection rule $\Delta S = 0$.

- **Magnetic quantum number:** The selection rule for the magnetic quantum number depends on the polarization state of the incident electric field, e.g. for unpolarized light $\Delta M = 0, \pm 1$ has to be applied.

Electric-dipole transitions which obey these selection rules are so called *dipole-allowed* transitions.

2.2.1. Group-Theoretical Considerations

For crystalline solids, group theory is a very helpful tool because an electric-dipole transition of e.g. a Bloch electron can be forbidden by the crystal symmetry. Moreover, group theory gives clear predictions for the number and symmetry of the observable modes (e.g. phonons, see Sec. 2.4.1). A detailed introduction can be found in [60, 61].

Table 2.2.: Representation products of the irreducible representations of the orthorhombic point group D_{2h} (mmm). The bold marked entries are possible finial states of dipole-allowed transitions.

$\otimes$	A_g	B_{1g}	B_{2g}	B_{3g}	A_u	B_{1u}	B_{2u}	B_{3u}
A_g	A_g	B_{1g}	B_{2g}	B_{3g}	A_u	$\mathbf{B_{1u}}$	$\mathbf{B_{2u}}$	$\mathbf{B_{3u}}$
B_{1g}	B_{1g}	A_g	B_{3g}	B_{2g}	B_{1u}	$\mathbf{A_u}$	$\mathbf{B_{3u}}$	$\mathbf{B_{2u}}$
B_{2g}	B_{2g}	B_{3g}	A_g	B_{1g}	B_{2u}	$\mathbf{B_{3u}}$	$\mathbf{A_u}$	$\mathbf{B_{1u}}$
B_{3g}	B_{3g}	B_{2g}	B_{1g}	A_g	B_{3u}	$\mathbf{B_{2u}}$	$\mathbf{B_{1u}}$	$\mathbf{A_u}$
A_u	A_u	B_{1u}	B_{2u}	B_{3u}	A_g	$\mathbf{B_{1g}}$	$\mathbf{B_{2g}}$	$\mathbf{B_{3g}}$
B_{1u}	B_{1u}	A_u	B_{3u}	B_{2u}	B_{1g}	$\mathbf{A_g}$	$\mathbf{B_{3g}}$	$\mathbf{B_{2g}}$
B_{2u}	B_{2u}	B_{3u}	A_u	B_{1u}	B_{2g}	$\mathbf{B_{3g}}$	$\mathbf{A_g}$	$\mathbf{B_{1g}}$
B_{3u}	B_{3u}	B_{2u}	B_{1u}	A_u	B_{3g}	$\mathbf{B_{2g}}$	$\mathbf{B_{1g}}$	$\mathbf{A_g}$

At first we consider a molecule with a given point symmetry at a specific ionic site. Whether an electronic transition is forbidden or not can be derived from the product of the irreducible representations of the initial state $\Gamma(\Psi_i)$ and the representation of the dipole operator $\Gamma(\hat{p})$ for the given point group. If this product $\Gamma(M)$ contains the irreducible representation of the final state $\Gamma(\Psi_f)$, the transition is allowed. This selection rule can be expressed as:

$$\Gamma(M) = \Gamma(\Psi_i) \otimes \Gamma(\hat{p}) \supset \Gamma(\Psi_f). \tag{2.17}$$

For each of the 32 crystallographic point groups the product of the irreducible representations and those transforming as the dipole operator are tabulated [62–64].

As an example we consider the orthorhombic point group D_{2h} (mmm). The number of irreducible representations for the D_{2h} point group is eight: A_g, B_{1g}, B_{2g}, B_{3g}, A_u, B_{1u}, B_{2u}, and B_{3u}.[3] The irreducible representation of the dipole operator in the D_{2h} point group is $\Gamma(\hat{p}) = B_{1u} \oplus B_{2u} \oplus B_{3u}$, e.g. $\Gamma(\hat{x}) = B_{3u}$, $\Gamma(\hat{y}) = B_{2u}$, and $\Gamma(\hat{z}) = B_{1u}$ [64]. From the representation products given in Tab. 2.2 the dipole-allowed transitions could be read directly. The bold entries are possible final states of dipole-allowed transitions, e.g. a transition from an initial state with $\Gamma(\Psi_i) = A_g$ to a final state with $\Gamma(\Psi_f) = B_{1u}$ is dipole-allowed in z polarization with the dipole operator representation $\Gamma(\hat{z}) = B_{1u}$. In particular Tab. 2.2 shows that transitions from even (odd) to even (odd) states are dipole-forbidden.[4] This holds true whenever inversion symmetry is present at the particular ionic site.

The symmetry of a crystal is generally described by its space group which contains the usual symmetry elements as the point groups and additionally specific elements like translations, screw axes, and glide planes. Each atom in the unit cell occupies a specific site which is characterized by one or more symmetry elements, defining the

---

[3]The used nomenclature for the irreducible representations goes back to Robert S. Mulliken. For a detailed description of the specific symbols see e.g. [65] and the footnote in Sec. 4.1.

[4]Even states are labeled by an index g ('gerade'), while odd states are labeled by u ('ungerade').

site group. The site group is always one of the 32 crystallographic point groups and must be a subgroup of the space group. To deduce selection rules in crystals, e.g. for phonon modes observed in Raman and infrared spectra, one has to go beyond the description for molecules. Two approaches are reported in the literature: the site group analysis and the factor group analysis [62, 66]. An example for the application of the latter is given in Sec. 2.4.1.

2.3. Electronic Excitations

For a classical undoped semiconductor the lowest electronic excitations are inter-band transitions between the valance band and the conduction band. In the case of many transition-metal oxides with half-filled d shells insulating behavior was found which cannot be explained in a conventional band-structure picture. The latter predicts a metallic ground state for these materials in contrast to experimental observations. Hence the Mott-Hubbard model [3, 4] has been introduced, taking into account the strong electron-electron interaction in these materials. The single-band Mott-Hubbard model reads

$$\mathcal{H} = -t \sum_{<i,j>;\sigma} c_{i,\sigma}^{\dagger} c_{j,\sigma} + U \sum_{i} n_{i,\uparrow} n_{i,\downarrow}, \qquad (2.18)$$

with t is the hopping-matrix element between nearest-neighbor sites i and j, and U is the Coulomb repulsion between two electrons on the same site. The operator $c_{i,\sigma}^{\dagger}$ creates an electron on site i with spin $\sigma \in \{\uparrow, \downarrow\}$ and $n_{i,\sigma} = c_{i,\sigma}^{\dagger} c_{i,\sigma}$ is the corresponding number operator. The first term is the conventional band term, describing the energy gain due to delocalization of the electrons. The second term pays regard to the strong electron-electron correlations with a sizeable d-d Coulomb interaction U between two electron on the same site. These correlations are pronounced in several transition-metal compounds, due to the fact that the radial wave functions of the $3d$ orbitals are less expanded, giving rise to only narrow bands. The on-site Coulomb repulsion U becomes significant as soon as U is of the order of the band width, i.e. $U/W \sim 1$ at $T = 0$ [67]. The simplest form of the Mott-Hubbard Hamiltonian 2.18 is not always sufficient because it implies that the band gap is a d-d gap, which is not correct for most of the late transition-metal compounds, e.g. Co, Ni, or Cu
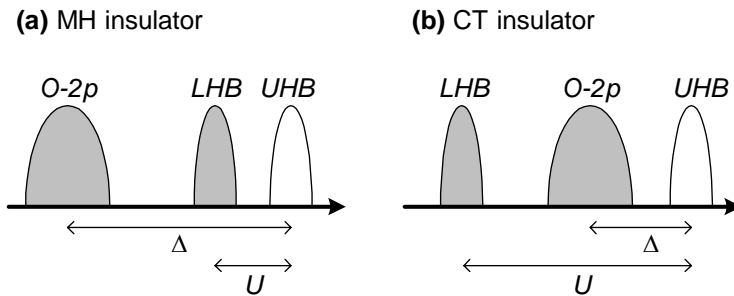
Figure 2.1.:
Schematic density of states for (a) Mott-Hubbard (MH) and (b) charge-transfer (CT) insulators.

oxides. Here another charge-fluctuation energy is relevant, the charge-transfer energy Δ. Whether the gap is of d-d or charge-transfer type depends on the relative size of U and Δ, summarized in the so-called Zaanen-Sawatzky-Allen scheme [68]. For the sake of simplicity we have specified just the single-band Hubbard model in Eq. 2.18, but a consistent description of the above-mentioned transition-metal oxides certainly requires more realistic models, which include the orbital degrees of freedom. To take into account several transition-metal d orbitals as well as the oxygen orbitals, instead of Eq. 2.18 a multi-band Hubbard model has to be considered [69–71]. In addition Eq. 2.18 can be extended to include hopping between next-nearest neighbors and/or third nearest neighbors [72].

The most important difference to conventional semiconductors is that the internal degrees of freedom, spin and orbital, still survive in Mott insulators [5].[5] The lowest electronic excitation corresponds to the transfer of one electron from the lower Hubbard (LHB) band to the upper Hubbard band (UHB), and accordingly for a charge-transfer insulator from the LHB to the oxygen-$2p$ band (Fig. 2.1). The excitation in a Mott-Hubbard insulator then is equivalent to the transfer of one electron from one metal ion site with $3d^n$ electron configuration to another one, i.e., from $3d^n 3d^n$ to $3d^{n-1} 3d^{n+1}$, and for a charge-transfer insulator from $3d^n 2p^6$ to $3d^{n+1} 2p^5$.

Optical spectroscopy is a powerful tool to investigate such interband excitations (for a review see e.g. [71, 73]). In particular, the famous f-sum rule gives clear predictions. This rule relates the integrated optical conductivity directly to the density of charged objects, their charge and mass:

$$\int_0^\infty Re(\sigma(\omega))d\omega = \sum_i \frac{\pi q_i^2 N_i}{2m_i V}, \tag{2.19}$$

where N_i denotes the number of charges, V the volume, m_i the masses of the particles in the solid, and q_i their charges. It reflects the fundamental property that also in strongly correlated matter the number of electrons is conserved [73].

2.4. Low-Energy Excitations in Correlated Insulators

The optical conductivity of undoped correlated insulators below the onset of interband excitations is purely determined by phonons, magnetic excitations, and orbital excitations.

---

[5]Because in a Mott insulator the double occupation of an orbital costs U, different spin and orbital states are available for an electron. In a conventional semiconductor the orbitals are occupied with spin-up and spin-down in the same manner.

2.4.1. Phonons

The optical conductivity for energies below $\sim 100\,\text{meV}$ (FIR) is dominated by lattice vibrations. Due to the strong phonon absorption, measurements of the transmittance are only possible with powder samples or extremely thin samples ($<10\,\mu\text{m}$), which are hard to prepare. Therefore the phonon spectra are typically investigated by reflectance measurements and a subsequent Kramers-Kronig analysis to determine the optical conductivity [74].

Again, group theory is very helpful, because the number and symmetry of dipole-allowed phonon modes for a given space group can be calculated by applying the so-called factor group analysis [62, 66]. The factor group approach assumes that all modes of a crystal can be determined by considering only one unit cell [66]. The atomic positions in the unit cell build the basis for the formation of reducible representations of a group composed of the symmetry elements of the unit cell. The advantage is that the factor group is always isomorph to one of the 32 crystallographic point groups, for which the character tables are known [62–64] (e.g. for D_{2h} see Tab. 2.2). As an example for the factor-group analysis, the phonon modes of YVO$_3$ are briefly discussed in the following. The symmetry of YVO$_3$ is described by the space group *Pbnm* using the Herman-Mauguin symbols, or by D_{2h}^{16} using the
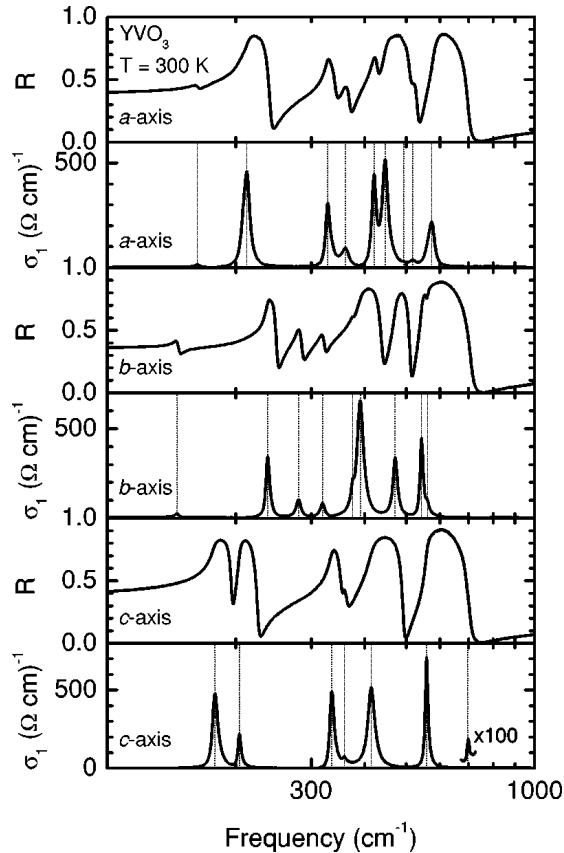
Figure 2.2.:
Room-temperature reflectance and corresponding optical conductivity of YVO$_3$ for polarization to the three crystallographic directions, i.e. $E \parallel a$, b, and c. Dashed lines indicate positions of the TO phonon frequencies. There are nine, nine, and seven modes for the a, b, and c axes, respectively, in agreement with the *Pbnm* symmetry. Reproduced from [75].

Schoenflies notation [29, 76]. The number of formula units per unit cell is $Z = 4$. Therefore 3 acoustic and $3(N-1) = 3(4 \cdot 5 - 1) = 57$ optical modes are expected. To determine the irreducible representations, the symmetry-equivalent positions termed by the Wyckoff symbols have to be considered. For YVO_3 they are $4a$ for $V(1)$, $4c$ for $Y(1)$ and $O(1)$, and $8d$ for $O(2)$. The site symmetry is C_i ($\bar{1}$) for $4a$, C_s (m) for $4c$, and C_1 (1) for $8d$, respectively. Then the full representation M is given by the product of (multiples of) the representations for the site symmetries [63]

$$
\begin{aligned}
M &= M(C_1) + 2M(C_s) + M(C_i) \\
&= 3A_g + 3A_u + 3B_{1g} + 3B_{1u} + 3B_{2g} + 3B_{2u} + 3B_{3g} + 3B_{3u} \\
&\quad + 2(2A_g + 1A_u + 1B_{1g} + 2B_{1u} + 2B_{2g} + B_{2u} + B_{3g} + 2B_{3u}) \\
&\quad + 3A_u + 3B_{1u} + 3B_{2u} + 3B_{3u} \\
&= 7A_g + 8A_u + 5B_{1g} + 10B_{1u} + 7B_{2g} + 8B_{2u} + 5B_{3g} + 10B_{3u}.
\end{aligned}
$$

These include 3 acoustic modes $B_{1u} + B_{2u} + B_{3u}$, 24 Raman-active modes $7A_g + 5B_{1g} + 7B_{2g} + 5B_{3g}$, 25 infrared-active modes $9B_{1u} + 7B_{2u} + 9B_{3u}$ and 8 silent modes $8A_u$.[6] The infrared vibrations split into $9 B_{1u}$ ($E \parallel a$), $9 B_{3u}$ ($E \parallel b$), and $7 B_{2u}$ ($E \parallel c$). The number as well as the proposed polarization dependence of the infrared-active modes is verified by reflectivity measurements on YVO_3 at room temperature [75] (see Fig. 2.2). Another example of the application of the factor group analysis is given in Sec. 5.2.2, where we consider the phonon modes of $SrCuO_2$.

2.4.2. Orbital Excitations: Local Crystal-Field Excitations vs. Orbitons

Strongly correlated transition-metal compounds are discussed as promising candidates for the observation of novel orbital excitations, which exhibits a collective, dispersive nature. For the identification of the so-called orbitons by optical spectroscopy it is crucial to exclude that local, single-site excitations or excitons are responsible for the observed absorption features. For a single ion embedded in a host crystal the crystal-field theory often gives clear predictions for local crystal-field excitations. Therefore molecular-orbital theory or cluster calculations including the full Madelung potential are often helpful tools. In the subsequent paragraphs possible absorption processes for local and collective orbital excitations are consecutively introduced.

Local Crystal-Field Excitations

In many cases it is justified to describe $3d$ transition-metal compounds in a local limit because the double occupancy of a single site costs about U (or Δ), which is about several eV. The local crystal field of the surrounding ligands affects the energy

---

[6]Neither infrared nor Raman active.

level diagram on the metal ion site and has to be considered. The ligand field lifts the degeneracy of the atomic $3d$ levels, depending on its symmetry. For example, the $3d$ levels of a $3d^1$ ion in an octahedral ligand field split into a lower-lying triply degenerate t_{2g} and a higher-lying two-fold degenerate e_g level. The energy difference of these levels is denoted by $10Dq$. For the same ion in a tetrahedral ligand field the order of the levels is reversed, i.e. the e_g are lower in energy than the t_{2g} levels. However, for more than one electron the level diagram is much more complicated because the electron-electron interaction has to be taken into account (see Fig. 4.28). For the case of an octahedral ligand field the corresponding multiplets for $3d^n$ ions are tabulated in the so-called Sugano-Tanabe-Kamimura diagrams [77].

Restricting ourselves to the easiest case of a $3d^1$ ion in an octahedral ligand field, the single electron occupies the t_{2g} level in the ground state. Then the lowest excitation corresponds to a transfer of the electron to the e_g level. This is a local excitation, no charge is transferred between different metal ions. For the contribution to the optical conductivity the selection rules for electric-dipole transitions have to be considered (Tab. 2.1). As mentioned above d-d excitations are *not* infrared-allowed because of the orbital and parity selection rule. However, in real spectra d-d transitions are often observed because there are effects that evade the strict selection rules. The most relevant, according to Ref. [78], are the following:

(i) Spin-orbit coupling can be responsible for the admixing of terms of different spin multiplicity which gives rise to the observation of spin-forbidden transitions. As an example we consider a transition from $^1W + \alpha\,^3Z$ to $^3X + \beta\,^1Y$ with α and β being the mixing coefficients that are parameterized by the spin-orbit coupling coefficient λ

$$\langle\,^3X + \beta\,^1Y|\hat{p}|^1W + \alpha\,^3Z\rangle = \underbrace{\langle\,^3X|\hat{p}|^1W\rangle}_{=0} + \underbrace{\alpha\beta\langle\,^1Y|\hat{p}|^3Z\rangle}_{=0} \qquad (2.20)$$
$$+ \underbrace{\alpha\langle\,^3X|\hat{p}|^3Z\rangle}_{\neq 0} + \underbrace{\beta\langle\,^1Y|\hat{p}|^1W\rangle}_{\neq 0}.$$

While terms with different spin multiplicity vanish, terms with equal ones contribute to the optical conductivity, and it is said that the transition '$^1W \rightarrow\,^3X$' becomes weakly 'allowed', certainly depending on λ.

(ii) If no inversion symmetry is present at the metal site it is possible that proper wave functions involve a mixture of e.g. d and p wave functions:

$$\langle d' + \delta p'|\hat{p}|d + \gamma p\rangle = \underbrace{\langle d'|e\mathbf{r}|d\rangle}_{=0} + \underbrace{\gamma\delta\langle p'|e\mathbf{r}|p\rangle}_{=0} + \underbrace{\gamma\langle d'|e\mathbf{r}|p\rangle}_{\neq 0} + \underbrace{\delta\langle p'|e\mathbf{r}|d\rangle}_{\neq 0}. \quad (2.21)$$

The last two terms survive both, the parity and the orbital selection rule to the extent that the mixing coefficients γ and δ are non-zero in non-centric complexes. In this case spin-allowed transitions are observed with intensities
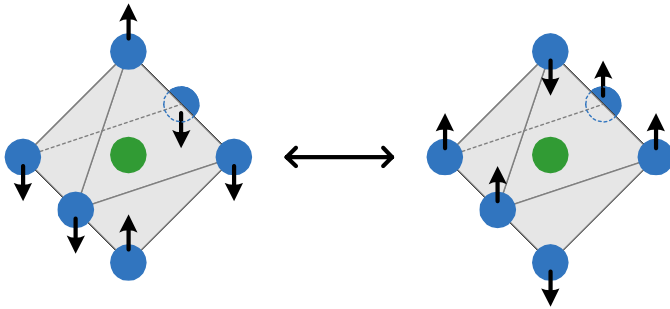
Figure 2.3.:
An *ungerade* vibration of an octahedron. Reproduced from [78].

100 times larger than spin-forbidden ones, but still a few orders of magnitude less intense than fully allowed transitions.

(iii) If inversion symmetry is present on the metal site the only way to avoid the selection rules is the simultaneous excitation of a phonon that removes the center of inversion. An example of such a symmetry-breaking mode is depicted in Fig. 2.3. At any instant during the vibration, *d-p* mixing can occur and, in the manner of Eq. 2.21, a *d-d* transition can become partially allowed. Because the *p-d* mixing is smaller in the dynamic environment than in the static one, the intensity of phonon-induced transitions is expected to be noticeably weaker.

(iv) In real samples, inversion symmetry may additionally be broken by impurities or other lattice imperfections, e.g. oxygen non-stoichiometry. However, the contribution is expected to be still much smaller than the phonon-assisted one in the case of low impurity concentrations.

If the crystal structure shows no inversion symmetry on the transition-metal site (item (ii)), clear predictions on the polarization dependence of the orbital absorption features can be made. The (local) symmetry of the mixed states can be determined unambiguously within a point-charge model [15, 79]. In the case of a simultaneously excited odd-symmetry phonon (item (iii)), the polarization dependence is less pronounced because in general phonons of arbitrary polarization may contribute, i.e. p_x, p_y as well as p_z character can be mixed into the $3d$ states. In order to determine the orbital excitation energy, the phonon energy has to be subtracted from the experimentally observed peak position. However, different phonons may participate in breaking the symmetry. Typically, stretching and bending modes of the metal-oxygen bonds are most effective in doing so (Fig. 2.3). These modes have typical energies of the order of $50\text{-}80\,\mathrm{meV}$ for the compounds considered here.

Independent of the mechanism to evade the strict selection rules, the absorption bands identified with local *d-d* transitions typically show a pronounced broadening due to the Franck-Condon effect [80–83]. The Franck-Condon principle assumes that a crystal-field transition most likely occurs without changing the positions of the nuclei [78], i.e. crystal-field transitions taking place in about $10^{-15}\,\mathrm{sec}$ are essentially instantaneous compared with the time scale of nuclear motions of about $10^{-13}\,\mathrm{sec}$. Therefore the transition is vertical in the corresponding energy diagram
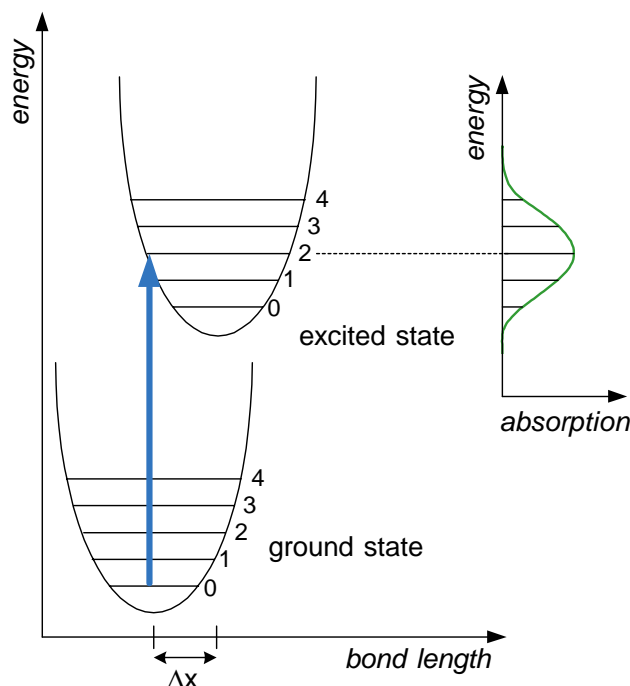
Figure 2.4.: Sketch of the Franck-Condon principle depicting the energy diagram of a crystal-field transition coupled to phonons. The two curves (parabola) corresponds to the orbital ground (excited) state and represents the harmonic potential of the lattice. The horizontal bars within each potential represent the energy levels of the normal modes of the lattice. Strong bonds correspond to steep potentials with large spacings between the energy levels, while weak bonds have shallow potentials with smaller separations. The horizontal offset Δx between the minima of the two potentials indicates that the relaxed bond length differs between ground state and excited state. The upward arrow represents the absorption process. Quantum mechanically, the intensity of a vibronic transition is proportional to the square of the overlap integral between the phonon wave functions of the two orbital states that are involved in the transition. By summing up the contributions from the different excited states, a broad absorption peak is obtained as shown on the upper right side of the figure. Due to the phonon dispersion and the contribution of phonons with different energies, the sharp sub-bands of individual excited states are usually not resolved in a solid, yielding a single broad band. For details see [80–83] and text books, e.g. [54, 78].

(for details we refer to the caption of Fig. 2.4). At low temperatures an incident phonon yields a transition from the zero-vibronic ground state that ends in a higher vibronic excited state (higher, with respect to the relaxed one). The probability for the transition to end in a particular vibronic excited state is determined by the overlap of the phonon wave functions at the initial and final state. In Fig. 2.4 the

transition from the relaxed ground state (0) to the second-vibronic excited state (2) is the most likely. But also the transitions to the 0, 1, 3, 4 states may exhibit a finite probability, resulting in several absorption lines for the corresponding *d-d* transition.

Beside spin-orbit coupling (item (i)), there is another possibility to evade the spin selection rule. This is, to excite two spin-carrying modes simultaneously such that the total spin equals zero. An orbital excitation from e.g. a triplet to a singlet state may gain finite spectral weight by the simultaneous excitation of a magnon, giving rise to a so-called magnon-exciton sideband [84–86]. Typically, the spectral weight of these processes is even smaller than in the cases where spin was not involved. But, occasionally some bands which otherwise are expected to be weak are observed to be quite strong, e.g. when the energy of a spin-forbidden excitation is comparable with those of spin-allowed transitions [78]. Such an effect can be due to the so-called 'intensity stealing' where a spin-forbidden transition acquires intensity by 'stealing' from e.g. a spin-allowed (e.g. as described above in item (i)) or a charge-transfer band.

Collective Orbital Excitations (Orbitons)

As mentioned in the beginning, transition-metal oxides with strong electron correlations are promising candidates for the observation of so-called orbital waves or orbitons [11, 17, 87–89]. It is known for a long time that the orbital degree of freedom shows long-range order, the so-called orbital order [34]. There exists different mechanisms that can cause orbital order, e.g. the electron-lattice coupling, the Jahn-Teller interaction [6], or a purely electronic (exchange) interaction [90]. The latter is of particular interest, because in general any kind of order from a spontaneously broken symmetry gives rise to new elementary excitations [91]. In the case of e.g. long-range magnetic order these new excitations are the well-known spin waves or magnons. In analogy, a collective orbital excitation is termed orbital wave and its quantized objects are called orbitons [11, 17, 87–89].

Orbital and spin degrees of freedom are intimately connected with each other
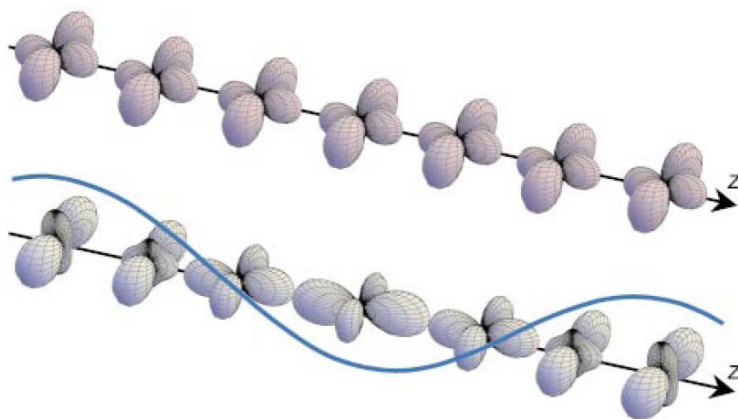
Figure 2.5.:
Illustration of an orbital wave (bottom) for a ferroorbital ordered ground state (top). Taken from [11].

[92], giving rise to an active discussion on novel quantum phenomena related to the orbital degrees of freedom, such as orbital liquids [8, 93, 94], an orbital Peierls state [9, 16, 28, 95, 96], and orbital waves [11, 17, 87–89].

All these phenomena are based on the approach that the (virtual) exchange interaction between orbitals on adjacent sites with strong Coulomb interaction causes the interaction between the orbitals, i.e. the superexchange between orbitals is the dominant interaction. However, this means on the other hand that the coupling of the orbitals to the lattice may play a crucial role [97].

Considering the five d orbitals, in a cubic crystal field the d levels split into the triply-degenerate t_{2g} levels xy, xz, yz and a doubly-degenerate e_g levels $x^2 - y^2$ and $3z^2 - r^2$. In the following we will briefly address the doubly-degenerate orbital system with e_{2g} symmetry. Here the orbital degree of freedom is usually represented by pseudospins $\mathbf{T}_i$ [34, 90] and the interaction between spins and pseudospins can be described by the generalized Heisenberg Hamilton [7]

$$\mathcal{H} = \sum_{i,j} J_{ij}(\mathbf{T}_i, \mathbf{T}_j)\, \mathbf{S}_i \cdot \mathbf{S}_j + K_{ij}(\mathbf{T}_i, \mathbf{T}_j) \tag{2.22}$$

with the exchange interactions $J_{ij}(\mathbf{T}_i, \mathbf{T}_j)$ and $K_{ij}(\mathbf{T}_i, \mathbf{T}_j)$. Because the symmetry of orbital Hamiltonians in a lattice is not continuous but discrete, orbital excitations in orbitally ordered states are gapped [98]. The dispersion and the excitation energy may be of comparable magnitude, giving rise to interesting new effects. For a detailed review on the topic of orbital physics and in particular on orbital excitations and their observation see Ref. [5, 13–15, 34, 90, 99] and references therein.

So far, optical conductivity has been considered only rarely as a tool for the investigation of orbitons [15]. The optical spectra of a crystal-field excitation with a dispersion much smaller than its energy is in principle very similar to the local crystal-field excitation of a single impurity ion embedded in a host lattice, mentioned in the former section. The optical spectroscopy is restricted to the observation of excitations with momentum $k = 0$ and the selection rules are the same as for the case of a single impurity ion. However, the dispersion may be experimentally observable due to a coupling between orbitons and phonons. Recent theoretical studies on a (simplified) one-dimensional model have revealed the formation of a dispersive orbiton-plus-one-phonon resonance which carries significant spectral weight, even though the orbiton-phonon coupling is not small [97]. Another possibility is the simultaneous excitation of two modes, e.g. a magnon sideband [100] or a two orbiton excitation. Here, only the total momentum $k_{\text{tot}} = k_1 + k_2$ of the two participating excitations needs to be zero. Therefore contributions from the entire Brillouin zone of the orbital excitation have to be summed up.

One of the problems that complicate or even may preclude an experimental observation of orbitons is the Jahn-Teller coupling of the orbital degree of freedom to the lattice, which usually is rather strong [98]. The onset of orbital order is always accompanied by a structural phase transition with a reduction of symmetry,

the so-called cooperative Jahn-Teller effect [90]. However, octahedrally coordinated t_{2g} systems are more promising, because the coupling to the lattice is expected to be weaker compared with e_g systems.[7] The difference between orbital t_{2g} and e_g systems in this context are described in detail in [34, 90], but we also address this point again, later in Chap. 4. There we will also discuss a possible infrared-active two-orbiton excitation for the intermediate phase of RVO$_3$ with $R =$ Y, Ho, and Ce.

2.4.3. Magnetic Excitations: Phonon-Assisted Multimagnon Absorption

An important part of this work is concerned with the investigation of magnetic excitations of low-dimensional spin systems (Chap. 5). A more general introduction to low-dimensional spin systems and their excitation is given in Sec. 5.1. Here, we consider the optical absorption process.

To study the magnetic excitation of low-dimensional spin systems we analyze the so-called phonon-assisted multimagnon absorption observed in the optical conductivity. Meanwhile, optical spectroscopy of phonon-assisted multimagnon absorptions is an established technique to investigate low-dimensional spin systems and a lot of progress has been made by different theoretical and experimental groups [44–46, 101–107]. In particular the theoretical predictability of the line shape turns phonon-assisted multimagnon absorption into a powerful tool [44, 45, 108, 109]. For a review see Ref. [110].

The low-energy properties of magnetic insulators are often well described by the so-called Heisenberg model, which is a low-energy version of the Hubbard model, if the orbital degree of freedom is negligible.[8] For a given spin dimensionality of $n = 3$ ($S^2 = S_x^2 + S_y^2 + S_z^2$) and just nearest-neighbor interactions, the Heisenberg Hamiltonian reads

$$\mathcal{H} = \sum_{i,j} J \, \mathbf{S_i S_{j+1}}, \qquad (2.23)$$

with localized quantum spins $\mathbf{S_i}$ and a magnetic exchange coupling J. For the systems of interest to us, the magnetic exchange is realized by superexchange via an intermediate oxygen ion.

In general, excitations changing the spin quantum number S are not allowed in optical spectroscopy (see the spin selection rule in Tab. 2.1). Therefore only transitions with $\Delta S = 0$ can be observed. Restricting ourselves to antiferromagnetic $S = 1/2$ systems, the lowest order process justifying $\Delta S = 0$ is the excitation of two spin flips, which translates in leading order to two magnons, two triplons or two

---

[7]The electron density pointing towards the ligands is much smaller for t_{2g} orbitals compared with e_g orbitals.

[8]In the copper oxides of interest, the Cu^{2+} ion with $3d^9$ electron configuration is quadratic-planar coordinated by four oxygens, which yields a crystal field splitting comparable to that depicted in Fig. 5.6. The remaining hole occupies the $d_{x^2-y^2}$ orbital which is lower in energy than the other d orbitals.

spinons (see Sec. 5.1). Beside the conservation of the total spin, the total energy as well as the total momentum $k_{\text{total}} \approx 0$ have to be conserved. The latter follows from the dispersion $\omega = ck/\sqrt{\varepsilon}$ of the photons. Because the velocity of light c is huge, the energy of photons and magnetic excitations is solely comparable for very small k values, i.e. at $k \approx 0$. Furthermore, the excitation of two spin flips on nearest-neighbor sites is not dipole-allowed if there is inversion symmetry in-between two magnetic ions. If so, the Madelung potentials are equal on both lattice sites and the excitation of two spin flips, equivalent to the exchange of two neighboring up and down spins yields no dipole moment. Nonetheless, in the middle of the nineties Lorenzana and Sawatzky have shown that dipole-allowed excitation of two magnons is possible if additionally a symmetry-breaking phonon is excited [44, 45]. This simultaneous excitation of three quasi-particles is also referred to as 'bimagnon-plus-phonon' absorption, or more general as phonon-assisted multimagnon absorption. With a virtually excited phonon the Heisenberg Hamilton operator is given by

$$\mathcal{H} = \sum_{i,\delta} J_{i,\delta}(\mathbf{E}, u_{i+\delta/2}) \, S_i S_{i+\delta} \tag{2.24}$$

with the superexchange coupling J depending on the electric field $\mathbf{E}$ and the ionic displacement u due to the phonon. Then the dipole moment $P = \partial\mathcal{H}/\partial E \neq 0$ is non-vanishing. For illustration we consider a local superexchange process along a linear Cu-O-Cu bond in the presence of an electric field $\mathbf{E} = \{E, 0, 0\}$ parallel to the x direction (Fig. 2.6). The in-between lying oxygen ion is shifted by u along x. The presence of the electric field and the displacement yield a change of the Madelung potentials on the Cu ions. Following Lorenzana and Sawatzky [44, 45] the effective superexchange coupling is obtained by considering the Cu-O-Cu hopping in fourth-order perturbation theory and performing a Taylor expansion up to the first order in E and u, i.e. restricting ourselves to linear spectroscopy and 'plus-*one*-phonon' absorption processes. As usual, the superexchange J is defined by the difference between the singlet and triplet states. The result reads

$$J(\mathbf{E}, u) = J_0 - E(q_I + 2q_A)u \tag{2.25}$$

with the effective charges q_I, q_A describing one-phonon-plus-multi-magnon processes and the superexchange coupling J_0 for $\mathbf{E} = 0$ and $u = 0$. The configuration for an electric field parallel to the linear Cu-O-Cu bond in shown in Fig. 2.6. The change of the inter-site hopping is approximately linear in u: $t_{pd} \mapsto t_{pd} \pm \alpha u$. The change of the Madelung potentials in the presence of $\mathbf{E}$ and u is

$$
\begin{aligned}
E_d^{\text{Cu1}} &= E_d + \beta u \\
E_p^{\text{O}} &= E_p + eE\left(\frac{a}{2} + u\right) \\
E_d^{\text{Cu2}} &= E_d - \beta u + eEa
\end{aligned}
$$
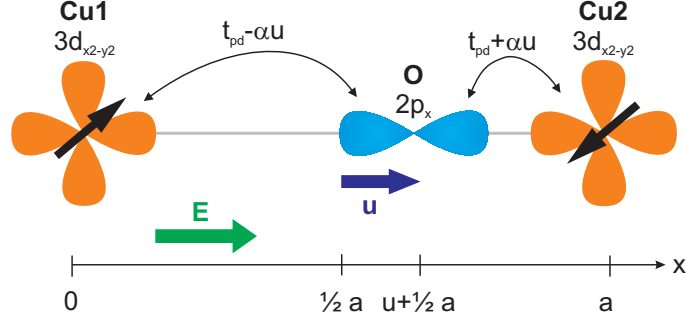
Figure 2.6.: Illustration of the virtual hopping processes along a linear Cu-O-Cu bond in the presence of an electric field E, relevant for the calculation of the superexchange $J(E, u)$ (see text). The simultaneous excitation of a phonon yields a shift u of the oxygen ion e.g. along the x direction. With the virtually excited phonon the Madelung potentials on neighboring Cu ions are no more equal, and the so-called phonon-assisted multimagnon absorption is dipole allowed.

with the elementary charge e, and Madelung potentials E_d, and E_p for $\mathbf{E} = 0$ and $u = 0$. Then J_0 and the effective charges q_I, q_A read

$$J_0 = \frac{4t_{pd}^4}{\Delta_{pd}^2} \left(\frac{2}{\epsilon} + \frac{1}{U_d} \right)$$

$$q_I = -e\frac{8t_{pd}^4}{\Delta_{pd}^2} \left(\frac{1}{\Delta_{pd}} \left(\frac{1}{U_d} + \frac{2}{\epsilon} \right) + \frac{2}{\epsilon^2} \right) \qquad (2.26)$$

$$q_A = -e\frac{4t_{pd}^4}{\Delta_{pd}^2} a\beta \left(\frac{2}{\Delta_{pd}^2} \left(\frac{1}{U_d} + \frac{2}{\epsilon} \right) + \frac{1}{U_d} \left(\frac{1}{\Delta_{pd}} + \frac{2}{U_d} \right)^2 \right)$$

with the transfer integrals t_{pd}, the charge transfer energy Δ_{pd}, the on-site Coulomb repulsion U_d for the double occupation of the copper $d_{x^2-y^2}$ orbital, the energy $\epsilon = U_p + 2\Delta_{pd}$ for the double occupation of the oxygen p_x orbital, and a is the Cu-O distance (see also Fig. 2.6). From Eq. 2.25 it appears that the terms proportional to the effective charges q_I and q_A contribute to the dipole moment. Referring to [44], the so-called 'isotropic'[9] term proportional to q_I, can be understood as a correction to the charge at the rest position of the oxygen ion ($a/2$ in Fig. 2.6). In particular this correction is spin-dependent, i.e. just for antiparallel spins a double occupation of the oxygen in the intermediate hopping state is possible. The 'anisotropic' term, proportional to q_A, is only present for an in-plane electric field, i.e. the situation we considered in Fig. 2.6. The effect of q_A is to create an effective displacement of charge from the left to the right copper ion. Again this process is spin-dependent,

---

[9]In Ref. [44] different configurations of the direction of the electric field and different oxygen displacements in 2D are considered. It is found that the term proportional to q_I is relevant for each configuration, and therefore called 'isotropic'.

Table 2.3.: Set of standard parameter for Cuprates. Taken from [111, 112].

Δ_{pd}	U_d	U_p	U_{pd}	t_{pd}	ϵ
3.6 eV	8 eV	6 eV	0.5-1 eV	1.2 eV	13.2 eV

because also the double occupation of the Cu site is not possible for two parallel spins.

The spectral weight of the multimagnon-plus-phonon contribution to the optical conductivity is proportional to the size of the effective charges. Referring to [113], q_A is expected to be dominating due to the high covalency in the considered cuprates. The term q_A/e can be estimated by

$$
\begin{aligned}
\frac{q_A}{e} &\approx -a\beta \frac{4t_{pd}^4}{\Delta_{pd}^2} \left[\frac{3}{\Delta_{pd}^2 U_d} + \frac{4}{\Delta_{pd}^2 \epsilon} + \frac{4}{\Delta_{pd} U_d^2} + \frac{4}{U_d^3} \right] \\
&\approx -0.05 \frac{a\beta}{\text{eV}} \approx -0.1 \frac{U_{pd}}{\text{eV}} \approx -0.05 \ldots -0.1,
\end{aligned}
\tag{2.27}
$$

using the set of standard parameters summarized in Tab. 2.3. For the last approximation we used $a\beta \approx 2U_{pd}$, from an estimate within a point charge model [45, 112]. Using the same set of parameters we obtain $J_0 \approx 177$ meV. Experimental values of J_0 vary from ~ 125 meV [104] in two-dimensional La_2CuO_4 and 180-260 meV [46, 47] in the spin chain compound Sr_2CuO_3. However, it should be noted that Eq. 2.27 is a quite rough estimate. For real systems, the considered hopping is insufficient, i.e. higher-order hopping terms in Eq. 2.25 (e.g. t_{pd}^6) may yield a non-negligible contribution.

For an interpretation of the line shape of the magnetic contribution to the optical conductivity $\sigma(\omega)$ it is important to note that the momentum conservation of the phonon-assisted multimagnon absorption is $k = k_{\text{phonon}} + k_{\text{2magon}}$. As a consequence the magnetic contribution to $\sigma(\omega)$ shows a weighted average over the entire magnetic Brillouin zone weighted by the phonon form factor. From the energy conservation it follows that the energy position of the magnetic peaks is shifted by the energy of the phonon $\hbar\omega_{\text{phonon}}$.

3. Experimental Setup

3.1. Fourier Transform Spectroscopy

The major part of the measurements reported in this work have been carried out with the Fourier transform spectrometer Bruker IFS 66/v. The setup is schematically depicted in Fig. 3.1. We distinguish between the far-infrared (FIR), mid-infrared (MIR), near-infrared (NIR), visible-light (VIS), and ultraviolet-light (UV) region, see Tab. 3.1. Also the corresponding range of some typical units are summarized in Tab. 3.1. In particular, it is common to use wave numbers $\omega = 1/\lambda$ instead of the wave length λ in infrared spectroscopy.

The optical path through the spectrometer is as follows (compare to Fig. 3.1). The lamp is a white-light source. In order to cover the large spectral range mentioned, different light sources are required to gain enough intensity. Optionally a mercury-vapor lamp[1], a globar[2], and a tungsten lamp are available in our setup. The intensity of these lamps is optimized for the FIR, MIR, and NIR-VIS range, respectively. The emitted light hits a parabolic mirror focussing it on the so-called aperture wheel. This is a rotatable wheel made of steel with holes of 0.5 mm up to 8 mm in diameter to choose the focus size. Reflected by a second parabolic mirror, a parallel beam enters the Michelson interferometer and passes the beam splitter.[3] One part of the beam is reflected off the beam splitter and hits the fixed mirror, the other part is transmitted and hits the movable mirror (scanner). The two back-reflected parts of

---

[1] Here we use the heat radiation emitted from the quartz enclosure.

[2] A globar is an electrically heated ($> 1000°$C) bar typically made of silicon carbide. The phrase 'globar' is build by the abridgment of the words 'glow' and 'bar'.

[3] There are different beam splitters available, each optimized for the respective spectral range.

Table 3.1.: Considered spectral ranges and typical units used in this work.

Spectral range	Abbr.	$\omega\,[\text{cm}^{-1}]$	$\lambda\,[\mu\text{m}]$	$E\,[\text{eV}]$
far infrared	(FIR)	50 - 500	200 - 20	0.0006 - 0.06
mid infrared	(MIR)	500 - 5000	20 - 2.0	0.06 - 0.6
near infrared	(NIR)	5000 - 12000	2.0 - 0.8	0.6 - 1.5
visible light	(VIS)	12000 - 25000	0.8 - 0.4	1.5 - 3.1
ultraviolet light	(UV)	25000 - 50000	0.4 - 0.2	3.1 - 6.2
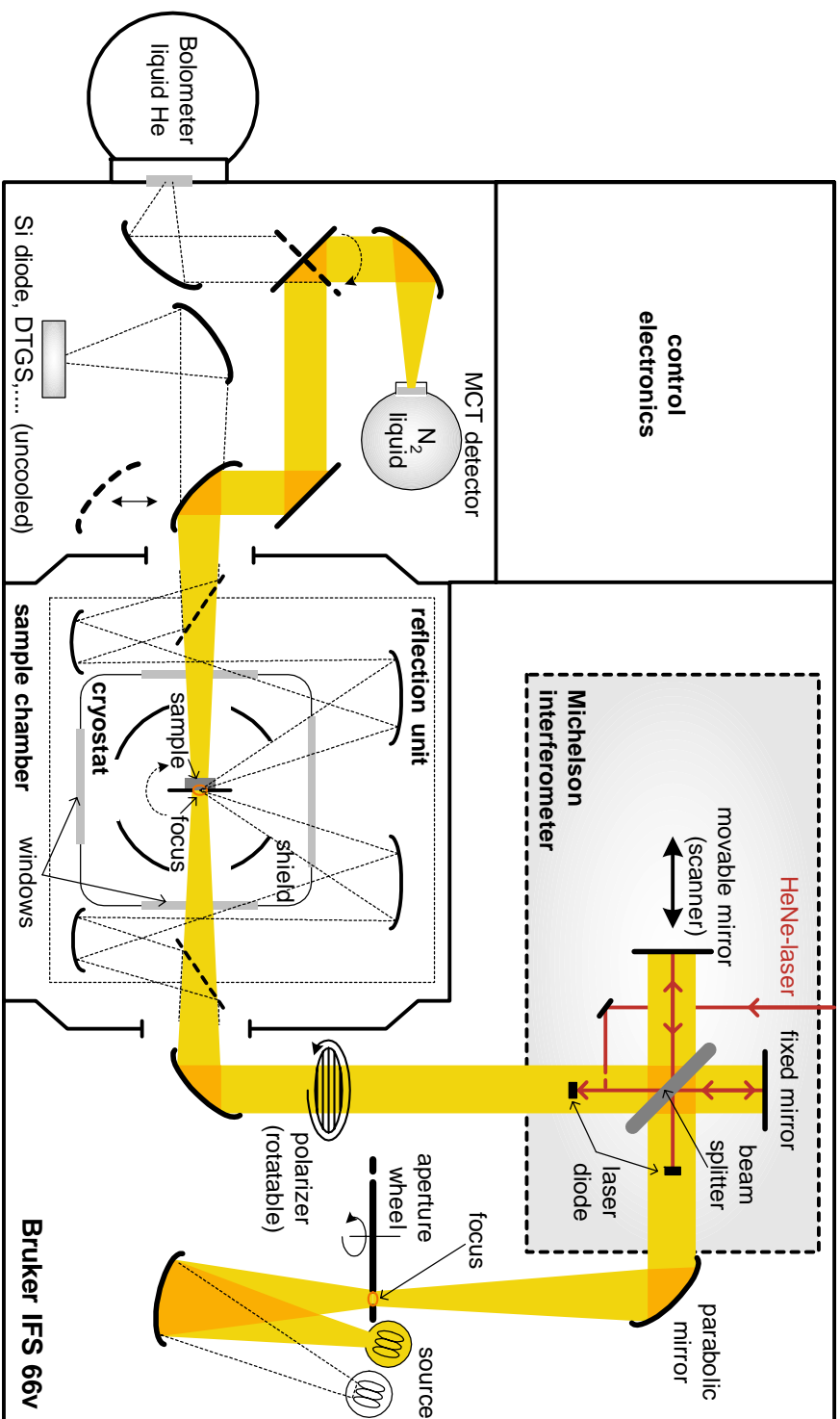
Figure 3.1.: Top view of the Fourier transform spectrometer Bruker IFS 66v. The optical path of the transmittance setup using the MCT detector is yellow colored. Dashed lines depict alternative optical pathes for a second source, the reflection unit, and different (interchangeable) detectors, respectively (for details see text).

the beam interfere with each other after passing the beam splitter a second time. By moving the scanner uniformly back and forth this gives a position(time)-dependent modulation of the intensity of the beam. By likewise sending the light of a HeNe laser with well known frequency through the interferometer, the position of the scanner can be determined in a very precise way.[4] Utilizing this time-modulated intensity of the light the interferogram (intensity vs. time) measured at the detector can be transformed into the spectrum (intensity vs. frequency) by performing a discrete Fourier transformation (for details see [114]).

Back to the optical path, the beam coming from the Michelson interferometer optionally passes a rotatable linear polarizer. The choice between different available polarizers depends on the considered spectral range. The polarizers for the FIR and MIR region consist of a transparent material (PE or BaF_2) coated with an optical grating. Above $5500\,\mathrm{cm}^{-1}$ a Glan-Thompson prism has been used. After passing the polarizer, in the transmission setup the beam is directly focused on the sample position in the cryostat which is located inside the sample chamber. For the measurement of the reflectance, four additional mirrors, fixed on the so-called reflection unit, are needed to focus the beam on the sample (rotated by 90°). The angle of incident of 11° is chosen as small as possible.[5] Within the cryostat the pressure has to be less than $10^{-5}\,\mathrm{mbar}$ to avoid the formation of ice layers on the sample surface. Because the pressure within the spectrometer is roughly $10\,\mathrm{mbar}$, the cryostat is separated from the sample chamber by transparent windows made of polyethylene and potassium bromide (KBr) for the FIR and MIR/NIR setup, respectively. The transmitted light of the sample is diverted and focused to the detector by further mirrors. For the different spectral ranges different detectors, e.g. bolometer, MCT, Si-diode, and Ge-diode are available.

3.1.1. Measurement of the Transmittance and Reflectance

To determine the transmittance $T(\omega)$ and reflectance $R(\omega)$ of a sample the measurement of a reference spectrum is necessary:

$$T(\omega) = \frac{S(\omega)_{\mathrm{sample}}}{S(\omega)_{\mathrm{ref}}}, \qquad R(\omega) = \frac{S(\omega)_{\mathrm{sample}}}{S(\omega)_{\mathrm{ref}}} \cdot R(\omega)_{\mathrm{ref}}. \tag{3.1}$$

Here $S(\omega)$ labels the single-channel spectrum of the sample and the reference, respectively. The reflectance measurement have been performed using a gold (MIR,NIR) or aluminum (NIR,VIS) mirror as reference material. Because the reflectance of gold and aluminum is not $100\,\%$ in the considered frequency range, the reflectance has to be corrected with the known reflectance of the reference material $R(\omega)_{\mathrm{ref}}$. If not indicated separately, the frequency (energy) resolution of the spectra obtained in this work is $5\,\mathrm{cm}^{-1}$ ($0.6\,\mathrm{meV}$).

---

[4]The intensity of the laser light is measured separately with two laser diodes (see Fig. 3.1).

[5]Far away from the Brewster angle, the Fresnel formulas at normal incidence are still valid, since $R_\perp \approx R_\parallel$ for small angles of incidence.
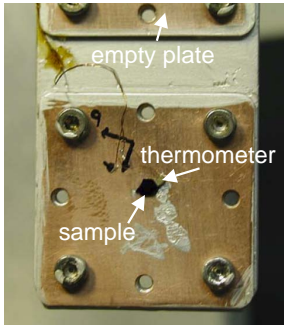
Figure 3.2.:
The aperture plates for the sample (lower position) and for the reference (upper position) are mounted above each other on the copper sample holder. During the measurement on YVO$_3$ additionally a second thermometer was directly attached on the sample surface to pick up the true sample temperature.

When using the cryostat the sample is fixed with conductive silver paint[6] on top of an aperture plate made of copper (Fig. 3.2). As reference for the transmittance measurements an identical empty aperture plate is used. Accordingly, for the reflectance measurement the reference mirror is fixed on the aperture plate with conductive silver paint. Both aperture plates, that for the sample and that for the reference are mounted above each other on the copper sample holder which is fixed on the cold finger. The single-channel spectra $S(\omega)_\mathrm{sample}$ and $S(\omega)_\mathrm{ref}$ are easily measured by driving the cold finger up and down.

With the described cryostat, measurements in a temperature range from 5 K to 800 K are possible. The control of the temperature as well as the measurement of the sample temperature is typically done by a FeRh thermometer mounted directly above the copper sample holder. It turned out that the thermal coupling of the cold finger to the RVO$_3$ samples was sometimes bad. We suppose that the heat conductivity of some samples was bad because they crack while passing the first-order structural phase transition (Sec. 4.1). To collect the real sample temperature a second thermometer (Cernox, LakeShore Cryotronics Inc.) has been directly attached on the sample surface (Fig. 3.2). It turned out that in general both thermometers are in good agreement.

3.1.2. Problems to Take Care of

In the following some problems to take care of are listed. This is just a small selection of effects which are the most relevant for the present work. For more detailed information see [114, 115]. Note, that the problems discussed in the following in general cause just *small* effects which can be either easily corrected or mostly be neglected.

Correction for the BaF$_2$ Polarizer The BaF$_2$-polarizer has a slightly frequency-dependent leakage. With increasing frequency the contribution of the perpendicular

---

[6]G 3303A, Plano GmbH

polarization is less blocked and has to be corrected. Instead of equation 3.1

$$T^{P1} = \frac{S^{P1}_{\text{sample}} - p(\omega) \cdot S^{P2}_{\text{sample}}}{S^{P1}_{\text{ref}} - p(\omega) \cdot S^{P2}_{\text{ref}}} \tag{3.2}$$

is used to calculate the transmittance T^{P1} (or reflectance) for polarization $E \parallel P1$. The correction file $p(\omega)$ (extinction ratio vs. frequency) for the BaF_2 polarizer was determined in our group from measurements on a highly anisotropic sample [115].

Fabry-Perot Fringes   In transmittance measurements on thin polished samples often multiple-beam interferences, so-called Fabry-Perot fringes, are observed. They result from multiple reflections at both coplanar faces of the sample. Let us consider a plane-parallel plate with refractive index n, as indicated in Fig. 3.3. The incoming beam with angle of incident α is refracted when entering the plate by an angle of refraction β. The total optical path difference between the two out-coming parallel beams (1) and (2) is $\Delta = n \cdot 2l - n_{vac} \cdot d'$ ($n_{vac} = 1$). From simple trigonometry follows: $l = d/\cos\beta$ and $d' = 2l \sin\beta \sin\alpha$. Using Snell's law the path difference is $\Delta = 2nd \cos\beta$. At nearly normal incidence the equation is further simplified: $\alpha \approx \beta \approx 0 \rightarrow \cos\beta \approx 1$. The condition for constructive interference then is:

$$\Delta \approx 2nd \stackrel{!}{=} m \cdot \lambda, \tag{3.3}$$

where $m = 0,1,2,...$ is the order of the maxima. In $T(\omega)$ two adjacent interference maxima at $\omega_1 = \lambda_1^{-1}$ and $\omega_2 = \lambda_2^{-1}$ occur for

$$2nd = m\lambda_1 = (m+1)\lambda_2, \tag{3.4}$$

i.e. when m times the wave length λ_1 exactly fits $2nd$, the wave length λ_2 must even fit one time more. Thus for the distance $\Delta\omega = \omega_2 - \omega_1$ between adjacent maxima in $T(\omega)$ follows

$$\Delta\omega = \frac{1}{2nd}. \tag{3.5}$$

To summarize, on the one hand, fringes restrict the resolution of the transmittance measurement to $\Delta\omega$, on the other hand, fringes are often very useful to check the thickness d of the sample, or to estimate the index of refraction n and the reflectance $R \approx (n-1)^2/(n+1)^2$, respectively.
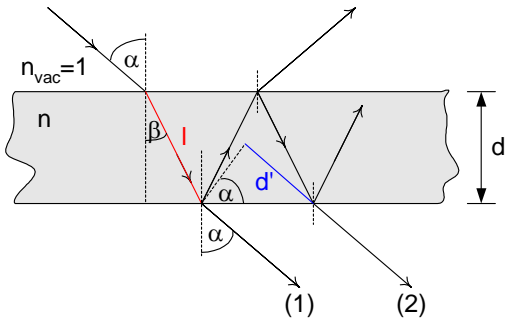
Figure 3.3.:
Fabry-Perot fringes result from multiple reflections at opposite surfaces of the sample. The optical path difference between parallel beams at normal incidence is approximately $\Delta \approx 2nd$ (see text).

Absorption of Ice To avoid the formation of thick ice layers when cooling the samples, typically pressures of 1×10^{-6} mbar within the cryostat are ensured. Nevertheless, sometimes small signatures of the absorption of ice/water are found. In the case of the $R\mathrm{VO_3}$ measurements, those clearly originate from ice films deposited on the sample surface when cooling.[7] Fortunately, these absorptions are relatively sharp and small, and at least well investigated in astrophysics (see e.g. [117, 118]). Depending on temperature and pressure, $\mathrm{H_2O}$ ice exists in several modifications [119]. The natural modification is hexagonal ice. In particular, at normal pressure

---

[7]Inclosures of water in the hygroscopic KBr windows may are sometimes the cause for similar absorptions.
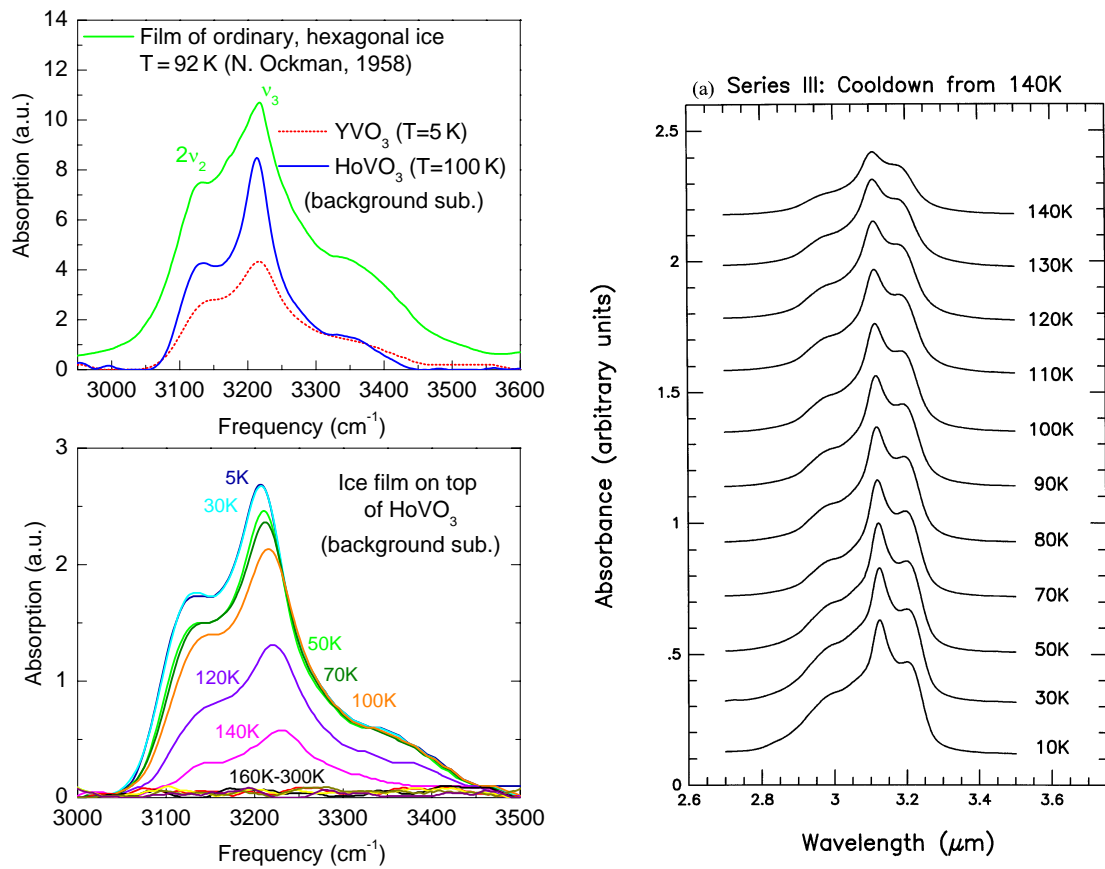
Figure 3.4.: Absorption bands of hexagonal ice, observed in measurements on $\mathrm{YVO_3}$ and $\mathrm{HoVO_3}$ (left upper and lower panel). In comparison with the literature, the two absorption bands at $3200\,\mathrm{cm^{-1}}$ and $3125\,\mathrm{cm^{-1}}$ can be assigned to the stretching mode of the O-H bond (ν_3 and $2\nu_2$) in films of ordinary hexagonal ice [116]. The observed temperature dependence of these peaks (left lower panel) is in good agreement with recent data of Maldoni *et al.* of a $0.1\,\mu\mathrm{m}$ $\mathrm{H_2O}$ film initially deposited at $140\,\mathrm{K}$ (right panel; taken from [117]). For details see text.

and low temperatures an amorphous-to-crystalline phase transition above $110\,\mathrm{K}$ is well-documented [119]. The strongest absorption band of ice is found at about $3200\,\mathrm{cm}^{-1}$. On the left hand side in Fig. 3.4 the corresponding features observed in measurements on YVO_3 and $HoVO_3$ are shown. In comparison with the transmittance data of a film of ordinary hexagonal ice measured by N. Ockman [116], two absorption bands at $3200\,\mathrm{cm}^{-1}$ and $3125\,\mathrm{cm}^{-1}$ can be assigned to the stretching mode of the O-H bond (ν_3 and $2\nu_2$ mode). It is found, that the absorption spectra depends on the preparation temperature of the ice film [117]. If the film is deposited at $140\,\mathrm{K}$, above the amorphous-to-crystalline phase transition it stays irreversibly crystalline in the hexagonal phase, at least at low pressure. This is affirmed by the observed temperature dependence (left bottom and right panel in Fig. 3.4). With decreasing temperature the peaks shift to higher frequencies/lower wavelengths, the shape becomes sharper, and the structure within it more prominent, contradictory to amorphous ice [117]. Above $140\,\mathrm{K}$ the absorption band disappears, as expected because under a pressure of $1.33 \cdot 10^{-7}\,\mathrm{mbar}$ ($1.33 \cdot 10^{-6}\,\mathrm{mbar}$) the melting temperature of ice is $153\,\mathrm{K}$ ($162\,\mathrm{K}$) [120].

3.1.3. Applying an External Magnetic Field

For YVO_3 the transmittance has additionally been determined as function of an external magnetic field. For that purpose, measurements were performed at the Grenoble High Magnetic Field Laboratory (GHFML) in France.[8] We considered the MIR and NIR frequency range in magnetic fields up to $17\,\mathrm{T}$ using two different setups. The measurements in the MIR range from $800\,\mathrm{cm}^{-1}$ up to $6000\,\mathrm{cm}^{-1}$ were performed using a Fourier transform spectrometer. In comparison with the standard setup described above, the intensity-modulated light coming from the Michelson interferometer is diverted by a concave mirror into a liquid-helium cryostat with a superconducting magnet. For this purpose a special probe was available at GHFML. A waveguide is used to bring down the light to the sample which is fixed on the sample holder with conducting silver paint in the center of the magnet. The maximum magnetic field of the superconducting magnet is $13\,\mathrm{T}$. Unfortunately, the waveguide does not work at shorter wavelengths. Therefore, the measurement in the NIR frequency range have been performed using a grating spectrometer (Raman setup at GHFML) with a white-light source. The probe in use was equipped with fiber optics guiding the light into a liquid-helium cryostat centered between the pole shoes of a resistive magnet. The maximum attainable field of the resistive magnet is $23\,\mathrm{T}$.

3.2. Alignment and Preparation of the Samples

For an exact determination of the optical conductivity, samples with plane surfaces are required to avoid scattering at the surfaces. For that purpose all samples were

---

[8]Special thanks go to our contact persons at GHFML, M. L. Sadowski and G. Martinez.

lapped, i.e. fine-grinded, and afterwards polished. Beside the removal of the surface roughness, this procedure guarantees the preparation of transmittance samples with two parallel surfaces in order to have a well-defined thickness. Additionally, polarization-dependent measurements of anisotropic samples imply an accurate orientation of the considered crystal surface.

3.2.1. Sample Alignment

The single crystals investigated in this work have been oriented using the Laue method (for detailed introduction see e.g. [121]). We typically use the backscattering setup, where the incoming polychrome ('white light') x-ray beam first passes the imaging plate and then hits the sample. Wavelengths fulfilling the Bragg condition are scattered at the lattice planes of the crystal. The backscattered monochromatic reflexes are detected by an image plate. Sometimes the interpretation of Laue pattern is difficult, in particular for crystal systems with lattice constants deviating from 90°. Therefore we performed simulations of the Laue pattern using the 'OrientExpress V3.3' software[9] in each case. Additionally, some sample orientations have been verified by single-crystal diffractometer measurements.[10]

3.2.2. Lapping & Polishing

Before polishing the samples to high gloss, the sample surfaces have to be lapped, i.e. fine-grinded. Both treatments, polishing and lapping have been done using a commercial polishing machine (Logitech PM2) which is available at our institute. The machine basically consists of an interchangeable turn table with a sample holder on top that allows an accurate control of the grinding pressure. For the fine-grinding process a lapping plate made of cast iron in combination with a suspension of abrasive aluminum-oxide powder (fused aluminum oxide, 3 micron, Logitech LDT) in water has been used. For the samples of $SrCuO_2$ which are sensitive to water, the suspension was replaced by aluminum-oxide powder in ethylene glycol (ethan diole, $HOCH_2CH_2OH$). The polishing plate in use is coated with a polyurethane foam, which has small holes to hold the suspension. Here an etch-polishing suspension with finer particles has been used (SF1, colloidal silica, Logitech LTD). For water-soluble samples a suspension of cerium-oxide polishing powder (0.5 micron, Logitech LDT) in ethylene glycol was available.

---

[9]by J. Laugier and B. Bochu (Laboratoire des Materiaux et du Génie Physique de l'Ecole Supérieure de Physique de Grenoble, France)

[10]Our best thanks go to M. Cwik (Institute of physics II, University of Cologne, Germany) for performing these measurements.

4. Orbital Excitations in Orbitally Ordered Vanadates

The chapter on hand is divided into three parts. At first the structural and physical properties of the RVO$_3$ compounds are introduced, then an experimental part follows, and finally the results are discussed in comparison to other experimental results and theoretical predictions.

4.1. The Compounds RVO$_3$ ($R =$ Y, Ho, Ce)

The oxovanadates RVO$_3$ with $R =$ rare-earth ion have recently attracted a lot of interest because of their unusual structural, orbital and magnetic properties [19, 20, 22–24, 26–32, 75, 122, 123]. Depending on the R ion the compounds undergo a series of temperature-induced phase transitions accompanied by a change of orbital and magnetic order.

Perovskite-type RVO$_3$ has a distorted orthorhombic crystal structure at room temperature, which emerges from the cubic cell by a tilting and rotation of the corner-sharing VO$_6$ octahedra, the so-called GdFeO$_3$ distortion (see Fig. 4.1). The room-temperature space group is $Pbnm$ (No. 62(2)).[1] The lattice constants result in

---

[1]We have choosen $Pbnm$ instead of the standard notation $Pnma$(No. 62) to retain the denotation
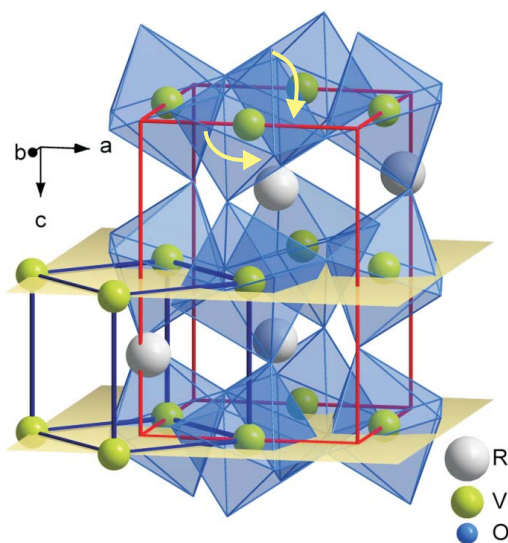
Figure 4.1.:
Room-temperature crystal structure of RVO$_3$. The rotation and tilting of the octahedra (marked by arrows) yield a lowering of the symmetry compared to the ideal cubic perovskite structure. For illustration the orthorhombic unit cell ($Pbnm$; red) and the cubic unit cell ($Pm\bar{3}m$; dark blue) are shown.
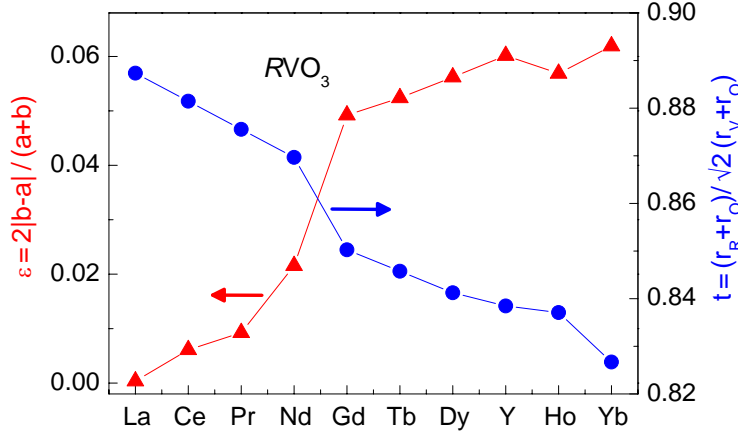
Figure 4.2.: Tolerance factor t for the $R\mathrm{VO_3}$ structure, defined by Goldschmidt [125] (right axis, blue curve). The values were obtained using the ionic radii of Ref. [126] for 8-fold coordination. On the left axis (red curve) the orthorhombic splitting ε at room temperature is displayed (values of a, b were taken from [25–27, 29–31].)

$a \sim b \sim \sqrt{2}a_c$ and $c \sim 2a_c$ with a_c being the lattice constant of the cubic perovskite (space group $Pm\bar{3}m$ (No. 221)). In first approximation, the deviation from the cubic parent structure can be estimated by the relative ionic sizes. For a comparison of the $R\mathrm{VO_3}$ compounds, the ionic radius of the R ion and its stability in twelvefold coordination (12 or 8+4) are crucial [124]. An empirical prediction for the size of the orthorhombic distortion is given by the tolerance factor t for perovskites defined by Goldschmidt [125]:

$$t = \frac{r_R + r_O}{\sqrt{2}(r_V + r_O)}.$$

To obtain this value we used the ionic radii of vanadium (r_V), oxygen (r_O) and the rare earth (r_R) ions from Ref. [126]. By geometry, the ideal cubic structure should have $t = 1$. The distorted perovskite structure occurs within the range $0.8 < t < 0.89$ [127].[2] As shown in Fig. 4.2 (right axis) the value of t is closest to 1 for $\mathrm{LaVO_3}$, and t continuously decreases with decreasing ionic radius, i.e. the distortion is much more pronounced for smaller R ions, in agreement with structural investigations [25–27, 29–31]. A second indicator is the so-called orthorhombic distortion ε defined by

$$\varepsilon = \frac{2|b - a|}{a + b},$$

reflecting the difference of the orthorhombic lattice constants a and b. As shown in Fig. 4.2 (left axis) the difference of a and b, obtained by [25–27, 29–31], is less than $0.5\,\%$ for $\mathrm{LaVO_3}$ whereas it is about $3\,\%$ for compounds with smaller rare-earth ions (Y, Ho, Yb). This gradual change from a nearly cubic to a distinctly distorted perovskite structure gives rise to various magnetic and orbital ordering patterns which have recently caused a lot of research activity [19, 24–32].

---

of the axes in the monoclinic low-temperature phase.

[2] The analysis of Goldschmidt strictly holds true just for purely ionic compounds [127].
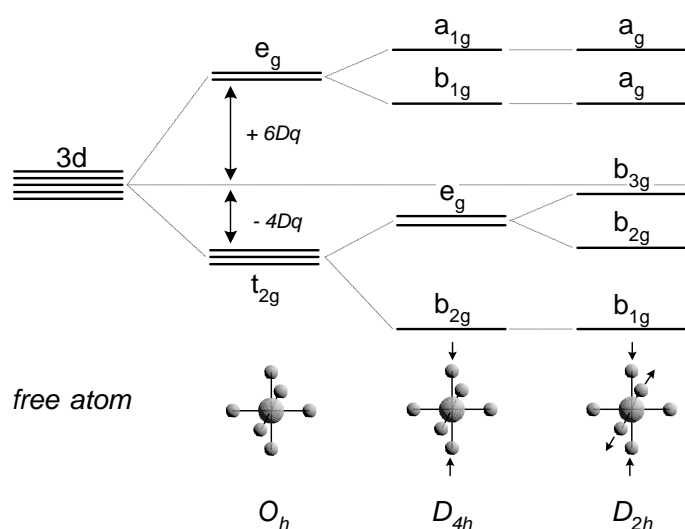
Figure 4.3.:
Illustration of the qualitative splitting of the five-fold degenerate atomic $3d$ levels in a crystal-field of O_h (cubic), D_{4h}, and D_{2h} symmetry (from left to right). In the cubic crystal field the levels split into a lower-lying triply degenerate t_{2g} level and a doubly degenerate e_g level by $10Dq$. The degeneracy of these levels is lifted by further lowering of the symmetry, e.g. due to a Jahn-Teller distortion of the octahedron.[3] Reproduced from [128].

Electronically, the undoped RVO_3 compounds are Mott insulators, with two electrons occupying the $3d$ shell according to a nominal valence of 3+ for the vanadium ion. The predominantly cubic crystal field of the surrounding oxygen-octahedron causes a splitting of the $3d$-levels into a lower-lying triply degenerate t_{2g}-level and a higher-lying doubly degenerate e_g level (O_h symmetry; see Fig. 4.3). The size of the t_{2g}-e_g splitting is given by the value of $10Dq$ which is ∼ 2 eV for YVO₃ [75]. The degeneracy of the t_{2g}-levels is further lifted due to a distortion of the octahedra, e.g. because of steric effects or the so-called Jahn-Teller (JT) distortion. The latter is expected, whenever degenerate orbitals are occupied in a non-uniform manner, e.g. two electrons occupying three initially degenerate t_{2g} orbitals. Under these conditions the energy gain by lowering two energy levels with respect to the third one is larger than the elastic energy required for the structural distortion, e.g. an elongation or a compression of the octahedron. This further lowering of the local symmetry (e.g. D_{4h} or D_{2h} (Fig. 4.3)) of one octahedron in a network of corner-sharing octahedra

---

[3]The used nomenclature for the irreducible representations goes back to Robert S. Mulliken, see e.g. [65, 129]. The used symbols are specified as follows:

- A and B are one-dimensional (non-degenerate) representations which are symmetric and antisymmetric with respect to a n-fold rotation about the principal axis (C_n), respectively. E and T denote doubly and triply degenerate species, respectively.

- The numerical index (1,2) specify wether a species is symmetric (index 1) or antisymmetric (index 2) under σ_v or C_2 about an axis perpendicular to the principal axis.

- If two species differ in the character of inversion i they are distinguished by index g ('gerade') and u ('ungerade').

Note that lower case letters a, b, e, t, ... are used for symbols describing the symmetry of one-electron systems (wave functions), while capitals A, B, E, T,... are usually used for many-electron systems.

(a) *a*-type JT

(b) *d*-type JT

z = 0

z = 0

z = ½

z = ½
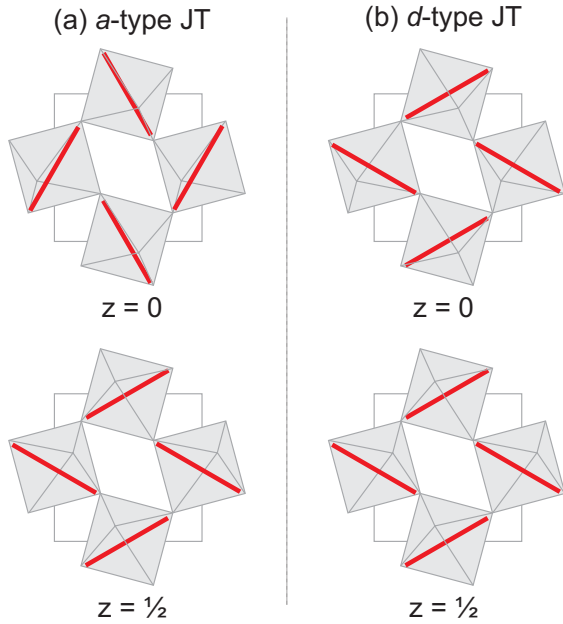
Figure 4.4.:
Sketch of the V-O bond-length anisotropy within the ab plane (in $Pbnm$) for (a) the a-type Jahn-Teller (JT) and (b) the d-type JT distortion [19]. Within each octahedron there are two short (not shown) and one long bond (red bar). The difference between a- and d-type JT distortion is the stacking pattern of the long bond along the c direction. While in the d-type phase the long bonds point in the same direction for $z = 0$ and $z = 1/2$, in the a-type phase they are rotated by 90° with respect to each other.

causes a collective distortion of all neighboring octahedra, the so-called collective JT effect. In the perovskite-type lattice two collective JT distortion patterns are possible, a- and d-type [19] (Fig. 4.4). These differs with respect to the stacking of the elongated octahedra along the c direction. For an a-type distortion the long bonds within the ab plane are stacked alternatingly along c, i.e. the long bond on a particular site is rotated by 90° compared to the neighboring one. In the d-type JT distorted structure the arrangement of the long bonds is equal for neighboring sites along the c direction.

The different JT distortion patterns give rise to different orbital orderings (OO). From a d-type JT distortion a C-type OO is expected, i.e. the occupation of neighboring orbitals alternates within the ab plane, while along c equal orbitals are occupied (see also Fig. 4.7(a)). An a-type JT effect yields G-type OO which corresponds to an alternating occupation of neighboring orbitals along all three directions (Fig. 4.7(b)). According to the Goodenough-Kanamori-Anderson rules [92, 130, 131], the different structures favor different types of spin order (SO), G-type for the d-type distortion and C-type for the a-type distortion.

From Hartree-Fock calculations [19] it has been shown, that perovskite-type compounds, which additionally have a sufficiently large GdFeO$_3$-type distortion, tent to have the d-type JT distortion. As mentioned above the size of the GdFeO$_3$-type distortion is tuned by the R ion radius in the RVO$_3$ compounds.

Considering the low-temperature physical properties, the RVO$_3$ series can be divided into two groups: compounds with the larger R ions La and Ce and the compounds with smaller ions Y, Pr - Lu [23]. By lowering the temperature the latter undergo a structural second-order phase transition at T_{OO} which is accompanied by the onset of orbital ordering. At T_N Néel ordering sets in, and at T_S a structural
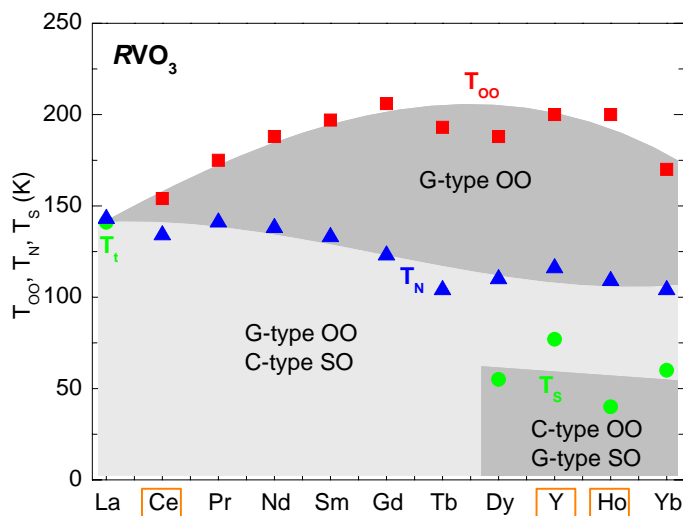
Figure 4.5.:
Spin-orbital phase diagram of RVO_3 ($R = $ Y, La-Yb). The compounds with $R = $ Ce, Y, and Ho are considered in this thesis. Squares, triangles, and circles indicate the transition temperatures of G-type orbital ordering (T_{OO}), C-type spin ordering (T_N), and G-type spin/C-type orbital ordering (T_S, T_t), respectively. Partly reproduced from [23]. The values for T_{OO}, T_N, and T_t for $LaVO_3$ and $CeVO_3$ are taken from Ref. [22] (see also Sec. 4.1.3).

first-order phase transition accompanied by a change of orbital and spin ordering is observed in the smaller R ion compounds (Dy, Y, Ho, and Yb). In particular T_N continuously increases with increasing radius of the R ion, from 104 K for $YbVO_3$ [27, 132] to 143 K for $LaVO_3$ [22]. This behavior can be explained by the decrease of the octahedra tilt with increasing R ion radius, which in turn yields a increasing of the V-O-V superexchange. For the systems with large R ions $LaVO_3$ and $CeVO_3$, in particular for the latter, controversial scenarios have been reported [22, 23]. From a comparison of specific heat and magnetization data it is reported that in $LaVO_3$ and $CeVO_3$ the magnetic ordering takes place first with decreasing temperature, and subsequently the structural phase transition accompanied by G-type OO occurs [23]. For $LaVO_3$ this is in agreement with results from synchrotron x-ray diffraction [22]. However, for $CeVO_3$ the onset of G-type OO is found clearly above the spin ordering temperature [22]. We will go into details, later in Sec. 4.1.3. The versatile properties of the RVO_3 series are summarized in a spin-orbital phase diagram shown in Fig. 4.5 [22, 23]. For $LaVO_3$ and $CeVO_3$ we used the data reported in [22].

In this work the optical conductivity of the compounds YVO_3, $HoVO_3$ and $CeVO_3$ has been investigated. In the following paragraphs these compounds are introduced in more detail.

4.1.1. YVO₃

Amongst the RVO_3 series YVO_3 is the most investigated compound and its properties have been reported by several groups [10, 18, 20, 28, 29, 32, 33, 75, 76, 122, 133–135]. At room temperature YVO_3 crystallizes in the orthorhombic space group *Pbnm* [21, 29, 76] (left panel in Fig. 4.6). The system undergoes a second-order structural phase transition around $T_{OO} = 200$ K to the intermediate monoclinic phase

(a) *Pbnm*: $T < 77$ K & $T > 200$ K

(b) *P2₁/b11*: 77 K $< T < 200$ K
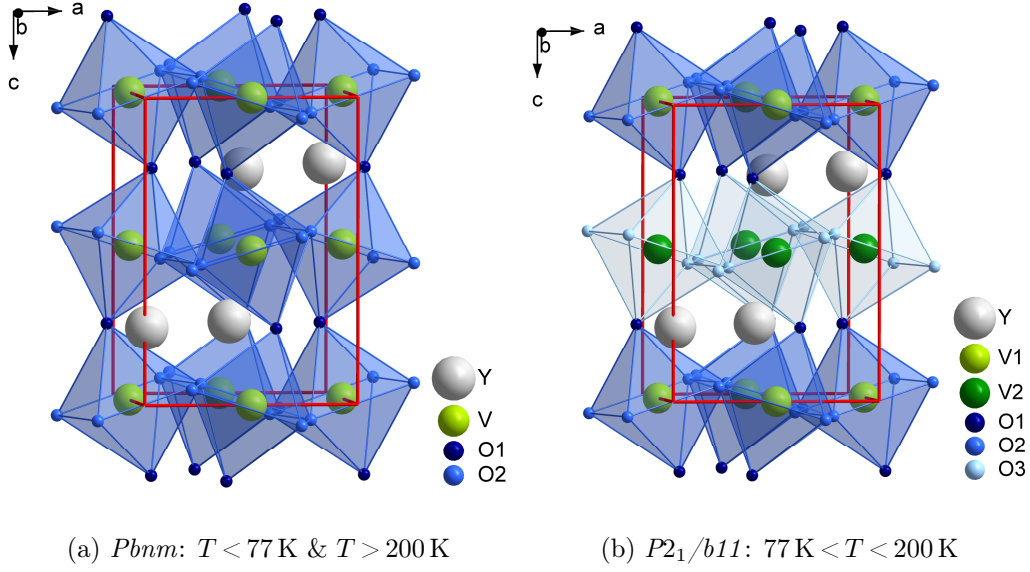
Figure 4.6.: Crystal structure of YVO$_3$ in several phases reported by [29, 76]. (a) Orthorhombic crystal structure of YVO$_3$ below 77 K and above 200 K. (b) Intermediate monoclinic phase with two distinct vanadium sites V(1) and V(2).

(a) T<77K (*Pbnm*)

(b) T>77K (*P2₁/b*)
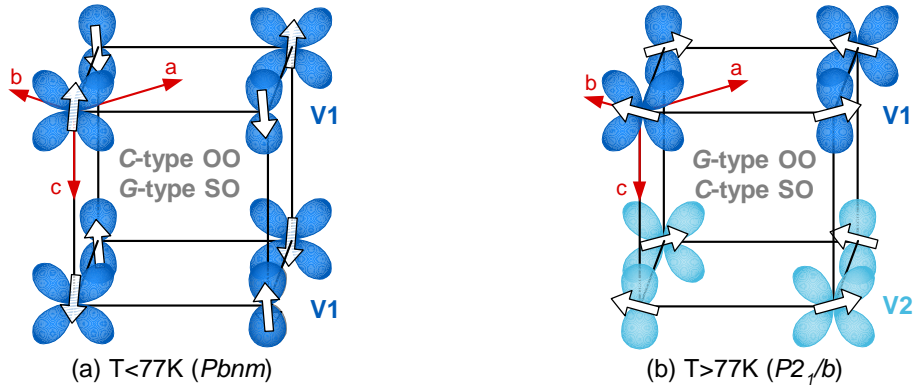
Figure 4.7.: Orbital ordering in (a) the low-temperature and (b) the intermediate phase of YVO$_3$ [21, 76, 133]. The shown direction of the spins is reproduced from [20, 122] who have suggested that the spins lie in the ab plane above T_S, while they point almost in c direction below T_S. For a discussion see the paragraph 'Unusual Magnetic Properties' below.

with space group $P2_1/b11$ (right panel in Fig. 4.6), which is accompanied by the onset of G-type orbital ordering. From synchrotron x-ray diffraction studies [133] an orbital occupation has been derived which is approximately $d_{xy}^1 d_{yz}^1$ and $d_{xy}^1 d_{zx}^1$ for neighboring sites in the cubic coordinate system (see Fig. 4.7), in good agreement

with earlier theoretical predictions [18, 134]. Below $T_N = 116$ K antiferromagnetic ordering is observed which is of C-type. At $T_S = 77$ K a first-order structural phase transition to the low-temperature orthorhombic phase takes place which is accompanied by a change of orbital and magnetic order. Here the spin ordering is of G-type, while the orbital ordering is of C-type [20, 21, 28, 29, 76] (Fig. 4.7).

Structural Details

The crystal structure of YVO$_3$ has been investigated very carefully by synchrotron x-ray diffraction as well as neutron diffraction studies by two different groups, namely Blake *et al.* [76] and Reehuis *et al.* [29]. The lattice parameters are summarized in Tab. 4.1 for several temperatures and phases.

The different orbital ordering patterns, mentioned above, have been proposed on basis of the different V-O bond lengths within the VO$_6$ octahedra, determined in detail by the combined analysis of neutron powder and synchrotron x-ray single-crystal diffraction data [21, 76]. It has been shown that above ~ 200 K there are three different V-O bond distances which split into two, just slightly different, short distances and one long distance [21, 29, 76] (see Fig. 4.8). In the intermediate monoclinic phase below 200 K there are overall six different distances, three within each V(1)O$_6$ and V(2)O$_6$ octahedron stacked alternatingly along c. In both orbitally ordered phases the long distance lies in the ab plane. As a result of their observations, Blake *et al.* claimed that the orbital degeneracy, present at high temperatures is completely removed at 200 K [21, 76]. They argue that below 200 K a clear JT distortion exists, because the difference between the short and the long bond in the ab plane becomes much more pronounced and in addition, the short bond lengths along c and within the ab plane become very similar, at least the averaged values [21, 76]. However,

Table 4.1.: Lattice parameters for YVO$_3$.

Temp.	Space group	a(Å)	b(Å)	c(Å)	α(°)	Ref.
5 K	*Pbnm*	5.28551(6)	5.59264(5)	7.55615(7)	90	[29]
65 K	*Pbnm*	5.28164(3)	5.58868(3)	7.55030(4)	90	[76]
80 K	*P2$_1$/b*	5.27243(3)	5.62058(3)	7.53254(4)	89.977(3)	[76]
85 K	*Pbnm*	5.28547(7)	5.62399(7)	7.53979(11)	90	[29]
85 K	*P2$_1$/b*	5.27650(5)	5.62401(5)	7.53980(7)	89.980	[29]
100 K	*P2$_1$/b*	5.27272(3)	5.61940(3)	7.53499(4)	89.979(3)	[76]
140 K	*P2$_1$/b*	5.27393(3)	5.61602(3)	7.54235(4)	89.973(3)	[76]
180 K	*P2$_1$/b*	5.27474(4)	5.61126(3)	7.55316(4)	89.978(3)	[76]
230 K	*Pbnm*	5.27953(8)	5.61072(8)	7.57214(13)	90	[29]
240 K	*Pbnm*	5.27574(3)	5.60679(3)	7.56714(4)	90	[76]
295 K	*Pbnm*	5.27722(3)	5.60453(3)	7.57294(4)	90	[29]
295 K	*Pbnm*	5.27839(3)	5.60608(3)	7.57421(4)	90	[76]
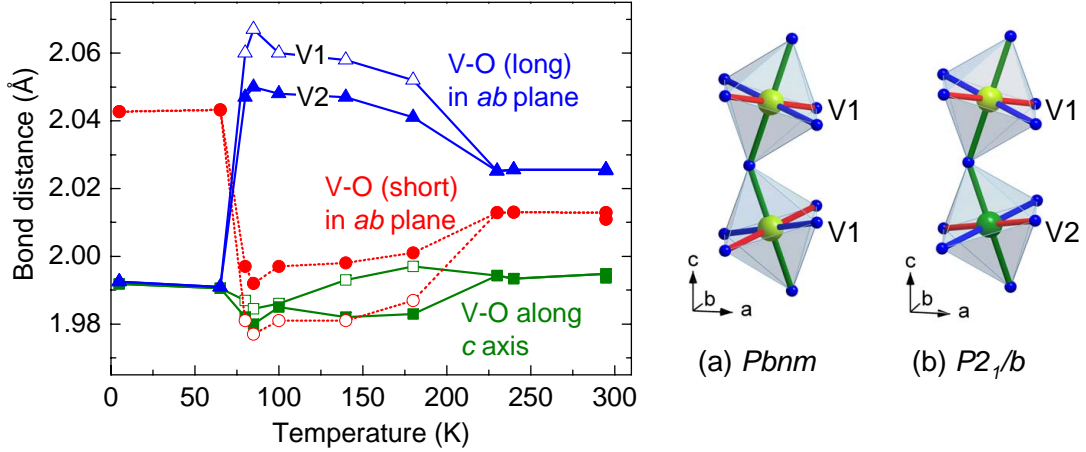
Figure 4.8.: Temperature dependence of the three vanadium-oxygen bond length within the VO$_6$ octahedra of YVO$_3$. The values summarized in the figure were obtained by neutron diffraction [21, 29, 76]. On the right hand site the corresponding bonds (also red, blue and green) within the octahedra in the (a) low-temperature and high-temperature orthorhombic phase (*Pbnm*) and (b) in the intermediate monoclinic phase (*P2$_1$/b*) are shown. In the intermediate phase open and full symbols denote the bond lengths of the V1 and V2 sites, respectively.

the JT distortion is small compared with e_g systems, e.g. LaMnO$_3$ regarding the difference of the shortest and longest bond which is about ~ 0.06 Å in YVO$_3$ [21] and ~ 0.27 Å in LaMnO$_3$ [136]. Nevertheless above 200 K three unequal V-O bond lengths are observed, which are clearly distinguishable from each other. Therefore, we suggest that the orbital degeneracy is lifted already at room temperature, as confirmed by our cluster calculation (see Sec. 4.3). Reehuis *et al.* conclude that the lattice distortion away from the ideal cubic perovskite are entirely determined by ionic-size effects. From their point of view a cooperative JT effect is active in the low-temperature phase, while in the intermediate phase the correlations between V t_{2g} orbitals are held to be responsible for the unusual magnetic properties (see below), and thus appear to be only very weakly coupled to the lattice.

From the synchrotron x-ray diffraction analysis some indications of merohedral twinning in the intermediate phase has been found which has made an accurate determination of space group $P2_1/b$ difficult [29, 76].[4] To verify the existence of

---

[4]A twin is called merohedral, if the symmetry of the twins belongs to the same crystal system, but do not have the same point symmetry, i.e. the two twin domains have the same translation symmetry. In other words, the lattices of all twin components coincide perfectly in both direct and reciprocal space. Such twins often occur after a phase transition from a higher to a lower symmetric phase [137]. In particular, a tendency of pseudo-merohedrally twining is well known in monoclinic structures that are metrically orthorhombic ($\alpha \approx 90°$). The samples tent to twin on planes perpendicular to the b and c axes, with a is the unique axis (in $P2_1/b$). With b

a lower-symmetry phase, Tsvetkov *et al.* [75] investigated YVO₃ by optical spectroscopy. They analyzed the temperature-dependent phonon spectrum obtained by Kramers-Kronig analysis of the reflectance (see Sec. 2.4.1 and Fig. 2.2). The analysis revealed three different phases. Above 200 K and below 75 K the orthorhombic symmetry with space group *Pbmn* is affirmed. Below 200 K a number of additional phonons are observed which continuously evolve and reach a maximum at 75 K. The new modes, which are about two magnitudes smaller than the original ones abruptly disappear below 75 K. In combination with group-theoretical considerations the authors have ruled out $P2_1/b$ symmetry and proposed the monoclinic *Pb11* symmetry to be the most probable structure in the intermediate phase. In *Pb11* symmetry the VO₆ octahedra form a dimerized chain along the *c*-axis, in agreement with results from neutron scattering, proposing an 'orbital Peierls state' for the intermediate phase [28] (see also the paragraph after next). However, Reehuis *et al.* have tried to resolve the exact positions of the vanadium ions along *c* in a subsequent synchrotron x-ray diffraction experiment [29]. Despite of the high experimental resolution, they could not refine the very small deviation of the atomic position in *Pb11* compared to $P2_1/b$ [29].

Electronic Structure

The inter-band transitions in RVO_3 where first investigated by reflectivity measurements up to 40 eV [135]. The temperature-dependent optical conductivity from 0.06 up to 5 eV of LaVO₃ and YVO₃ has been subsequently obtained by a Kramers-Kronig analysis. In both compounds an absorption band consisting of two peaks is observed around 2 eV, which has been assigned to a Mott-Hubbard gap transition, i.e. a transition from the lower to the upper Hubbard band. In both vanadates, this contribution to $\sigma(\omega)$ for $E \parallel c$ shows a large temperature dependence, while the spectra for $E \perp c$ are almost independent of temperature [135] (Fig. 4.9(b)). The strong anisotropy of the electronic structure as well as the temperature dependence is attributed to spin and orbital order [135].

Later, the electronic excitations across the Mott-Hubbard gap have been investigated by means of ellipsometry [75] (Fig. 4.9(a)). In combination with LDA+U calculations an optical gap of about 1.6 eV was determined [75]. Furthermore, the optical response at low temperatures is determined by three optical bands at 1.8 eV, 2.4 eV, and 3.3 eV. These were identified with the inter-vanadium transitions $d^2 d^2 \rightarrow d^1 d^3$, i.e. excitations from the LHB to the UHB in this multi-orbital system (see also Sec. 2.3). Charge-transfer excitations, involving the transfer of an electron between V and O ions $d^2 \rightarrow d^3\bar{L}$ are located above 4 eV. The strong anisotropy and temperature dependence found in the earlier experiments [135] are less pro-

---

initially fixed, a twin may choose the *c* direction either with 'positive' or 'negative' sign, i.e. choose a 'left'- or 'right'-handed coordinate system. In the presence of inversion symmetry, a change of the handedness is equivalent to perform a 180° rotation around *b*, or *c* which are equivalent by symmetry in the point group *2/m*. Therefore only two twin domains are expected.
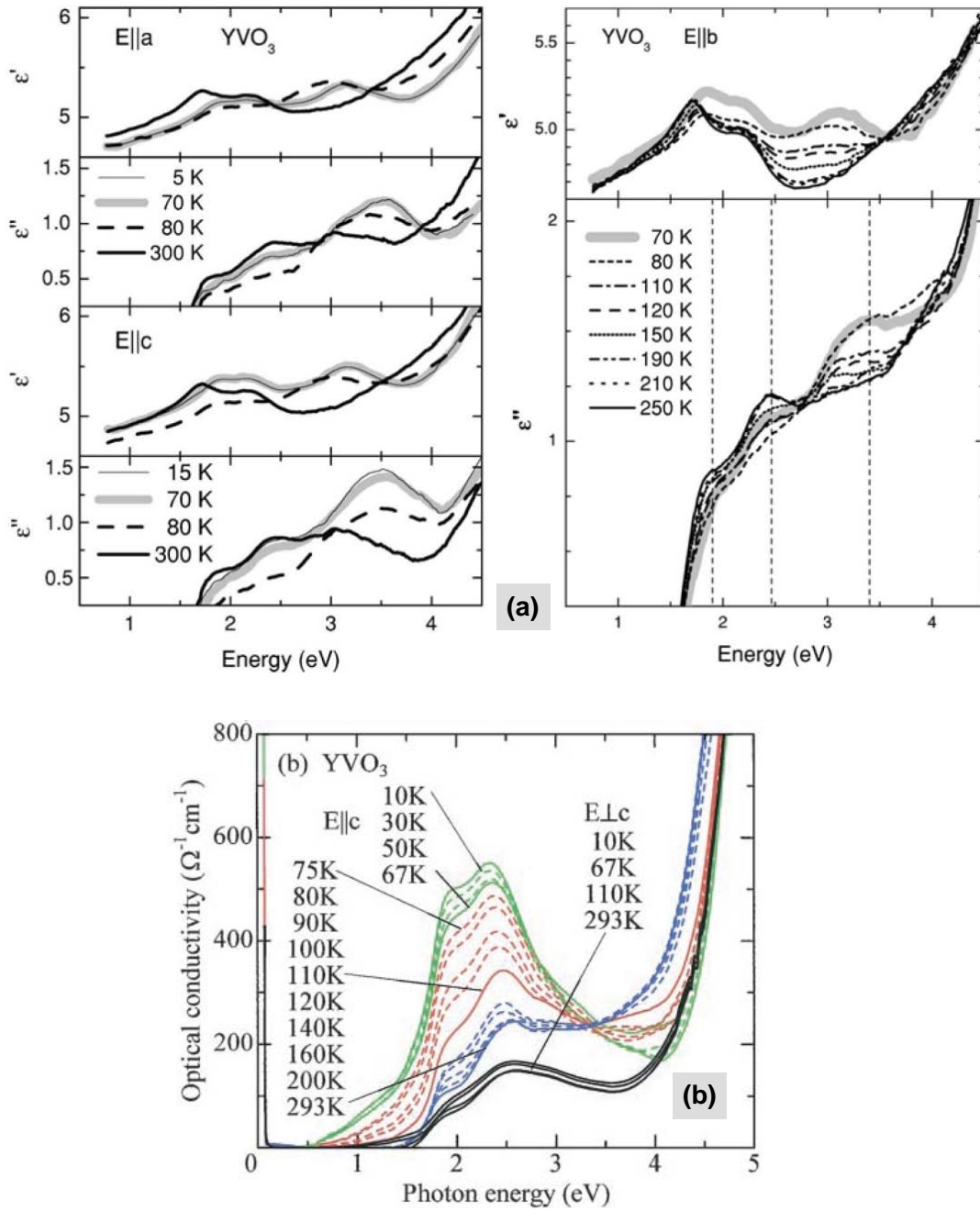
Figure 4.9.: Comparison of the results of the two optical studies of the electronic structure of YVO$_3$ [75, 135]. (a) Real and imaginary parts of the dielectric function of YVO$_3$ obtained by ellipsometry (left panel: $E \parallel a, c$; right panel: $E \parallel b$). Taken from [75]. (b) Temperature dependence of the optical conductivity for $E \parallel c$ and $E \perp c$ obtained by a Kramers-Kronig analysis. Taken from [135].

nounced in the later data [75]. In particular, the considerably reduced temperature dependence suggests a rather small influence of the spin and orbital order on the electronic transitions. However, this aspect is controversially discussed in several related perovskite-type compounds. While for LaMnO$_3$ and LaSrMnO$_4$ a pronounced redistribution of spectral weight at the magnetic ordering is observed [138, 139], in the t_{2g} systems YTiO$_3$ and SmTiO$_3$ the changes of the weight of the electronic transitions are rather small at T_C and T_N, respectively [139].

Recent first-principles computations have shown that YVO$_3$ exhibits an indirect charge gap, which is estimated to be around 0.7 eV [140]. Concerning to this matter, we will go into detail in Sec. 4.3.

Unusual Magnetic Properties

In the magnetically ordered phase below $T_N = 116$ K, YVO$_3$ is a canted antiferromagnet, where a net ferromagnetic moment arises due to a small canting angle of approximately 0.2° between the antiferromagnetically oriented spins of the V^{3+} ions [20]. The magnetization along the a direction is always larger than that along b and c (Fig. 4.10). A gradual magnetization reversal is observed at about 95 K, while the magnetization reverses abruptly at $T_S = 77$ K [122]. The reversal at 95 K is proposed to be due to a competition between the single-ion anisotropy and the Dzyaloshinskii-Moriya interaction [20, 122]. However, both the latter and the mechanism responsible for the magnetization reversal at T_S are still controversially discussed [28, 29, 123, 141]. Based on the magnetization data in combination with symmetry considerations, it is suggested that the spins lie in the ab plane above T_S, while they point almost in c direction below T_S [20, 122] (Fig. 4.7(a) & (b)). While measurements of the magneto-optical Kerr effect [75] have confirmed that the spins
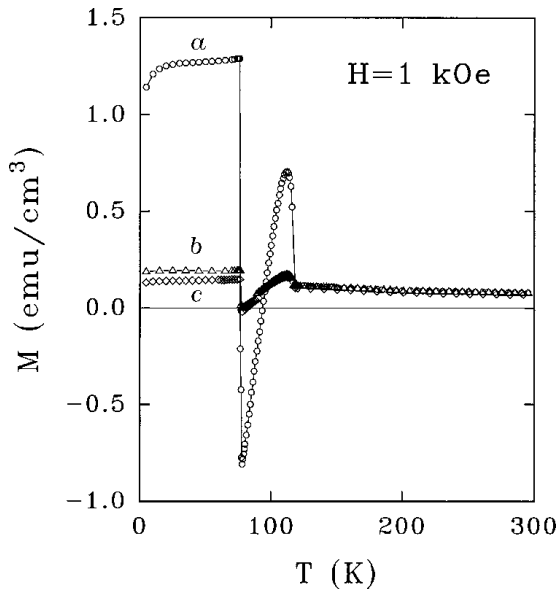
Figure 4.10.:
Temperature dependence of the magnetization in an applied magnetic field of 1 kOe along the a, b, and c axis, respectively. Taken from [122]

are aligned along c in the low-temperature phase, the results for the intermediated phase are contradictory to [122]. Here an alignment of the spins along c instead of b has been suggested [75]. However, recent results from magnetic neutron scattering [29] again have confirmed the observation from [20, 122].

From magnetic neutron scattering an unusual magnetic structure and dynamics in the intermediate phase of YVO_3 have been reported by Ulrich *et al.* [28]. They have found that for $T_S < T < T_N$ the magnetic moments are canted by $16.5°$ out of the ab plane and the total ordered moment has an anomalously small magnitude of $1.05(2)\,\mu_B$ (the free-ion value is $2\,\mu_B$). From the latter the authors concluded that strong quantum fluctuations are present in the intermediate phase [28]. The magnon dispersion has been determined in an energy range up to $50\,meV$ with energy resolution $1 - 5\,meV$ [28] (Fig. 4.11). While in the low-temperature phase the magnon dispersion is well described by a simple isotropic Heisenberg model with exchange parameters $J_c = J_{ab} = 5.7 \pm 0.3\,meV$ (Fig. 4.11(a)), the magnon dispersion in the intermediate phase shows several unexpected features [28] (Fig. 4.11(b)). These are mainly two distinctive features, namely, (i) $|J_c| > |J_{ab}|$ with J_c and J_{ab} are the c-axis and ab-plane superexchange couplings, and (ii) the c axis spin wave spectrum splits into an acoustical and optical branch with a gap of $5\,meV$. From the latter it is argued that the ferromagnetic exchange bonds strongly alternate along c [28]. The authors reasoned that this modulation has to be regarded as a signature of highly unusual orbital correlations [28]. Based on a model which requires degenerate xz and yz orbitals occupied by one electron on each site (the first one occupies the xy orbital), a one-dimensional 'orbital Peierls' state has been proposed for the intermediate phase [28]. While the exchange interaction between spins within an orbital singlet is strong and ferromagnetic, nearest-neighbor spins in adjacent singlets are coupled through a weak, antiferromagnetic interaction. However, as mentioned above, the model assumes degenerate xz and yz orbitals. This is in contradiction to our cluster calculation based on the reported structure data [29, 76]. We find a distinct splitting
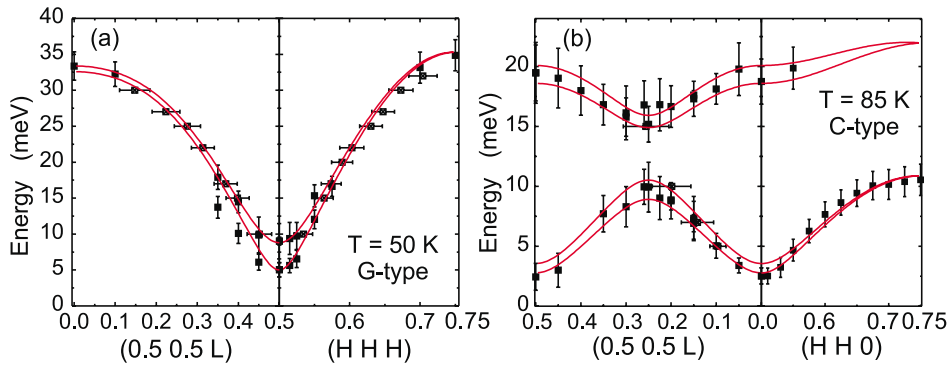
Figure 4.11.: Magnon dispersion relations in the (a) low and (b) high temperature magnetic phases obtained by magnetic neutron scattering. Taken from [28].

of the corresponding energy levels (see Tab. 4.6 and the text there).

Recent LDA$+U$ calculations by Fang and Nagaosa have shown that the reported unusual magnetic properties of YVO$_3$ can be reasonably explained by a JT picture [24]. For the intermediate monoclinic phase they argue that the two inequivalent VO$_2$ layers exhibit a different amount of JT distortion (4% for layer 1 and 2% for layer 2 in YVO$_3$ at 100 K), which yields two different J_{ab} stacked alternatingly along c.[5] They obtain $J_{ab} = 0.8$ meV and 5.3 meV for the two different layers. Fang and Nagaosa show that the experimental spin-wave dispersion is reproduced when using these exchange parameters, in particular the spin-wave dispersion definitely shows a c-axis splitting [24]. Therefore, they conclude that the spin-wave splitting is due to the two inequivalent JT distorted VO$_2$ layers in the monoclinic phase. The same predictions are made for LaVO$_3$ at 10 K because of the same symmetry [24].

Quest for Orbitons

The compounds RVO_3 with two electrons occupying the t_{2g} orbitals, are promising candidates for the observation of collective orbital excitations (orbitons) (see also Chap. 2.4.2). For LaVO$_3$ and YVO$_3$ orbitons have been theoretically investigated by Ishihara [17] and Khaliullin, Horsch and Oleś [16]. Ishihara has calculated the dispersion relation for orbital waves in the G-type OO and C-type OO phases, based on effective spin-orbital coupled Hamiltonians associated with the Jahn-Teller (JT) type couplings (Fig. 4.12). In both phases, four modes of orbital waves have been considered, y_A, z_A, x_B, and z_B which are attributed to two differently occupied sites A and B in the unit cell (see left panel in Fig. 4.12). While the modes y_A and x_B were identified with local modes that show no dispersion within the linear spin-wave theory, the remaining modes z_A and z_B are dispersive along z [17] (right panel in Fig. 4.12). The dispersion relations were calculated for different values of the spin-spin correlation function $|\langle SS \rangle|$, where a decrease of $|\langle SS \rangle|$ corresponds to an increase of the temperature towards T_N [17]. In particular, Ishihara has found that the orbital wave in the C-type OO phase ($T < T_S$ in YVO$_3$) is barely stable compared to that of the G-type OO phase ($T > T_S$ in YVO$_3$), because the dispersion shows a remarkable softening at $\vec{k} = \{0, 0, \pi\}$ with increasing temperature. The energy gap at $k_z = \pi$ is attributed to the JT-type interaction which is supposed to stabilize the C-type OO at low temperatures.[6] Ishihara argue that this is consistent with the change from C-type to G-type OO at $T_S = 77$ K in YVO$_3$ [17], i.e. the phase

---

[5]In contrast, Ulrich *et al.* have assumed alternating J_c, but the same J_{ab} to fit the experimental data [28].

[6]The JT interaction yields a shift of the dispersion relation in the C-type OO phase of $\sqrt{\frac{3}{2}} g_E Q_E = \sqrt{\frac{3}{2}} 0.8 J_0 \approx J_0$ [17]. The orbital exchange coupling has been estimated to $J_0 \sim 33$ meV for LaVO$_3$ by LDA+U calculations [142]. The value of the dispersion at $k_z = \pi$ is only about $2/3 J_0$ for $|\langle SS \rangle| = 1$, i.e. without the shift due to the JT interaction the state would be unstable (see Fig. 4.12).
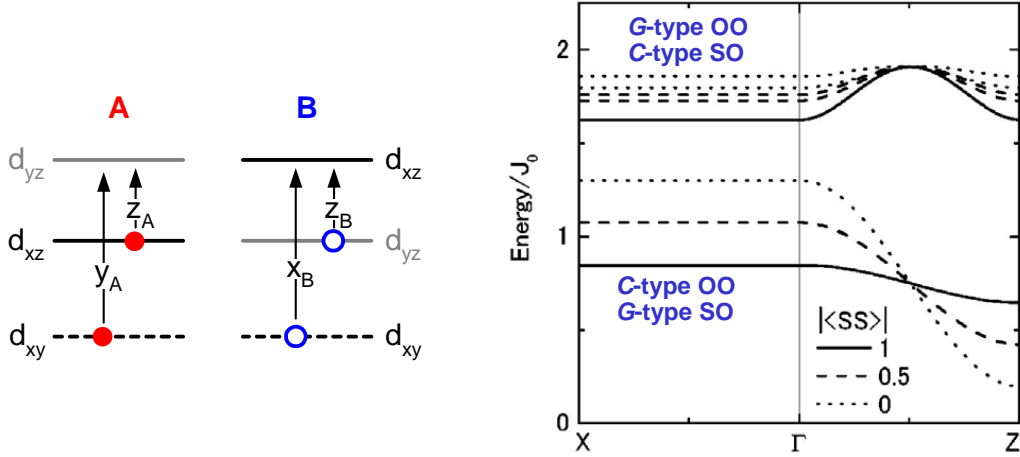
Figure 4.12.: In both phases, the G-type OO/C-type SO and the C-type OO / G-type SO, four modes of orbital waves (y_A, z_A, x_B, and z_B) are expected. The corresponding orbital excitations are depicted in the left panel. Note that the JT-splitting of the t_{2g} level is assumed to be equal on site A and B. The modes y_A and z_A correspond to the excitation from the d_{xy} to the d_{yz} orbital and from the d_{xz} to the d_{yz} orbital at site A. The modes x_B and z_B correspond to the excitation from the d_{xy} to the d_{xz} orbital and from the d_{yz} to the d_{xz} orbital at site B. While y_A and x_B do not show dispersion, the modes z_A and z_B are dispersive along z [17]. The dispersion of the latter two degenerate modes from Γ to X or Z for the G-type OO/C-type SO (upper branch) and the C-type OO/G-type SO (lower branch) phase in LaVO$_3$ and YVO$_3$ are shown in the right panel. The energy is normalized by the effective exchange parameter for the orbitals $J_0 = 4t^2/U' - J_H$ which has been estimated by LDA+U calculations to 33 meV for LaVO$_3$ [142]. A decrease of the spin-spin correlation function $|\langle SS \rangle|$ corresponds to an increase of the temperature towards T_N. Reproduced from [17].

transition may be driven by the orbital exchange interaction associated with a JT-type interaction. This is in agreement with the result of Khaliullin, Horsch and Oleś [16], who found from a spin-orbital model that the C-type OO in the low-temperature phase of LaVO$_3$ and the intermediate phase of YVO$_3$ is stabilized by a ferromagnetic superexchange of the spins caused by fluctuations of degenerate t_{2g} orbitals [16]. They claim that the transition to G-type OO in YVO$_3$ at low temperatures is explained by the JT distortion overbalancing the large entropy due to quantum fluctuations.

Recently, two-orbiton Raman scattering in RVO$_3$ has been reported by Miyasaka *et al.* [10, 33] and Sugai and Hirota [32]. The former report on two-orbiton excitations in RVO$_3$ with $R = $ La, Nd, and Y that have been observed in resonant Raman scattering around 43 meV and 62 meV in the C-type SO and G-type OO phases, respectively. Note that these bands only occur below $T_N = 116$ K in YVO$_3$

Table 4.2.: Assignment of Raman modes [10, 32, 33]. Note that in Ref. [33] the optical axes x, y, and z are taken parallel to the cubic crystal axes (nearly parallel to the V-O-V bonds), $a + b$, $a - b$, and c (in *Pbnm*).

Energy (meV)	Assignment	Temperature	Ref.
11	1-magnon (k=0)	0 - 77 K	[32]
31	2-orbiton	0 - 77 K	[32]
43	2-orbiton	77 - 116 K	[33]
45	1-orbiton	77 - 150 K	[32]
50	2-magnon	0 - 77 K	[33]
50	2-orbiton	0 - 77 K	[32]
54	A_g^3 phonon	0 - 280 K	[32]
58	JT phonon	0 - 300 K	[33]
57	2-magnon	0 - 116 K	[33]
57	2-magnon	0 - 77 K	[32]
62	2-orbiton	77 - 116 K	[33]
63	JT phonon	77 - 140 K	[32]
83	phonon	0 - 280 K	[32]
83	phonon	0 - 200 K	[33]
84	2-orbiton	77 - 200 K	[32]
86	oxygen-stretching mode	0 - 200 K	[33]
88	breathing mode	0 - 280 K	[32]
172	2-phonon breathing	77 - 280 K	[32]

although orbital ordering is proposed to set in at 200 K [21, 76]. Sugai and Hirota have chosen a different assignment of the observed modes in YVO₃, in particular of the two-orbiton modes (see Tab. 4.2). First, the two-magnon peak is assigned at 57 meV at 5 K in agreement with the observed magnon dispersion [28]. The peak at 62 meV in the intermediate phase (which had been assigned to the two-orbiton peak in Ref. [10, 33]) is identified with the JT phonon mode in Ref. [32]. Instead, two peaks observed at 31 meV and 50 meV in the *G*-type OO phase at 5 K are assigned to one-orbiton and two-orbiton excitations, respectively. In the intermediate monoclinic phase with *C*-type OO the peak energies shift to 45 meV and 84 meV. In particular, Sugai and Hirota analyse the resonance behavior and find that the one-orbiton feature increases with increasing laser frequency in the *C*-type OO/*G*-type SO phase but decreases with increasing laser frequency in the *G*-type OO/*C*-type SO phase. This is interpreted in terms of the changes observed in the optical conductivity in the energy range of Mott-Hubbard excitations [135]. However, in our

opinion the decrease of the peak at $84\,\text{meV}$ with increasing photon energy is inadequately described in the proposed two-orbiton scenario. Sugai and Hirota argued that the increase of the one-orbiton peak is due to the resonance with the Mott-Hubbard excitation at $U'\text{-}J_H$ observed at $1.88\,\text{eV}$ in the optical conductivity [10]. Because in the G-type OO/C-type SO phase the intermediate state in the Raman process is the same for one-orbiton and two-orbiton excitations [17], we expect the same resonance behavior for both peaks with increasing photon energy, in contrast to the observations [32].

In this thesis we present the mid-infrared optical conductivity of YVO$_3$ which gives evidence for two-orbiton excitations around $0.4\,\text{eV}$ for $E \parallel c$ in the intermediate G-type OO/C-type SO phase (see Chap. 4.3). Our results are neither consistent with those of Miyasaka *et al.* [10, 33] nor those of Sugai and Hirota [32]. We note that the analysis of the Raman spectra in this energy range is difficult and discussed controversially in the literature, in particular the distinction between peaks originating from phonon, multi-phonon, magnon, and orbiton scattering (e.g. see [11, 12, 143]). The contradicting assignment of the peaks by Miyasaka *et al.* and Sugai and Hirota, see Tab. 4.2, gives reason to question the above-mentioned assignment with one- and two orbiton peaks at all. In particular, the peak assigned with the two-phonon breathing mode at $172\,\text{meV}$ in [32] shows a very similar temperature and polarization dependence compared with the peak at $84\,\text{meV}$ assigned with the two-orbiton scattering. Altogether, we annotate that the observed 'additional' peaks may arise due to multi-phonon scattering. A detailed analysis is difficult because fundamental Raman-active as well as fundamental infrared-active modes can contribute to the Raman-active multi-phonons. Furthermore, a symmetry lower than $P2_1/b$ for the intermediate phase may have to be taken into account [75].

4.1.2. HoVO$_3$

Up to now, much less is known about the compound HoVO$_3$. The lattice parameters at room temperature are $a = 5.3032\,\text{Å}$, $b = 5.6137\,\text{Å}$, and $c = 7.6259\,\text{Å}$ in space group $Pbnm$ (D_{2h}^{16}) [144]. From susceptibility measurements a transition from a paramagnetic to an antiferromagnetic state at $T_N = (108 \pm 2)\,\text{K}$ has been determined [144], in good agreement with the transition temperature derived from neutron data [145]. An ordering of the Ho^{3+} moments is found below $8.8\,\text{K}$ [145]. The structural transition temperatures are $T_S \sim 40\,\text{K}$ and $T_{OO} \sim 200\,\text{K}$ [146].

4.1.3. CeVO$_3$

The lattice parameters of CeVO$_3$ have been obtained by neutron powder diffraction [26]. At room temperature the data are compatible with space group $Pbnm$, while at $2\,\text{K}$ the monoclinic space group $P2_1/b$ is adopted.[7] The lattice constants

---

[7]In Ref. [26] the space groups $Pnma$ and $P2_1/n$ are used, respectively. For an easier comparison with the structure of the other RVO$_3$ compounds we transformed them from $Pnma$ ($P2_1/n$) (a,

are summarized in Tab. 4.3. Magnetic neutron-scattering experiments revealed a transition from a paramagnetic to an antiferromagnetic state at $T_N = 136\,\text{K}$ [145], in agreement with recent results from susceptibility measurements [26]. Additionally, an anomalous diamagnetism effect below $T_t \sim 124\,\text{K}$ is reported from a combined study of neutron powder diffraction, specific heat and magnetization measurements [26]. In particular, the structural phase transition to the low-temperature monoclinic phase is observed also at T_t. This is in contrast to a second study from high-energy synchrotron x-ray diffraction in combination with specific-heat measurements, which revealed two phase transitions occurring at $T_S = 154\,\text{K}$ (second order) and at $T_N = 134\,\text{K}$ (first order) [22]. In particular the transition at T_S is identified as a structural phase transition to a low-temperature monoclinic phase with space group $P2_1/b11$, accompanied by the formation of G-type orbital order [22].

Table 4.3.: Lattice parameters of CeVO$_3$ [26].

	Space group	$a(\text{Å})$	$b(\text{Å})$	$c(\text{Å})$	$\alpha(°)$	Vol (Å^3)
T = 295 K	$Pbnm$	5.5039(2)	5.5376(2)	7.7864(3)	90	237.32(2)
T = 2 K	$P2_1/b$	5.5148(3)	5.5730(4)	7.7038(5)	89.954(9)	236.77(3)

4.2. Experimental Details

In this work, we use the optical conductivity $\sigma(\omega)$ to study the orbital excitations of RVO$_3$ with $R =$ Y, Ho, and Ce as a function of polarization of the incident light and temperature. For this purpose we have measured the transmittance *and* reflectance in the mid- and near-infrared range. At first the preparation and characterization of the samples are briefly summarized. Likewise the compounds VOCl and Dy(Sc,V)O$_3$ are introduced, which serve as reference materials. The spectrum of VOCl ought to demonstrate the local crystal-field bands of V^{3+} $(3d^2)$ in a strongly distorted octahedral environment, just as it has been probed for Ti^{3+} $(3d^1)$ in TiOCl [15, 79, 147]. The idea of preparing Dy(Sc,V)O$_3$ was to demonstrate the absorption spectra of a 'single' V^{3+} $(3d^2)$ ion in a predominantly octahedral ligand field embedded in an electronically inactive Sc^{3+} $(3d^0)$ matrix. Finally our optical data are presented.

4.2.1. Samples of RVO$_3$

Single crystals of RVO$_3$ with $R =$ Y, Ho, and Ce have been grown by the traveling-solvent floating-zone method by A. A. Nugroho[8] in the work group of T. T. M. Pal-

---

b, c) to $Pbnm$ ($P2_1/b$) (a', b', c') by a cyclic exchange of the atomic positions and the lattice constants: $a' = c$, $b' = a$, and $c' = b$.

[8]actual address: Jurusan Fisika, Institut Teknologi Bandung, Indonesia
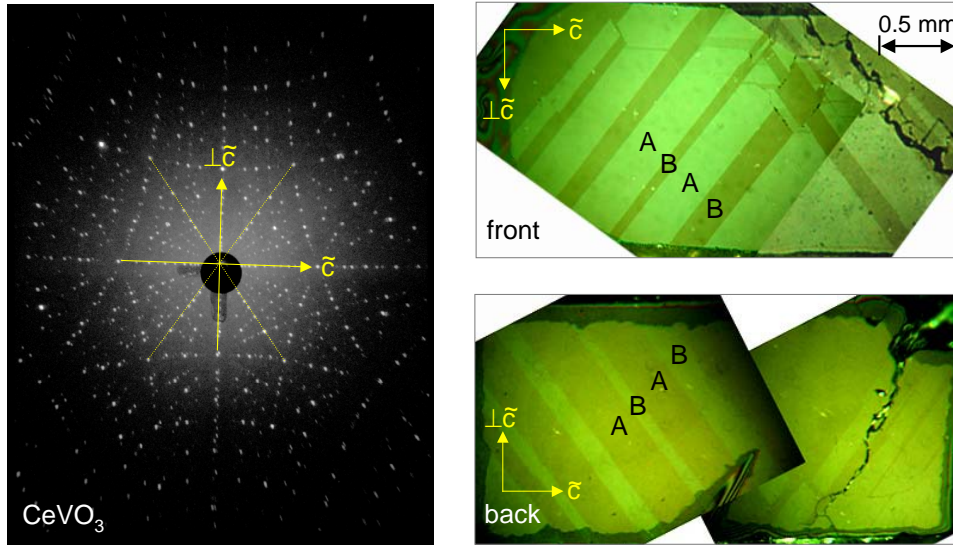
Figure 4.13.: Laue picture of $CeVO_3$ (left panel). Although the sample is twinned this
picture indicates a preference direction of the twin domains (marked with
tilde), i.e. the diffraction pattern does not show cubic symmetry but rather
the familiar pattern of the orthorhombic *ac* and *bc* plane, respectively. This
is supported by the photos obtained with a polarization microscope (right
panels).

stra.[9] The purity, stoichiometry and single-phase structure of the crystals was
checked by x-ray diffraction and thermogravimetric analyses. Typical dimensions
of the as-grown rods are a few mm along all three crystallographic axes. In the
case of YVO_3 a large part of such a rod was available for our measurements. It was
cut and the obtained samples were oriented with the Laue method. Afterwards the
samples were grinded and polished using the procedure described in Sec. 3.2. In the
same way the transmittance samples of $HoVO_3$ and $CeVO_3$ were prepared. For the
$CeVO_3$ sample some indications of twinning are found by analyzing the Laue pic-
ture (Fig. 4.13). The picture shows many reflexes lying close together and it seems
that there are two patterns lying on top of each other which are slightly shifted.
To verify this assumption a measurement with a single-crystal diffractometer has
been performed.[10] It has been shown that the sample of $CeVO_3$ is twinned in all
three directions of space. Within the space group *Pbnm* it is not possible to fully
describe all measured reflections. Altogether a cubic cell could be indexed with
$a = b = c \approx 7.7$Å. However, the Laue picture indicates a preference direction of the
twin domains, i.e. the patterns do not show cubic symmetry but rather the familiar

---

[9]Chemical Physics Dept.,Materials Science Center, University of Groningen, 9747 AG Groningen,
The Netherlands

[10]Our best thanks go to M. Cwik (Instiute of Physics II, University of Cologne) who performed
this measurement.

patterns of the orthorhombic ac and bc plane, respectively. Additionally we examined the sample with a polarization microscope. On the right hand side in Fig. 4.13 the front and back view pictures of the sample C1 (Tab. 4.4) are shown. A stripe pattern denoted by A and B is clearly seen. The stripes are a few hundred μm^2 in plane. While a rotation of 180° of the sample under the microscope yields an identical pattern, a rotation of 90° interchanges the colors. In between, according to a rotation of 45° there is no contrast. Because there are four positions without contrast we conclude that the stripes are single domain. The front and back view are congruent indicating that the twin domains are continuous throughout the entire sample (the interchanged colors are just due to a 90° rotation of the two pictures with respect to each other).

The denotation, orientation, thickness, and the spectral range considered for several RVO$_3$ samples are summarized in Tab. 4.4. The thickness d of the samples was determined using a microscope with a magnification of (6.3×32). The error of d is obtained by the standard deviation of typically 4-5 values, obtained from measurements at different positions of the sample. The difference in error for different samples is mainly due to the variable plane-parallelism.

Exemplary, two Laue pictures showing the reflection pattern at normal incident are shown in Fig. 4.14 for two lattice planes of YVO$_3$, the ab (top panel) and ac

Table 4.4.: Orientation, thickness d and denotation of the R(V,Sc)O$_3$ samples considered in this work. The samples labeled with * were prepared by R. Rückamp [79].

Sample	Denotation	Spectral range	T/R	Polari- zation	Magnetic field	d (μm)
YVO$_3$	(Y1)*	MIR	T	$E \parallel a, c$	-	450
YVO$_3$	(Y2)	MIR	T	$E \parallel a, c$	-	330 ± 2
YVO$_3$	(Y3)	MIR	T	$E \parallel a, b$	-	368 ± 2
YVO$_3$	(Y4)	MIR/NIR	T	$E \parallel a, c$	-	130
YVO$_3$	(Y5)	NIR	T	$E \parallel a, b$	-	130 ± 1
YVO$_3$	(Y6)	NIR	T	$E \parallel c$	$H \parallel c$	124 ± 1
YVO$_3$	(Y7)	MIR	T	$E \parallel a$	$H \parallel b$	260 ± 3
YVO$_3$	(Y8)*	MIR	R	$E \parallel a, c$	-	>2000
YVO$_3$	(Y9)	MIR/NIR	R	$E \parallel a, b$	-	1292 ± 9
HoVO$_3$	(H1)	MIR	T	$E \parallel a, b$	-	406
HoVO$_3$	(H2)	MIR	T	$E \parallel a, c$	-	448 ± 5
CeVO$_3$	(C1)	MIR	T	$E \parallel \perp \tilde{c}, \tilde{c}$	-	441 ± 1
DyScO$_3$	(Sc1)	MIR-VIS	T	$E \parallel b, c$	-	730 ± 10
DySc$_{0.9}$V$_{0.1}$O$_3$	(ScV1)	MIR-VIS	T	$E \parallel a, b$	-	1312 ± 10
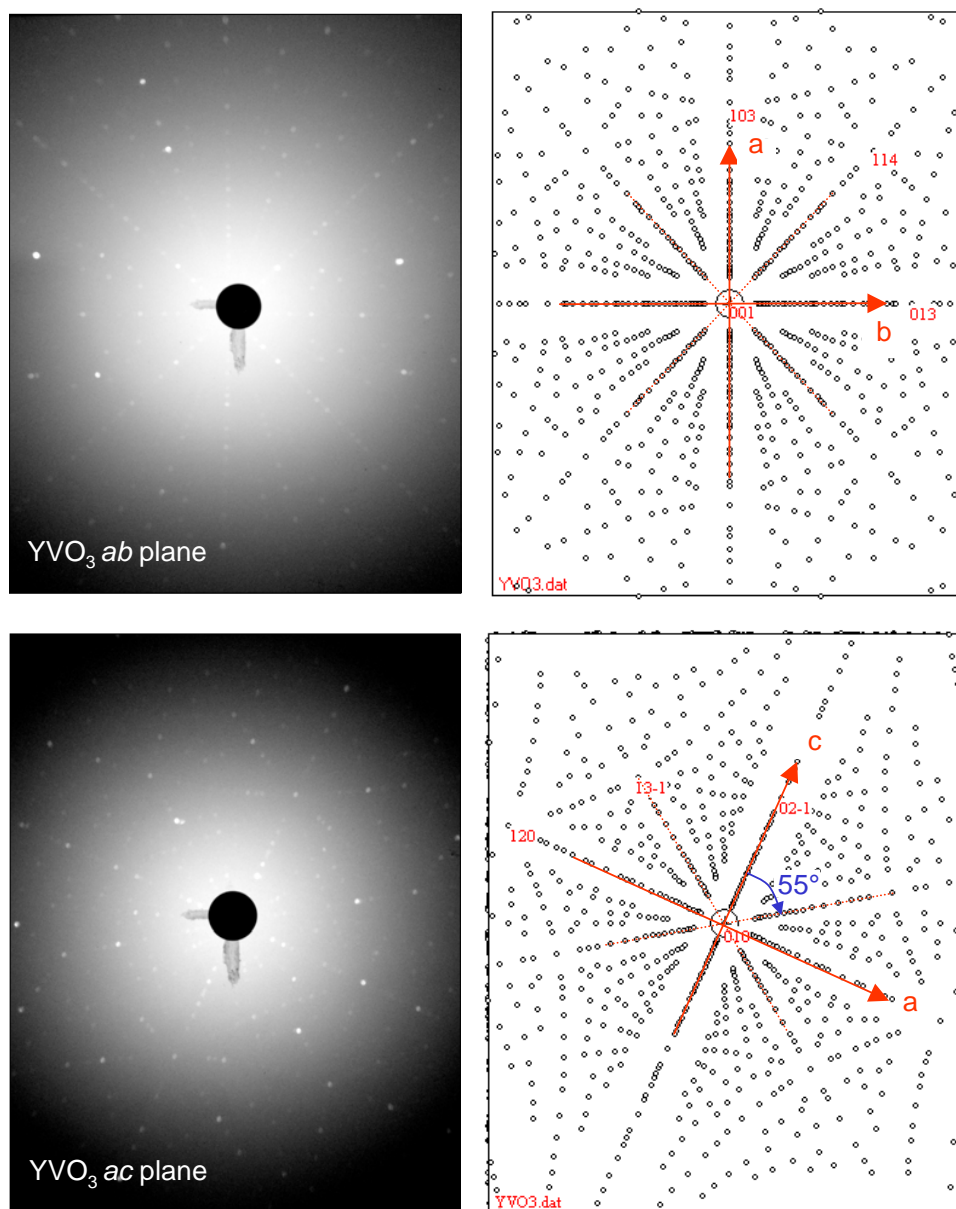
Figure 4.14.: Laue pictures and corresponding simulations (OrientExpress) of an *ab* plane (top panel) and an *ac* plane (bottom panel) of YVO$_3$. The rough orientation can be easily seen by examining the angles between the radial lines of reflexes. Because of the similarity of the *a* and *b* lattice constants (in *Pbnm*), the angle between e.g. the *a* axis and the 'diagonal' line within the *ab* plane is very close to 45°. This makes it difficult to distinguish between *a* and *b*. Therefore the orientation has been verified by a single-crystal diffractometer. The differentiation between *a* (*b*) and *c* is easier. Because the *c* axis is much longer (the reciprocal value c^* is correspondingly shorter), the angle between the *c* axis and the 'diagonal' line is about 55°.

plane (bottom panel).

Upon cooling across the first-order phase transition at T_S, often strain-induced microcracks occur in RVO$_3$ samples, which are sometimes visible with an optical microscope. This has also been reported from other groups, e.g. Ref. [123]. In certain cases, these microcracks are responsible for a decoupling of e.g. electric or thermal contacts. As a result of the microcracks the heat transport is reduced, which may give rise to errors in the determination of temperature, perceivable by slightly incorrect phase-transition temperatures. To avoid this problem, we usually use a 'new' (uncooled) sample for each measurement and were cautious in cooling across T_S. Additionally, we have attached a second thermometer directly on top of the sample to pick up the real sample temperature (see Sec. 3.1.1).

4.2.2. Samples of VOCl

The compound VOCl crystallizes in an orthorhombic structure with space group *Pmmn* [148, 149]. For details of the structure, see Fig. 4.15. Antiferromagnetic order is observed below $T_N = 150 \pm 5\,\mathrm{K}$ [150]. Previous optical and electrical measurements have shown that VOCl is a semiconductor with an activation energy of $\sim 2\,\mathrm{eV}$ [150].

Single crystals of VOCl have been grown by the chemical vapor transport technique by T. Taetz and A. Möller.[11] The purity of the crystals was checked by x-ray powder diffraction. Typical crystal dimensions are a few mm^2 in the ab planes and 10–100 μm along the c axis. Due to this given sample geometry measurements by T. Möller [151] and R. Rückamp [79] were solely performed with the electric field vector in the ab plane. For the same reason merely measurements of the transmittance were performed.

4.2.3. Samples of Dy(Sc,V)O$_3$

The ternary lanthanide orthoscandates LnScO$_3$ have recently attracted a lot of interest due to their possible applicability for oxide-based field-effect devices [152]. Because of their high melting temperature ($> 2000°C$), the high dielectric constant, and the stability in contact with silicon they are discussed for the use as gate oxides. However, our aim of the preparation of the V-doped scandates Dy(Sc,V)O$_3$ was to measure the absorption spectra of a 'single' V^{3+} ($3d^2$) ion in a predominantly octahedral ligand field embedded in an electronically inactive Sc^{3+} ($3d^0$) matrix. For this purpose, large single crystals have been grown by the traveling-solvent floating-zone method by N. Mufti in the work group of T.T.M. Palstra.[12] For our investigations two scandate samples were prepared: transparent yellow-colored DyScO$_3$ and opaque dark-green colored DySc$_{0.9}$V$_{0.1}$O$_3$ doped with 10 % vanadium. The amount

---

[11]Department of Inorganic Chemistry, University of Cologne, Germany

[12]Chemical Physics Dept., Materials Science Center, University of Groningen, 9747 AG Groningen, The Netherlands
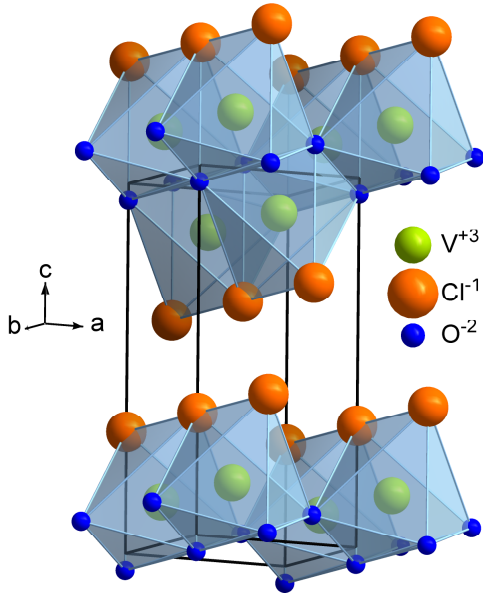
Figure 4.15.:
Crystal structure of VOCl (space group *Pmmn*). The V^{3+} ions occupy the centers of strongly distorted octahedra (light blue) formed by four O^{2-} and two Cl^{1-} ions. The local symmetry of the V site is C_{2v}. The V and O ions form double layers which are stacked along the c axis, well separated from each other by two layers of Cl ions [148, 149].

of of 10 % V doping is chosen to be below the percolation limit.[13] The purity and single-phase structure of the crystals was checked by powder and single-crystal x-ray diffraction at room temperature. Both compounds adopt the space group *Pbnm* and have similar lattice constants compared with RVO_3 (Tab. 4.5).

The successful growth and structural investigation of $DyScO_3$ are already reported in the literature [155]. Remarkably, the room-temperature lattice constants do not agree with our data within the given (statistical) error bars, although both data sets were obtained by a refinement of powder x-ray diffraction data in space group *Pbnm*. In particular our values for the lattice constants are overall somewhat higher which may be due to an off-set misalignment, i.e. the $\theta = 0$ point is shifted. However, the value for the orthorhombic splitting ε for the three refinements is very similar, about 0.0248. This value is similar to that found in RVO_3 for the smaller R ions (e.g. Gd, see Fig. 4.2). Therefore $DySc_{0.9}V_{0.1}O_3$ is an adequate reference material from the structural point of view. Typical dimensions of the as-grown rods are a few mm along all three crystallographic axes. From each rod we cut transmittance samples with well-known crystallographic orientation (see Tab. 4.4).

4.2.4. Resistivity of YVO₃

The resistivity of YVO_3 has been studied before in reference [156]. There a value of 0.25 eV for the activation gap has been reported which was estimated by an Arrhenius fit to the resistivity in a temperature range from 200 K to 300 K. This energy range is comparatively small. Therefore, we repeated the resistivity measurement

---

[13]Estimates for the critical percolation probability p_c for basic 3D lattices obtained by Monte Carlo techniques [153] and by series expansions [154] varies from 19 % for the close-packed fcc and hcp structures to 43 % for the open diamond structure.

Table 4.5.: Lattice constants of the Dy(Sc,V)O$_3$ samples considered in this work in comparison with data from [155]. Both of our data sets were obtained by a x-ray powder diffraction refinement in space group *Pbnm* at room temperature by N. Mufti.

Sample	a (Å)	b (Å)	c (Å)	ε	Ref.
DyScO$_3$	5.45250(9)	5.73024(9)	7.91856(12)	0.02483	N. Mufti
DyScO$_3$	5.4494(1)	5.7263(1)	7.9132(1)	0.02477	[155]
DySc$_{0.9}$V$_{0.1}$O$_3$	5.44330(4)	5.71949(5)	7.90299(7)	0.02474	N. Mufti

on our YVO$_3$ samples. Because of the resistivity is too high at low temperatures, we performed measurements up to high temperatures, i.e. from 180 K to 600 K. For this purpose we used a setup which enables measurements from 4 K up to 800 K without modifications [157]. This setup is based on a vaporizer unit embedded in a liquid-helium cryostat.[14] For the four-probe resistance measurement at high temperatures, a probe was designed which is embedded in a furnace and mounted in the vaporizer unit [157, 158]. The sample has been prepared with four sputter-coated gold contacts which were bonded with varnish-isolated copper wires, using a two-component silver epoxy (Fig. 4.16). The sample was fixed on the sample holder by using a ceramic high-temperature glue.[15] The connection of the wires with the pins of the probe was made using conductive silver paint.[16] The measurement was performed in high vacuum. The result of one temperature cycle (cooling and heating) is shown in Fig. 4.17(1). The conformity of both curves is very good. The resistivity shows the expected temperature dependence for a semiconductor: with decreasing temperature the resistivity is increasing. At room temperature (300 K), the value of the resistivity is about (2800±100) Ωcm.

To explain the conduction mechanism and to get an estimate of the energy gap we considered four different models, each predicting a different temperature dependence of the resistivity. The most simple model is a single-particle band-structure picture, where the resistivity of a semiconductor follows the well-known exponential temperature dependence

$$\rho = \rho_0 \cdot exp\left(\frac{\Delta_{act}}{k_B T}\right), \tag{4.1}$$

where k_B is Boltzmann's constant and Δ_{act} is the activation energy.[17] The corre-

---

[14]Oxford Instruments Ltd. (UK)

[15]Respond 940; two components; stable up to 1400 K

[16]G 3303A, Plano GmbH

[17]For a comparison with the optical conductivity one has to keep in mind that the optical gap Δ_{opt} is twice the energy gap obtained by resistivity measurements Δ_{act}. In resistivity measurements the one-particle excitations are examined, i.e. the excitation of one electron and one hole,
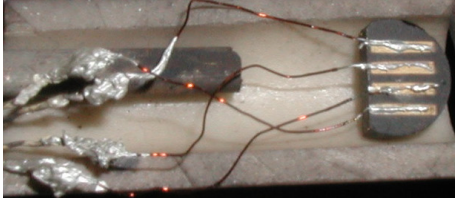
Figure 4.16.:
Setup for the resistance measurement on YVO_3. The picture shows the half-moon shaped sample with four sputter-coated gold contacts which were connected with copper wires to the measurement instruments.

sponding Arrhenius plot ($\ln(\rho)$ vs. $1/T$) shown in Fig. 4.17(2) seems to indicate linear behavior at low temperatures with deviations above room temperature. However, the derivative $d(\ln(\rho))/d(1/T) \propto \Delta_{act}$ displayed in Fig. 4.17(3) clearly shows that YVO_3 does not show simple activated behavior in the considered temperature range, not even at lower temperatures. Rather, the activation energy Δ_{act} shows a linear decrease with increasing temperature (Fig. 4.17(3)). A temperature-dependent energy gap is expected in the presence of impurities, which was described by Mott for the first time [159]. He introduced the Variable-Range-Hopping (VRH) mechanism describing the resistivity of doped insulators (typically band insulators) by

$$\rho_{\text{VRH}} = \rho_0 \cdot \exp\left(\frac{T_0}{T}\right)^{\alpha} \qquad (4.2)$$

with the exponent $\alpha = 1/(d+1)$ depending on the dimension d of the conductor. Later, Efros and Shklovskii (ES) found that the Coulomb interaction between localized electrons results in a different temperature dependence of the DC resistivity, which has the same form as in Eq. 4.2, but with a modified exponent of $\alpha = 1/2$ [160]. In particular, the ES hopping law is expected to be relevant for disordered systems at low temperatures (compared to the magnitude of the gap). The hopping exponent α can be determined without prior assumptions about the hopping mechanism (VRH or ES type) by a double-logarithmic plot of $d(\ln(\rho))/d(1/T)$ versus T because the slope of the expected straight line is $(1 - \alpha)$:

$$
\begin{aligned}
\ln\left(\frac{d(\ln(\rho))}{d(1/T)}\right) &= \ln(\alpha) + (\alpha - 1)\ln(T_0) - (\alpha - 1)\ln(T) \\
&= (1 - \alpha)\ln(T) + \text{const.} \qquad (4.3)
\end{aligned}
$$

However, analyzing the data shown in Fig. 4.17(4) with Eq. 4.3 leads to an exponent $\alpha > 1$ which is inconsistent with both Mott's law and the ES law.

The last model we considered is the small polaron hopping model [161].[18] Here one can imagine that the polaron is trapped inside a local energy well of height

---

respectively. Each electron (hole) carry the energy Δ_{act} which corresponds to the distance from the Fermi level to the conductance (valence) band, assuming the density of electrons being equal to the density of holes. Optical spectroscopy examines an electron-hole pair with energy of $\Delta_{opt} = 2\Delta_{act}$.

[18]The unit of an excess charge carrier together with its induced lattice deformation is called a 'small polaron' (for a review see e.g. [162]). The formation of small polarons is expected whenever the coupling between electrons and optical phonons is strong, e.g. in transition-metal oxides.
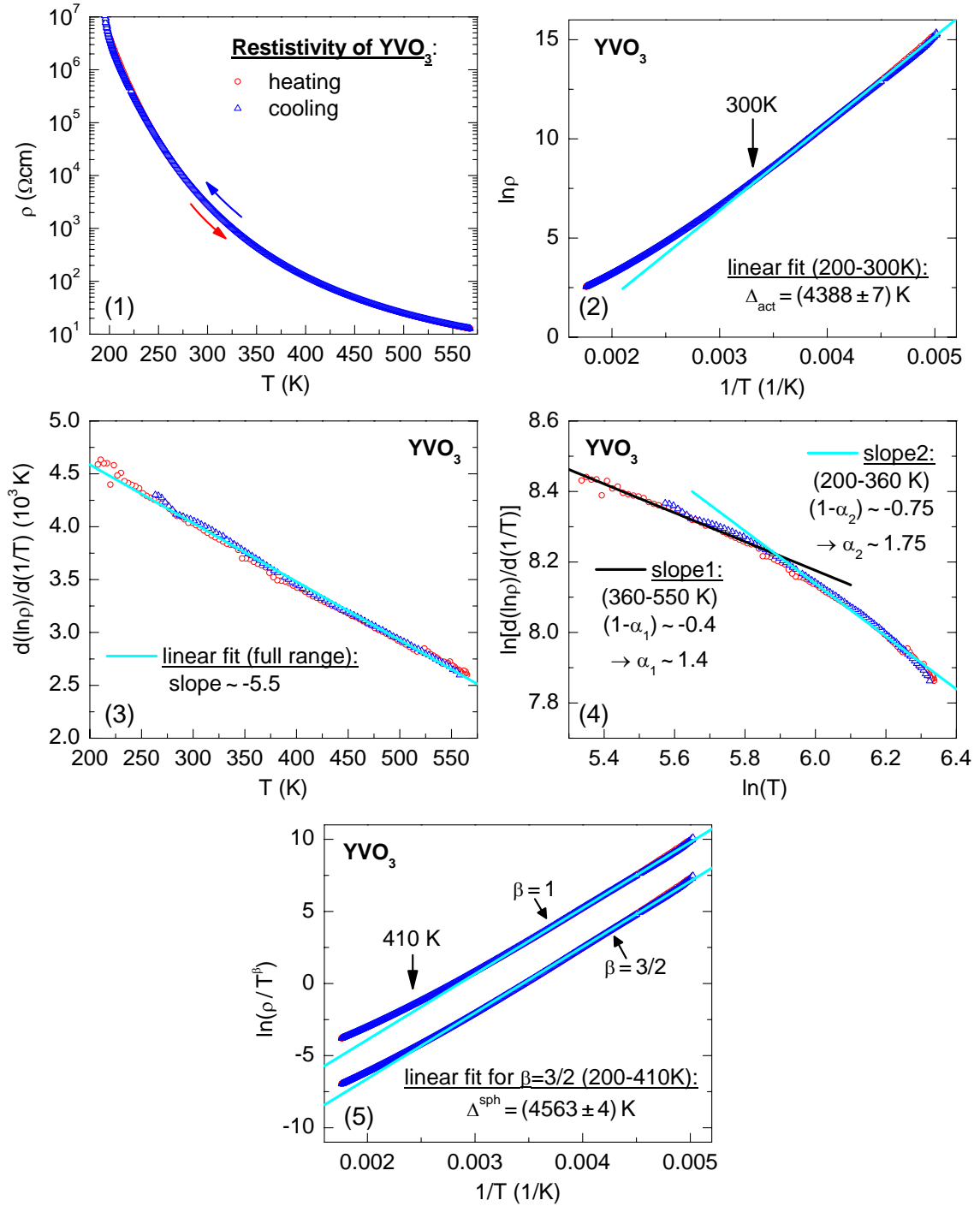
Figure 4.17.: (1) Resistivity $\rho(T)$ of YVO$_3$ from 180 K to 600 K. (2) Arrhenius plot: $d(ln(\rho))/d(1/T)$ versus $1/T$. (3) $d(ln(\rho))/d(1/T)$ versus T. (4) Double-logarithmic plot of $d(ln(\rho))/d(1/T)$ versus T. (5) Fit with the non-adiabatic small polaron hopping model (for details see text).

Δ^{sph} [163]. If an electric field is applied, one side of the well is lowered slightly with respect to the other one. This makes it more likely for the polaron to move in this direction. For the temperature dependence of the resistivity, the expression

$$\rho^{\mathrm{sph}} = CT^{\beta} \exp\left(\frac{\Delta^{\mathrm{sph}}}{k_B T}\right) \tag{4.4}$$

is found [161]. One has to distinguish between the adiabatic and the non-adiabatic case, resulting in two different values of the exponent β. In the adiabatic case, the charge carrier has a high probability to jump to the neighboring site, and goes backward and forward several times during each excitation of the lattice. In this case the exponent is $\beta = 1$ [164]. In the non-adiabatic approximation, the charge carrier has a low probability to make a jump during a lattice excitation, and $\beta = 3/2$ is expected [161]. As shown in Fig. 4.17(5) the non-adiabatic approximation fits the data best. From a fit in the temperature range of 200 - 410 K we obtain $\Delta^{\mathrm{sph}} = 4563\,\mathrm{K} \sim 0.39\,\mathrm{eV}$. Within the simple hopping model, the activation energy is given by the slope in the Arrhenius plot in Fig. 4.17(2). Here we obtain $\Delta_{act} = 4388\,\mathrm{K} \sim 0.38\,\mathrm{eV}$ by a linear fit in the temperature range 200 - 300 K. However, neither of both theories describes our data sufficiently in the complete temperature range. Nevertheless, both values for the activation energy lie close together and we guess that the error is about 0.01 eV. In any case, the activation energy is higher than the value of 0.25 eV obtained in earlier experiments [156]. We take this result as an indication for the high quality of our samples. It should be noticed that the gap obtained by resistivity measurements in general is highly sensitive to impurities. The influence of impurities is pronounced if the clean compound has a large energy gap. In this case, small amounts of impurities determine the experimentally obtained value and the energy gap of the clean compound is underestimated.

4.2.5. Transmittance of YVO$_3$

The transmittance measurements of YVO$_3$ were performed on several samples summarized in Tab. 4.4 using the experimental setup described in Chap. 3. All measurements were performed using linearly polarized light with the electric-field vector aligned parallel to a room-temperature orthorhombic axis, i.e. $E \parallel a$, b, or c in *Pbnm*. For convenience, we use the same set of axes at all temperatures, i.e. we neglect the monoclinic structure in the intermediate phase. This is justified because the monoclinic angle of $\alpha = 89.98°$ is very close to 90° [29, 76], thus the off-diagonal elements of the σ tensor in the monoclinic phase are negligible (see Chap. 2.1.1). Exemplarily the transmittance $T(\omega)$ for $E \parallel a, b, c$ (T_a, T_b, T_c) of two samples (Y2 and Y3 with thickness 330 μm and 368 μm, respectively) is shown in Fig. 4.18. Both measurements were performed in the MIR frequency range (see Chap. 3). Compared with the reflectance, the transmittance of thin samples is very sensitive to weak absorption features and shows a stronger polarization and temperature dependence.

Because the thickness of both samples is comparatively large, interference fringes are unresolved ($\Delta\nu = 1/(2nd) \approx 7\,\mathrm{cm}^{-1}$). Below $125\,\mathrm{meV}$ the samples are opaque, i.e. $T(\omega) = 0$, because of the strong absorption by the bond-stretching phonon also observed in the reflectance (Sec. 4.2.8). Above $0.7\,\mathrm{eV}$ the transmittance is suppressed to nearly zero. In the intermediate energy range, values of $20\text{-}60\,\%$ for the transmittance are observed. Intrinsic, small and broad absorption features are centered at about $0.2\,\mathrm{eV}$. These are superposed by sharper, small multi-phonon bands observed for all three polarization directions. In T_a additionally a small, broad absorption at about $0.55\,\mathrm{eV}$ is observed already at room temperature. By lowering the temperature the overall transmittance increases and both absorption features become more pronounced. When crossing the orbital ordering temperature $T_{OO} = 200\,\mathrm{K}$ the spectra change drastically. The two peaks in T_a move towards each other. The result is a very broad dent. The shift of the $0.2\,\mathrm{eV}$ absorption in the intermediate temperature range is more clearly seen in T_b where no absorption a $0.55\,\mathrm{eV}$ is observed. However, the largest changes when crossing T_{OO} occur for $E \,||\, c$. Here an absorption at $0.4\,\mathrm{eV}$ smoothly increases with decreasing temperature and reaches a maximum at $80\,\mathrm{K}$, right above the first-order phase transition at $T_S = 77\,\mathrm{K}$. Below T_S it abruptly disappears. At the same time the $0.55\,\mathrm{eV}$ absorption in T_a shifts again to higher energies and becomes more pronounced. Qualitatively, except for the absolute values, the data at $10\,\mathrm{K}$ are comparable with the room-temperature data, with absorption features around $0.2\,\mathrm{eV}$ in T_a, T_b, and T_c and a second one at $0.55\,\mathrm{eV}$ in T_a.[19]

Exemplarily, also T_a, T_b, and T_c in the near-infrared (NIR) frequency range are shown in Fig. 4.19. Here much thinner samples were considered (Y4 and Y5, both with a thickness of $130\,\mu\mathrm{m}$). Above $1.05\,\mathrm{eV}$ the transmittance is strongly suppressed in all three polarization directions, i.e. $T(\omega) \lesssim 2\,\%$. However, the enlargement shown in the insets of Fig. 4.19 brings out some very small, sharp absorption features extending up to $1.7\,\mathrm{eV}$. These also show a pronounced temperature and polarization dependence, in particular the peaks become sharper around $T_N = 116\,\mathrm{K}$.

4.2.6. Transmittance of HoVO$_3$

In the case of HoVO$_3$ we performed two measurements of the transmittance, one on each sample H1 and H2 (see Tab. 4.4). The results are shown in Fig. 4.20. The spectra are very similar to those of YVO$_3$ except for additional stronger and sharper absorption bands around $0.63\,\mathrm{eV}$. These are so strong that $T(\omega) \approx 0$ at some frequencies. The absolute value of the transmittance is somewhat higher, up to $70\,\%$, despite of the larger thickness compared with the YVO$_3$ samples. Here as well small absorption features of films of hexagonal ice are recognizable at $0.4\,\mathrm{eV}$ below $150\,\mathrm{K}$ (for details see Chap. 3).

---

[19]In both T_a and T_c, very small absorption peaks appear at about $0.4\,\mathrm{eV}$ below $T = 150\,\mathrm{K}$. These can be attributed to the formation of films of hexagonal ice on the samples surfaces (see Chap. 3).
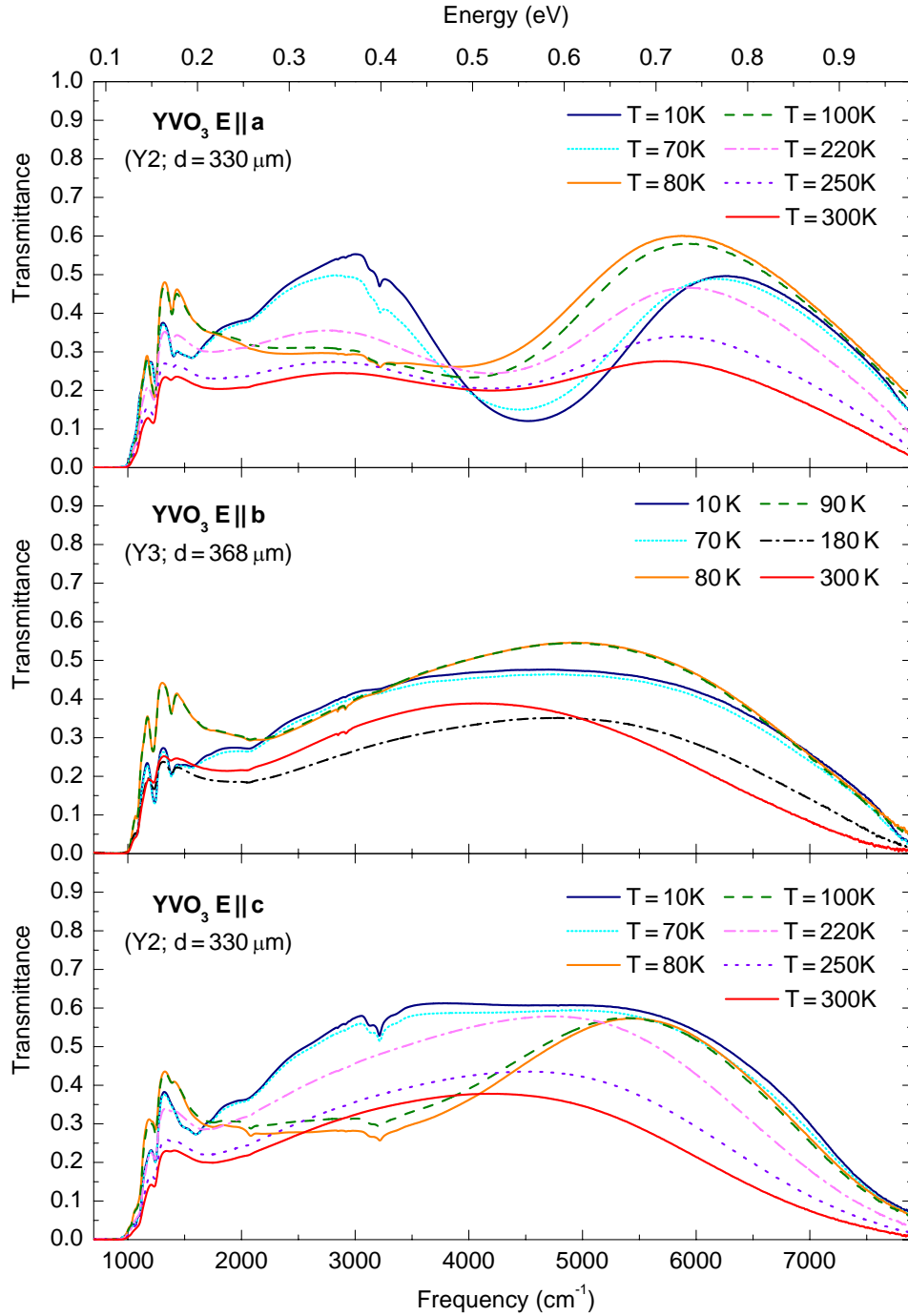
Figure 4.18.: Temperature dependence of the mid-infrared (MIR) transmittance of YVO_3 for $E \parallel a, b, c$ (T_a, T_b, T_c from top to bottom panel). T_a and T_c have been obtained in the same measurement on sample Y2 (see Tab. 4.4). T_b has been measured on sample Y3. Both measurements were performed using the same components, i.e. the globar, the BaF_2 polarizer, the KBr beam splitter, and the MCT detector. Just some selected temperatures are shown.
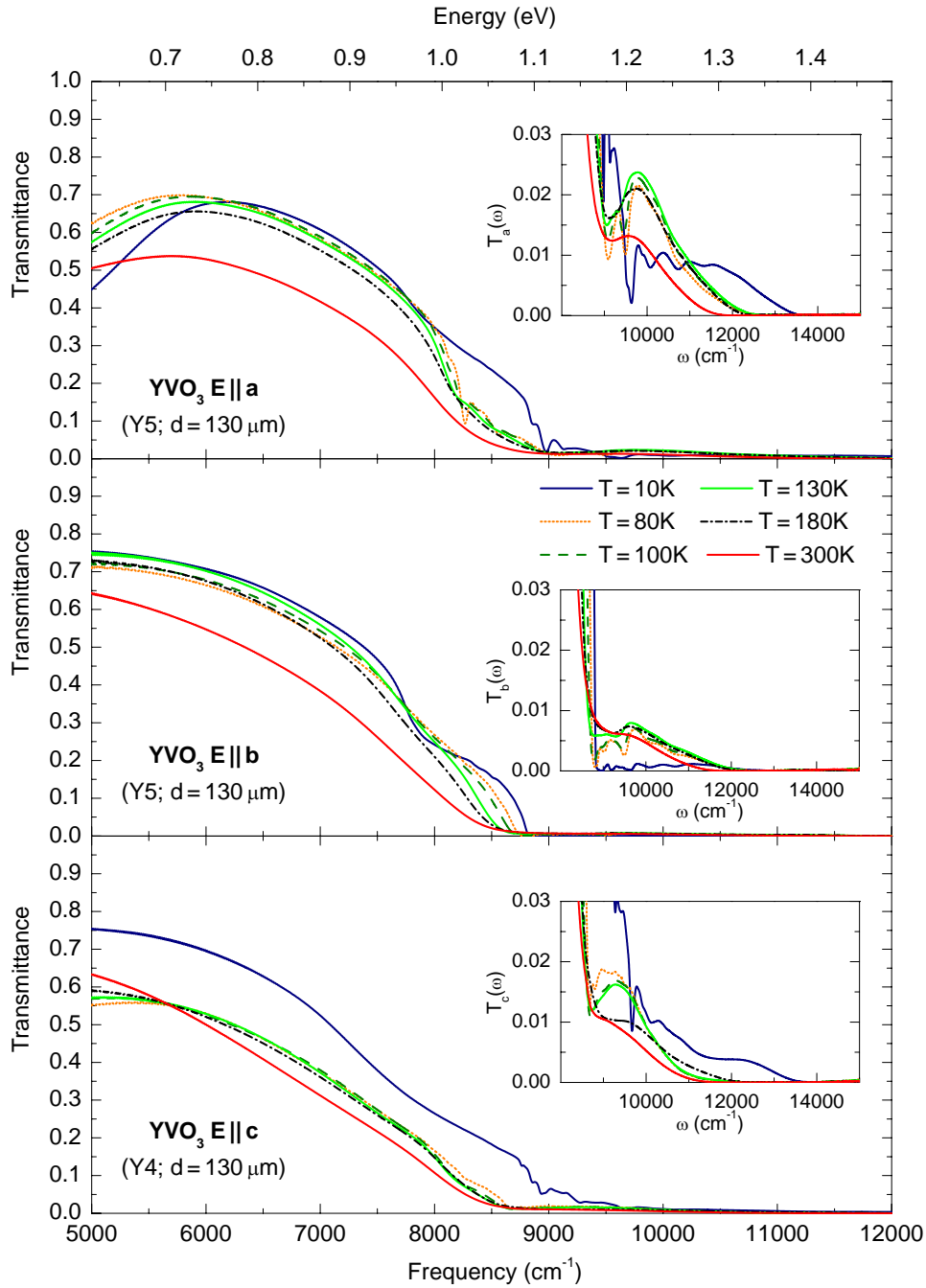
Figure 4.19.: Temperature dependence of the near-infrared (NIR) transmittance of YVO_3 for $E \parallel a, b, c$ (T_a, T_b, T_c from top to bottom panel). T_a and T_b have been obtained in the same measurement on sample Y5 (see Tab. 4.4). T_c has been measured on sample Y3. Both measurements were performed using the tungsten lamp, the Glan-Thompson prism as polarizer, the VIS beam splitter, and the MCT detector and the Si-diode, respectively. Note that the spectra measured with the MCT detector and the Si-diode were merged around 1.1 eV. The insets show an extended view in each case.
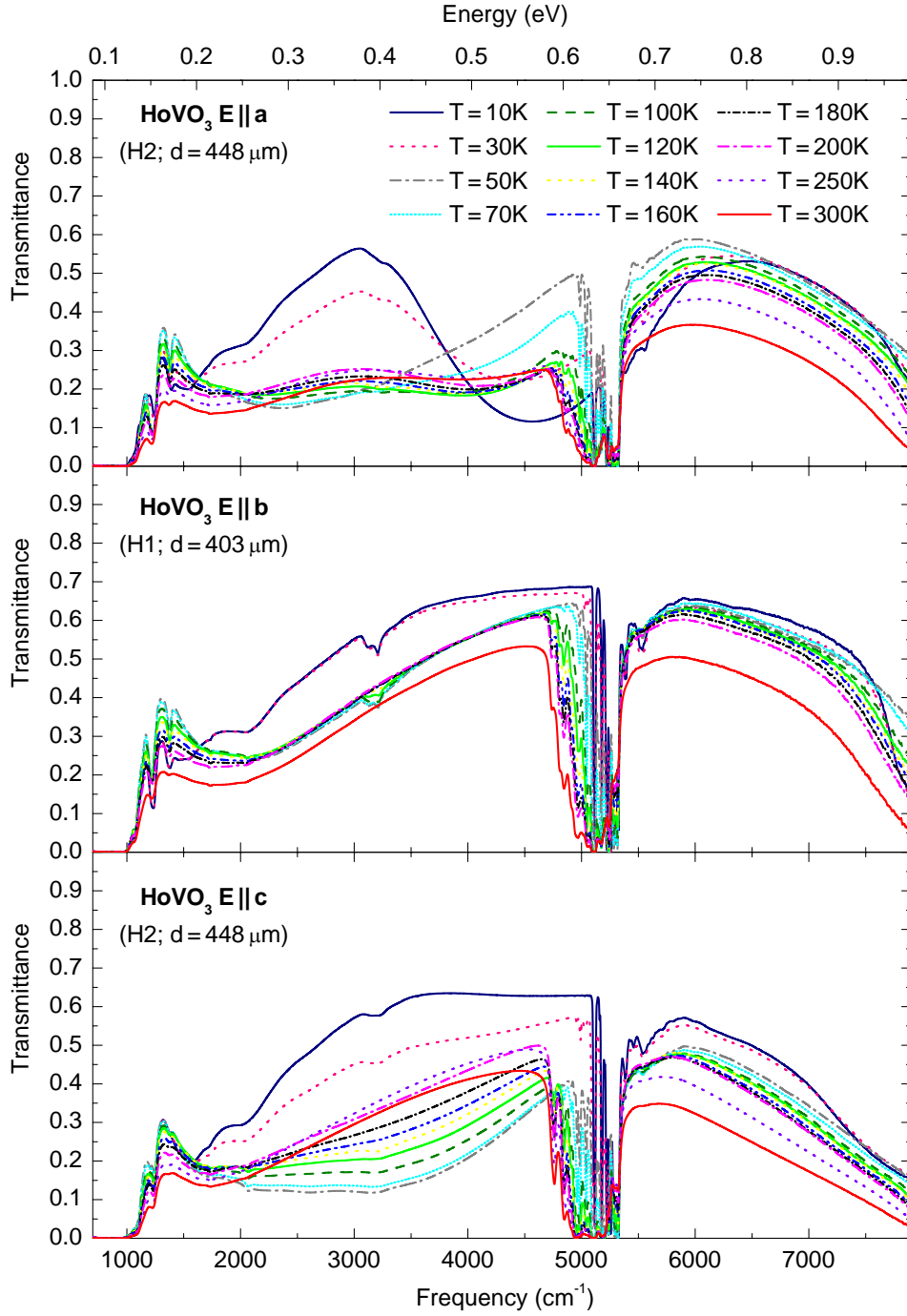
Figure 4.20.: Temperature dependence of the mid-infrared (MIR) transmittance of HoVO$_3$ for $E \parallel a, b, c$ (T_a, T_b, T_c from top to bottom panel). While T_a and T_c have been obtained in same measurement on sample H2, T_b has been measured on sample H1 (see Tab. 4.4). Both measurements were performed using the same components, i.e. the globar, the BaF$_2$ polarizer, the KBr beam splitter, and the MCT detector.
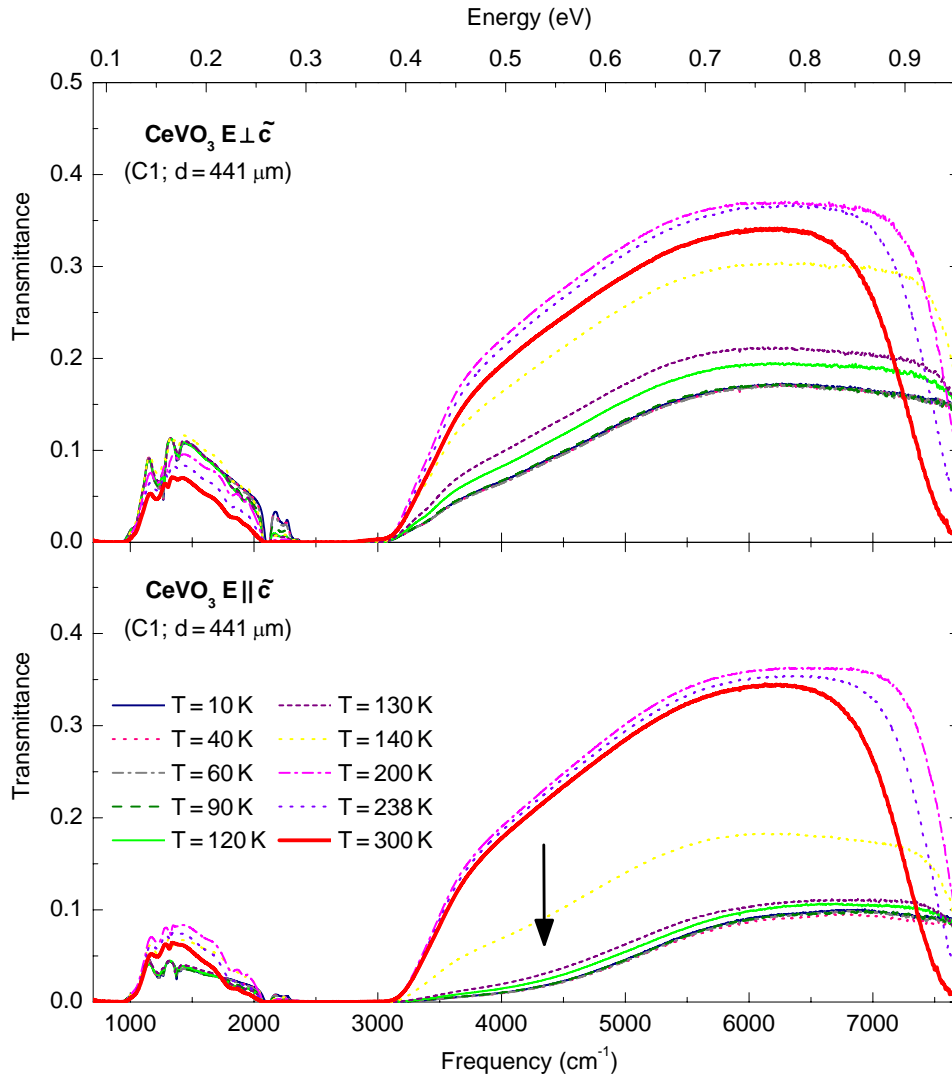
Figure 4.21.: Temperature dependence of the mid-infrared (MIR) transmittance of CeVO$_3$ for $E \parallel \tilde{c}$ (top panel) and $E \perp \tilde{c}$ (bottom panel; see also Fig. 4.13). The measurement was performed using the globar, the BaF$_2$ polarizer, the KBr beam splitter, and the MCT detector.

4.2.7. Transmittance of CeVO$_3$

The transmittance of CeVO$_3$ was measured just on one sample, C1 (Tab. 4.4), using an aperature of 1 mm in diameter. Because the twin domains are about $0.25 \times 2 \, \text{mm}^2$ in plane as illustrated above (Chap. 4.2.1 & Fig. 4.13), with the 1 mm aperature a region of at least five domains is considered. However, at room temperature two perpendicular polarization states, denoted $E \parallel \tilde{c}$ and $E \perp \tilde{c}$ (see Fig. 4.13) with slightly different transmittance were found. The temperature dependence of the transmit-

tance for polarization along these two directions is shown in Fig. 4.21. Between $0.25\,\mathrm{eV}$ and $0.4\,\mathrm{eV}$ and below $0.12\,\mathrm{eV}$ the transmittance is almost zero. The absolute value of the transmittance compared with that of YVO_3 and $HoVO_3$ is small ($\lesssim 40\,\%$), although the sample thickness is similar. By lowering the temperature below $T_N = 134\,\mathrm{K}$ the spectra change drastically. The absolute value of $T(\omega)$ is strongly reduced and the polarization dependence becomes more pronounced. While the maximum value of $T(\omega)$ is about $10\,\%$ for $E\,||\,\tilde{c}$ it is about $20\,\%$ for $E\perp\tilde{c}$ at low temperatures. For $E\,||\,\tilde{c}$ we find a weak absorption band between 0.5 and $0.6\,\mathrm{eV}$ at low temperatures, which may already be present at higher temperatures (see discussion of $\alpha(\omega)$ in Chap. 4.3).

4.2.8. Reflectance of YVO$_3$

The reflectance $R(\omega)$ of YVO_3 was measured between 0.06 and $1.86\,\mathrm{eV}$ in a temperature range between $10\,\mathrm{K}$ and $300\,\mathrm{K}$ using the experimental setup described in Chap. 3. The measurements were performed using linearly polarized light with the electric-field vector aligned parallel to a room-temperature orthorhombic axis, i.e. $E\,||\,a$, b, or c in *Pbnm*. The results are shown in Fig. 4.22. For 0.2 - $1.8\,\mathrm{eV}$ $R(\omega)$ has an almost constant, small value and is featureless. The change below $0.2\,\mathrm{eV}$ reflects the strong phonon absorption observed at about $0.07\,\mathrm{eV}$ in all three polarization directions, i.e. in $R_a(\omega)$, $R_b(\omega)$, and $R_c(\omega)$. A nearly constant $R(\omega)$ is typical for insulators above the highest phonon absorption and below the band gap. The different absolute values of $R_a(\omega)$, $R_b(\omega)$, and $R_c(\omega)$ reflect the difference in the index of refraction: $n_a \approx 2.21\pm0.01$, $n_b \approx 2.30\pm0.01$, and $n_c \approx 2.16\pm0.03$.[20] The difference between these values is small, revealing the pseudo-cubic symmetry. Our data are in good agreement with the FIR reflectance repeated in [75] up to $0.12\,\mathrm{eV}$ (Fig. 2.2).

The reflectance R_a has been obtained twice, in the measurements on samples Y8 and Y9 (see Tab. 4.4). While the room-temperature data of both measurements agree well, the low-temperature data show small deviations. However, we take advantage of the Fabry-Perot fringes (Sec. 3.1.2) observed in the transmittance measurement on the Y4 sample. From the temperature-dependence of the relative period $\Delta\nu_a$ and $\Delta\nu_c$ of the fringes and the thickness $d = (130\pm2)\,\mu\mathrm{m}$ we calculated the corresponding temperature-dependent values of the reflectance using $R(T) = (n(T)-1)^2 / (n(T)+1)^2$ with $n(T) = 1/(2\,d\,\Delta\nu(T))$. These values are shown in Fig. 4.23 together with values for R_a and R_c which were read off by assuming a constant reflectance from the data obtained on the Y8 and Y9 sample. The comparison shows that the correct reflectance has an almost temperature-independent value. Therefore we believe that the data obtained in measurement Y9 are correct.[21] However, the low-temperature data of R_c had to be corrected by a

---

[20]These values were estimated from $n \approx (1+\sqrt{R})/(1-\sqrt{R})$. This formula is deduced from Eq. 2.6 by neglecting κ. The errors have been estimated to 0.01 for n_a and n_b. The error for n_c is 0.03 because the data have been corrected (see below).

[21]The measurement on the sample Y9 was repeated in the NIR range, with significant overlap to
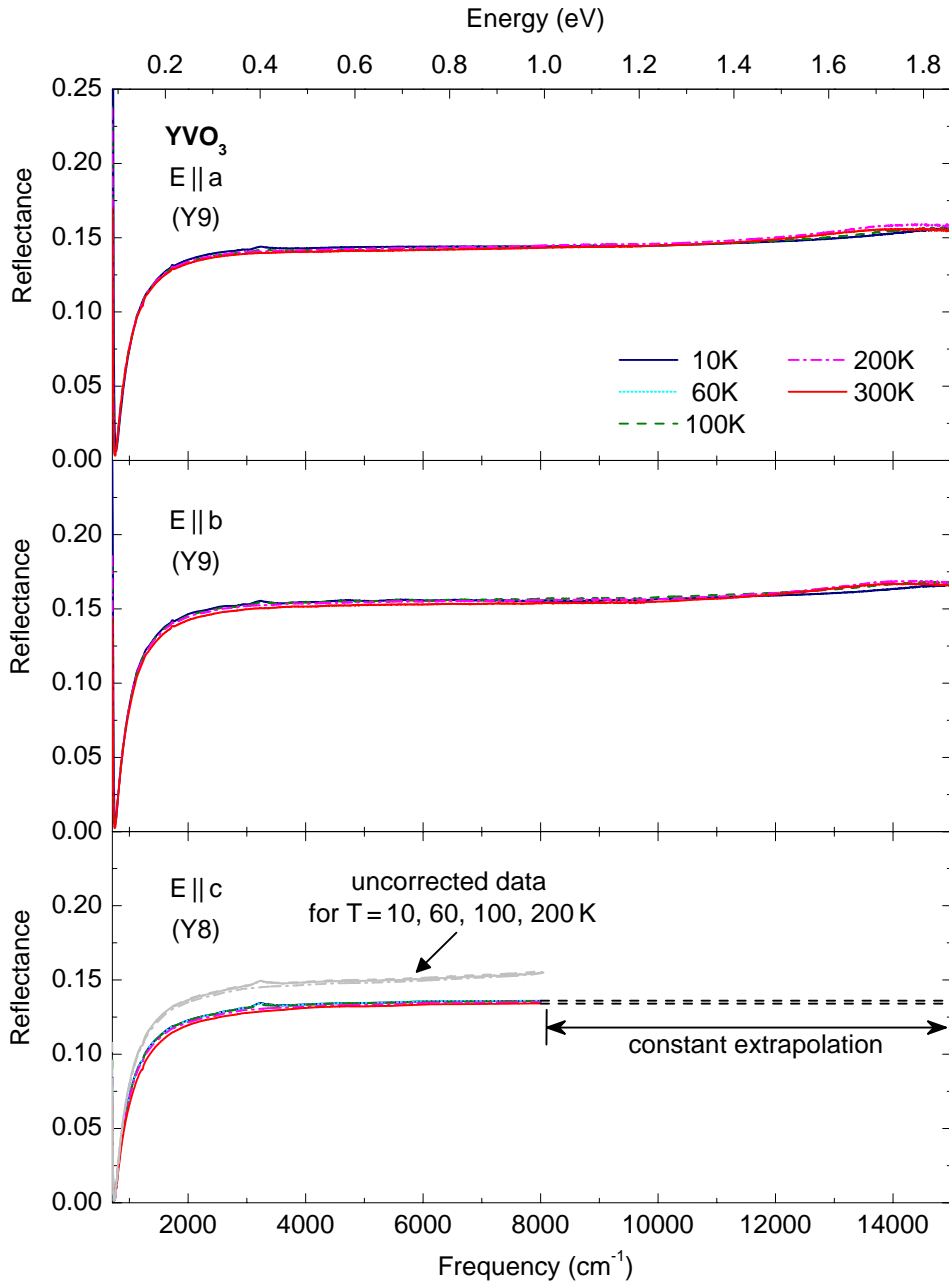
Figure 4.22.: Temperature dependence of the reflectance of YVO_3 for polarization of the incident electric field parallel to the orthorhombic a (top panel), b (middle panel), and c axis (bottom panel). The reflectance R_c was measured only in the MIR (up to $1\,eV$). At higher frequencies we used a constant extrapolation, which is justified by comparison with R_a and R_b. The small changes observed in R_a and R_b are crucial for a Kramers-Kronig analysis, but they are negligible for the combined analysis of transmittance *and* reflectance (for details see text).
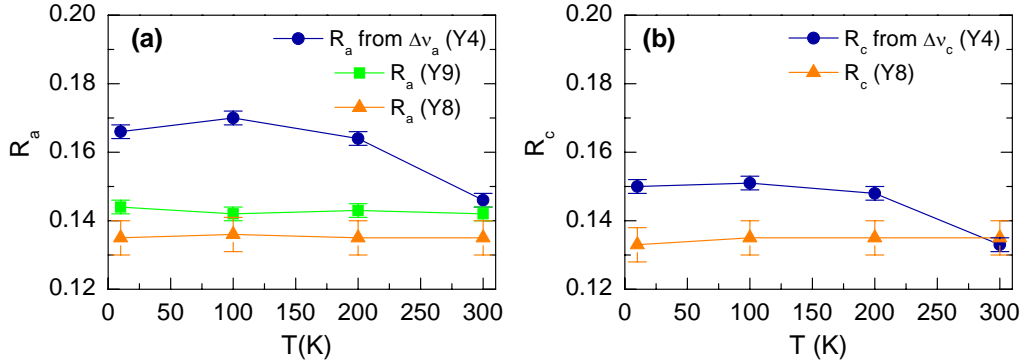
Figure 4.23.: Temperature dependence of the reflectance (a) R_a and (b) R_c of YVO$_3$. The values of have been estimates in two ways: (i) R_a and R_c were estimated by assuming a constant reflectance for the measurements of the Y8 and Y9 sample (Tab. 4.4). Here the errors due to the deviation from a constant value were estimated to 0.002. (ii) R_a and R_c were derived by analyzing the Fabry-Perot fringes with periodicity $\Delta\nu_a$ and $\Delta\nu_c$ in the transmittance measurement on the Y4 sample ($d = (130 \pm 2)\,\mu$m). In this case we assumed that the error is determined by the error of the thickness Δd, i.e. $\Delta R = \frac{8\Delta\nu(2d\Delta\nu-1)}{(2d\Delta\nu+1)^3}\Delta d$.

factor of 0.9 for $T = 10, 60, 100, 200$ K (Fig. 4.23(b)). The room-temperature data remain uncorrected.

Since R_c has been measured only up to 0.95 eV we extrapolated the spectra with a constant value up to 1.85 eV. As a test we compare our data to the reflectance obtained from ε_1 and ε_2 measured by Tsvetkov *et al.* [75] (Fig. 4.9). The reflectance calculated from the fit of ε_1 and ε_2 and the measured data together with the constant extrapolation are in good agreement (bottom panel in Fig. 4.24). The high-energy electronic excitations only give rise to small changes of the reflectivity. These are crucial if one wants to determined $\sigma(\omega)$ of the interband excitation via Kramers-Kronig analysis. However, our aim is to determine $\sigma(\omega)$ for frequencies below the interband excitations from a combined analysis of $T(\omega)$ and $R(\omega)$. Here the result is largely determined by $T(\omega)$, in particular as far as absorption feature are concerned. Thus for our purpose the error in R_c is negligible. As a demonstration the determination of $\sigma(\omega)$ from $T(\omega)$ and $R(\omega)$ for YVO$_3$ at $T = 10$ K is shown in Fig. 4.25. The used formulas have been deduced already in Chap. 2.

---

the MIR range. This additionally provides evidence for a correct measurement.

[22]The fit has been performed using the program RefFIT 1.2.56 by A. Kuzmenko (Département de Physique de la Matière Condensée, Université de Genève, Switzerland).
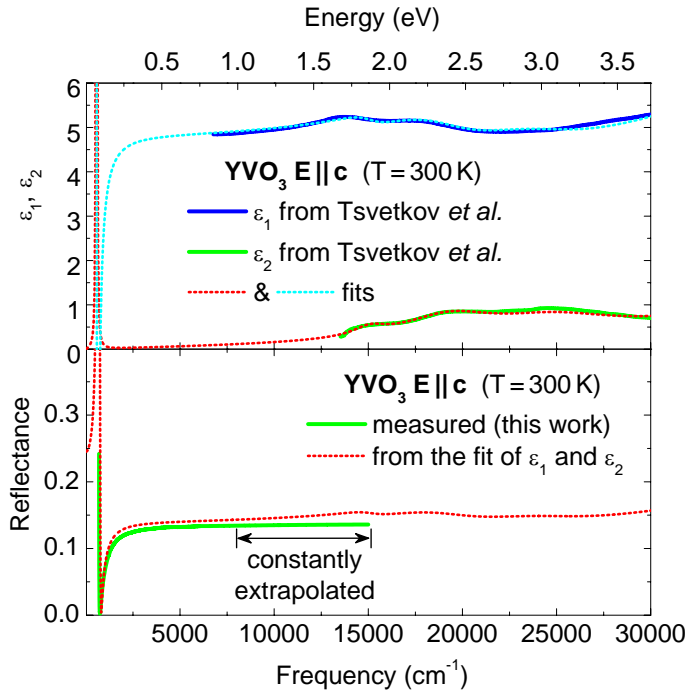
Figure 4.24.:
Real and imaginary part of the dielectric function at 300 K for $E \parallel c$ obtained by Tsvetkov *et al.* [75] and the corresponding fits (top panel).[22] The bottom panel shows the reflectance obtained by fitting ε_1 and ε_2 together with the reflectance of YVO_3 measured in this work. To fit $\varepsilon_{1,2}$ we used four Lorentzian oscillators plus one at low energies (70 meV) simulating the highest phonon mode [75].
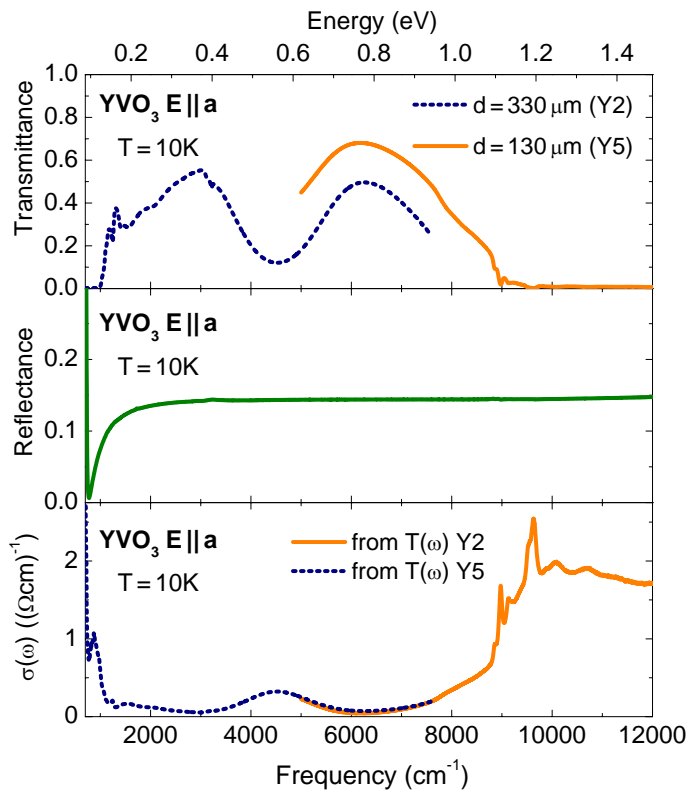
Figure 4.25.:
Demonstration of the determination of the optical conductivity $\sigma(\omega)$ (bottom panel) from the transmittance of samples with thickness d (top panel) and the reflectance (middle panel). Exemplarily the data of YVO_3 at $T = 10$ K are shown. In particular $\sigma(\omega)$ is calculated separately for spectra obtained by different transmittance measurements, e.g. on the sample Y2 and Y5 in the top panel of Fig. 4.25, i.e. if so, the optical conductivity data are merged.

4.3. Results: Optical Conductivity of RVO$_3$

In this work we use optical spectroscopy to study the orbital excitations in orbitally ordered RVO$_3$ with $R =$ Y, Ho, and Ce as a function of temperature and the polarization of light. The comparison with other d^2 systems, VOCl and Dy(Sc,V)O$_3$ in combination with the results of our cluster calculations shows that absorption features at about 0.2 and 1.1 eV can be explained in terms of local crystal-field excitations of the V^{3+} ions. However, the polarization and temperature dependence of two absorption bands at 0.4 eV and 0.55 eV are hard to reconcile with a local crystal-field scenario.

4.3.1. Optical Conductivity of YVO$_3$

Initially we focus on YVO$_3$. As illustrated in Fig. 4.25 the optical conductivity was calculated directly from $T(\omega)$ and $R(\omega)$. The spectra of the MIR and NIR region were merged together afterwards. The real part of $\sigma(\omega)$ is shown in Fig. 4.26 between 10 K and 300 K from 0.12 eV up to 1.7 eV. An extended view of the low-energy range is shown in Fig. 4.27. The considered energy range covers the transparent window of the Mott insulator YVO$_3$ between strong phonon absorption and electronic interband excitations.

Charge-transfer excitations, involving the transfer of an electron between V and O ions $d^2 \rightarrow d^3\bar{L}$, are located above about 4 eV [75]. The lowest Mott-Hubbard excitations are located right below. These correspond to the transfer of one electron from one V^{3+} site to another one, i.e. from $3d^2 3d^2$ to $3d^1 3d^3$ (see Sec. 2.3). The onset of the Mott-Hubbard gap has been identified at 1.6 eV by the combination of ellipsometry and LSDA$+U$ calculations [75] (see also Fig. 4.9). The subsequent strong increase of σ_1 above 1.6 eV is attributed to the onset of transitions across the direct (optical) gap. This is in agreement with the steep rise of $\sigma_1(\omega)$ observed in our data. However, σ_1 becomes appreciable usually at the onset of the lowest *direct* transition [165]. Very recent first-principles calculations have shown that YVO$_3$ exhibits an *indirect* gap which is estimated to be around 0.7 eV [140]. Indirect optical transitions are just possible with the involvement of phonons because of momentum conservation [165]. Therefore, they are much weaker than direct transitions [165]. Indeed, σ_1 already starts to rise at about 0.7 eV, which may reflect the indirect gap. The excellent agreement with the theoretically obtained value of 0.7 eV should not be taken too seriously, since the theoretical value sensitively depends on the choice of U. In fact, the same calculations [140] predict that the difference between the direct and indirect gap is only 0.1 eV, i.e. the direct gap is strongly underestimated. The value of 0.7 eV for the indirect gap is in good agreement with the result of our DC resistivity measurements from which we estimated $\Delta_{opt} = 0.76$ eV (see Sec. 4.2.4). However, the resistivity clearly did not show simple activated behavior. The best description was obtained based on the small-polaron model. The gradual onset of σ_1 around 0.7 eV thus may also reflect the activation energy of trapped polarons.
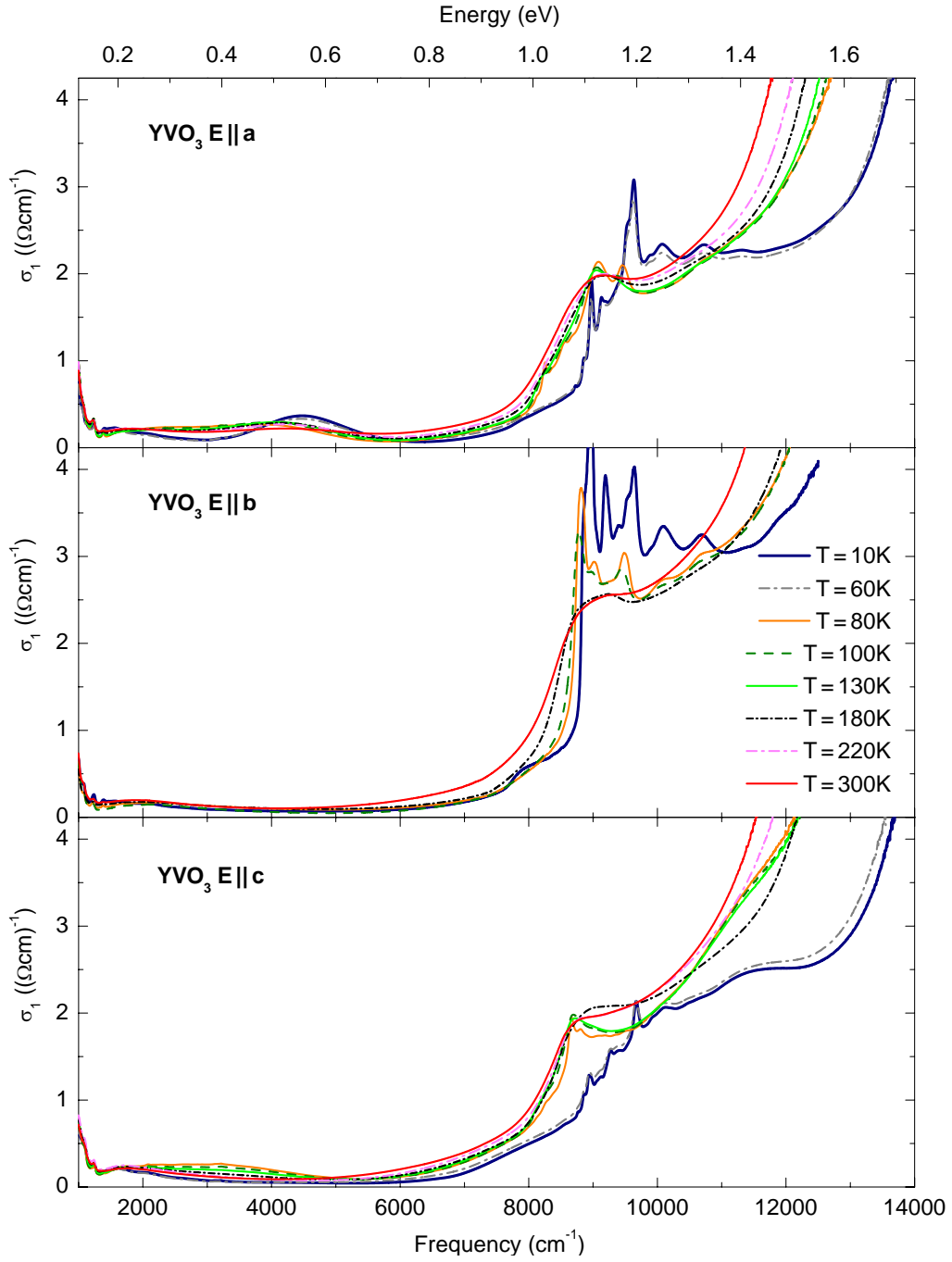
Figure 4.26.: Temperature dependence of $\sigma_1(\omega)$ of YVO₃ for E∥a (top panel), E∥b (middle panel), and E∥c (bottom panel). The figure shows the spectra over the entire energy range considered in this work.
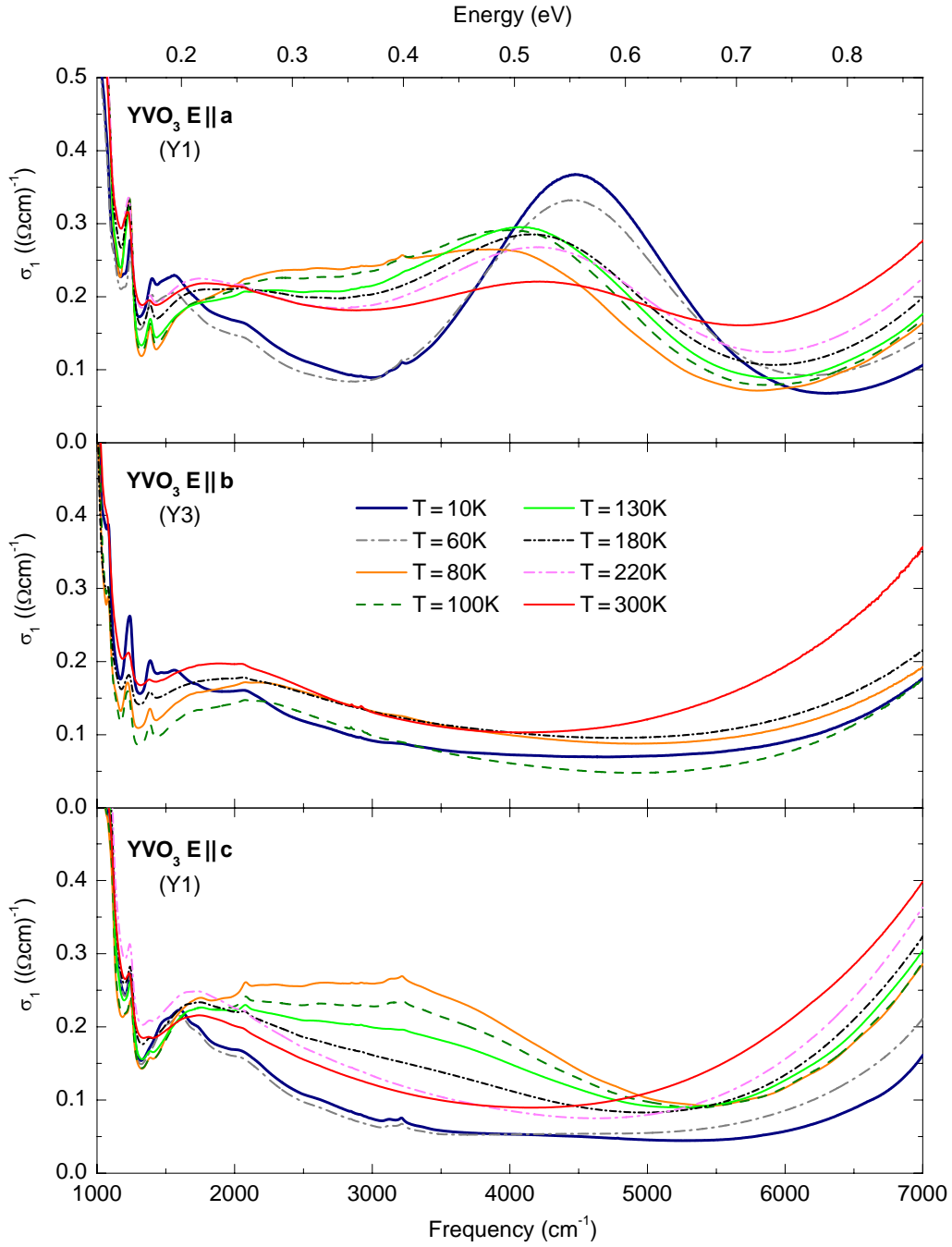
Figure 4.27.: Mid-infrared optical conductivity of YVO$_3$ for $E \parallel a$ (top panel), $E \parallel b$ (middle panel) and $E \parallel c$ (bottom panel) at several temperatures. The small absorption at $0.40\,\mathrm{cm}^{-1}$ observed in σ_a and σ_c below $130\,\mathrm{K}$ is due to the absorption of thin surface layers of ice (see Sec. 3.1.2).

Extracting a more exact value from the optical conductivity is difficult because the onset is not that sharp, and because of the superposition with local crystal-field excitations around 1.1 eV, which will be discussed later in Sec. 4.3.3.

All absorption features below at least 0.7 eV have to be attributed to phonons, magnetic excitations, and orbital excitations (Fig. 4.27 and 4.30). In particular, we claim that the absorption features at 0.2 eV, 0.4 eV, 0.55 eV, and 1.1 eV have to be attributed to orbital excitation. Phonons and magnetic excitations are excluded due to the following arguments: (1) Phonons give rise to the steep increase of $\sigma_1(\omega)$ below about 80 meV, and some weak multi-phonon features are observed up to about 200 meV. These features are very similar for all three polarization directions. The highest phonons are in good agreement with previous results [75]. From a Kramers-Kronig analysis of reflectivity data the highest IR-active phonon is found at about 85 meV [75] (see also Fig. 2.2). From Raman spectroscopy the V-O bond-stretching mode as the highest in energy is identified by two different groups at 83 meV [32] and 86 meV [33], respectively (see also Tab. 4.2). A two-phonon absorption is not necessary two times an IR-active mode. The symmetry of a multi-phonon has to be deduced from the symmetries of the contributing fundamental modes, and an IR-active multi-phonon mode may have contributions from Raman-active fundamental modes. Anyhow, from the energies of the highest modes mentioned, it can be deduced that two-phonon excitations must be below 200 meV in YVO$_3$. Higher-order phonon absorption becomes more unlikely with increasing number of involved phonons and therefore we expect a much smaller spectral weight. (2) The spin-wave dispersion does not exceed 40 meV in YVO$_3$ [28]. Thus phonon-assisted two-magnon absorption is not responsible for the features observed between 0.2 and 0.7 eV. Consequently we conclude that these features have to be ascribed to orbital excitations.

Local crystal-field scenario

At first we check an interpretation in terms of local crystal-field excitations. To illustrate the absorption spectrum of local crystal-field excitations of V^{3+} ions with two electrons in a predominantly cubic, but distorted environment, we (i) measured spectra of two other d^2 systems, VOCl and Dy(Sc,V)O$_3$, and (ii) performed a cluster calculation for each system.

To get an overview on the energy levels involved, we first consider the 'Sugano-Tanabe' [77] diagram for V^{3+} (N = 2 electrons) shown in the left panel of Fig. 4.28. In addition we have calculated the energy levels for the V^{3+} ion in the orthorhombic structure of YVO$_3$ at 5 K (right panel of Fig. 4.28).[23] Because effects of hybridization remain unconsidered here (see Sec. A.1), the energy values for YVO$_3$ are less reliable compared to those obtained with the program of A. Tanaka discussed below

---

[23]Both diagrams in Fig. 4.28 have been calculated using the program 'crystal-field theory including full multiplets' written by M. Haverkort [168].
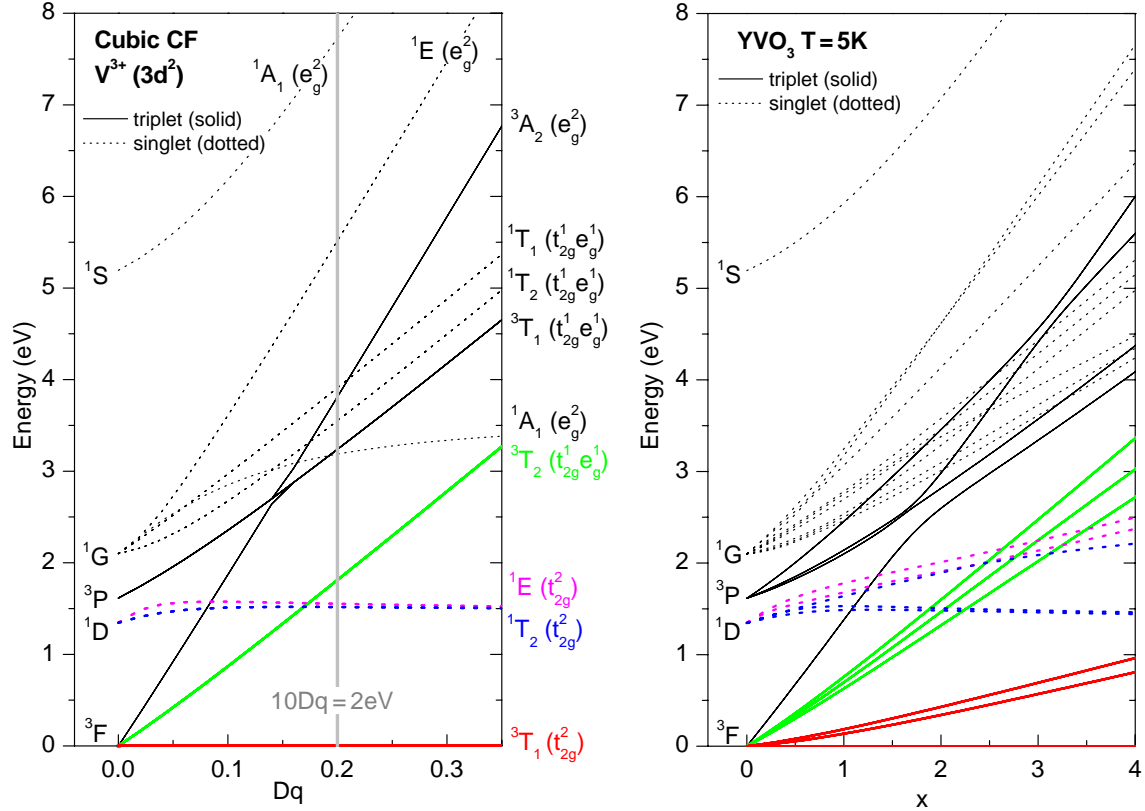
Figure 4.28.: Energy-level diagrams for V^{3+} ($N = 2$ electrons) in a cubic crystal field as a function of the t_{2g}-e_g splitting Dq (left panel) and for the orthorhombic structure of YVO_3 at 5 K (right panel). The latter is based only on the Madelung potential from a point charge estimate (see Sec. A.1). $x = 1$ corresponds to the full Madelung potential, $x = 0$ to the free-ion case. Because hybridization has not been considered here, the level diagram for $x > 1$ is appropriate. In the left panel the vertical line marks the value of the t_{2g}-e_g splitting for RVO_3 of $10Dq \sim 2$eV ([166] and this work (Sec. 4.3.5)). The labels given on the right side of the left panel indicate the occupation in the crystal-field limit [167].

(Tab. 4.6).[24] Concerning the energy values we will therefore refer to the latter in following.

The ground state of a d^2 system in a cubic field is the nine-fold degenerate $^3T_1$ level with total spin $S = 1$ (triplet) [77] (see left panel of Fig. 4.28). If the crystal-field splitting $10Dq$ is much larger than the Coulomb interaction energies (crystal-field limit), it is a good approximation to calculate term energies within an independent-electron picture, i.e. neglect the configuration mixing of t_{2g}^2, $t_{2g}^1 e_g^1$ for the $^3T_1$ ground

---

[24] The cluster calculations were performed using the code XTLS8 written by A. Tanaka (Hiroshima University, Japan).

state [77] (for an estimate of the mixing, see App. A.2). The corresponding labels are given on the right side of the left panel in Fig. 4.28 [167]. For $10Dq \sim 2\,\mathrm{eV}$ in YVO$_3$ it is reasonable to use the single-electron notation (for a discussion of $10Dq$ in the related compound Dy(Sc,V)O$_3$ see Sec. 4.3.5). Then in the ground state both electrons occupy the degenerated t_{2g} orbitals and have parallel spin, according to Hund's rule. The first excited states correspond to intra-t_{2g} transitions involving a spin flip, i.e. transitions from the $^3T_1$ ground state to the $^1T_2$ and ^1E states.

In a crystal field of orthorhombic or lower symmetry, the $^3T_1$ term splits into three distinct levels, each showing three-fold spin degeneracy (right panel in Fig. 4.28).[25] Because the deviation from cubic symmetry in YVO$_3$ is small, for the lowest levels no crossing is observed, i.e. the degeneracy of the $^3T_1$ level is fully lifted, but it is still the lowest in energy. The orbital occupation in the ground state is approximately $d^1_{xy}d^1_{yz}$ and $d^1_{xy}d^1_{zx}$ for neighboring sites in the cubic coordinate system [18, 133, 134] (see Fig. 4.7 in Sec. 4.1.1). The lowest excitations then correspond to intra-t_{2g} transitions with parallel spins, e.g. $d^1_{xy}d^1_{yz} \to d^1_{xy}d^1_{zx}$ and $d^1_{xy}d^1_{yz} \to d^1_{yz}d^1_{zx}$. Our cluster calculation predicts values for these transitions below $0.3\,\mathrm{eV}$ for YVO$_3$ and slightly above $0.3\,\mathrm{eV}$ for VOCl (Tab. 4.6).[26] Well above in energy ($\sim J_H$), the intra-t_{2g} transitions involving a spin flip are the next higher lying excitations.

We compare the low-temperature spectra of YVO$_3$ (10 K, top panel) and VOCl (20 K, bottom panel) in Fig. 4.29. As argued in Chap. 2, local d-d excitations are in general not dipole-allowed, if there is inversion symmetry on the transition-metal site, like in YVO$_3$ (C_i ($\bar{1}$) point symmetry [29, 76]). However, they become weakly allowed by the coupling to phonons. In VOCl there is no inversion symmetry on the V sites (C_{2v} ($mm2$) point symmetry [169]) and the d-d excitations are weakly allowed *without* the additional excitation of a phonon. The structural differences are quantified by the energies of the crystal-field levels obtained by the cluster calculation (see Sec. A.1 and Tab. 4.6). The spectrum of VOCl shows absorption features around $0.35\,\mathrm{eV}$, $1.2\,\mathrm{eV}$, and $1.6\,\mathrm{eV}$. The broad feature at $0.35\,\mathrm{eV}$ results from a superposition of two peaks attributed to the intra-t_{2g} transitions with $S = 1$, in excellent agreement with our cluster calculation which predicts $0.31\,\mathrm{eV}$ and $0.39\,\mathrm{eV}$, respectively. The small polarization dependence may be a result of the different hybridization with the Cl$^-$ and O^{2-} ligands in VOCl giving rise to different dipole moments for $E \parallel a$ and $E \parallel b$. The tiny, sharp features around $1.2\,\mathrm{eV}$ are typical examples for spin-forbidden excitations with magnon sidebands (see Sec. 2.4.2). Our cluster calculation predicts the first $S = 0$ states at $1.30\,\mathrm{eV}$ and $1.32\,\mathrm{eV}$. The broad peak observed around $1.6\,\mathrm{eV}$ is attributed to the transition to the $t^1_{2g}e^1_g$ state, predicted at $1.5\,\mathrm{eV}$ by the cluster calculation. Both observed peak positions are slightly higher in energy than the predicted values. However, the energies of the higher lying states are more sensitive

---

[25]Spin-orbit coupling lifts the spin degeneracy, but the respective splitting is of the order of only a few meV in case of V^{3+} ions and will be neglected in the following. For a quantitative estimate of the splitting due to spin-orbit coupling see Fig. A.2 (e)&(f).

[26]The higher values for VOCl are expected because of the larger distortion of the octahedra.

[27]Institute of Physics II, University of Cologne, Germany
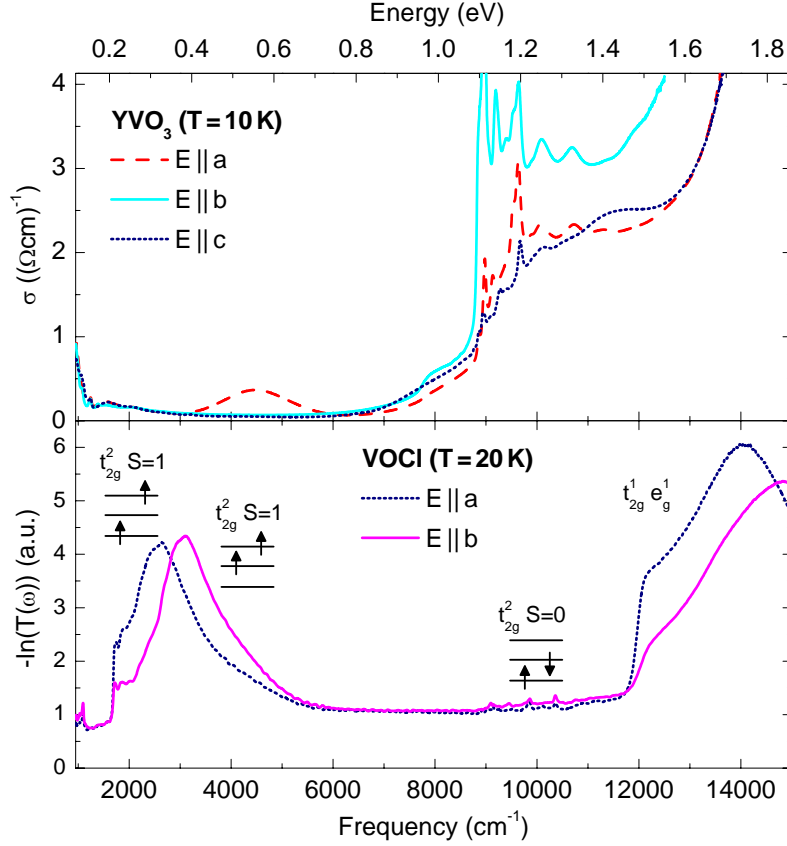
Figure 4.29.: Comparison of $\sigma_1(\omega)$ of YVO_3 (top panel) and $-\ln(T(\omega))$ of VOCl (bottom panel) at low temperatures. All measurements on VOCl were performed by R. Rückamp and T. Möller.[27]

to the chosen parameters in the cluster calculation, i.e. U_{dd}, Δ, etc. (see Fig. A.2). In particular the energies for excitations involving a spin flip are very sensitive to the parameter J_H, which in turn depends on the chosen Slater integrals.[28]

The spectrum of YVO_3 at $10\,K$ shows absorption features around $0.2\,eV$, $0.5\,eV$ (just for $E \parallel a$), and $1.2\,eV$. In comparison with VOCl the sharp features around $1.2\,eV$ are assigned with the spin-flip transitions (a detailed discussion can be found in Sec. 4.3.3). In a local crystal-field scenario the features below $1\,eV$ have to be interpreted as intra-t_{2g} transitions with $S = 1$. Our cluster calculation predicts transition

---

[28]Hund's coupling J_H can be expressed by $J_H = \frac{5}{2}B + C = \frac{2.5}{49}F^2 + \frac{22.5}{441}F^4$ with the Slater integrals F^2 and F^4 and the Racah parameters B and C [77, 168]. For our cluster calculation we used values for the Slater integrals which are $80\,\%$ of the atomic Hartree-Fock values [170]. Using $F^2 = 0.8 \cdot 10.126\,eV$ and $F^4 = 0.8 \cdot 6.353\,eV$ we obtain $J_H = 0.67\,eV$ [168]. Our results indicate that for this parameter larger values may are more appropriate. However, J_H does not affect the energies of the intra-t_{2g} transitions.

[29]The cluster calculations were performed using the program XTLS8 written by A. Tanaka (Hiroshima University, Japan)

Table 4.6.: Energies (in eV) of the nine lowest crystal-field levels of $3d^2$ V^{3+} in YVO$_3$ and VOCl as obtained by a cluster calculation, using $U_{\mathrm{dd}} = 4.5\,\mathrm{eV}$, $\Delta = 4\,\mathrm{eV}$ and $U_{\mathrm{pp}} = 5\,\mathrm{eV}$ (for details see App. A.1).[29] The $S{=}0$ states are underlined, the other states and the ground state carry $S{=}1$. In YVO$_3$, there are two inequivalent V sites for $77\,\mathrm{K} < T < 200\,\mathrm{K}$.

YVO$_3$ 5 K *Pbnm*	YVO$_3$ 65 K *Pbnm*	YVO$_3$ 85 K *Pbnm*	YVO$_3$ 85 K *P2$_1$/b* (V1/V2)	YVO$_3$ 100 K *P2$_1$/b* (V1/V2)	YVO$_3$ 230 K *Pbnm*	YVO$_3$ 295 K *Pbnm*	VOCl 295 K *Pmmn*
0.00	0.00	0.00	0.00/0.00	0.00/0.00	0.00	0.00	0.00
0.21	0.21	0.01	0.04/0.22	0.03/0.21	0.11	0.09	0.31
0.26	0.26	0.21	0.20/0.28	0.19/0.26	0.20	0.18	0.39
$\underline{1.31}$	$\underline{1.31}$	$\underline{1.30}$	$\underline{1.25}/\underline{1.31}$	$\underline{1.26}/\underline{1.31}$	$\underline{1.31}$	$\underline{1.32}$	$\underline{1.30}$
$\underline{1.32}$	$\underline{1.33}$	$\underline{1.32}$	$\underline{1.34}/\underline{1.33}$	$\underline{1.34}/\underline{1.33}$	$\underline{1.32}$	$\underline{1.33}$	$\underline{1.32}$
$\underline{1.55}$	$\underline{1.55}$	$\underline{1.44}$	$\underline{1.36}/\underline{1.56}$	$\underline{1.36}/\underline{1.56}$	$\underline{1.45}$	$\underline{1.44}$	1.29
$\underline{1.58}$	$\underline{1.58}$	$\underline{1.54}$	$\underline{1.47}/\underline{1.60}$	$\underline{1.48}/\underline{1.58}$	$\underline{1.53}$	$\underline{1.51}$	1.50
1.61	1.61	1.56	$\underline{1.53}/1.61$	$\underline{1.52}/1.60$	$\underline{1.55}$	$\underline{1.53}$	-
$\underline{1.63}$	$\underline{1.63}$	$\underline{1.56}$	$\underline{1.56}/\underline{1.65}$	$\underline{1.54}/\underline{1.63}$	1.57	1.57	-
1.69	1.69	1.62	1.58/1.68	1.60/1.67	1.61	1.61	-

energies at 0.21 and 0.26 eV in the low-temperature orthorhombic phase, which are in good agreement with results from recent first principles [171] and LDA+DMFT [172] calculations predicting the intra-t_{2g} excitations in the range of $0.10\text{-}0.20\,\mathrm{eV}$ and $0.06\text{-}0.24\,\mathrm{eV}$, respectively. For all three polarization directions we observe a broad peak around 0.25 eV (Fig. 4.27). This energy is in reasonable agreement with the second lowest value obtained by the cluster calculation. The value is lower than in VOCl because of the smaller distortion of the oxygen octahedron in YVO$_3$. Furthermore the polarization dependence of the 0.25 eV peak affirms the interpretation in terms of an intra-t_{2g} transition. Due to inversion symmetry, the spin-allowed local crystal-field excitations are not directly infrared active in YVO$_3$. They become weakly allowed by the simultaneous excitation of a phonon. Since the phonon polarization is nearly arbitrary, one does not expect strict polarization selection rules [15].[30] In the monoclinic phase above $T_S = 77\,\mathrm{K}$ the cluster calculation predicts two slightly shifted values for the V1 ions at lower and for the V2 ions at higher energies compared with the low-temperature phase. When readopting the orthorhombic structure again above $T_{OO} = 200\,\mathrm{K}$, the predicted transition energies barely reach 0.2 eV. Altogether, within the different structural phases the values for the intra-t_{2g} transitions are always well below 0.3 eV. However, the distinction from multi-phonon

---

[30]Even in VOCl, which does not show inversion symmetry on the V site, the absorption depends only quantitatively on the polarization.
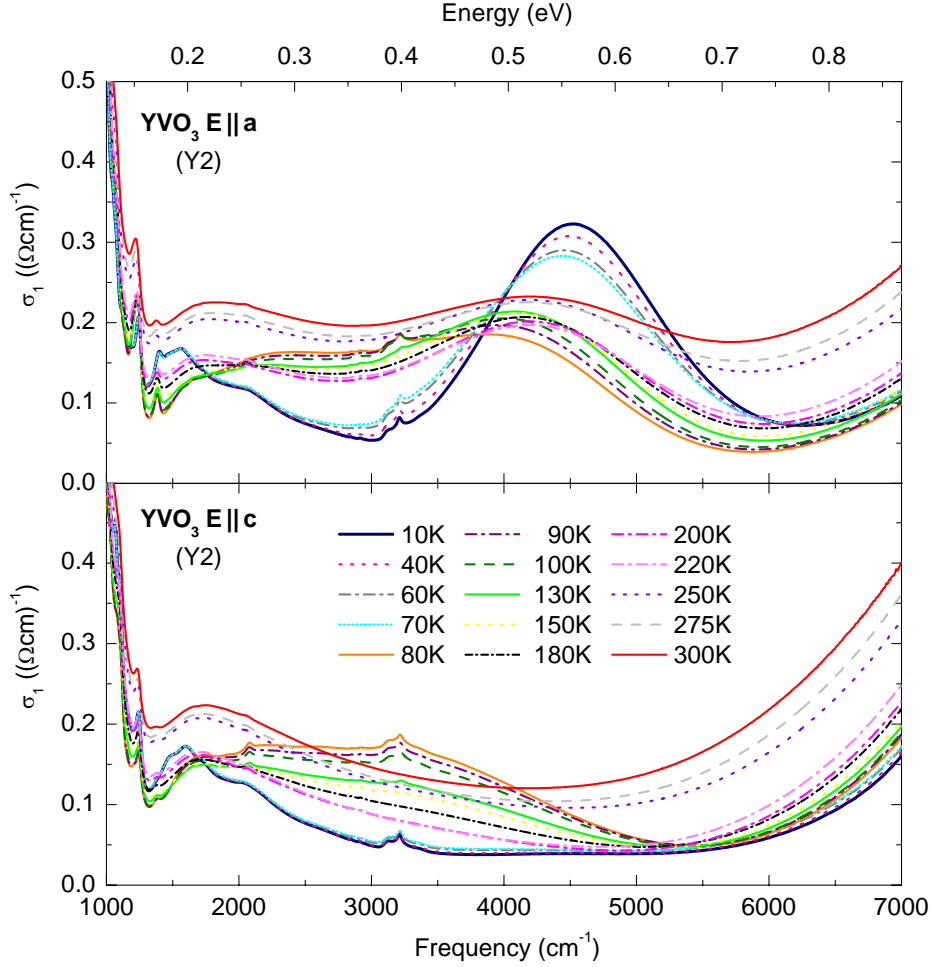
Figure 4.30.: Optical conductivity of sample Y2 of YVO$_3$ for $E \parallel a$ (top panel) and $E \parallel c$ (bottom panel) at several temperatures.[31] A close view on the results derived from different measurements (Y1, Y2, and Y3) reveal that the spectra deviates slightly from each other (compare to Fig. 4.30). More precisely, a different offset is observed at some temperatures (e.g. 4 K), which is maybe due to a small misalignment of the sample and/or the reference position.[32] However, the observed differences are very small and only affect the absolute value of σ_1. The frequency dependence, as well as the line shape of σ_1 is unambiguously reproduced.

absorption is difficult in this frequency region. Therefore no ultimate assignment of the 0.25 eV peak with the intra-t_{2g} transition can be derived from the present data.

---

[31] The small absorption at 0.40 eV observed in the spectra below 130 K is due to the absorption of thin surface layers of ice (see Sec. 3.1.2).

[32] When cooling, the sample holder contracts (for a picture of the sample holder see Fig. 3.2). The vertical contraction (the main effect) is usually corrected by driving the sample holder a little
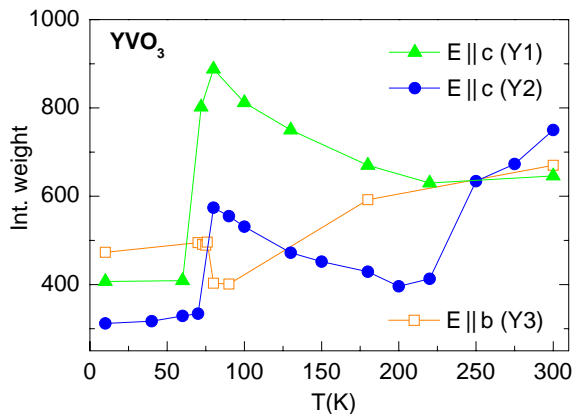
Figure 4.31.:
Temperature dependence of the integrated weight of the low-energy peaks in σ_b and σ_c. The values were obtained by integrating the spectra obtained by several measurements (Y1, Y2, Y3; see Tab. 4.4 and Fig. 4.27 & 4.30) in the range 0.16 - 0.74 eV. The difference in spectral weight for the two data sets from sample Y1 and Y2 are due to a different 'offset' (see Fig. 4.30 and the caption). The overall increase of spectral weight with increasing temperature is due to the arising background.

Collective Orbital Excitations

Our main experimental result is the observation of the two remaining features which cannot be explained within a local crystal-field scenario, namely the peaks at 0.55 eV for $E \parallel a$ and 0.4 eV for $E \parallel c$ (Fig. 4.27 & 4.30). As follows from the discussion above, the energies of both peaks are hard to reconcile with a local crystal-field scenario. The same holds true for the strong polarization and temperature dependence of both peaks, which is entirely unexpected for phonon-assisted crystal-field excitations.

At first we focus on the peak at 0.4 eV for $E \parallel c$. This peak is solely observed in the monoclinic phase, i.e. $77\,\mathrm{K} < T < 200\,\mathrm{K}$. By cooling below $T_{OO} = 200\,\mathrm{K}$ the peak smoothly increases until it reaches its maximal weight right above $T_S = 77\,\mathrm{K}$. At T_S it abruptly drops down. At low temperatures the spectrum is qualitatively comparable with the room-temperature data, except for the more pronounced fine structure. The temperature dependence of the 0.4 eV peak is reflected by the increase of the spectral weight shown in Fig. 4.31. These values are obtained by integrating the spectra shown in Fig. 4.27 & 4.30 in the frequency range from 0.16 eV up to 0.74 eV. The change in spectral weight for the spectrum observed for $E \parallel b$ is also shown for comparison. Here as well temperature-dependent changes are observed, in particular at T_S. However, they are about a factor of five smaller compared with those observed for $E \parallel c$.

Altogether, we suggest that this feature reflects collective orbital excitations, i.e. orbital excitations that are based on the orbital exchange coupling between neighboring V sites, in contrast to the single-site physics of a local crystal-field excitation (see Sec. 2.4.2). Inspired by the discussion of the well-known two-magnon excitations in terms of the exchange of two electrons between adjacent sites [44, 45] (see

---

up or down. However, a horizontal deformation of the sample holder cannot be corrected with our actual setup. If so, the signal of the sample may be underestimated, resulting in a too small value of transmittance, which in turn may cause the observed offset in σ_1.

also Sec. 2.4.3), we address the contribution of a two-orbiton excitation to $\sigma_c(\omega)$. The intermediate phase exhibits G-type orbital ordering, i.e. the d_{xy} orbital is occupied on each V site, whereas the occupation of the d_{xz} and d_{yz} orbitals alternates between neighboring sites, both within the ab plane and along the c axis (Fig. 4.7). In an ideal cubic perovskite structure, the coupling of the d_{xy} orbital to orbitals on adjacent sites vanishes along the c axis. In YVO$_3$ this does not hold strictly due to the rotation and tilt of the octahedra (see Sec. 4.1), but for the discussion of the dominant exchange process along the c axis it is sufficient to consider d_{xz} and d_{yz} orbitals. With t we denote the matrix elements for the hopping of an electron between the d_{xz}^{α} orbital on site V(1) and the d_{xz}^{β} orbital on site V(2), and between the corresponding d_{yz}^{α} and d_{yz}^{β} orbitals, respectively (see Fig. 4.32). In the ground state, e.g. the d_{xz}^{α} and the d_{yz}^{β} orbitals are occupied. The exchange of these two electrons via t leads to the configuration d_{yz}^{α} and d_{xz}^{β} being occupied, i.e. both V sites are in an orbitally excited state. Note that both V sites are still occupied with two electrons each after this charge-neutral excitation. Therefore no Coulomb repulsion U has to be paid for this exchange process. Because the spins are coupled ferromagnetically along the c axis in the intermediate phase (C-type SO, see Fig. 4.7), neither Hund's coupling J_H has to be paid. Neglecting kinetic effects and orbiton-orbiton interactions, one roughly expects a two-orbiton energy of about twice the intra-t_{2g} splitting, in agreement with the experimental result. However, to satisfy the optical selection rules a two-orbiton excitation has to yield a dipole moment in the presence of an applied electric field E (in form of the incident light wave).

In collaboration with G. S. Uhrig[33] we derived an estimate of the dipole moment for the two-orbiton excitation in the monoclinic phase of YVO$_3$ (for details see [173]). For the second electron per site we consider the fermionic Hamiltonian

$$
\begin{aligned}
\mathcal{H}_F &= \mathcal{H}_{F0} + t(c_{\alpha 1}^{\dagger} c_{\beta 0} + c_{\alpha 0}^{\dagger} c_{\beta 1} + \text{h.c.}) &(4.5)\\
\mathcal{H}_{F0} &= \sum_{\tau \in \{\alpha,\beta\}} \Big((\varepsilon_{\tau} + \Delta_{\tau}) c_{\tau 1}^{\dagger} c_{\tau 1} + \varepsilon_{\tau} c_{\tau 0}^{\dagger} c_{\tau 0} \\
&\quad + U' c_{\tau 1}^{\dagger} c_{\tau 1} c_{\tau 0}^{\dagger} c_{\tau 0} \Big) &(4.6)
\end{aligned}
$$

where t denotes the hopping matrix element, $c_{\tau i}^{\dagger}$ ($c_{\tau i}$) creates (annihilates) an electron in orbital $i = 0$ or 1 on site $\tau \in \{\alpha, \beta\}$, $U' = U - 3J_H$ where U is the on-site Coulomb repulsion between two electrons in the same orbital, J_H is the Hund's coupling constant, and the energies ε_{τ} and Δ_{τ} are illustrated in Fig. 4.32.

In analogy to the derivation of Heisenberg exchange, an effective Hamiltonian in terms of orbiton creation operators ($\beta_{\tau}^{\dagger} := c_{\tau 1}^{\dagger} c_{\tau 0}$ for sites $\tau \in \alpha, \beta$) can be derived for the mixture of states (a) and (b) (see Fig. 4.32):

$$
\mathcal{H}_{\text{orb}} = J(\beta_{\alpha}^{\dagger} \beta_{\beta}^{\dagger}) + \text{const.} \tag{4.7}
$$

---

[33]Theoretische Physik I, Technische Universität Dortmund, 44221 Dortmund, Germany
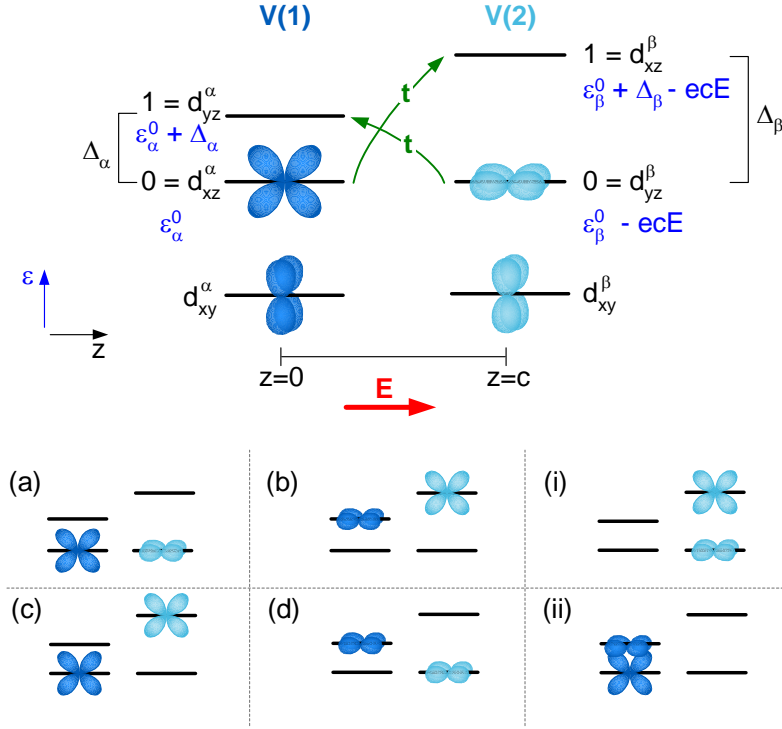
Figure 4.32.: Top: Sketch of the local energy levels and of the virtual hopping processes for the two-orbiton excitation in the monoclinic phase of YVO₃ (G-type orbital and C-type spin ordering). On each vanadium site the first electron occupies the d_{xy}^{α} and the d_{xy}^{β} orbital, respectively. The second electron alternately occupies the d_{xz}^{α} and the d_{yz}^{β} orbitals on neighboring sites V(1) and V(2). The $S=1$ spins on neighboring sites V(1) and V(2) (not shown) are ferromagnetically coupled. Bottom: There are six possibilities for two electrons on sites V(1) and V(2) to occupy the d_{xz} and d_{yz} orbitals: (a) orbital ground state, (b) two-orbiton excited state, (c)&(d) one-orbiton excited state, and (i)&(ii) states in the upper Hubbard band with a doubly occupied V site. Because we solely consider hopping t between orthogonal orbitals, there are just two relevant states (i)&(ii) in the upper Hubbard band. In particular the states (c) and (d) are not realized.

In this effective description no virtual double occupancies appear because we assumed that the on-site Coulomb interaction is the largest energy

$$U' >\mid \varepsilon_\alpha + \Delta_\alpha - \varepsilon_\beta \mid \quad \text{and} \quad U' >\mid \varepsilon_\beta + \Delta_\beta - \varepsilon_\alpha \mid .$$

This assumption is certainly met in YVO₃ where the Coulomb repulsion is $U' = U - 3J_H \approx 2\,\mathrm{eV}$ and all other energies are of the order of fractions on an eV. The result reads [173]

$$J = \frac{2t^2 U'}{(U')^2 - (\delta - ecE)^2} \tag{4.8}$$

where e is the elementary charge, c the distance between the two sites, E denotes the electric field applied along c, and

$$\delta = \varepsilon_\beta^0 - \varepsilon_\alpha^0 + \frac{1}{2}(\Delta_\beta - \Delta_\alpha).$$

The two-orbiton excitation is dipole allowed if $\partial \mathcal{H}_{\mathrm{orb}}/\partial E \neq 0$. We find

$$\partial J/\partial E \approx -\frac{4t^2}{(U')^3}\delta e c. \tag{4.9}$$

In the denominator we neglected δ because the ratio $\Delta_\tau/U' \sim 0.2\,\mathrm{eV}/2\,\mathrm{eV} = 0.1$ is well below 1. Assuming a mirror plane between the two V sites ($\varepsilon_\alpha = \varepsilon_\beta$ and $\Delta_\alpha = \Delta_\beta$), this exchange process does not carry a dipole moment and thus does not contribute to $\sigma_c(\omega)$. However, such a mirror plane is present only below $T_S = 77\,\mathrm{K}$ and above $T_{OO} = 200\,\mathrm{K}$, but it is absent in the monoclinic phase with two distinct V sites. Thus we conclude that the two-orbiton excitation is directly infrared active for $E \parallel c$ in the intermediate phase. The situation is similar to the case of the phonon-assisted two-magnon absorption discussed by Lorenzana and Sawatzky [44, 45] (see Sec. 2.4.3). They demonstrated that two-magnon absorption becomes weakly infrared active, when the inversion symmetry on the metal-oxygen-metal bond is broken by the simultaneous excitation of a phonon. In the present case, it is not necessary to involve a phonon because the mirror plane is already absent due to the lower crystal symmetry in the intermediate phase. Here two different vanadium sites with an unequal energy splitting between the d_{xz} and d_{yz} orbitals (labeled Δ_α and Δ_β) exist. Upon cooling below T_S, the mirror plane is restored and the absorption peak vanishes abruptly. The strong temperature dependence observed between $T_S = 77\,\mathrm{K}$ and $T_{OO} = 200\,\mathrm{K}$ (Fig. 4.31) can be attributed to the loss of coherence of the orbitons when approaching the second-order phase transition to the high-temperature orthorhombic phase. The assumption of the loss of coherence in this temperature range is in accordance with the relative change of the lattice constants of about $2 \cdot 10^{-5}\,\mathrm{K}^{-1}$ obtained by thermal expansion [174].

So far, we conclude that the feature at $0.4\,\mathrm{eV}$ in σ_c observed in the monoclinic phase of YVO_3 gives evidence for collective orbital excitations. In terms of k space, the optical conductivity is restricted to the observation of two-orbiton absorption processes with $k_{\mathrm{total}} = k_1 + k_2 \approx 0$. This means that the two orbitons have opposite momenta $k_1 = -k_2$ with arbitrary k_1. Thus the two-orbiton continuum is probed throughout the entire Brillouin zone. However, at this stage the existence of a orbiton dispersion is hard to prove from our data. In this regard a theoretical prediction of the line shape of the contribution to the optical conductivity would be highly desirable. Additionally an investigation by means of resonant inelastic x-ray scattering (RIXS) could be very instructive, because this comparatively new technique is able to probe additionally the momentum dependence of the orbital excitations (for a review see [34] and references therein).

Now we turn to the feature at $0.55\,\text{eV}$ observed in $\sigma_a(\omega)$. The pronounced anisotropy within the ab plane puts severe constraints on the interpretation in terms of a two-orbiton excitation. Within the ab plane, the V-O-V bonds are rotated by about 45° with respect to the orthorhombic axes with antiferroorbital ordering in the entire temperature range (Fig. 4.34). Therefore an orbital exchange process between nearest-neighbor V sites cannot explain the observed anisotropy between σ_a and σ_b, because a similar contribution to σ_a and σ_b is expected for the electric field being aligned diagonal to the orbital exchange path. We also considered the next-nearest neighbor exchange via *two* oxygen orbitals. Due to the rotation and tilting of the octahedra there are two different distances between two mediative oxygens within one unit cell (see Fig. 4.34). However, for adjacent ab planes at $z = 0$ and $z = 1/2$ in *Pbnm* these short bonds are rotated by 90°. Therefore the next-nearest neighbor exchange also cannot explain the observed anisotropy within the ab plane.

While we observe a pronounced peak around $0.5\,\text{eV}$ in σ_a in the entire temperature
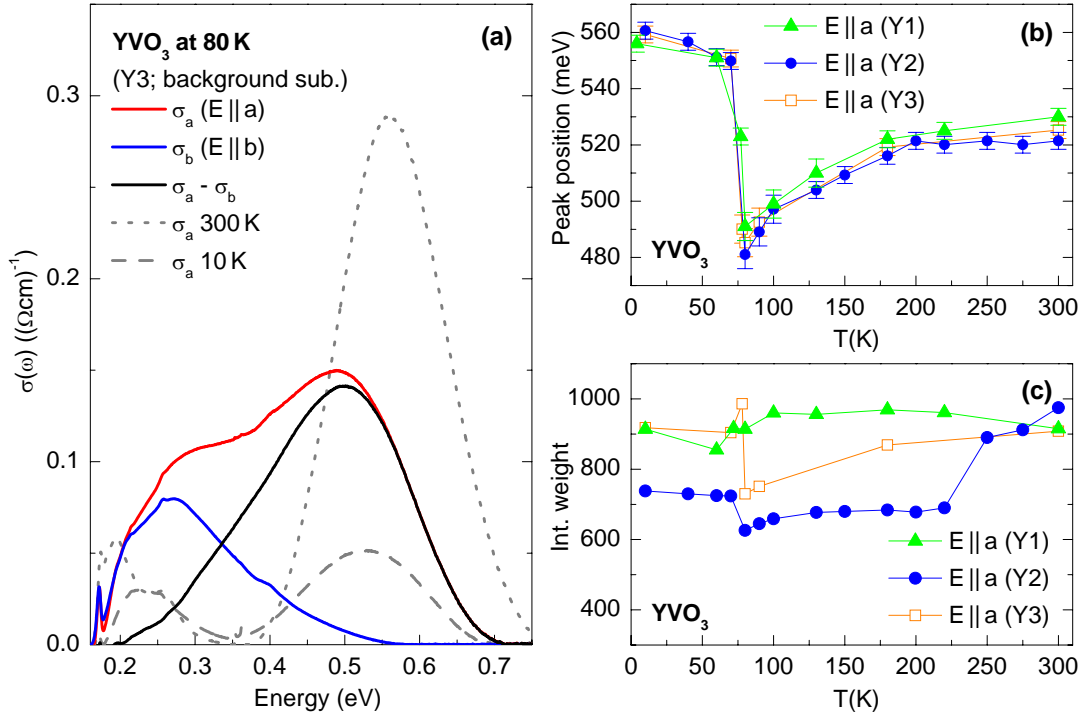
Figure 4.33.: Estimate of the spectral weight of the peak around $0.5\,\text{eV}$ in σ_a. (a) For illustration we subtracted σ_b from σ_a. The background of the shown spectra was subtracted for this purpose. (b) Peak position of the low-energy peak in σ_a as a function of temperature. (c) Integrated weight of σ_a versus temperature, obtained by integrating the spectra in the range 0.16 - $0.74\,\text{eV}$. Both, (b) and (c) were determined for three different data sets (measurement Y1, Y2 and Y3, see Tab. 4.4).
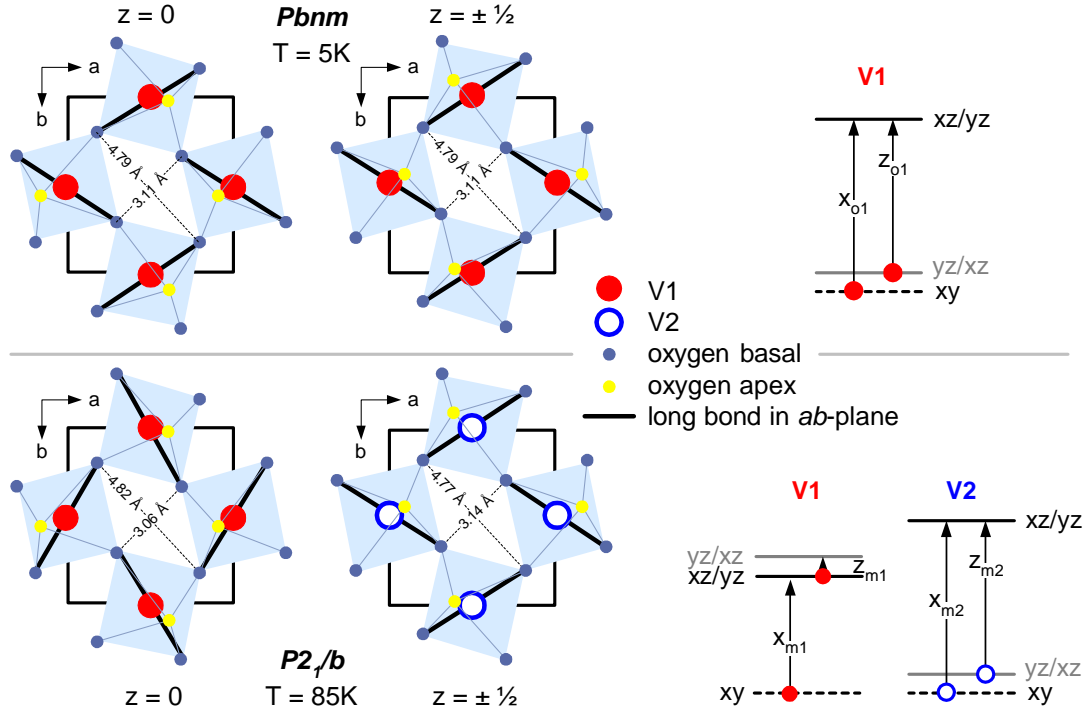
Figure 4.34.: Sketch of adjacent *ab* planes along the *c* axis ($z = 0$ and $z = 1/2$) in the orthorhombic (top panel) and the monoclinic (bottom panel) structure [29]. Due to the rotation and tilting of the octahedra the bond length between two mediative oxygens is clearly different in all phases. On the right hand side the corresponding t_{2g} level diagrams are depicted. The labeled transition energies obtained by our cluster calculation are: $x_{o1} = 0.26$ eV, $z_{o1} = 0.21$ eV, $x_{m1} = 0.20$ eV, $z_{m1} = 0.04$ eV, $x_{m2} = 0.28$ eV, and $z_{m2} = 0.22$ eV. While the energy levels for V(1) in *Pbnm* and V(2) in *P2$_1$/b* are as expected for Jahn-Teller distorted octahedra, the level diagram for the V(1) ion in *P2$_1$/b* is highly unusual. Here the *xz* and *yz* orbital are very close together (z_{m1}).

range, at this energy no relevant contribution to σ_b is observed (see Fig. 4.27). With decreasing temperature the position of the peak in σ_a at first continuously shifts to lower energies, from 0.53 eV at 300 K down to 0.49 eV at 80 K (Fig. 4.33(b)). Due to the increasing overlap with the peak at 0.25 eV in the intermediate phase, below 180 K a broad double peak structure is observed. To resolve the two peaks and make our estimates of the peak position more reliable, we have calculated the difference spectrum σ_a - σ_b, exemplarily shown for the 80 K data in Fig. 4.33(a). Note that we subtracted a background for this purpose.[34] However, it is clearly seen that the peak at about 0.5 eV possesses spectral weight comparable to the peak observed

---

[34]The subtracted baseline has been constructed with the Rubberband correction method in OPUS 3.1 (Bruker Optik GmbH).

in σ_c. When crossing the orbital-ordering temperature at $T_{OO} = 200$ K the peak position starts to shift to lower energies with decreasing temperature (Fig. 4.33(b)). At the first-order phase transition at 77 K the peak abruptly shifts from 0.49 eV to 0.55 eV and, more or less, stays there down to the lowest temperatures. The spectral weight shows within the accuracy no drastic changes. Unfortunately the deviation between different measurements is rather large, as shown for the three different data sets (Y1, Y2, and Y3) in Fig. 4.33(c).[35] However, a noticeable change in spectral weight at the phase transition at $T_S = 77$ K is observed in all three measurements. A change around $T_{OO} = 200$ K is only observed in the measurement on sample Y2.

4.3.2. Absorption spectrum of HoVO$_3$ and CeVO$_3$

Because of the difficulties in interpretation of the 0.5 eV peak in σ_a and to corroborate our suggestion of a two-orbiton excitation for σ_c, we performed further experimental research. At first the corresponding absorption spectrum of HoVO$_3$ with similar structural distortions, and that of the nearly cubic compound CeVO$_3$ have been of particular interest. In addition the influence of an external magnetic field on the absorption spectrum of YVO$_3$ was examined (see the paragraph below).

The obtained absorption coefficient $\alpha(\omega)$ of HoVO$_3$ show qualitatively the same mid-infrared features as YVO$_3$, i.e. a peak at about 0.5 eV for $E \parallel a$ in the whole
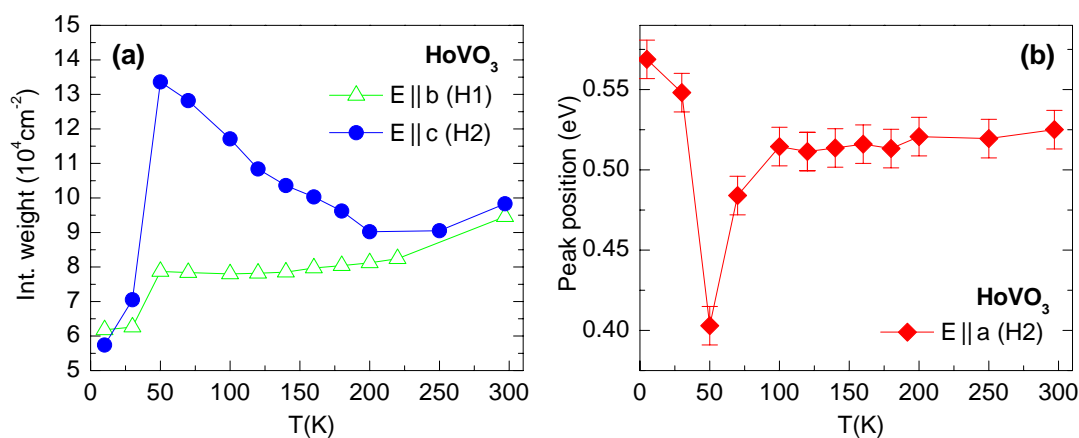
Figure 4.35.: (a) Temperature dependence of the integrated weight of the low-energy peaks observed for $E \parallel b, c$ in the absorption of HoVO$_3$. The values were obtained by integrating the spectra in the range 0.16 - 0.57 eV (without the contribution due to f-f transitions; see Fig. 4.36). (b) Position of the peak around 0.5 eV in $E \parallel a$ in HoVO$_3$ as a function of temperature. For the labels of the measurements on sample H1 and H2 we refer to Tab. 4.4.

---

[35]As mentioned already in the caption of Fig. 4.30 a different offset at low temperatures is observed by a comparison of different measurements. This offset is the main cause for the differences in spectral weight of the three data sets.
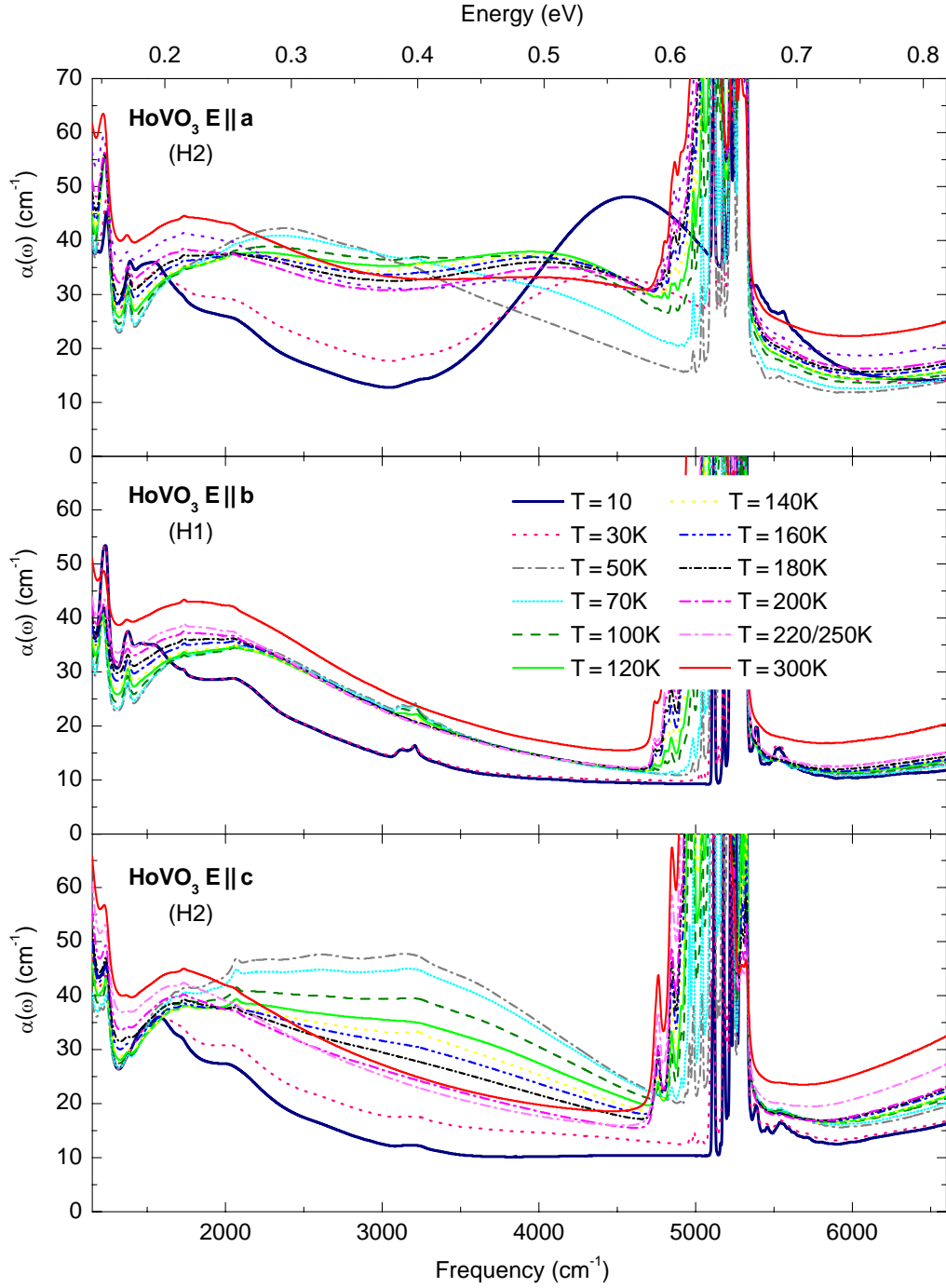
Figure 4.36.: Absorption coefficient $\alpha(\omega) = -\ln(T)/d$ of $HoVO_3$ for $E \parallel a$ (top panel), $E \parallel b$ (middle panel) and $E \parallel c$ (bottom panel) at several temperatures. Except from 220 K for $E \parallel b$ and 250 K for $E \parallel a, c$ the spectra where obtained at the same temperatures in measurement H1 and H2 (see Tab. 4.4).

Table 4.7.:
Energies (in eV) of the lowest crystal-field levels of $3d^2$ V^{3+} in CeVO$_3$ as obtained by the cluster calculation, using $U_{dd} = 4.5$ eV, $\Delta_O = 4$ eV and $U_{pp} = 5$ eV. The $S = 0$ states are underlined, the other states and the ground state carry $S = 1$. In CeVO$_3$, there are two inequivalent V sites for $T < 155$ K (see Sec. 4.1.3). The calculation is based on the structural data reported in [26].

CeVO$_3$ 2 K $P2_1/b$ (V(1)/V(2))	CeVO$_3$ 295 K *Pbnm*
0.00/0.00	0.00
0.05/0.05	0.03
0.17/0.22	0.10
$\underline{1.24}$/1.14	$\underline{1.30}$
$\underline{1.32}$/1.22	$\underline{1.33}$
$\underline{1.35}$/$\underline{1.24}$	$\underline{1.36}$
$\underline{1.51}$/$\underline{1.30}$	$\underline{1.43}$
$\underline{1.53}$/$\underline{1.38}$	$\underline{1.44}$
1.68/$\underline{1.58}$	1.59

temperature range with the same anisotropy compared to $E \parallel b$, and a peak at 0.4 eV for $E \parallel c$ in the intermediate phase (Fig. 4.36).[36] Of course, the phase transition temperatures are different, $T_S \sim 40$ K and $T_{OO} \sim 200$ K [146] (Fig. 4.35). Additionally an absorption band consisting of several sharp lines are observed around 0.64 eV, which are identified with the f-f transitions of the Ho^{3+} ion (for details see App. A.5).

The spectrum for $E \parallel a$ shows an apparent resemblance with σ_a obtained for YVO$_3$. Except for a small shift of the peak position of about 10 meV, the 0.5 eV peaks at 10 K are nearly identical in both compounds. However, in contrast to YVO$_3$, the peak position in HoVO$_3$ does not show any significant shift at T_{OO}, it rather has a constant value already above T_S (Fig. 4.35(b)).

The position of the feature at 0.4 eV in $E \parallel c$ bears also a striking similarity to YVO$_3$. The appearance and temperature dependence of the this peak is intimately connected with the orbital ordering temperatures (Fig. 4.35(a)). This is in accordance with the interpretation of this peak in terms of a two-orbiton absorption. For the same underlying orbital ordering pattern, the required energy to excite two orbitals on adjacent sites should considerably depend on the V(1)-V(2) distance. This distance is expected to be very similar for both compounds and may give an indication for the very similar peak position.[37]

---

[36]As mentioned in Sec. 4.2.1 we performed just transmittance measurements on HoVO$_3$ samples. Therefore we present $\alpha(\omega) = -\ln(T)/d$ (see Eq. 2.8) for an easier comparison with the optical conductivity.

[37]Unfortunately, no structural data of HoVO$_3$ in the intermediate and low-temperature phase are
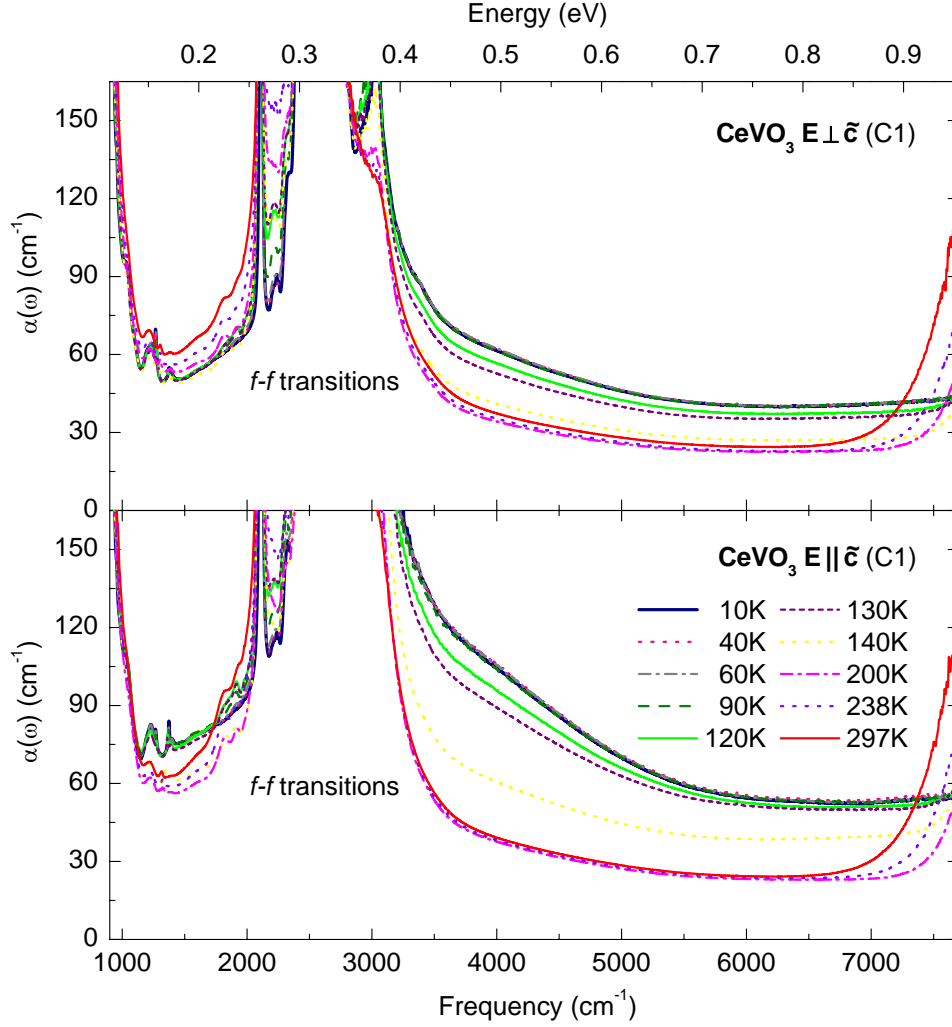
Figure 4.37.: Absorption coefficient $\alpha(\omega) = -\ln(T)/d$ of $CeVO_3$ for the two different polarization directions $E \perp \tilde{c}$ (top panel) and $E \parallel \tilde{c}$ (bottom panel) at several temperatures (for details see text and Sec. 4.2.1). The f-f transition band around $0.3\,eV$ is discussed in App. A.4.

Referring to this point the spectrum of $CeVO_3$ is of particular interest, because the direct V(1)-V(2) distance parallel to the c axis is more distinct, about $3.78\,Å$ for YVO_3 at $85\,K$ and $3.85\,Å$ for $CeVO_3$ at $2\,K$. Additionally the $GdFeO_3$-type distortion is very small in this compound, i.e. the structure is close to the cubic perovskite. Therefore the splitting of the t_{2g} levels is expected to be considerably smaller than in YVO_3 and $HoVO_3$. This is quantified by the crystal field levels obtained by our cluster calculation for $CeVO_3$ (Tab. 4.7) and verified by recent results from

---

available at this time. But at room temperature the direct V-V distance is $3.79\,Å \lesssim 3.81\,Å < 3.89\,Å$ for YVO_3, $HoVO_3$, and $CeVO_3$, respectively.

first principles [171] and LDA+DMFT [172] calculations predicting the intra-t_{2g} excitations in LaVO$_2$ in the range of 0.09 - 0.14 eV and 0.01 - 0.15 eV, respectively.

Unfortunately, as a result of the twinning of the samples (see Sec. 4.2.1), the interpretation of the data for CeVO$_3$ is rather difficult. The absorption coefficient $\alpha(\omega)$ is shown in Fig. 4.37 for $E \perp \tilde{c}$ and $E \parallel \tilde{c}$. It should be noted that the denotation of the directions of polarization is not strict (Sec. 4.2.1). Due to the superposition of the contributions from different twin domains, the polarization direction is rather a preference direction. Accordingly, the polarization dependence is less pronounced. At room temperature it is apparently just a small difference in absolute value. Below the first-order phase transition temperature $T_S \sim 150$ K a broad shoulder on the right hand side of the f-f transition band is observed for $E \parallel \tilde{c}$. It can be excluded that this shoulder is a f-f transition (see App. A.4). Due to the similarity of the peak position and the small but clear polarization dependence we suggest that this feature also can be attributed to a two-orbiton excitation.

4.3.3. Spin-forbidden transitions in YVO$_3$

The sharp features observed around 1.2 eV in YVO$_3$ are assigned to the lowest spin-forbidden excitations from the ground state with $S = 1$ to the lowest five-fold degenerate $S = 0$ state ($^3T_1 \rightarrow (^1T_2, ^1E)$ in a cubic crystal field). An extended view is shown in Fig. 4.38 for different polarization directions and several temperatures. Our cluster calculation predicts values of 1.31 eV and 1.32 eV for the first two transitions into the $S = 0$ multiplet at $T = 5$ K (Tab. 4.6), in good agreement to [167] where an energy of 1.36 eV for the lowest spin-forbidden state $^1T_2$ is obtained.[38] However, in Sec. 4.3 we have already noticed for VOCl that these values of the cluster calculation are very sensitive to the chosen values for the Slater integrals. Because the features observed in VOCl cover the identical energy range compared to those in YVO$_3$ (Fig. 4.29), we argue that these values of the cluster calculation are slightly too high. In Fig. 4.39 the data of YVO$_3$ are shown again, but with a subtracted background due to the electronic transitions. Five distinct peaks in the range 1.1 - 1.4 eV, labeled A - D in Fig. 4.39 are observed at 10 K. Probably the spin-forbidden transitions become weakly allowed due to spin-orbit coupling in combination with a simultaneous excitation of an odd vibration destroying the inversion symmetry (see Sec. 2.4.2). However, also the simultaneous excitation of magnon sidebands, assuring $\Delta S = 0$, have to be considered. In particular the sharpness of the peaks militates for the latter. Additionally this interpretation is supported by the temperature dependence of the features, more precisely by the emergence and/or the change in position with decreasing temperature. Above the spin-ordering temperature $T_N = 116$ K, magnons are not well defined and only broad features are observed. Sharp magnon sidebands arise upon cooling below T_N. With a further decrease of

---

[38]In [167] the levels are specified as a function of the M-O distance. The value 1.36 eV is stated for a M-O distance of 2 Å.
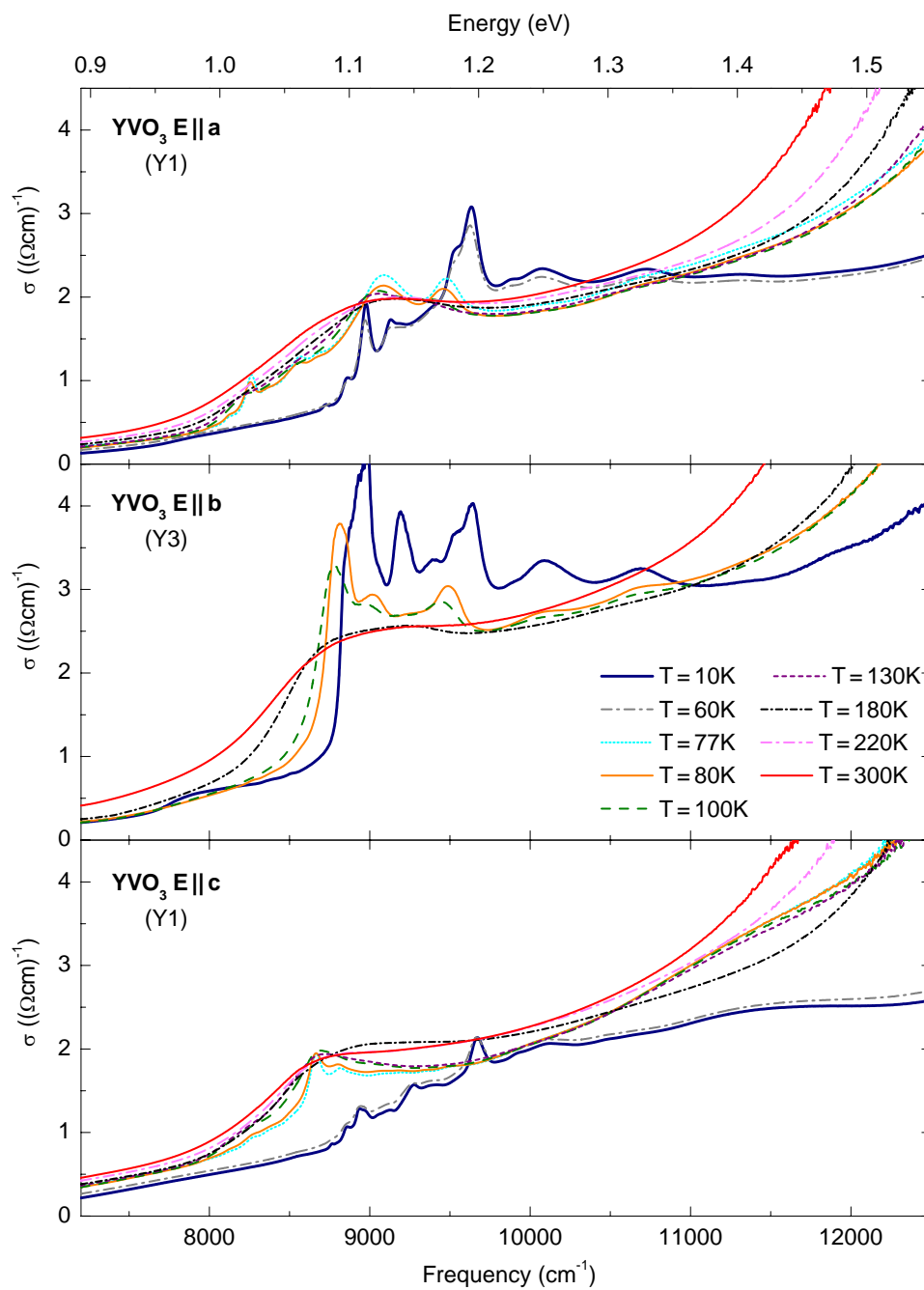
Figure 4.38.: Real part of the optical conductivity $\sigma_1(\omega)$ of YVO$_3$ for $E \parallel a$ (top panel), $E \parallel b$ (middle panel), and $E \parallel c$ (bottom panel) at several temperatures in the energy range of the spin-forbidden crystal-field excitations.
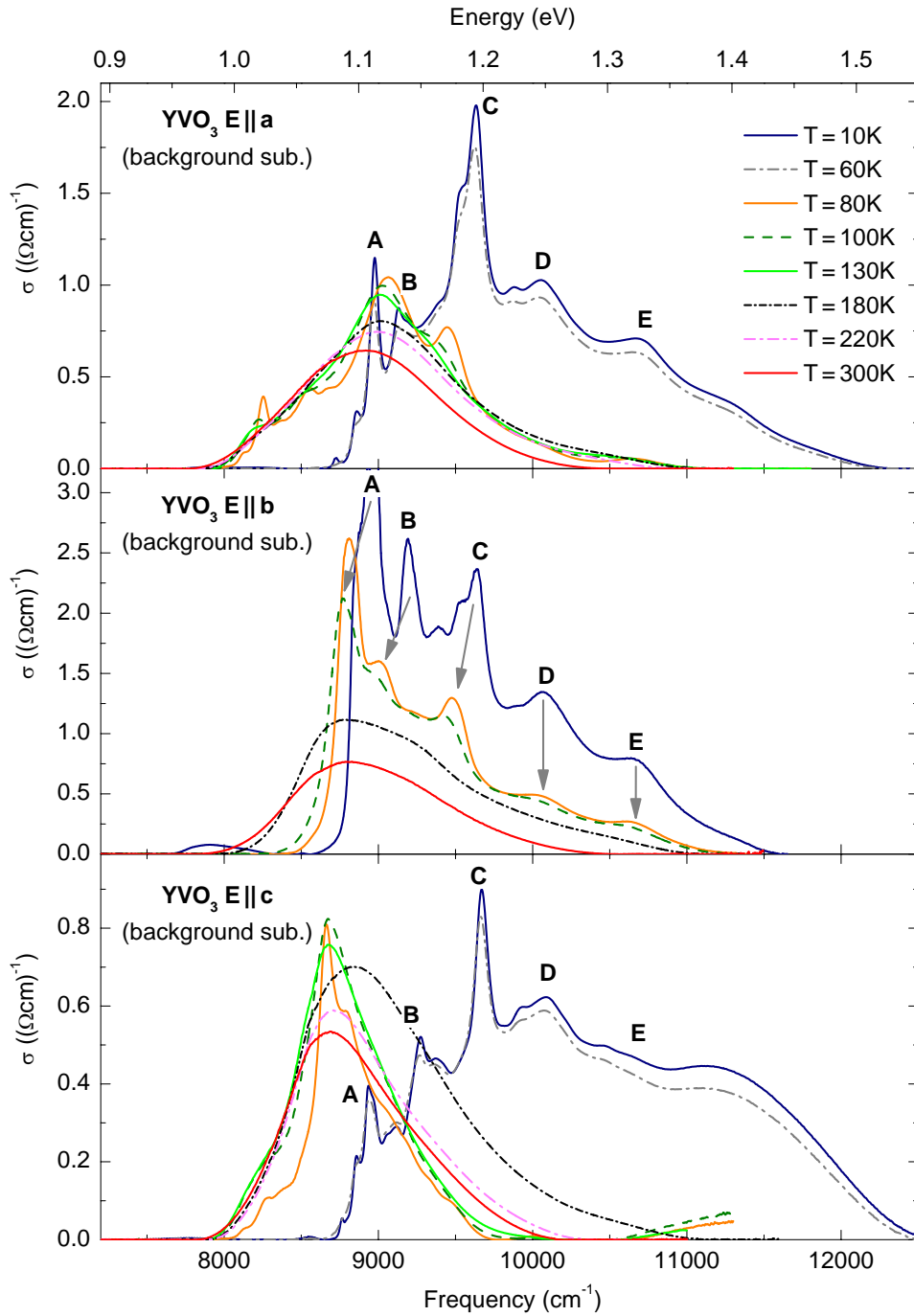
Figure 4.39.: Optical conductivity of YVO₃ for $E \parallel a$ (top panel), $E \parallel b$ (middle panel), and $E \parallel c$ (bottom panel) at several temperatures. A background due to the electronic transitions was subtracted from the original data. The peaks labeled A‑E are assigned to spin-forbidden transitions to the lowest $S = 0$ multiplet (for details see text).

temperature the total spectral weight increases and the center of the peaks shifts to higher frequencies. The change of the spin-ordering pattern at $T_S = 77\,\mathrm{K}$ gives rise to a drastic change of the magnon energy at the Brillouin zone boundary from about $20\,\mathrm{meV}$ for $T > 77\,\mathrm{K}$ to about $35\,\mathrm{meV}$ for $T < 77\,\mathrm{K}$ [28]. The optical spectrum also shows a drastic change at $T_S = 77\,\mathrm{K}$. While the peaks A, B, and C are collectively shifted to lower energies in the monoclinic phase, peak D and E show no detectable change in position. The oscillator strength of the spin-forbidden excitations is clearly enhanced in YVO_3 compared with those in VOCl (Fig. 4.29). Presumably, this is due to the overlap with the onset of excitations across the Mott-Hubbard gap. Mixing the two kinds of excitations will transfer some weight to the orbital bands, resulting in an effect which is called intensity stealing [78] (see also Sec. 2.4.2).

Altogether an exact understanding of the optical spectrum of the spin-forbidden excitations in YVO_3 is missing up to now. In particular, some additional, smaller peaks/shoulders are observed at low temperatures which remain unexplained.

4.3.4. Absorption of YVO₃ in a Magnetic Field

The results of our measurements on YVO_3 in an external magnetic field revealed no field-dependent changes, neither on the low-energy peaks nor on the spin-flip transitions up to $17\,\mathrm{T}$ (Fig. 4.40). This finding is in accordance with the results from magnetostriction, where no spin flip and no changes are observed in high magnetic fields up to $35\,\mathrm{T}$ [146, 174].

4.3.5. Estimate of 10*Dq* in Dy(Sc,V)O₃

Optical absorption studies on reduced vanadium centers in $Ca_2NaMg_2V_3O_{19}$ have specified a value of $10Dq \sim 1.95\,\mathrm{eV}$ for octahedrally coordinated V^{3+} [166]. Recent first-principles electronic structure calculations for octahedrally oxo-coordinated $3d^2$ systems yield an effective ligand-field splitting of $1.82\,\mathrm{eV}$ [167]. This corresponds to the energy of the $^3T_2(t_{2g}^1 e_g^1)$ state and can be identified with $10Dq$ [167]. However, the exact value strongly depends on the M-O distance, whereas for a middle M-O distance a value of $1.24\,\mathrm{eV}$ is stated. The values for $10Dq$ from the literature are in pretty good agreement with our data of the optical absorption of single V^{3+} ions embedded on island positions in $DySc_{0.9}V_{0.1}O_3$.[39] The corresponding data of $DyScO_3$ and $DySc_{0.9}V_{0.1}O_3$ are shown in Fig. 4.41. The spectra are dominated by dipole-forbidden f-f transitions of the Dy^{3+} ion. We observe up to nine line groups, each consisting of several sharp lines which are assigned to transitions between the Dy^{3+}: $^{2D+1}L_J$ levels by a comparison with the absorption spectrum of $DyCl_3$ [175]

---

[39]The chosen amount of $10\,\%$ vanadium in $DyScO_3$ is below the percolation limit. Estimates for the critical percolation probability p_c for basic 3D lattices obtained by Monte Carlo techniques [153] and by series expansions [154] vary from 0.19 for the close-packed fcc and hcp structures to 0.43 for the open diamond structure.
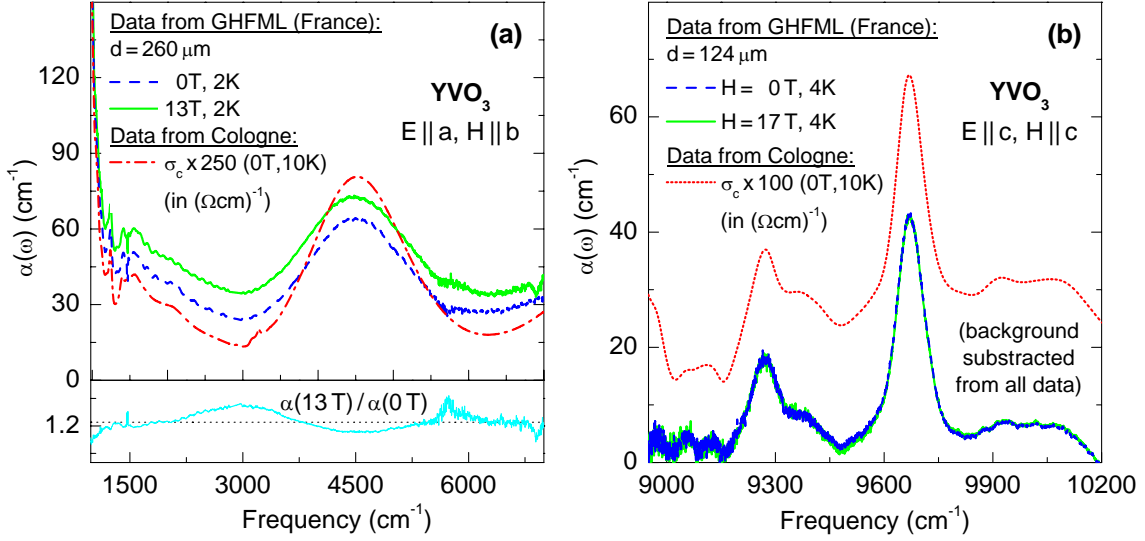
Figure 4.40.: Absorption coefficient $\alpha(\omega)$ of YVO_3 in an external magnetic field. (a) For an applied magnetic field up to $13\,T$ no significant changes of the $0.5\,eV$ peak are observed for $E \parallel a$ and $H \parallel b$. To clarify this, the ratio of α at $13\,T$ and $0\,T$ is shown in the lower part of the left panel. The observed deviation is ascribed to the field dependence of the bolometer, insufficiently included in the reference measurement. (b) As well for the spin-flip transitions no changes are observed in a magnetic field up to $17\,T$ for $E \parallel c$ and $H \parallel c$.

(for details see App. A.3). In particular, in the range of 1.7-$2.5\,eV$ *f-f* transitions are neither expected nor observed in $DyScO_3$ [176] (top panel in Fig. 4.41). In contrast the absorption spectrum of $DySc_{0.9}V_{0.1}O_3$ exhibits a broad peak at $1.92\,eV$ (bottom panel in Fig. 4.41). This peak thus can be attributed to the V^{3+} ions, more precisely to the $^3T_1 \rightarrow {}^3T_2$ ($t_{2g}^2 \rightarrow t_{2g}^1 e_g^1$) transition (inset in Fig. 4.41). In other words, we find $10Dq \approx 1.9\,eV$ for V^{3+} in $DySc_{0.9}V_{0.1}O_3$. Because the M-O bond distances in the V-doped scandate are very similar to those of YVO_3 (close to $2\,\text{Å}$, see Fig. 4.8), we conclude that the given value is also valid for the latter. Unfortunately, the observation of the lower lying V^{3+} intra-t_{2g} transitions is impossible because of the superposition with the predominant *f-f* transitions.

4.3.6. Summary

To conclude, orthovanadates RVO_3 with $R = Y$, Ho, and Ce have been investigated by means of optical spectroscopy. We determined the optical conductivity as a function of polarization and temperature in the mid-infrared frequency region. Based on a comparison with two other d^2 systems, VOCl and Dy(Sc,V)O_3, in combination with the results of our cluster calculation we found that absorption features at about 0.2 and $1.1\,eV$ in principle can be explained in terms of local crystal-field
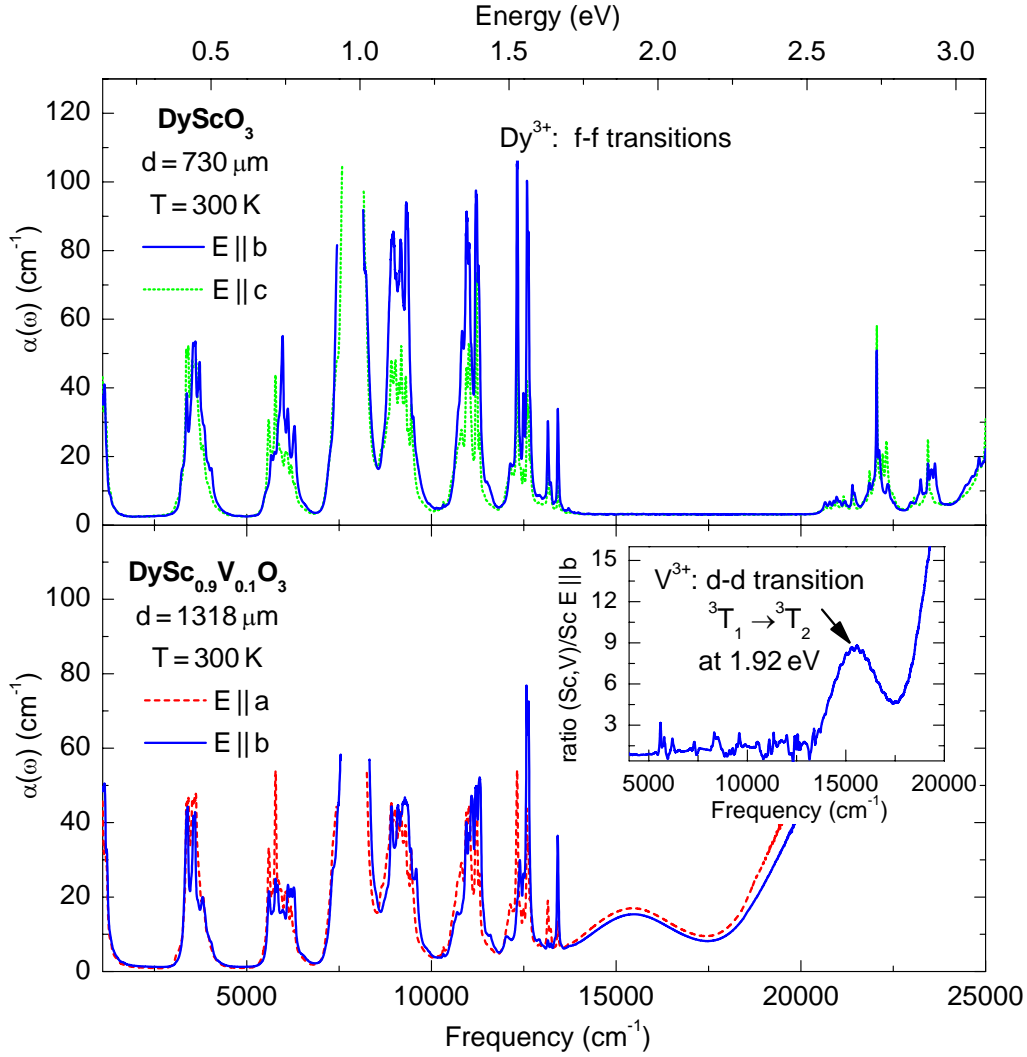
Figure 4.41.: Comparison of the absorption coefficient $\alpha(\omega) = -\ln{(T)}/d$ of $DyScO_3$ (top panel) and $DySc_{0.9}V_{0.1}O_3$ (bottom panel) at room temperature. In the wide energy range considered (0.1 eV - 3.1 eV), the spectrum of $Dy(Sc,V)O_3$ is dominated by absorptions due to dipole-forbidden f-f transition of the Dy^{3+} ion (see App. A.3). However, the broad peak at 1.92 eV in $DySc_{0.9}V_{0.1}O_3$ is attributed to the $^3T_1 \rightarrow ^3T_2$ ($t_{2g}^2 \rightarrow t_{2g}^1 e_g^1$) transition of the V^{3+} ions (see text). The inset shows the ratio of the spectrum of $DySc_{0.9}V_{0.1}O_3$ compared to that of $DyScO_3$ for $E \parallel b$. Both, the f-f and the d-d transitions in $Dy(Sc,V)O_3$ depend only quantitatively on the polarization.

excitations of the V^{3+} ions. However, the polarization and temperature dependence of two absorption bands at 0.4 eV and 0.55 eV are hard to reconcile with a local crystal-field scenario. Therefore we have tried an interpretation in terms of collec-
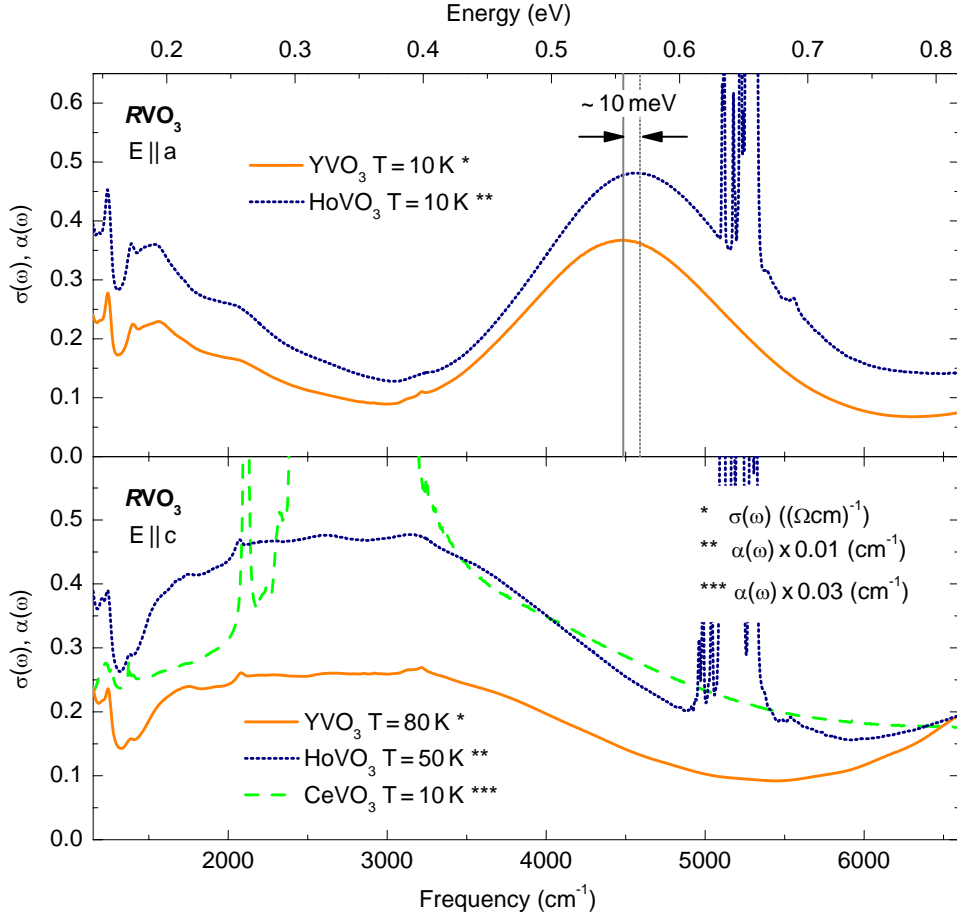
Figure 4.42.: Comparison of the low energy peaks observed in RVO$_3$. Top panel: optical conductivity $\sigma(\omega)$ and absorption coefficient $\alpha(\omega)$ for $E \parallel a$ of YVO$_3$ and HoVO$_3$ at 10 K. Bottom panel: $\sigma(\omega)$ and $\alpha(\omega)$ for $E \parallel c$ of YVO$_3$ at 80 K, HoVO$_3$ at 50 K, and CeVO$_3$ at 10 K.

tive orbital excitations, which has been proposed by theory [16, 17]. In fact, we suggest that the feature at 0.4 eV, observed in the G-type orbitally ordered phase of all three compounds (bottom panel in Fig. 4.42), has to be interpreted in terms of a collective intersite exchange of orbitals along the c direction. We have discussed the microscopic exchange process and conclude that this feature reflects a direct two-orbiton excitation. The feature observed at about 0.55 eV for $E \parallel a$ in YVO$_3$ and HoVO$_3$ (top panel in Fig. 4.42) is not completely understood up to now. In particular the pronounced anisotropy within the ab plane puts severe constraints on the interpretation in terms of a two-orbiton excitation. In this regard theoretical efforts would be desirable. Altogether our results strongly suggest that in RVO$_3$ the orbital exchange interaction play a decisive role.

5. Magnetic Excitations in Quasi-1D Quantum Spin Systems

5.1. Low-Dimensional Quantum Spin Systems

Low-dimensional quantum spin systems have attracted renewed interest due to the discovery of high-T_c superconductivity in cuprates in 1986 [35], because a close relationship between magnetism and high-T_c superconductivity has been suggested [36]. A common characteristic of these cuprates is the presence of CuO_2 planes stacked on top of each other. It is widely believed that the relevant low-energy physics are described by the degrees of freedom of these planes. In the undoped case, each CuO_2 plane corresponds to an antiferromagnetic 2D square lattice with nearest-neighbor coupling of the Cu^{2+} $S = 1/2$ spins. Adjacent planes are magnetically nearly decoupled, i.e. $J_{in-plane} \gg J_{out-of-plane}$. Strong quantum fluctuations are responsible for the absence of long-range magnetic order in low dimensions. The 2D $S = 1/2$ square lattice shows long-range magnetic order only at $T = 0$ [177–179]. A finite 3D coupling
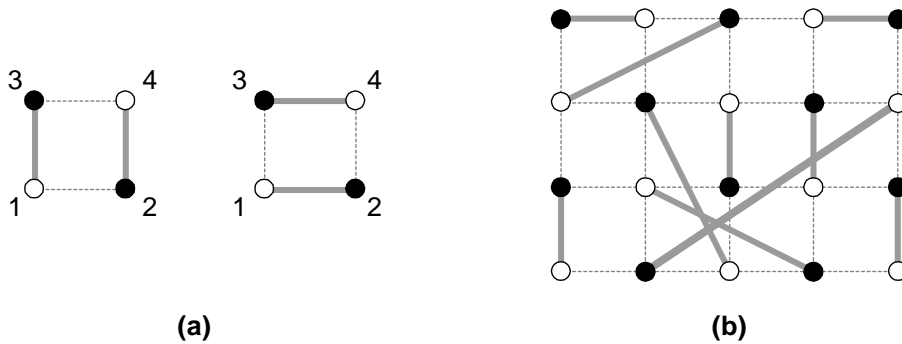
Figure 5.1.: (a) The singlet basis of four spins on a plaquette can be chosen to consist of two states represented by non-crossing bonds (grey bars). The quantum mechanical system 'resonates' between two different configurations of the singlet bonds, which are energetically equivalent. (b) Sketch of a possible contribution to a RVB ground state on a 2D square lattice. Grey bars again represent the valence bonds. The full ground state is a superposition of all 'resonating' bond configurations. Reproduced from Ref. [67].
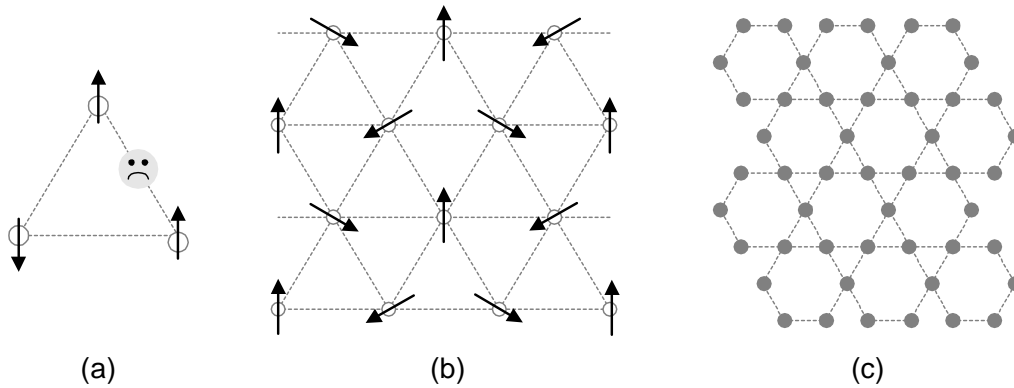
Figure 5.2.: (a) Unfavorable situation for antiferromagnetic coupling between three spins with triangular bond arrangement. For two antiparallel neighboring spins, the third one is 'frustrated' in satisfying both bonds. (b) Despite of high frustration, the triangular lattice is expected to possess a long-range ordered ground state because of the comparatively large coordination number of $N = 6$ [182, 183]. (c) In contrast, the *kagome* lattice with $N = 4$ is discussed as an example of a spin liquid with a RVB ground state [184–186].

is necessary for ordering at $T > 0$. A 1D $S = 1/2$ chain does not even order at $T = 0$ [179]. Instead of a long-range ordered Néel state these systems have a spin-liquid ground state with short-range spin correlations. These spin-liquid ground states are often described by the so-called resonance valence bond (RVB) state introduced by Anderson [36]. This model assumes the ground state to consist of 'resonating' singlet pairs (Fig. 5.1(a)). The actual state of a system is a weighted linear superposition of such valence-bond singlets [180] (Fig. 5.1(b)). As a rule of thumb [181], a RVB ground state is more probable, i.e. the spin fluctuations become more important, upon (i) lowering the lattice dimensions d, (ii) decreasing the number of nearest-neighbor spins N, (iii) reducing the involved spin values, (iv) increasing the spin dimension n, and (v) enhancing frustration (Fig. 5.2). According to this rule of thumb, quantum fluctuations are particularly pronounced for the $S = 1/2$ Heisenberg chain ($S = 1/2$, $N = 2$, $d = 1$, and $n = 3$). Here, frustration becomes relevant when e.g. taking the next-nearest neighbor interactions into account. In 2D, a triangular arrangement of spin gives rise to a no-win situation due to frustration, e.g. in a *kagome* lattice (Fig. 5.2).

The absence of long-range order in spin liquids gives rise to new magnetic excitations, quite different from the spin waves or magnons of a long-range ordered state. The excitations of the $S = 1/2$ Heisenberg chain and the n-leg $S = 1/2$ ladder are briefly introduced in the following paragraphs. A more detailed introduction can be found in [43, 187].

Spin Chains

The Hamiltonian of the Heisenberg spin chain can be written as

$$\mathcal{H} = \sum_i J\mathbf{S}_i\mathbf{S}_{i+1}, \tag{5.1}$$

with an isotropic exchange coupling J between nearest-neighbor spins S_i and S_{i+1}. Various theoretical and experimental studies have shown that the excitations of the spin 1/2 chain are well described in terms of spinons with $S = 1/2$, in contrast to e.g. $S = \pm 1$ for magnons [38, 46, 188, 189] (Fig. 5.3). Because the smallest change of the z component of the total spin is ± 1, i.e. flip one spin from -1/2 to +1/2 or vice versa, spinons always are excited in pairs. In a semiclassical picture a spinon can be visualized as a domain wall between two antiferromagnetic domains [181]. For a Néel-type ground state this is pictured in Fig. 5.3(a).[1] The lowest excitation, i.e. flipping one spin, results in the creation of two domain walls, that is two spinons.[2] For the creation of such a pair of spinons with momentum k_1 and k_2 only the total momentum k is defined, i.e. only $k = k_1 + k_2$ is fixed. Therefore the excitation spectrum $E(k)$ shows a two-spinon *continuum* (Fig. 5.3(b)), in contrast to the well-defined dispersion branch of magnons. The upper (index u) and lower (index l) boundary of the two-spinon continuum are given by the relations

$$\frac{\hbar\omega_u(k)}{J} = \pi|\sin\left(\frac{k}{2}\right)| \qquad \text{and} \qquad \frac{\hbar\omega_l(k)}{J} = \frac{\pi}{2}|\sin\left(k\right)|, \tag{5.2}$$

respectively [37, 38, 188, 191]. The excitation spectrum is gapless with $\hbar\omega = 0$ at $k = 0, \pi$.
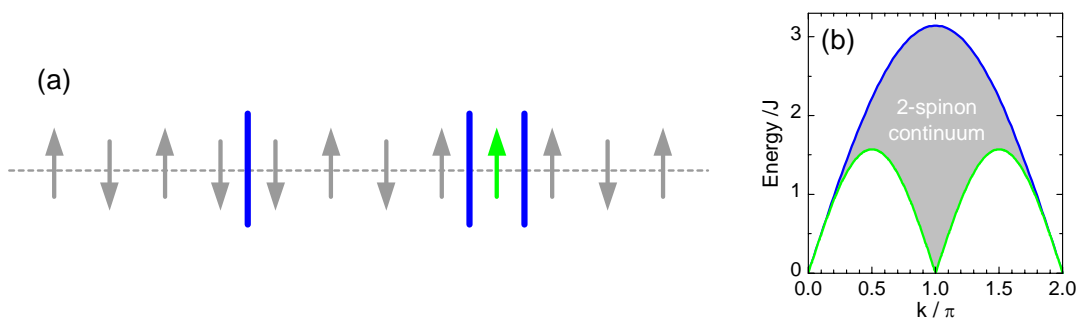
Figure 5.3.: (a) Illustration of a spinon as a domain wall (blue bars) between two antiferromagnetic aligned domains. By flipping one spin (highlighted in green) always *two* spinons will be created and annihilated, respectively. (b) The corresponding excitation spectrum shows a gapless two-spinon continuum.

n-leg Spin Ladders

The 1D spin chain shows a spin-liquid ground state, whereas in 2D systems long-range order is present at $T = 0$ [179]. In particular for the $S = 1/2$ antiferromagnetic Heisenberg model on a 2D square lattice an ordered ground state is predicted at zero temperature [177, 178]. The so-called n-leg spin-1/2 ladders, i.e. systems of n coupled spin-1/2 chains have caused a lot of interest because they realize a crossover between one and two dimensions [39]. The simplest realization is the two-leg ladder, consisting of two spin-1/2 chains with intra-chain exchange coupling $J_\parallel$, coupled by an additional Heisenberg interaction $J_\perp$ (Fig. 5.4(a)). The Hamiltonian then reads

$$\mathcal{H} = \sum_i J_\parallel (\mathbf{S}_{1,i}\mathbf{S}_{1,i+1} + \mathbf{S}_{2,i}\mathbf{S}_{2,i+1}) + J_\perp \mathbf{S}_{1,i}\mathbf{S}_{2,i}, \qquad (5.3)$$

where the first index of each spin operator denotes the leg number, i.e. 1 and 2, and the second one, i, counts the rungs. The immediate effect of the rung coupling $J_\perp$ is to confine pairs of fractional $S = 1/2$ spinons to integer $S = 1$ triplets [192]. In the limit $J_\perp \gg J_\parallel$, the dominant configuration in the ground state is the product state

---

[1] This picture also works for a RVB ground state.

[2] It should be noted that a spinon is not just a domain wall, rather it polarizes the environment leading to a kind of polarization cloud [190].
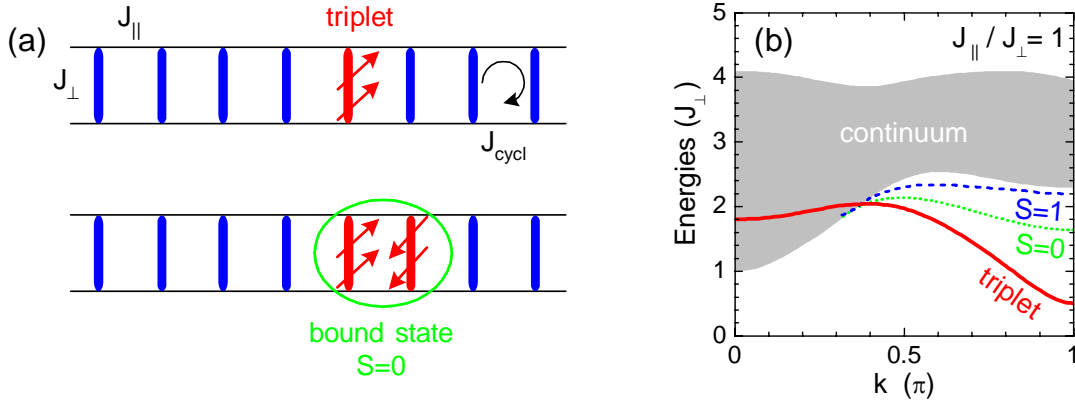
Figure 5.4.: (a) Illustration of a triplet and the $S = 0$ bound state of two triplets in the case of strong rung coupling. The ground state is built by rung singlets. The lowest excitation is a triplet. The antiferromagnetic interaction between two triplets with antiparallel spin on neighboring rungs leads to a positive binding energy, i.e. to a $S = 0$ bound state. (b) One and two triplet excitation spectrum for $J_\parallel = J_\perp$ (reproduced from [192]). The red solid line shows the one-triplet dispersion with a spin gap at $k = \pi$. The corresponding two-triplet excitation spectrum exhibits a two-triplet continuum and a two-triplet bound state with $S = 0$ (green doted line) and $S = 1$ (blue dashed line) at large k values. Not shown is the $S = 2$ anti-bound state, which is predicted to exist outside the continuum in the limit of strong rung coupling ($J_\parallel \ll J_\perp$) [193].

with the spins on each rung forming a spin singlet $|\Psi\rangle_S = (|\uparrow\downarrow\rangle - |\downarrow\uparrow\rangle)/\sqrt{2}$ (blue bars in Fig. 5.4).[3] The ground state has total spin $S = 0$ because each rung is in a spin-singlet state. For an excitation a rung singlet must be promoted to a $S = 1$ triplet $|\Psi\rangle_T = \{|\uparrow\uparrow\rangle, |\downarrow\downarrow\rangle, (|\uparrow\downarrow\rangle + |\downarrow\uparrow\rangle)/\sqrt{2}\}$ (red bars in Fig. 5.4). For $J_\parallel > 0$ the triplet starts to hop from rung to rung. The one-triplet dispersion exhibits a spin gap at $k = \pi$ [42, 192] (Fig. 5.4). It should be noted that the excitation of the ladder with $J_\perp \sim J_\parallel$ can also be described coming from the limit $J_\perp \ll J_\parallel$ because a finite spin gap is present for any $J_\perp > 0$ [192]. The one and two triplet excitation spectrum for $J_\perp/J_\parallel = 1$ is shown in Fig. 5.4(b), depicting the gapped one-triplet dispersion, the two-triplet continuum, and the bound states with $S = 0, 1$. For $J_\perp/J_\parallel = 1$ the $S = 0$ and the $S = 1$ bound state appear only for $k \neq 0$. Recent investigations by inelastic neutron scattering and infrared absorption on the undoped, nearly ideal spin-ladder compound $(La,Sr)_{14}Cu_{24}O_{41}$ are in very good agreement with the theoretical predictions [42, 106].[4] From the results from optical spectroscopy two peaks in the optical conductivity are identified with the 1D van Hove singularities in the density of states of the $S = 0$ two-triplet bound state [106, 115]. The two-triplet continuum is observed around 0.5 eV. From the energy position of the two peaks in $\sigma(\omega)$ the magnetic parameter $J_\parallel$ and $J_\perp$ were determined in comparison with calculations with the density-matrix renormalization group (DMRG) [109]. The latter have shown that the cyclic exchange of four spins on a plaquette plays an important role in 2-leg ladders [109], confirmed by recent results from neutron scattering [42].

It has been predicted by numerical calculations that the crossover from one to two dimensions is not smooth [39]. While ladders with an even number of legs are gapped spin liquids, ladders with an odd number of legs exhibit no energy gap to the lowest magnetic excitations [40, 41]. These theoretical predictions have reinforced a lot of experimental interest on n-leg ladders. Unfortunately just a few realizations of such ladders are known up to now. Additionally experimental progress is hindered by the difficulties of the growth of large single crystal in some cases.

---

[3]Here $\uparrow$ and $\downarrow$ denote the spin-up and spin-down eigenvectors of the spin operator in the z direction.

[4]The $S = 1$ and $S = 2$ (anti-)bound state are optically inactive because $\Delta S = 0$ must be conserved (see Chap. 2.4). However, the $S = 1$ bound state can be probed by neutron scattering.

5.2. Spin-1/2 Chains in (Sr,Ca)CuO$_2$

5.2.1. Introduction

During the last 10 years the compound (Sr,Ca)CuO$_2$ has been the subject of many studies. In the following paragraphs the most relevant results with regard to this thesis are summarized.

Structure

The compound SrCuO$_2$ crystallizes in an orthorhombic crystal structure with space group *Cmcm* (No. 63) [194, 195]. The lattice constants are summarized in Tab. 5.1. The Cu^{2+} ions are quadratically planar coordinated by four oxygen ions each, building CuO$_4$ units. These CuO$_4$ plaquettes are slightly distorted, with two equal (2×1.9588 Å) and two different (1.9063 and 1.9325 Å) Cu-O bond lengths on opposite sides, respectively (Fig. 5.5). The plaquettes are arranged in double chains (zig-zag chains) running along the *c* axis (Fig. 5.5). The double chains are stacked on top of each other along *a*, separated by the Sr^{2+} ions.
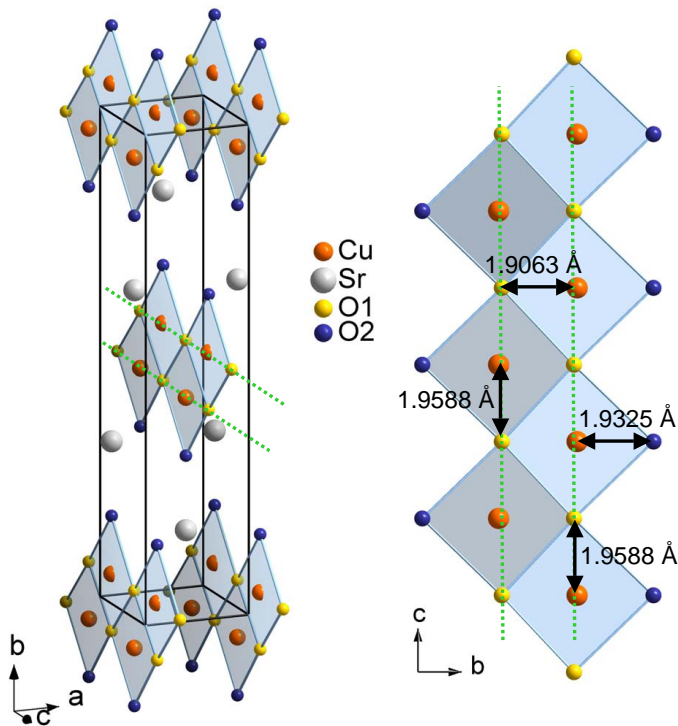
Figure 5.5.:
Crystal structure of SrCuO$_2$ with space group *Cmcm*. The CuO$_4$ plaquettes are arranged in double chains running along the *c* direction (green dotted lines).

Electronic Structure

The Cu^{2+} ions in SrCuO$_2$ have the electronic configuration [Ar] $3d^9$. The local crystal field of the four oxygen ions on a plaquette yields a crystal-field splitting of the five

Table 5.1.: Lattice constants of SrCuO$_2$ from powder neutron diffraction at room temperature [195].

Space group	$a(\text{Å})$	$b(\text{Å})$	$c(\text{Å})$
$Cmcm$	3.5766(1)	16.3354(4)	3.9143(1)

Cu-3d orbitals (Fig. 5.6). The single hole occupies the $d_{y^2-z^2}$ orbital in the ground state, experimentally affirmed by x-ray absorption spectroscopy studies [196].

The electronic structure of SrCuO$_2$ has been investigated by optical studies combined with model calculations by Popovic *et al.* [197]. Here an energy gap of 1.77 eV for $E \parallel a$ is stated, which is determined from the maximum of the first peak in the pseudo-dielectric function ε_2 at 300 K. For $E \parallel c$ the energy gap is obtained from the maximum of the lowest peak at 1.42 eV in $\sigma(\omega)$ obtained by Kramers-Kronig analysis of the *unpolarized* reflectance at 300 K [197]. In comparison with a tight-binding calculation for correlated electrons the gaps were assigned to an indirect and a direct correlation gap [197]. In particular the indirect gap is associated with the lowest-energy transition between the $3d_{y^2-z^2}$ - $3d_{y^2-z^2}$ states within each Cu atom. Popovic *et al.* argued that such a gap shows a negligible temperature dependence in agreement with a temperature-independent absorption edge observed in their data for $E \parallel c$. However, our data do not support this scenario, as we will discuss later in Sec. 5.2.3. Additionally, SrCuO$_2$ belongs to the CT-type Mott insulators, i.e. the lowest transition is expected between the $2p$ and $3d$ states. Therefore, the model proposed by Popovic *et al.*[197] is arguable.

Investigations of the site-specific unoccupied electronic structure by x-ray absorption spectroscopy have shown that the hole occupation on the two distinct oxygen
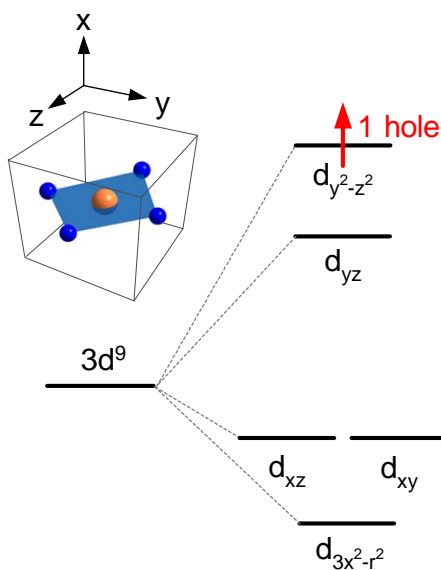
Figure 5.6.:
Qualitative crystal-field splitting of the five 3d orbitals of Cu^{2+} surrounded by four ligands on a regular square plane. The one hole of Cu^{2+} will occupy the $d_{y^2-z^2}$ orbital [196] (the coordinates are chosen that $x \parallel a$, $y \parallel b$, and $z \parallel c$ with a, b, and c being the lattice constants of SrCuO$_2$).
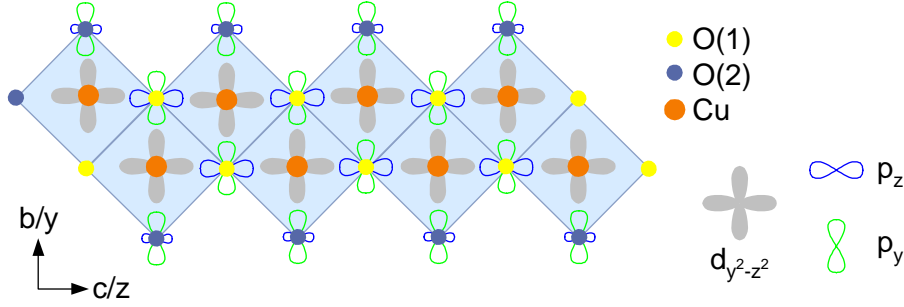
Figure 5.7.: Sketch of the unoccupied electronic structure in SrCuO$_2$ [196].

sites O(1) and O(2) is different [196] (see Fig. 5.7). While the hybridization of the O $2p_y$ orbital with the Cu $d_{y^2-z^2}$ orbital is found to be very similar for O(1) and O(2), the hybridization with the O $2p_z$ orbital is significantly higher at the O(1) site. The concentration of holes with O $2p$ character is centered with 70 % at O(1) and only with 30 % at O(2) [196].

In 1D, metals are believed to show no Fermi liquid behavior [198]. A model to describe the low-energy properties of 1D metals is the so-called Tomonaga-Luttinger liquid [199, 200]. The low-energy physics of such systems are expected to be dominated by collective modes of spin or charge, called spinons and holons [201], i.e. the spin and charge degrees of freedom of a real electron are separated (*spin-charge separation*). For SrCuO$_2$, which is not a metal, but a charge-transfer (CT) insulator the observation of spin-charge separation has been reported, from angle-resolved photoemission (ARPES) [202–205] and subsequently confirmed by inelastic neutron scattering [189] and inelastic x-ray scattering (RIXS) [206]. In ARPES experiments an electron is removed from the filled states below the CT gap. The created hole decays into a holon and a spinon, resulting in two-peak structure in the ARPES spectra, originating from the spinon and holon branch [203]. From a fit to the data $t = (0.71 \pm 0.04)$ eV (holon energy scale) and $J_c = (0.31 \pm 0.08)$ eV (spinon energy scale) in SrCuO$_2$ is obtained [202]. In a second study $t = 0.65$ eV and $J_c = 0.27$ eV were obtained [203].

In conventional band insulators a bound electron-hole pair, known as Wannier or Frenkel exciton is often observed in optical spectra right below the absorption edge. An exciton is called Wannier exciton if the Coulomb interaction between the electron and the hole is reduced due to large screening (materials with large dielectric function). Then the radius of the exciton is much larger than the lattice spacing and the exciton binding energy is rather small. In the case of Frenkel excitons the Coulomb interaction is large, resulting in a small radius and a large binding energy. In this context a local crystal-field excitations can also be regarded as a Frenkel exciton (see also Sec. 2.4). The analogue for strongly correlated insulators is the Mott-Hubbard exciton which also can be understood as a spinless bosonic excitation with zero charge. However, the excitonic properties of correlated insulators are
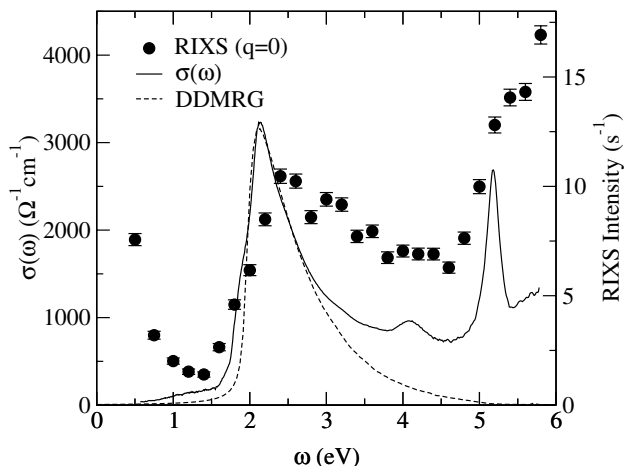
Figure 5.8.:
Optical conductivity $\sigma(\omega)$ obtained from a Kramers-Kronig analysis of the reflectance for $E \parallel c$ at $T = 90\,\mathrm{K}$ (solid line), RIXS spectra obtained at the Brillouin zone center (scatter plot), and DDMRG result for $\sigma(\omega)$ with an experimental broadening of $0.1\,t$. Taken from [209].

somewhat different from common band insulators, in particular in one dimension [207, 208]. For 1D Mott-Hubbard insulators, excitons have been described as bound pairs of holons (e^-) and antiholons (e^+). Theoretical predictions have been made for the exciton binding energy and size in 1D as a function of the nearest and next-nearest neighbor interaction V [207]. In particular these calculations show that V has to exceed a critical value of $2t$ in order to yield an excitonic bound state [208].

In a combined study of RIXS and optical spectroscopy the low-energy ($\gtrsim 1\,\mathrm{eV}$) electronic excitations have been investigated in SrCuO$_2$ [209] (Fig. 5.8). From the RIXS spectra a continuum of low-energy excitations is observed which is associated with the creation of holon and antiholon pairs [209]. For the lower edge of the holon-antiholon continuum a dispersion relation is observed which is similar to that of spinons (see Fig. 5.3 and Eq. 5.2) but shifted in energy. The optical conductivity $\sigma(\omega)$ has been obtained for $E \parallel c$ by a Kramer-Kronig analysis of the reflectance. A large part of the spectral weight of the peak observed at $1.7\,\mathrm{eV}$ is attributed to the one-holon-one-antiholon excited states. From the comparison of $\sigma(\omega)$ with results from the dynamical density-matrix renormalization group method (DDMRG) a good agreement is obtained for $t = 0.435\,\mathrm{eV}$, $V/t = 1.3$, and $U/t = 7.8$ (Fig. 5.8). According to the calculation in [208] no excitonic excitation, i.e. no holon-antiholon bound state is expected in this parameter regime. It is reasoned that the low-energy electronic excitation spectrum of SrCuO$_2$ consists of a continuum of excitations associated with the creation of holon and antiholon pairs [209].

Magnetic Properties

The magnetic coupling between neighboring copper spins is mediated by superexchange via the oxygen p orbitals. When considering holes, the p states are empty. According to the Goodenough-Kanamori-Anderson rules [130, 131] the exchange parallel to the c axis is strongly antiferromagnetic, i.e. $J_c \ll 0$ (Fig. 5.7). The coupling between parallel chains along the b axis proceeds through $\sim 90°$ Cu-O-Cu

bonds, and therefore should be weakly ferromagnetic, i.e. $J_b \gtrsim 0$. However, due to the triangular arrangement of the copper ions this exchange is strongly frustrated and parallel chains in $SrCuO_2$ must be regarded as nearly decoupled. Also the coupling J_a between pairs of double chains along the a axis is expected to be very small. This is affirmed by the relatively low temperature of $T_c \sim 2\,K$, below which static magnetic ordering is observed [210]. This value is obtained by a combined analysis of magnetic susceptibility, heat capacity, neutron diffraction, and muon-spin relaxation measurements. The remarkably small value of T_c is ascribed to the combined effects of quantum fluctuations and frustration. From neutron scattering an unusual magnetic phase below $T = 5.0(4)\,K$ is reported, indicating an anisotropic spin freezing in $SrCuO_2$ [211]. The magnetic correlation lengths in the frozen state have been estimated to $\xi_c > 200 \cdot c$, $\xi_b = 2.2(3) \cdot b$, and $\xi_a = 60(25) \cdot a$, indicating long range order only along the chain direction c [211].

Using inelastic neutron scattering the spin dynamics in $SrCuO_2$ were investigated up to energies of $0.6\,eV$ [189] (Fig. 5.9). A gapless continuum of magnetic excitations is observed in accordance with the expected excitation spectrum of a spin-1/2 chain. The lower boundary of the two-spinon continuum extends up to $\sim 360\,meV$, which corresponds to $J_c = 226(12)\,meV$. A larger value for the exchange coupling of $J_c = (260 \pm 25)\,meV$ was estimated from magnetic susceptibility measurements on $SrCuO_2$ between $5\,K$ and $800\,K$ [47]. As mentioned above, ARPES studies found $J_c = (310 \pm 80)\,meV$ [202]. Also for the closely related compound Sr_2CuO_3 the determination of J by different experimental techniques is controversial. From the temperature dependence of the magnetic susceptibility a value of $181(17)\,meV$ is estimated [47], while mid-infrared absorption data yield a $\sim 37\%$ larger value of
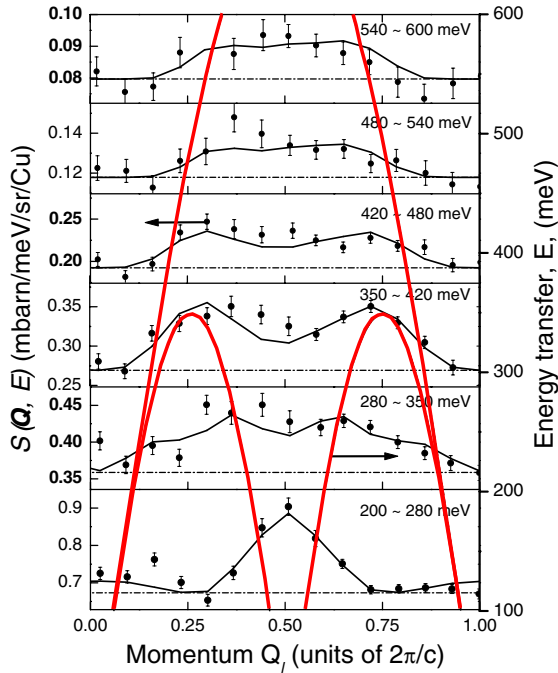
Figure 5.9.:
Constant-energy scans from inelastic neutron scattering on $SrCuO_2$ showing the lower and upper boundary of the two-spinon continuum (marked by red lines). Reproduced from [189].
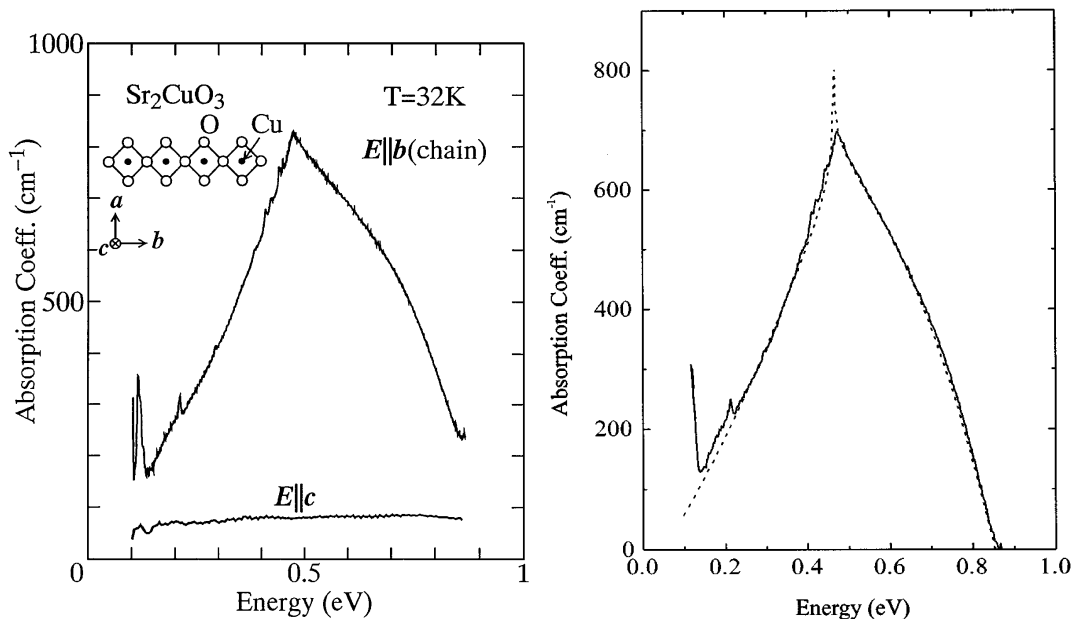
Figure 5.10.: (a) Two-spinon-plus-phonon contribution in the mid-infrared absorption
spectrum of the $S = 1/2$ chain compound Sr_2CuO_3 for $E \parallel b$ (chains). For
polarization perpendicular to the chains ($E \parallel c$) the spectrum is feature-
less. From this data $J_c = 0.26$ eV and $\omega_{ph} = 0.07$ eV for the involved phonon
were estimated. Taken from [46]. (b) Comparison of the experimental and
theoretical line shape for Sr_2CuO_3. Here the parameters are $J_c = 0.246$ eV
and $\omega_{ph} = 0.08$ eV. Note that a linear background was subtracted from the
experimental data. Taken from [103].

260 meV [46] (Fig. 5.10). Therefore one motivation was to determine the important
parameter J_c for $SrCuO_2$ by analyzing the mid-infrared absorption spectra. Addi-
tionally, the double chains in $SrCuO_2$ give the possibility to study the influence of
weak perpendicular couplings on the excitation spectrum, earlier investigated in the
buckled spin-ladder compound $CaCu_2O_3$ in our group [43, 48]. The investigation
of the compound $Sr_{0.9}Ca_{0.1}CuO_2$ was initiated by recent thermal conductivity mea-
surements [49]. Upon substitution of Sr by iso-valent Ca, the thermal conductivity
due to acoustic phonons is effectively suppressed, while it is suggested that the mag-
netic contribution is not strongly affected [49]. Therefore we determined J_c also for
$Sr_{0.9}Ca_{0.1}CuO_2$ by analyzing the mid-infrared absorption spectra.

5.2.2. Experimental Details

Samples of $Sr_{1-x}Ca_xCuO_2$

Measurements of the transmittance and reflectance of $Sr_{1-x}Ca_xCuO_2$ were per-
formed on several single crystals. The orientation, thickness and denotation of
the samples is summarized in Tab. 5.2. The growth of large single crystals of
$Sr_{1-x}Ca_xCuO_2$ was performed by two groups. While those labeled with SXa in
Tab. 5.2 were grown by A. Revcolevschi, U. Ammerahl, and G. Dhalenne[5] [212], the
SXb samples and $Sr_{0.9}Ca_{0.1}CuO_2$ were grown by P. Ribeiro, C. Hess, and B. Büch-
ner[6] [49].

The series $Sr_{1-x}Ca_xCuO_2$ forms in ambient atmosphere and $950°$ C a continuous
solid solution up to $x = 0.75$ [212]. The cell parameters decrease approximately lin-
early with x [213] (for $x = 0$ see Tab. 5.1). In both groups large single crystals were
grown using the traveling-solvent floating zone method [49, 212]. The purity, stoi-
chiometry and single-phase structure of the crystals was checked by x-ray diffraction
and polarization microscopy. The single crystals labeled with SXa were additionally
characterized by means of elastic neutron scattering [212]. Here the analysis of the
rocking curves has indicated a very good crystal quality.

Typical dimensions of the as-grown rods are a few mm along all three crystallo-
graphic axes. Both groups have made large parts of such a rod available for our
measurements. The rods were oriented with the Laue method and afterwards cut,

Table 5.2.: Orientation, thickness, and denotation of the $Sr_{1-x}Ca_xCuO_2$ samples consid-
ered in this work. In the last column the method of preparation of the shiny
surfaces is listed: p for 'polished' (with prior lapping) and c for 'cleaved'. The
thickness of the sample is obtained with a microscope. The error is determined
in the same way as for RVO_3 (see Sec. 4.2.1).

Sample	Denotation	Spectral range	T/R	Pol.	d (μm)	Prep.
$SrCuO_2$	(S1a)	FIR	R	$E \parallel a, c$	3910	p
$SrCuO_2$	(S2a)	FIR	R	$E \parallel b, c$	$\gtrsim 4000$	p
$SrCuO_2$	(S3a)	MIR/NIR	R	$E \parallel a, b$	1492	p
$SrCuO_2$	(S4a)	MIR/NIR	R	$E \parallel a, c$	2671	p
$SrCuO_2$	(S5a)	MIR/NIR	T	$E \parallel b, c$	243 ± 7	p
$SrCuO_2$	(S6a)	MIR/NIR	T	$E \parallel a, b$	289 ± 4	p
$SrCuO_2$	(S1b)	MIR/NIR	T	$E \parallel a, c$	51 ± 1	c
$Sr_{0.9}Ca_{0.1}CuO_2$	(SC1)	MIR	T	$E \parallel a, c$	52 ± 2	c

---

[5]Laboratoire de Chimie des Solides, Université Paris XI, 91405 Orsay Cedex, France
[6]Institute for Solid State Research, IFW Dresden, 01171 Dresden, Germany

lapped, and polished (Sec. 3.2). Because the samples are very sensitive to water and acetone, the handling of the samples is rather difficult with standard procedures. Therefore an anhydrous lapping and polishing procedure described in Sec. 3.2 has been used. Unfortunately, it turned out that also this procedure does not yield satisfactory results. It is possible that surface layers are built, which will be discussed later in more detail. To avoid the lapping and polishing procedure, we also used samples which were cleaved. Because the crystals of $Sr_{1-x}Ca_xCuO_2$ readily cleave along $(0\,k\,0)$ [212], solely samples with a large ac plane have been prepared this way. The comparison of the data of cleaved and of polished surfaces show that the surface layers on polished samples do not exhibit significant absorption bands in the MIR frequency range, but we will go into detail later. The preparation technique of the samples is specified in the last column of Tab. 5.2.

Reflectance of SrCuO₂

The reflectance $R(\omega)$ of SrCuO₂ was measured from 0.012 eV up to 1.73 eV in the temperature range between 10 K and 300 K using the experimental setup described in Chap. 3. The measurements have been performed on overall four samples (see Tab. 5.2) by the use of linearly polarized light with the electric field vector aligned parallel to the orthorhombic axes, i.e. $E \parallel a, b, c$ in *Cmcm*. The results are shown in Fig. 5.11. The spectra of different frequency ranges have been merged. For $E \parallel b$ we performed measurements just up to 1.24 eV. As already argued in Sec. 4.2.8 for YVO₃, the small changes of $R(\omega)$ are not crucial for the combined analysis of $T(\omega)$ and $R(\omega)$. Therefore a constant extrapolation of R_b from 1.24 to 1.73 eV is appropriate for the calculation of $\sigma_b(\omega)$ which is mainly affected by the transmittance.

At low frequencies (FIR), optical phonons give rise to several peaks in $R(\omega)$ with maximum values close to 1 at $T = 10$ K. For each direction of polarization three peaks are observed. For a detailed analysis we have considered a group-theoretical analysis on the number and polarization dependence of the observed modes, described in the following. For the compound SrCuO₂ with space group *Cmcm* [194] (D_{2h}^{17}) the number of formula units per cell is $Z = 4$, but due to the C centering of the unit cell there are only 2 formula units in the primitive cell, i.e. $3(N-1) = 3(2 \cdot 4 - 1) = 21$ optical phonon modes are expected. All atoms, Sr(1), Cu(1), O(1), and O(2) occupy the same type of Wyckoff position $4c$ with site symmetry $C_{2\nu}$ ($m2m$). The full representation obtained by the group-factor analysis [62] is (see also Sec. 2.4.1):

$$M = 4M(C_{2\nu}) = 4A_g + 4B_{1g} + 4B_{3g} + (3+1)B_{1u} + (3+1)B_{2u} + (3+1)B_{3u}.$$

The first 12 modes labeled with index g are Raman active. The remaining 12 odd modes include 3 acoustic modes $B_{1u} + B_{2u} + B_{3u}$ and nine infrared-active modes. The latter split into $3B_{3u}$ ($E \parallel a$), $3B_{2u}$ ($E \parallel b$), and $3B_{1u}$ ($E \parallel c$). To verify this, we derived the polarization-dependent far-infrared optical conductivity of SrCuO₂ by a fit of Drude-Lorentz oscillators to the reflectance (for details see Sec. 2.1.1
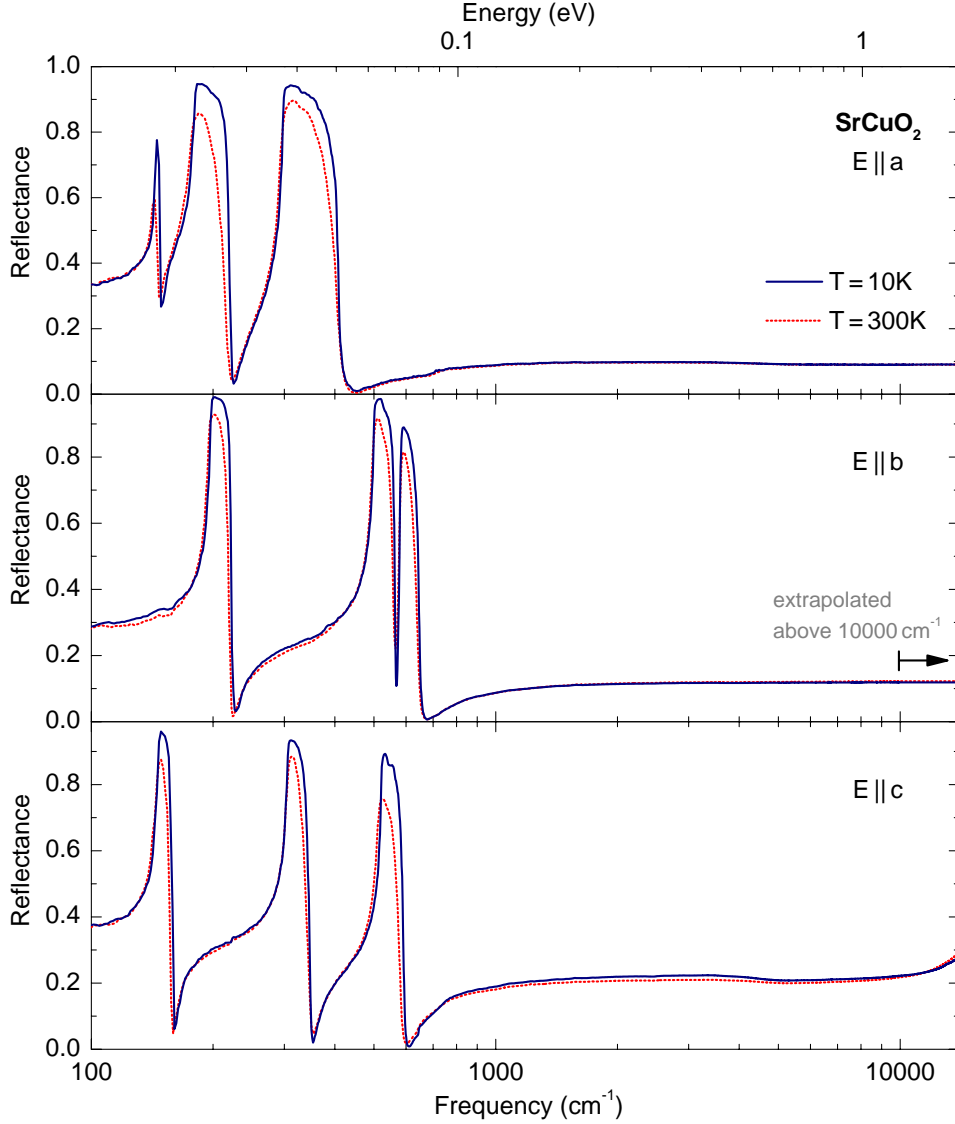
Figure 5.11.: Temperature dependence of the reflectance of $SrCuO_2$ for $E \parallel a$ (top panel), $E \parallel b$ (middle panel), and $E \parallel c$ (bottom panel). Note that the frequency and energy are shown on a logarithmic scale. The spectra obtained by several measurements were merged, i.e. S1a & S3a for $E \parallel a$, S2a & S3a for $E \parallel b$, and S1a & S4a for $E \parallel c$. For the denotation we refer to Tab. 5.2.

and Eq. 2.14).[7] The results are shown in Fig. 5.12 and the phonon parameters are summarized in Tab. 5.3. The obtained values of the transverse optical phonon frequencies ω_{0i} are in good agreement with previous experimental and theoretical

---

[7]The fit has been performed using the program RefFIT 1.2.56 by A. Kuzmenko (Département de Physique de la Matière Condensée, Université de Genève, Switzerland).
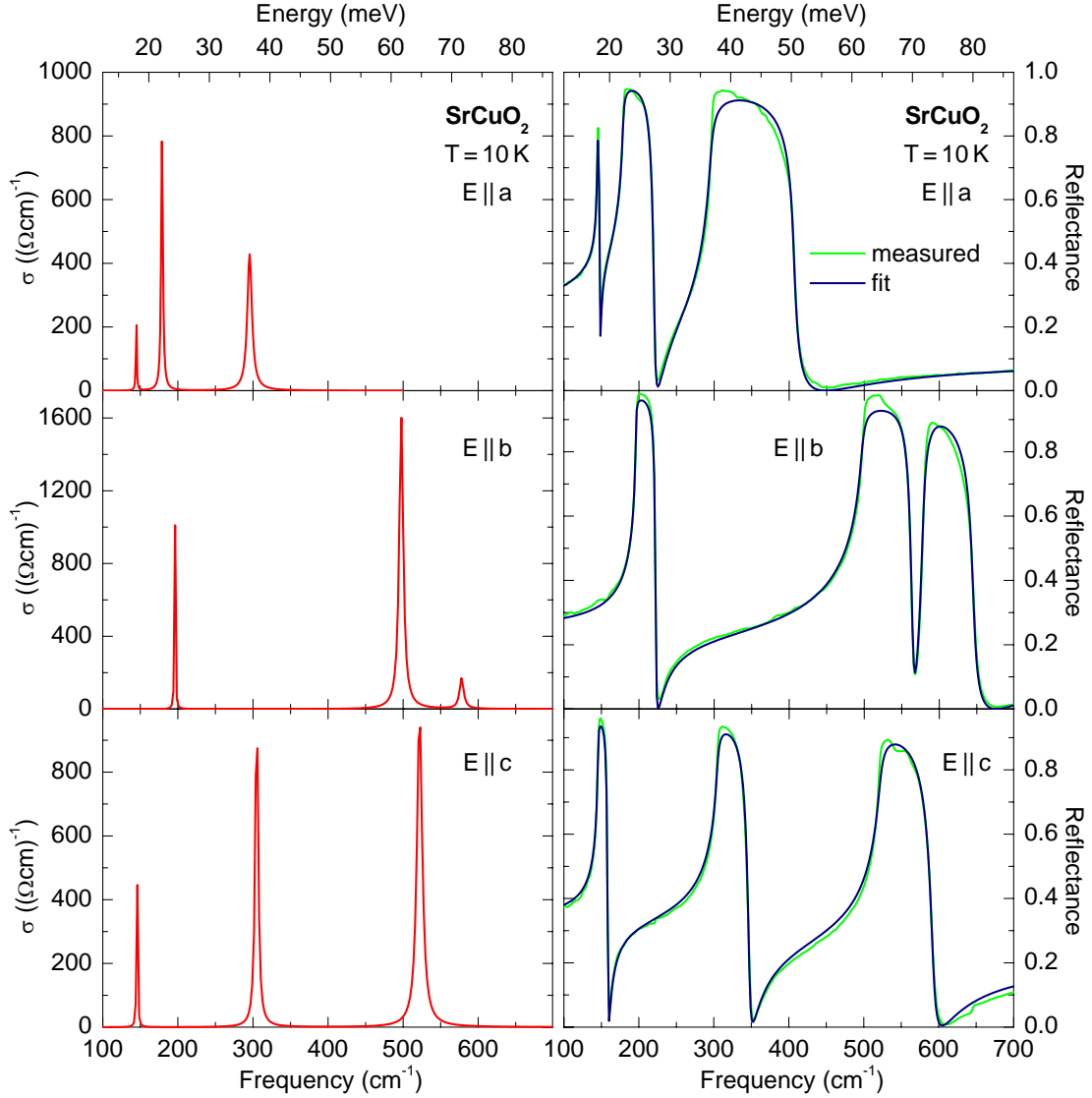
Figure 5.12.: Polarization-dependent far-infrared optical conductivity of SrCuO$_2$ (right panels) obtained by a fit of Lorentz oscillators to the reflectance (left panels). The optical phonon parameters are summarized in Tab. 5.3.

results [214, 215].[8] With increasing temperature the phonon peaks slightly shift to lower energies and $R(\omega)$ decreases a little.

Above 0.1 eV, $R(\omega)$ has an almost constant value and is featureless. The different absolute values for the three polarization directions $R_a \approx 9\,\%$, $R_b \approx 12\,\%$, and $R_c \approx 21\,\%$ reflect the difference in the index of refraction: $n_a = 1.86 \pm 0.01$,

---

[8]In Ref. [215] the value of the 305 cm^{-1} mode for E $\parallel c$ at 10 K is wrongly specified with 343 cm^{-1} in the table stated on page 5288. However, the optical conductivity spectra on page 5286 are in very good agreement with our results.

Table 5.3.: IR-active phonon parameters in $SrCuO_2$ at $T = 10\,K$. Here ω_{pi} denotes the plasma frequency, ω_{0i} the transverse frequency (eigenfrequency), γ_i the damping (scattering rate), and $S_i = \omega_{pi}^2/\omega_{0i}^2$ is the oscillator strength (see also Sec. 2.1.1 and Eq. 2.14).

Polarization	ε^∞	ω_0 (cm^{-1})	ω_p (cm^{-1})	γ	S
$E \parallel a$	3.55	145	137	1.25	0.89
		179	362	2.71	4.09
		296	436	7.39	2.17
$E \parallel b$	4.74	196	299	1.07	2.33
		497	790	6.46	2.53
		578	256	6.48	0.20
$E \parallel c$	7.53	146	235	1.11	2.59
		305	532	4.51	3.05
		522	703	8.30	1.81

$n_b = 2.06 \pm 0.01$ and $n_c = 2.69 \pm 0.01$.[9] The anisotropy of n reflects the large structural anisotropy. A change of temperature solely affects the absolute value of $R(\omega)$ in this energy range, but these changes are comparatively small ($\lesssim 1\,\%$).

Transmittance of SrCuO₂

The transmittance measurements of $Sr_{1-x}Ca_xCuO_2$ were performed on several samples with different thicknesses and surface treatments (see Tab. 5.2). Exemplarily the transmittance $T(\omega)$ for $E \parallel a, b, c$ (T_a, T_b, T_c) of $SrCuO_2$ at low temperatures (10 K) is shown in Fig. 5.13 (MIR range) and Fig. 5.14 (NIR range). For each polarization direction two spectra obtained by measurements on overall three different samples S1b, S5a, and S6a are shown (Tab. 5.2). Due to the different thickness of the samples, the spectra are not directly comparable. Up to 1.7 eV the spectrum for $E \parallel a$ has an almost constant and featureless shape, and the absolute value is comparatively high. Because of the small sample thickness of the *cleaved* sample S1b, Fabry-Perot fringes are observed. Using $d = 1/(2n\Delta\nu)$ (Eq. 3.5 in Sec. 3.1.2) we obtain $d^{S1b} = 55\,\mu m$ from the fringes with periodicity $\Delta\nu^{S1b}$ and $n_a = 1.86$ obtained from the reflectance (see the former paragraph). The value of d^{S1b} is in good agreement with the thickness $d = 51\,\mu m$ obtained with the microscope. This in turn affirms the value of n_a. Also $T(\omega)$ of the *polished* sample S6a shows fringes. From a closer examination we ascertain that a superposition of *two* fringe patterns

---

[9]The given values for the index of refraction were estimated using $n \approx (1 + \sqrt{R})/(1 - \sqrt{R})$, deduced from Eq. 2.6 by neglecting κ.
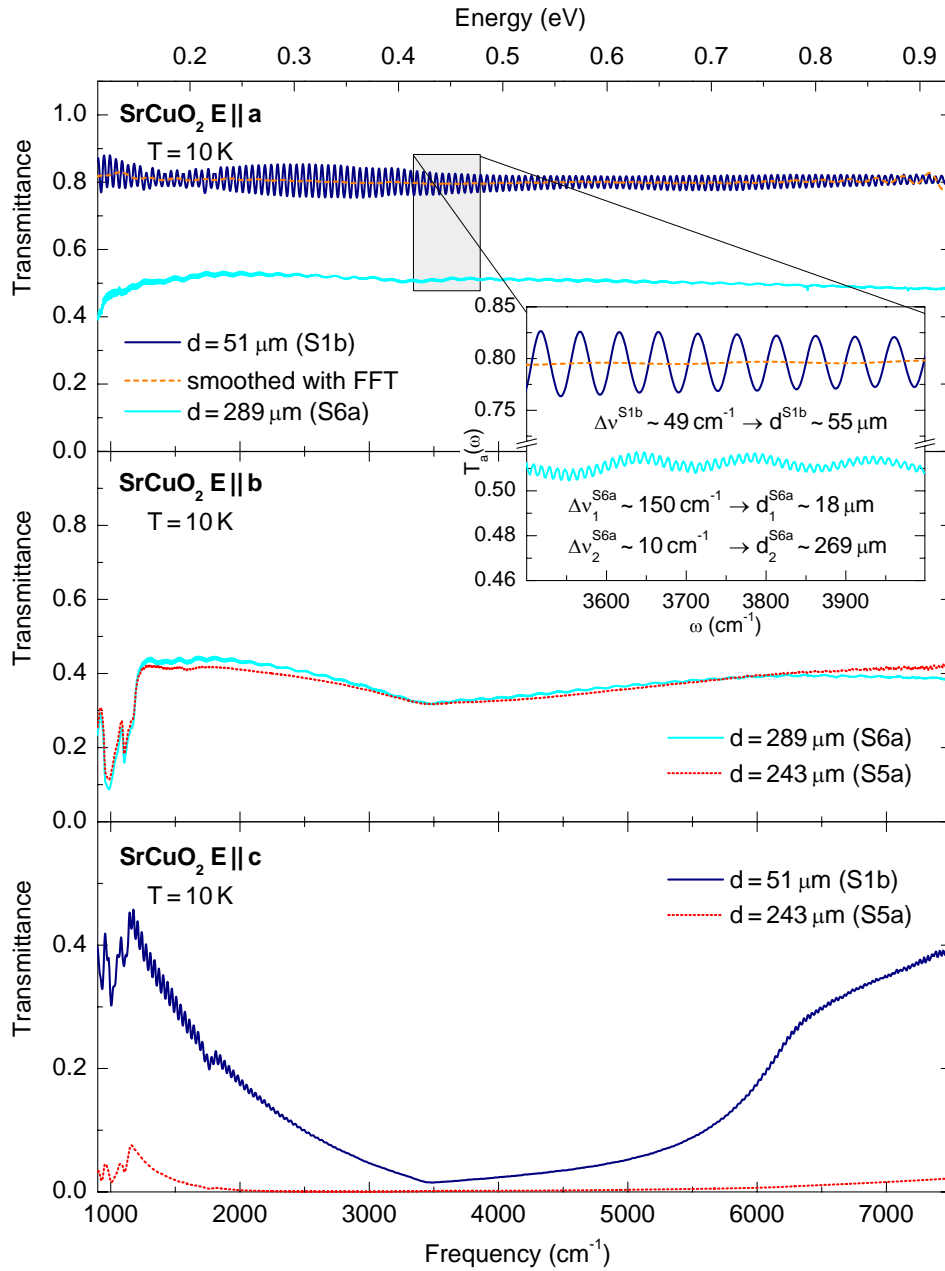
Figure 5.13.: Mid-infrared transmittance of several SrCuO₂ samples at 10 K for $E \parallel a, b, c$ in *Cmcm* (T_a, T_b, T_c from top to bottom panel). All three measurements were performed by the use of the same components, i.e. the globar, the BaF₂ polarizer, the KBr beam splitter, and the MCT detector (Chap. 3). For each polarization two transmittance spectra are shown, which were obtained by measurements on the 51 µm (S1b), the 243 µm (S5a), and the 289 µm (S6a) thick samples. The fringes in T_a of S1b were smoothed with a Fast Fourier transform filter (FFT). The inset shows the spectra for $E \parallel a$ on a larger scale. The spectra of the S5a sample show a superposition of *two* fringe patterns with different periodicity (for details see text).
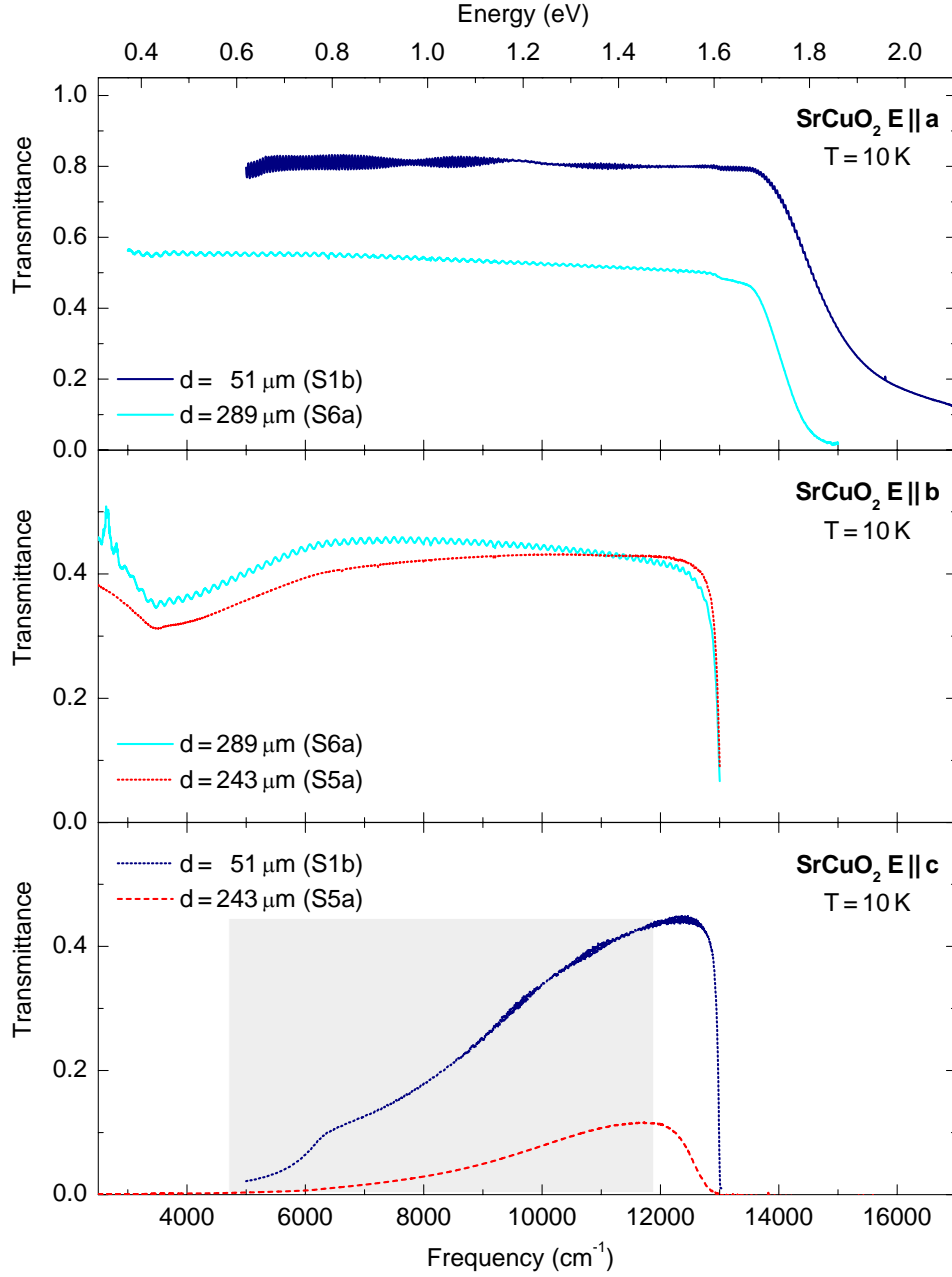
Figure 5.14.: Near-infrared transmittance of several $SrCuO_2$ samples at 10 K for $E \parallel a, b, c$ in $Cmcm$ (T_a, T_b, T_c from top to bottom panel). The measurements were performed by the use of the tungsten lamp, the BaF_2 polarizer (Glan-Thompson prisma), the VIS beam splitter, and the MCT (Si) detector (see Chap. 3). For the denotation and preparation technique of the samples see Tab. 5.2. The measurement of $T_c(\omega)$ shows a strong down-bending below 1.49 eV (shaded box) which is not observed in the MIR measurement (Fig. 5.13). This is attributed to a photoinduced absorption discussed in App. A.6.

with different periodicity overlay the spectrum of sample S6a (inset in Fig. 5.13). The fringes with short periodicity $\Delta\nu_2^{S6a}$ correspond to a thickness of $d_2^{S6a} = 269\,\mu$m, while $d_1^{S6a} = 18\,\mu$m is obtained from those with $\Delta\nu_1^{S6a}$.[10] How to understand such a superposition of *two* fringe patterns? Adding d_1^{S6a} and d_2^{S6a} we obtain a total thickness of $287\,\mu$m which is in agreement with the value of $d = 289\,\mu$m obtained with the microscope. Therefore, one may expect the formation of a (thick) surface layer of $18\,\mu$m thickness. Keeping in mind that the surfaces of sample S6a were treated by the anhydrous lapping and polishing procedure (Sec. 3.2), one may speculate about the formation of a strontium-copper ethylene glycol complex [216]. However, within the scope of this thesis we did not perform a detailed investigation on the chemical composition of these layers. Rather, we conclude from the comparison with the spectrum of the cleaved sample S1b, that the surface layer compound on sample S6a at least exhibits no significant absorption bands in the MIR frequency range. However, one has to keep in mind that a non-absorbing surface layer may cause an inaccurate absolute value of the measured transmittance because of additional reflection at the surface layer / sample interface. In general, the fraction of intensity which is reflected from the interface is given by the reflection coefficient $R = (n_1 - n_2)^2/(n_1 + n_2)^2$, where n_1 and n_2 are the refractive indices (real part) of the two media (Fresnel formula at normal incidence). If the refractive index of the surface layer compound is similar to that of SrCuO$_2$ with $n \sim 2$ (see the previous section) this effect is negligible. But, if the surface layer exhibits say $n_{SL} = 2.5$ (1.5), the intensity of incident light is already reduced by $18\,\%$ ($4\,\%$) at the vacuum / surface layer and again by $4\,\%$ ($2\,\%$) at the interface. In total a difference in transmittance of about $8\,\%$ ($5\,\%$) is expected for a sample with such a surface layer. Altogether we conclude that the measurement on sample S6a is reliable except for the absolute value. Thus the small dip observed around $0.4\,$eV in $T_b(\omega)$ is an intrinsic feature of SrCuO$_2$.

The comparison of T_a and T_b obtained from the same measurement shows that the overall value of the transmittance is similar for both polarization directions, i.e. 40-50 %. The most striking frequency dependence is observed for $E \parallel c$. For samples thicker than $100\,\mu$m just spectra with $T(\omega) \approx 0$ have been measured (see e.g. $T_c(\omega)$ of sample S5a). The corresponding spectrum of the $51\,\mu$m thin sample revealed a broad, strong suppression of $T_c(\omega)$ with a value close to zero around $0.43\,$eV, whereas $T_c(\omega)$ reaches 40 % elsewhere.

5.2.3. Results: Optical Conductivity of Sr$_{1-x}$Ca$_x$CuO$_2$

To investigate the magnetic excitations in SrCuO$_2$ we calculated the optical conductivity directly from $T(\omega)$ and $R(\omega)$ (see Chap. 2). The results for $E \parallel a, b$, and c

---

[10] The fringes with $\Delta\nu_2^{S6a}$ are resolved because the spectrum has been measured with high resolution ($\Delta\nu = 2\,\text{cm}^{-1}$). For comparison, the fringes in the spectrum of the $243\,\mu$m thick sample (S5a) with a corresponding periodicity of $\Delta\nu \sim 11\,\text{cm}^{-1}$ remain unresolved because of $5\,\text{cm}^{-1}$ resolution.
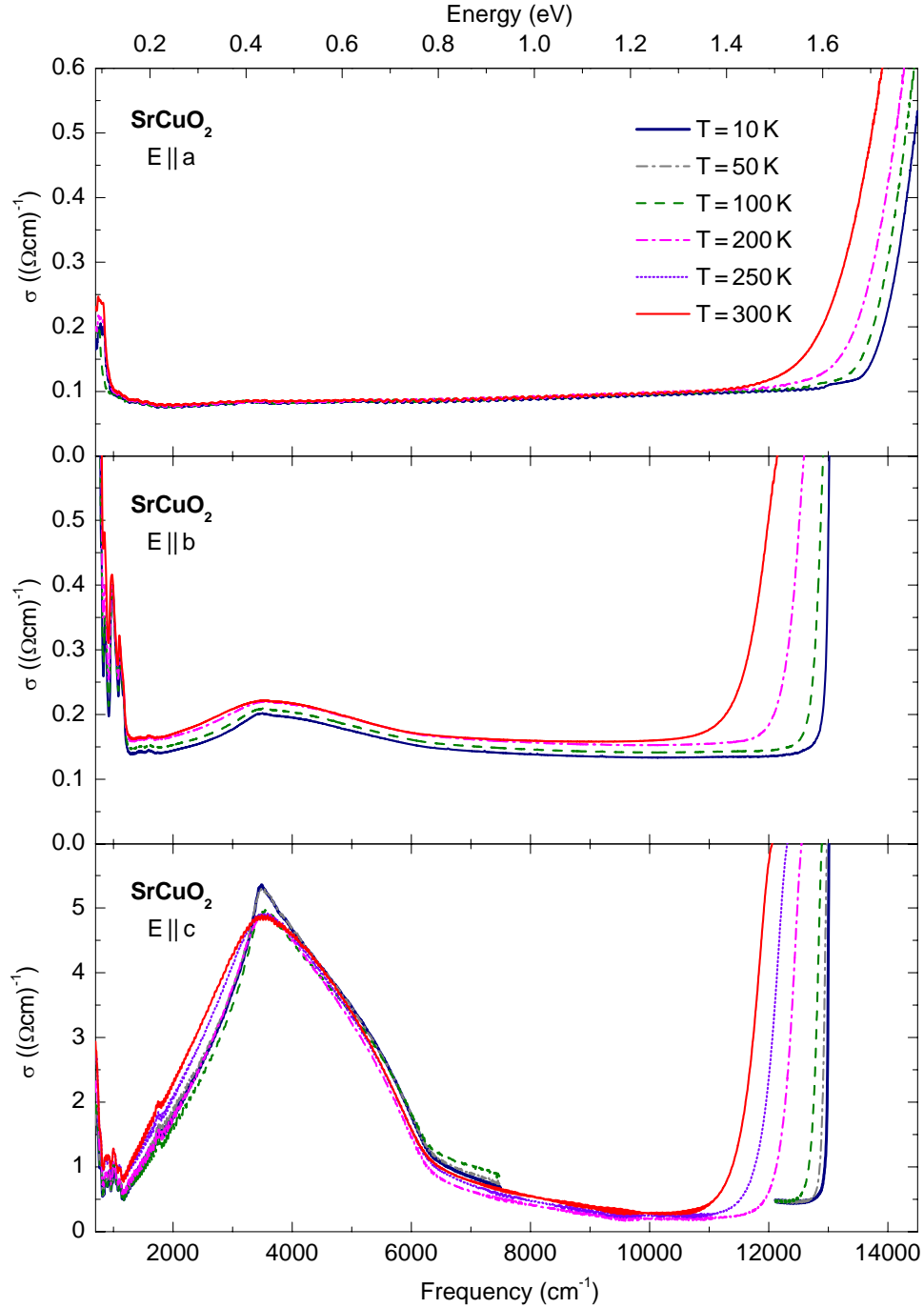
Figure 5.15.: Temperature dependence of the real part of the optical conductivity of SrCuO$_2$ for $E \parallel a$, $E \parallel b$, and $E \parallel c$ (top to bottom panel). The figure shows the spectra over the complete energy range considered in this work, i.e. $\sigma(\omega)$ obtained by in the MIR and NIR range on sample S6a ($E \parallel a$) and S5a ($E \parallel b$) were merged. For $E \parallel c$ the NIR spectra below 200 K and $\omega < 0.9$ eV show a photoinduced absorption and are not shown here (for details see App. A.6).

$(\sigma_a(\omega),\ \sigma_b(\omega),\ \sigma_c(\omega))$ are shown in Fig. 5.15. For $T < 200\,\mathrm{K}$ the $\sigma_c(\omega)$ is not shown for frequencies from 0.93 up to 1.51 eV in Fig. 5.15. This is because we have observed a photoinduced absorption in this energy range which we discuss in App. A.6.

Up to 140 meV, tiny and sharp absorption features are observed which are ascribed to multi-phonon absorption. While the highest infrared-active phonon mode is observed at 72 meV for $E \parallel b$ (Tab. 5.3), the highest Raman-active phonon mode is found around 75 meV [217]. Therefore two-phonon absorption is expected below 150 meV, in agreement with Raman studies [214] and our results (Fig. 5.15). The steep increase of $\sigma(\omega)$ above 1.6 eV (at 10 K) is identified with the onset Δ_{opt} of electronic transitions across the charge-transfer gap. In the intermediate energy range we expect magnetic excitations, significantly below the electronic gap. In fact, a broad absorption feature at about 0.4 eV is observed in σ_b and σ_c (middle and bottom panel in Fig. 5.15), while σ_a is featureless between 0.2 and 1.4 eV (top panel in Fig. 5.15). Due to the energy range, the characteristic line shape, and by comparison with spectra of other 1D cuprates ([46]), we identify the feature in σ_c with the two-spinon-plus-phonon absorption [103] (see Sec. 2.4.3). By comparison with theory, our result for σ_c enables us to evaluate the magnetic exchange coupling J_c with high accuracy. To explain the peak in σ_b, we discuss a possible exchange process of two spinons along c, which gives rise to a dipole moment along b.

Charge-Transfer Gap

First we discuss the onset of electronic transitions across the charge-transfer gap in SrCuO₂. The temperature and polarization dependence of Δ_{opt} is shown in Fig. 5.16. The room-temperature values $\Delta_{\mathrm{opt}}^a = 1.72\,\mathrm{eV}$ and $\Delta_{\mathrm{opt}}^c = 1.46\,\mathrm{eV}$ are similar to those reported in [197]. However, our values of Δ_{opt} have been obtained from the *onset* of electronic transition observed in the transmittance, while in [197] $\Delta_{\mathrm{opt}}^a = 1.77\,\mathrm{eV}$ and $\Delta_{\mathrm{opt}}^c = 1.42\,\mathrm{eV}$ were obtained from the *maximum* of the first peak. The assignment of Δ_{opt} with the energy of the maximum yields not an exact determination of Δ_{opt}
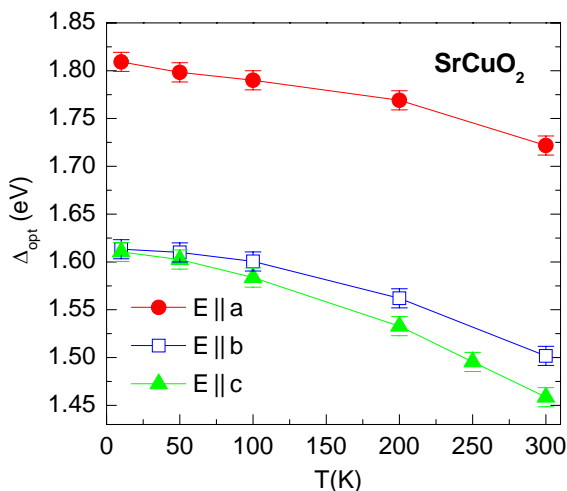
Figure 5.16.:
Temperature dependence of the onset of the optical gap Δ_{opt} in SrCuO₂ for the different polarization directions. The values of Δ_{opt} have been obtained by taking $\sigma(\Delta_{\mathrm{opt}}) = 0.6\,(\Omega\mathrm{cm})^{-1}$ for $E \parallel a$, b, and at $\sigma(\Delta_{\mathrm{opt}}) = 3\,(\Omega\mathrm{cm})^{-1}$ for $E \parallel c$.

because the peak width remains unconsidered. The similarity of the value of Δ_{opt}^c is just because of the steepness of the absorption edge for $E \parallel c$ (see Fig. 5.8). In contrast, for $E \parallel a$ where the absorption edge is less steep, our value is clearly lower. Altogether we claim that our values of Δ_{opt} are more accurate. In addition, no temperature-dependent changes of Δ_{opt}^c between $5\,\mathrm{K}$ and $300\,\mathrm{K}$ have been observed in Ref. [197]. In contrast our data show a distinct temperature dependence of Δ_{opt}^c which is comparable to those of Δ_{opt}^a and Δ_{opt}^b (Fig. 5.16). In particular the temperature dependence of our data has been reproduced several times on different samples (see Tab. 5.2). In comparison with model calculations, the difference between Δ_{opt}^a and Δ_{opt}^c is attributed to excitations across a direct and an indirect gap in Ref. [197] (see Sec. 5.2.1). Furthermore it has been argued that the nonexistent temperature dependence of Δ_{opt}^c confirms this interpretation. However, as already mentioned in Sec. 5.2.1, we argue that the underlying model is too simple. A more conclusive explanation of the observed anisotropy of the CT gaps in $SrCuO_2$ is obtained from the site-specific unoccupied electronic structure investigated by x-ray absorption [196]. Here it has been shown that the holes in $SrCuO_2$ predominately occupy 'planar' Cu $3d_{y^2-z^2}$ orbitals [196]. Therefore the hopping is expected to be noticeable larger in the bc (yz) plane, compared with the a (x) direction. Thus Δ_{opt}^b and Δ_{opt}^c are expected to be similar and Δ_{opt}^a is distinctly larger. With increasing temperature all three values Δ_{opt} continuously decrease (Fig. 5.16), in accordance with thermally excited phonons allowing electronic absorption already at lower energies (electron-lattice coupling). Such an temperature dependence of electronic gaps is observed in several correlated compounds (see e.g. [139]).

Two-Spinon-Plus-Phonon Absorption

As mentioned above, the features observed in the intermediate energy range of $\sigma_c(\omega)$ and $\sigma_b(\omega)$ are assigned with magnetic contribution. First, we focus on $\sigma_c(\omega)$ ($E \parallel$ chains). In Fig. 5.17 $\sigma_c(\omega)$ at $T = 10\,\mathrm{K}$ (solid line) is compared with the theoretical result for the two-spinon-plus-phonon contribution (dotted/dashed line) of a $S = 1/2$ chain at $T = 0$ calculated by Lorenzana and Eder [103] (Fig. 5.10(b)). For this purpose we have scaled the digitized data by applying $\omega = [(\tilde{\omega} - \tilde{\omega}_{ph})J_c/\tilde{J}_c] + \omega_{ph}$ to the x-coordinate and $A \cdot (\alpha/\alpha_{T=0})$ to the ordinate.[11] The theoretical curve shows two characteristic features: (i) a sharp cusp at $\omega_1 = \omega_{ph} + \pi J_c/2$ resulting from the van Hove singularity at $k = \pi/2$ in the density of states and (ii) a kink at $\omega_2 = \omega_{ph} + \pi J_c$ which results from the sharp upper boundary of the two-spinon continuum, the two-spinon cut-off at $k = \pi$ (see Fig. 5.3(b)) [103].[12] Here ω_{ph} denotes the phonon frequency.

From σ_c at $T = 10\,\mathrm{K}$ we extract $\omega_1 = (431 \pm 3)\,\mathrm{meV}$ and $\omega_2 = (788 \pm 6)\,\mathrm{meV}$ and obtain a coupling constant of $J_c = 2/\pi(\omega_2 - \omega_1) = (227 \pm 4)\,\mathrm{meV}$ (Fig. 5.17). From

---

[11] This is justified because of the values J_c and ω_{ph} of $SrCuO_2$ are very similar to those of $\tilde{J}_c$ and $\tilde{\omega}_{ph}$ of Sr_2CuO_3 which has been used to calculate the spectra in [103].

[12] The cut-off energy is equivalent to the maximum energy of two spinons.
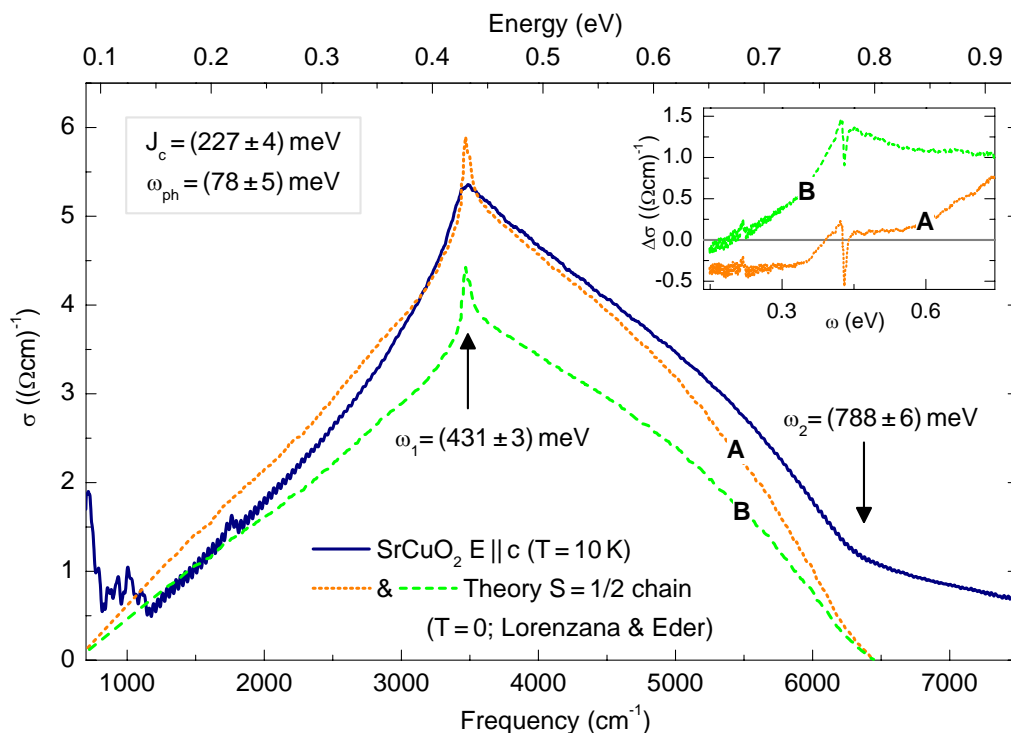
Figure 5.17.: Comparison of $\sigma_c(\omega)$ (solid line) with the theoretically predicted line shape for the two-spinon-plus-phonon absorption of a spin $1/2$ chain calculated by Lorenzana and Eder [103] (dotted/dashed line). The absolute value of the theoretical data is scaled twice, yielding spectrum A and B, respectively. The difference spectra of $\Delta\sigma_A = \sigma_c$ - A and $\Delta\sigma_B = \sigma_c$ - B are shown in the inset (for details see text).

$\omega_{ph} = 2\omega_1$ - ω_2 we derive $\omega_{ph} = (74 \pm 8)$ meV. However, by direct comparison between experiment and theory (for $J_c = 227$ meV), taking into account the entire line shape, we obtain $\omega_{ph} = (78 \pm 5)$ meV. Because of the superposition with multi-phonon absorption the 'onset' of the two-spinon-plus-phonon absorption at ω_{ph} is not clearly observed. However, the obtained value of ω_{ph} is typical for the breathing-phonon mode in cuprates which is relevant for the two-spinon-plus-phonon absorption [43, 44, 46, 103, 106, 218]. Our determination of J_c is very accurate and in very good agreement with previous results from inelastic neutron scattering yielding $J_c = 226(12)$ meV [189].

The experimental and theoretical line shapes show a good conformity, but there are small deviations. First, the sharp peak at ω_1 is less pronounced in the experimental data. For the related compound Sr$_2$CuO$_3$ also a similar rounding of the cusp at 32 K is observed [46] (Fig. 5.10). Probably this is an effect of finite temperatures (Fig. 5.18), but we will come to this point later. Second, the experiment shows a larger spectral weight as demonstrated in Fig. 5.17. Here the theoretical data are

shown two times, scaled with different factors for the absolute value, labeled with A (dotted curve) and B (dashed curve). To obtain curve A the absolute value is scaled such that the theoretical curve describes as much as possible of the experimental weight in σ_c. However, then the theoretical curve is too high at the left shoulder of the peak. Therefore curve B has been scaled by attaching importance to match theory and experiment in this energy region. The difference spectra $\Delta\sigma_A$ and $\Delta\sigma_B$ are shown in the inset of Fig. 5.17. To estimate the leftover spectral weight we have integrated $\Delta\sigma_{A(B)}$ and the experimental data as shown in Fig. 5.17, i.e. in an energy range from 149 to 799 meV. As result we find that A (B) describes roughly 97 % (74 %) of the observed spectral weight, which is actually expected because the theory only includes two-spinon excitations. Contributions due to multi-spinon excitations are not considered. Such contributions may emerge also at lower energies (below the two-spinon cut-off) and are probably responsible for the deviations there. For $\Delta S = 1$ the theory expects that two-spinon excitations account for 71 - 73 % of the total spectral weight at $T = 0$ [188, 219]. A large part, i.e. ~ 27 %, of the remaining weight is attributed to four-spinon excitations [219]. Unfortunately, no theoretical values for $\Delta S = 0$ are available, but we expect similar values.

A clear estimate of the spectral weight, in particular above the two-spinon cut-off is hindered by the background, which is observed for all three polarization directions, also for $E \parallel a$, showing no absorption features in this energy range. The origin of this background, perhaps disorder, is unclear up to now.[13] However, such a background has also been observed in several other cuprates with varying magnitude (see e.g. [43, 46, 106]), in particular also in the related compound Sr_2CuO_3 [46] (Fig. 5.10(a)).

---

[13] We also cannot absolutely rule out that contributions due to the photoinduced absorption observed in the NIR region may also contribute to σ_c in the MIR range (see App. A.6). However, we expect these contributions to be very small.
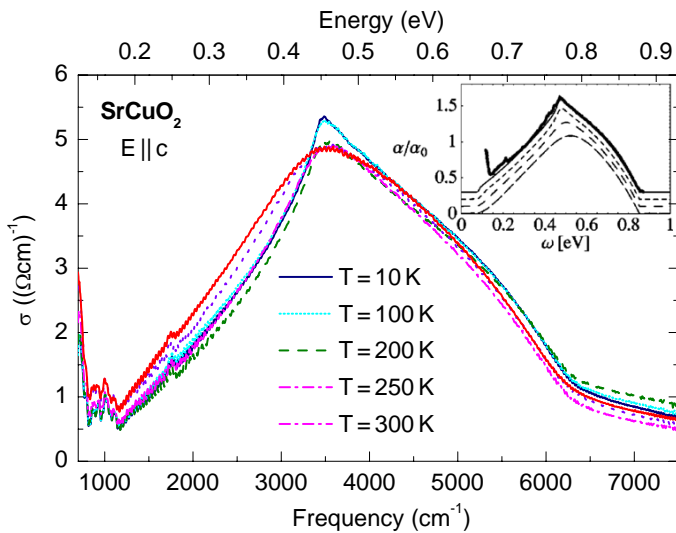
Figure 5.18.:
Temperature dependence of $\sigma_c(\omega)$ of $SrCuO_2$. For comparison the theoretical prediction of the normalized absorption $\alpha/\alpha_{T=0}$ for a $S = 1/2$ Heisenberg chain with $J = 246$ meV and $\omega_{ph} = 80$ meV are shown in the inset (for details see [108] and the text). The theoretical data are specified for different values of the inverse temperature, i.e. $J/k_B T = 100, 30, 10,$ and 5 from top to bottom. These values correspond to $T \approx 25, 85, 255,$ and 510 K for $J = 220$ meV.
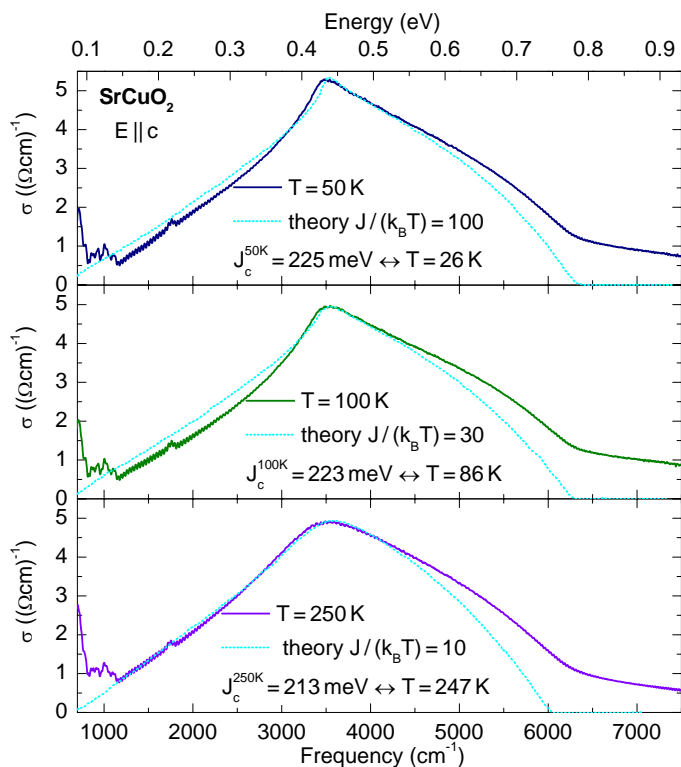
Figure 5.19.:
Comparison of σ_c at $T = 50$, 100, and 250 K of SrCuO$_2$ with the theoretical line shape at finite temperatures. The theoretical data have been digitized from [108] (inset in Fig. 5.18). From the direct comparison we obtain temperature-dependent $J_c(T)$ denoted in each panel. The corresponding temperatures for the theoretical data are also stated. The energy of the involved phonon is assumed to be temperature independent ($\omega_{ph} = (78 \pm 5)$ meV).

There the background was subtracted when comparing experimental and theoretical results [103], giving rise to an exceedingly good conformity with the theoretical result of the two-spinon contribution (Fig. 5.10(b)). However, as mentioned above this contradicts the expectations, i.e. the two-spinon contribution is expected to describe only a fraction of the observed spectral weight. Probably the missing weight is lost by subtracting the background. However, our result for SrCuO$_2$ shows about 3 - 25 % additional weight. In this regard theoretical results for the $\Delta S = 0$ channel would be highly desirable.

Furthermore, we compared the observed temperature dependence of σ_c with theoretical predictions from Gagliano *et al.* [108] (Fig. 5.18). They have used high-statistic quantum Monte Carlo and maximum entropy regularization methods to calculate the dynamical energy correlation function of the 1D $S = 1/2$ Heisenberg model at *finite* temperatures. In particular they calculated the normalized absorption $\alpha/\alpha_{T=0}$ for $\tilde{J} = 246$ meV, $\tilde{\omega}_{ph} = 80$ meV as a function of the inverse temperature $\tilde{J}/(k_B T) = 100$, 30, 10, and 5 (inset in Fig. 5.18). The results suggest that the main effect of increasing temperature on the line shape of the two-spinon-plus-phonon absorption is a rounding of the singularity at ω_1. Qualitatively, good agreement is observed. In particular the rounding of the cusp with increasing temperature is clearly observed in the experimental data.

For a quantitative analysis we compared the theoretical data directly with our results (Fig. 5.19). Again we have scaled the digitized data by applying $\omega = [(\tilde{\omega} -$
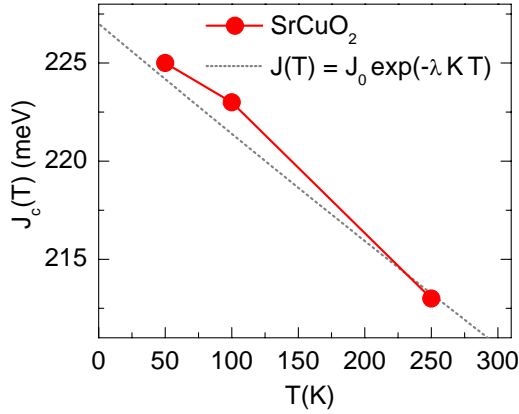
Figure 5.20.:
Temperature dependence of the exchange coupling $J_c(T)$ in SrCuO$_2$. The grey dotted line shows a fit using the relation $J(T) = J_0 \cdot \exp{(-\lambda K T)}$ [220] with $J_0 = 227\,\text{meV}$, $\lambda = 3\,\text{Å}^{-1}$, and $K = 8 \cdot 10^{-5}\,\text{ÅK}^{-1}$ (for details see text).

$\tilde{\omega}_{ph})J_c/\tilde{J}] + \omega_{ph}$ to the x-coordinate and $A \cdot (\alpha/\alpha_{T=0})$ to the ordinate. For $J_c \sim 220\,\text{meV}$, $J/k_B T = 100$, 30, 10, and 5 corresponds to $T \approx 25$, 85, 255, and 510 K. Because the coupling constant is expected to be temperature dependent, i.e. $J_c = J_c(T)$, we compared the spectra at similar temperatures (Fig. 5.19). A good agreement between theory and experiment is achieved for $J_c(T)$ shown in Fig. 5.20. A decrease of the exchange coupling with increasing temperature is expected to be mainly a result of the thermal expansion of the lattice. For the temperature dependence of the isotropic Heisenberg exchange constant the relation $J(T) = J_0 \cdot \exp{(-\lambda \langle x \rangle)}$ has been obtained theoretically in [220].[14] Here J_0 and $\langle x \rangle$ denote the coupling constant at $T = 0$ and the thermal expansion, respectively. The parameter λ can be estimated to q/r [220], where $q \approx 12$ [221], and the distance between the two magnetic Cu ions is approximately $r \approx 4\,\text{Å}$ (see Fig. 5.5). The thermal expansion can be roughly estimated by $\langle x \rangle = K \cdot T$. In Fig. 5.20 we show a fit to $J_c(T)$ for SrCuO$_2$ using this relation with $J_0 = J_c(T = 0) = 227\,\text{meV}$. A good agreement is obtained with $K \approx 8 \cdot 10^{-5}\,\text{ÅK}^{-1}$ for the thermal expansion coefficient. This is in reasonable agreement with K in related compounds, e.g. La$_{2-x}$Sr$_x$CuO$_4$ with $K \sim 5 \cdot 10^{-5}\,\text{ÅK}^{-1}$ [222]. Therefore the observed small temperature dependence of J_c is SrCuO$_2$ is consistent with changes of the Cu-Cu distance due to the thermal expansion of the lattice.

Altogether, our analysis of the magnetic contribution to σ_c gives clear evidence for the realization of spin $1/2$ chains in SrCuO$_2$. The magnetic excitation spectrum is well described by spinons, even at low temperatures.

Magnetic Contribution Perpendicular to the Chains

Now we turn to the magnetic contribution observed in σ_b around $450\,\text{meV}$. An extended view is shown in Fig. 5.21. The energy and the line shape of the absorption feature in σ_b is very similar compared with the two-spinon-plus-phonon peak in σ_c,

---

[14]Here we refer to the result for $J(T)$ which has been estimated in [220] from the result obtained in the harmonic approximation. Beside thermal expansion, here also contributions originating from the vibrational variation of the interatomic distance has been considered. However, the decrease of J with increasing temperature is mainly ascribed to the thermal expansion.

but the absolute value of σ_b is an order of magnitude smaller. From the comparison with σ_a measured on a cleaved and on a polished sample (S1b and S6a), we conclude that a surface layer is not responsible for this absorption. A leakage due to a misalignment of the sample is also excluded because for thicknesses larger than $200\,\mu$m the transmittance for $E \parallel c$ is zero from 0.27 up to 0.74 eV (Fig. 5.13). An admixture of n-times zero must be zero again. However, another possibility is that the sample exhibits a small misaligned domain.[15] This is also excluded because the measurements have been performed on two different samples S5a and S6a which have been cut from different parts of the crystal. For comparison $\sigma_b(\omega)$ at 10 K obtained in both measurements is shown in Fig. 5.21. As the case may be, we assume that the ratio, i.e. the effective thickness, of a misaligned domain is unequal in two different samples and therefore the measured σ_b must be different. However, the ratio of both spectra, shown in the bottom panel of Fig. 5.21, is constant in good approximation. The constant shift of $0.05\,(\Omega\text{cm})^{-1}$ of σ_b obtained on sample S6a may be the effect of a non-absorbing surface layer (see Sec. 5.2.2). Altogether we conclude that our results for $\sigma_b(\omega)$ are reliable.

Also in the pseudo-ladder compound CaCu$_2$O$_3$, earlier investigated in our group [43, 48, 223], we observed magnetic contributions to the optical conductivity for all three polarization directions in a comparable energy range. Also this compound exhibits strong anisotropic magnetic exchange couplings [224]. Because the analysis

---

[15]Imagine that the sample exhibits a domain which is differently aligned, e.g. the bulk is aligned perpendicular to c, while a small domain is aligned with the c direction parallel to the b direction of the bulk. Then a small amount of σ_c may admix to the measured spectrum of σ_b.
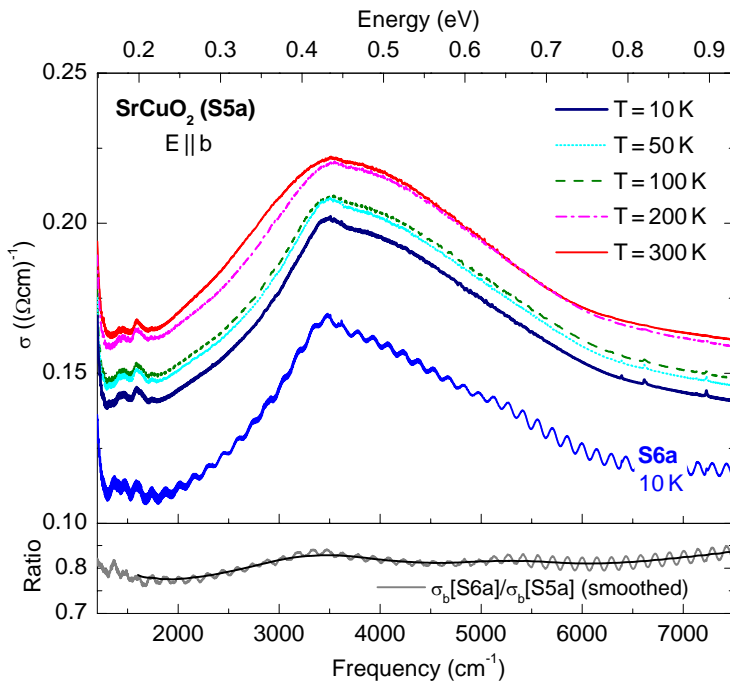
Figure 5.21.:
Temperature dependence of $\sigma_b(\omega)$ (S5a) in the energy range the magnetic absorption. For comparison we show $\sigma_b(\omega)$ obtained in measurement on sample S6a at 10 K. The ratio of the spectra $\sigma_b(\omega)$ is shown in the bottom panel. For the denotation of the samples see Tab. 5.2.

of $\sigma_c(\omega)$ gives evidence for the realization of spin $1/2$ chains in $SrCuO_2$, a magnetic contribution in the perpendicular direction is apparently unexpected. However, for the quasi-1D $S = 1/2$ spin ladder with $J_\parallel / J_\perp$ a contribution to $\sigma_\perp$ has been experimentally observed [106] and subsequently theoretically confirmed [218]. Because the coupling between the double chains in $SrCuO_2$ is proposed to be very small and frustrated (see Sec. 5.2.1), a similar magnetic contribution perpendicular to the chains is highly unexpected.

Alternatively, we consider magnetic contributions to $\sigma(\omega)$ for a system which magnetically is strictly one dimensional. Lorenzana and Sawatzky obtained two contributions to the phonon-induced two-magnon absorption in 2D cuprates, namely the anisotropic and isotropic term [45] (see also Sec. 2.4.3). The anisotropic term is based on the phonon-induced changes in the Madelung potential on neighboring Cu sites and only contributes for polarization parallel to the Cu-O-Cu bonds. The isotropic term arises from the displacement of the intermediate O ion and contributes for polarization parallel to the O displacement. However, the isotropic term is expected to be much smaller than the anisotropic one [113]. In fact, measurements in 2D cuprates with $E \perp$ planes [113] and our data for $E \parallel a$ in $SrCuO_2$ show that the isotropic contribution is negligible. However, both in $SrCuO_2$ and in Ca_2CuO_3 the symmetry on the Cu sites are different. Considering the double-chain structure in $SrCuO_2$ (Fig. 5.5), the O(2)-Cu-O(1) bond parallel to the b-axis does not show inversion symmetry. In the following we sketch an idea how such an asymmetry may give rise to a magnetic contribution in $\sigma_b(\omega)$.

There are two crystallographically different O sites, O(1) and O(2) in $SrCuO_2$ (Fig. 5.5). In particular, there are two effects which give rise to a different charge density on the two sites in the ground state. Both are mainly due to the different number of Cu neighbors. First, O(1) hybridizes with three Cu neighbors, while O(2) hybridizes with one Cu neighbor. Thus one expects more holes on O(1) than on O(2). Second, the Madelung potential $\mathcal{V}$ is different for O(1) and O(2). Within a point charge estimate we find $\mathcal{V}(O(2)) / \mathcal{V}(O(1)) \approx 85\,\%$ (see App. A.7). Again, one expects more holes on the O(1) sites, in agreement with the x-ray absorption data of [196] (see also Sec. 5.2.1).

Without hybridization, the hole occupies the $d_{y^2-z^2}$ orbital on each Cu site in the ground state. All O $2p$ orbitals are filled by electrons. Due to hybridization with the two inequivalent O sites, the Wannier orbital [111, 225, 226] of the ground state shows a finite admixture of y character,

$$| \, 0 \rangle = \alpha_0 \, | \, y^2 - z^2 \rangle + \beta_0 \, | \, y \rangle,$$

in contrast to the symmetric case (sketch in Fig. 5.22(c)). This corresponds to a dipole moment in y direction, $P_0^y = (\langle n_0 \rangle_{O(1)} - \langle n_0 \rangle_{O(2)}) \cdot d_{Cu\text{-}O}$, where $\langle n_0 \rangle_{O(i)}$ denotes the hole density on site O(i) in the ground state and $d_{Cu\text{-}O}$ the Cu-O distance. Now we consider an exchange process, i.e. the virtual hopping of 2 holes between neighboring Cu sites along the chain (c/z) direction. In the virtual intermediate
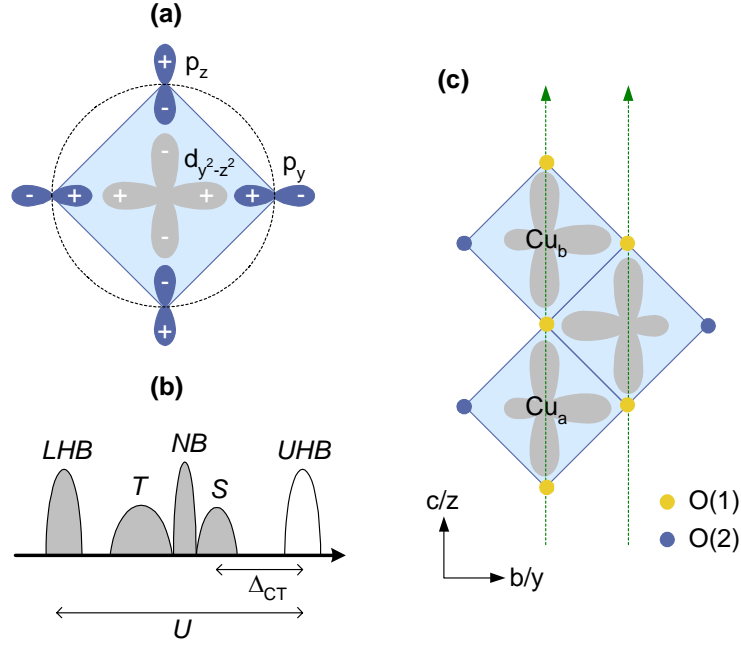
Figure 5.22.: (a) Sketch of the hybridization of the O hole ($2p^5$) and the Cu hole ($3d^9$). The signs $+$ and $-$ represent the phase of the wave functions. (b) Qualitative density of states for a charge-transfer insulator with singlet-triplet splitting. The non-bonding band is denoted by *NB* and the Zhang-Rice (*ZR*) triplet and singlet bands are labeled by *T* and *S*, respectively. (c) In SrCuO$_2$ the different sites O(1) and O(2) unequally hybridize with the central Cu ion, giving rise to a finite admixture of y character into the ground state orbital and the *ZRS*, as sketched.

state, the two holes are centered around the same site. There are a number of different possible states for the 2 holes, the most relevant is the Zhang-Rice singlet (*ZRS*) [225] (Fig. 5.22(a) & (b)). As discussed for the ground state, the inequivalent O sites will give rise to a finite admixture of y character also in case of the *ZRS*,

$$\mid 1 \rangle = \alpha_1 \mid y^2 - z^2 \rangle + \beta_1 \mid y \rangle.$$

Now it is crucial that $\beta_1 \neq \beta_0$, i.e. the dipole moment $P_1^y = (\langle n_1 \rangle_{O(1)} - \langle n_1 \rangle_{O(2)}) \cdot d_{\text{Cu-O}}$ of the excited state is different from P_0^y, the dipole moment of the ground state. Then the virtual exchange of two holes (spins) along the chain (c/z) will change the dipole moment *perpendicular* to the chains (along b/y). More precisely, due to P_i^y the energies $\mathcal{E}_0$ and $\mathcal{E}_1$ of the ground state and of the excited state depend on an electric field E_y applied along the y direction, i.e. $\mathcal{E}_i \mapsto \mathcal{E}_i \pm P_i^y E_y$. In lowest order perturbation theory, the exchange coupling is given by $J \propto t^2/(\mathcal{E}_1 - \mathcal{E}_0)$, where t denotes the effective Cu-Cu hopping. Thus J depends on E_y, to leading order $J = J_0 + q_{\text{eff}} d_{\text{Cu-O}} E_y$, where q_{eff} denotes the effective charge and $d_{\text{Cu-O}}$ is the Cu-O
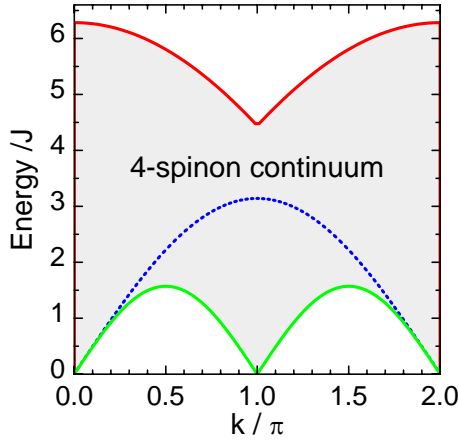
Figure 5.23.:
Four-spinon continuum for a $S = 1/2$ Heisenberg chain. The lower boundary (solid green line) coincides with that of the two-spinon continuum [191] (Eq. 5.2). However, the upper boundary (solid red line) extends above the upper boundary of the two-spinon continuum (dashed blue line). Reproduced from [219].

distance. Altogether, this describes a mechanism for optical absorption of spinons *without* a simultaneously excited phonon (see Sec. 2.4.3).

This mechanism may explain the magnetic contribution observed in σ_b, in agreement with the absence of absorption in σ_a. The energy scale is the same as for the contribution to σ_c. However, up to now there are no predictions for the line shape of σ_b. In the case of σ_c, the line shape has been calculated by integrating over the entire Brillouin zone with a weighting factor given by the phonon [103]. Without a phonon, only magnetic excitations with $k = 0$ contribute. For a homogeneous $S = 1/2$ chain, the two-spinon continuum at $k = 0$ only has a single point at $\omega = 0$. However, one may have to consider the four-spinon contribution (Fig. 5.23). In order to estimate the spectral weight, one has to determine the dipole moments P_0^y and P_1^y of the ground state and the virtual excited state. Corresponding calculations by E. Müller-Hartmann[16] are in progress to clarify the relevance of this mechanism.

$Sr_{0.9}Ca_{0.1}CuO_2$

Our measurements on $Sr_{1-x}Ca_xCuO_2$ have been motivated by recent results from heat transport [49]. In the case of $SrCuO_2$ the thermal conductivity κ is strongly anisotropic with an anomalously enhanced κ parallel to the chains [227]. This excess thermal conductivity has been attributed to the one-dimensional energy transport by spinons [227]. Upon substitution of Sr by iso-valent Ca, the thermal conductivity due to acoustic phonons (κ_{ph}) is effectively suppressed, whereas it is suggested that the magnetic contribution is not strongly affected [49]. To confirm the latter we have investigated the two-spinon-plus-phonon contribution to the optical absorption to determine J_c^{Ca} in $Sr_{0.9}Ca_{0.1}CuO_2$.

The absorption coefficient $\alpha(\omega) = -\ln(T(\omega))/d$ at several temperatures is shown in Fig. 5.24. Similar to $SrCuO_2$ we observe the two-spinon-plus-phonon absorption around 0.4 eV for $E \parallel c$ (bottom panel in Fig. 5.24). The spectrum for $E \parallel a$ is featureless and has a constant value in the considered energy range (top panel

---

[16]Institute of Theoretical Physics, University of Cologne, Germany
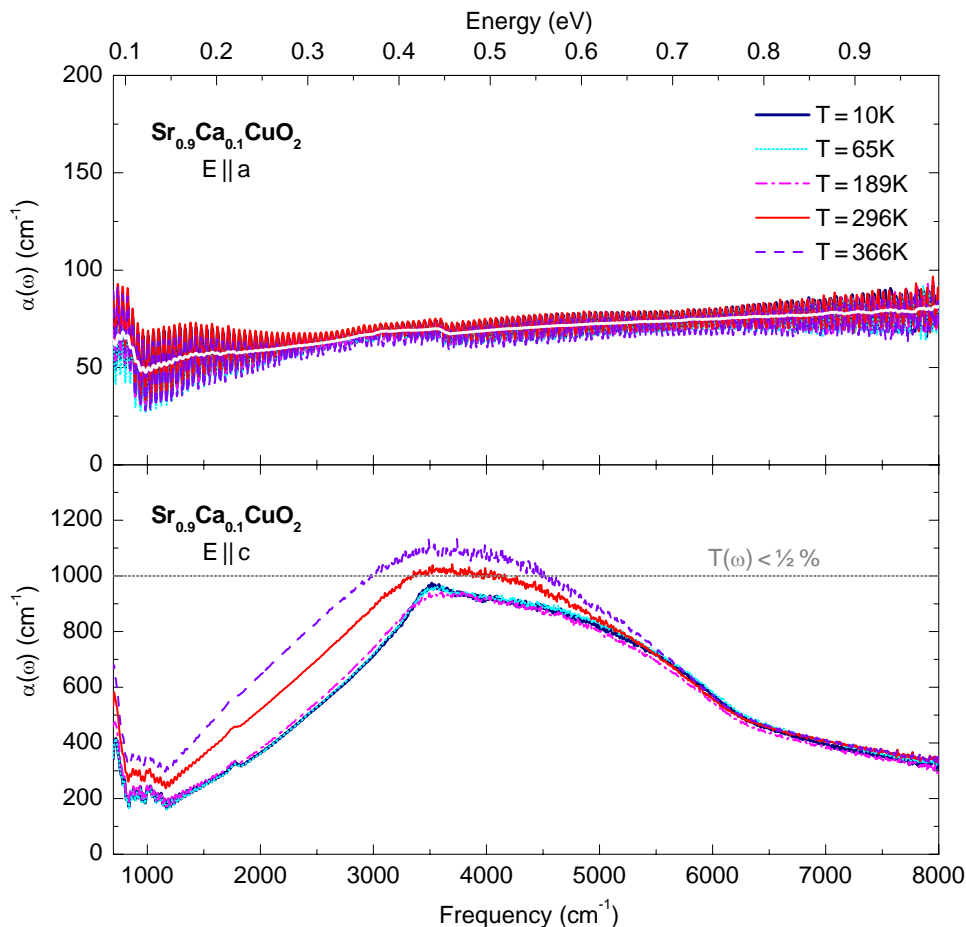
Figure 5.24.: Temperature dependence of $\alpha(\omega) \approx -\ln(T(\omega))/d$ of $Sr_{0.9}Ca_{0.1}CuO_2$ for $E \parallel a$ (top panel) and $E \parallel c$ (bottom panel). Because of the small sample thickness, Fabry-Perot fringes are observed which are pronounced for $E \parallel a$. Using a Fourier filter we exemplarily smoothed the spectrum at $T = 10\,K$ (white line). The gray dotted line in the bottom panel delimitates $\alpha(\omega)$ for which the transmittance $T(\omega)$ is lower than $0.5\,\%$.

in Fig. 5.24). We have applied the same analysis to the low-temperature data of $Sr_{0.9}Ca_{0.1}CuO_2$ as for $SrCuO_2$. The results for both compounds at $10\,K$ and the theoretically predicted line shape at $T = 0$ [103] are shown in Fig. 5.25.

It is reasonable to assume that the energy of the contributing phonon is very similar to pure $SrCuO_2$, i.e. ω_{ph} changes by less than $1\,meV$ with Ca substitution. From the position of the cusp $\omega_1 = (437 \pm 8)\,meV$ we thus obtain $J_c^{Ca} = (229 \pm 6)\,meV$. Within the error bars, this is identical to $SrCuO_2$. The larger error bars are due to the rounding of the cusp. Also the cut-off is less pronounced in $Sr_{0.9}Ca_{0.1}CuO_2$, but our estimate $\omega_2 = (791 \pm 16)\,meV$ supports that J_c^{Ca} is the same as for $SrCuO_2$. Because the thickness of the $SrCuO_2$ and $Sr_{0.9}Ca_{0.1}CuO_2$ sample is nearly identical
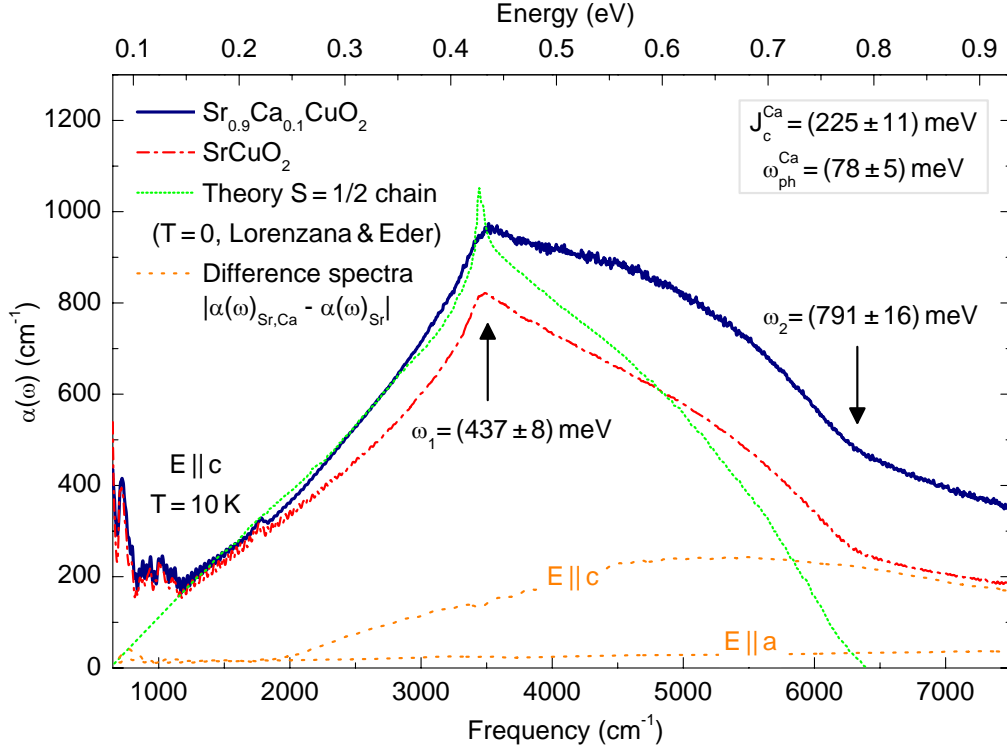
Figure 5.25.: Comparison of $\alpha(\omega)$ of $Sr_{0.9}Ca_{0.1}CuO_2$ ($d = 52\,\mu m$; solid line) with $\alpha(\omega)$ of $SrCuO_2$ ($d = 51\,\mu m$; dash-dotted line) and with the theoretically predicted line shape for a spin $1/2$ chain (dotted line) calculated by Lorenzana and Eder [103].

((SC1 & S1b, see Tab. 5.2)), $\alpha(\omega)$ for both compounds is comparable, except from a (nearly constant) change due to a possible difference in reflectance. In fact, in the multi-phonon region and at the onset of the two-spinon-plus-phonon peak the spectra of both compounds coincide almost perfectly. This is clearly seen from the difference spectra, also shown in Fig. 5.25. Deviations primarily occur above $0.25\,eV$ and become larger with increasing frequency. While the spectra for $E \parallel a$ deviate less than $40\,cm^{-1}$ from each other, those for $E \parallel c$ show a deviation of $240\,cm^{-1}$ in the maximum. Altogether the Ca-substituted sample shows enhanced spectral weight for $E \parallel c$ in the region of the two-spinon-plus-phonon peak and above the two-spinon-cut-off. Both observations are not clear until now. If the enhanced spectral weight can be unambiguously assigned to the magnetic contribution, this additional weight may be a sign of an enhanced contribution of multi-spinon absorption. However, for a final conclusion further experimental research is required. In summary, our data show that the value of J is not affected upon Ca-substitution of $10\,\%$. The change of the line shape suggests that the character of the excitations is somewhat different.

5.3. The 5-Leg Spin Ladders in $La_8Cu_7O_{19}$

5.3.1. Introduction

The successful preparation of large single crystals of the five-leg spin ladder compound $La_8Cu_7O_{19}$ has been reported for the first time in 2001 [228]. Up to now, there are just a few reports on the chemical and physical properties of this material.

The compound $La_8Cu_7O_{19}$ crystallizes in a monoclinic crystal system with space group $C2/c$ (No. 15) [228, 229]. The lattice constants are summarized in Tab. 5.4. Four crystallographically distinct Cu^{2+} ions are found within an unit cell. The $Cu(1)$ and $Cu(2)$ ions are coordinated by oxygen ions forming strongly Jahn-Teller distorted octahedra [229]. The $Cu(3)$ ions are surrounded by oxygen tetrahedra flattened to nearly planar geometry (see Fig. 5.26). The $Cu(1)$ and $Cu(2)$ octahedra are corner-sharing connected forming ribbons which are three octahedra wide. The ribbons are terminated by $Cu(3)$ edge-sharing double tetrahedra on either side. Subsequent Cu-O ribbons are bridged by flattened $Cu(4)$ tetrahedra pairs along the [1 0 0] direction.
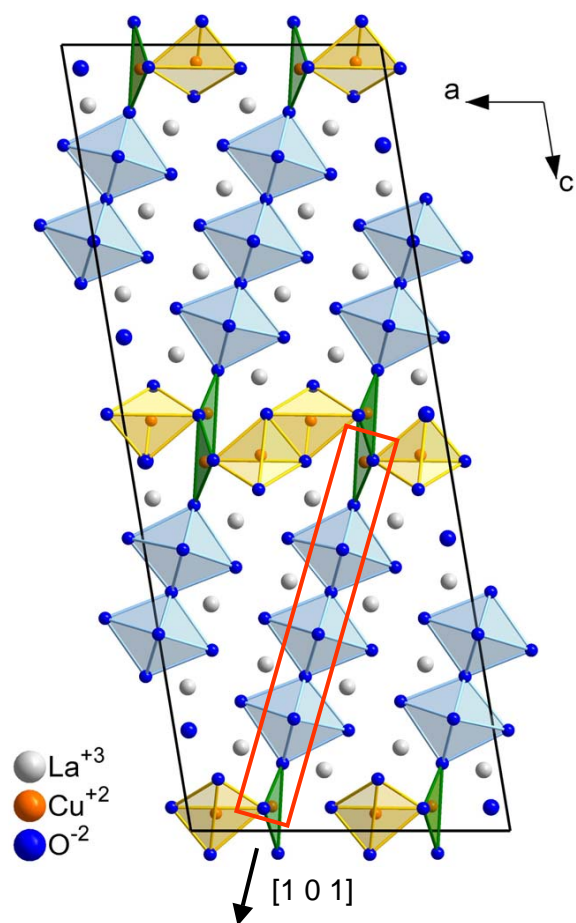
Figure 5.26.:
Crystal structure of $La_8Cu_7O_{19}$. The figure shows the monoclinic unit cell ($C2/c$) with the unique b axis being the line of sight ($\beta \sim 99°$). Four crystallographically distinct Cu^{2+} ions are found within one unit cell [228, 229]. While $Cu(1)$ and $Cu(2)$ ions are coordinated by oxygen ions forming octahedra (light blue), the $Cu(3)$ ions have a tetrahedral environment flattened to nearly planar geometry (green polyhedrons). Finally, edge-sharing $(Cu(4))_2O_6$ tetrahedra pairs (yellow) bridge adjacent $Cu(1,2,3)$-O planes along the a direction. The red box marks the five-leg ladder substructure which is shown in top view in Fig. 5.27.

129

Table 5.4.: Lattice constants of $La_8Cu_7O_{19}$.

	Space group	$a(\text{Å})$	$b(\text{Å})$	$c(\text{Å})$	$\beta(°)$	Ref.
T = 295 K	$C2/c$	13.8297	3.7580	35.5939	99.331	[230]
T = 295 K	$C2/c$	13.8310(4)	3.75827(9)	35.5917(8)	99.332(2)	[229]
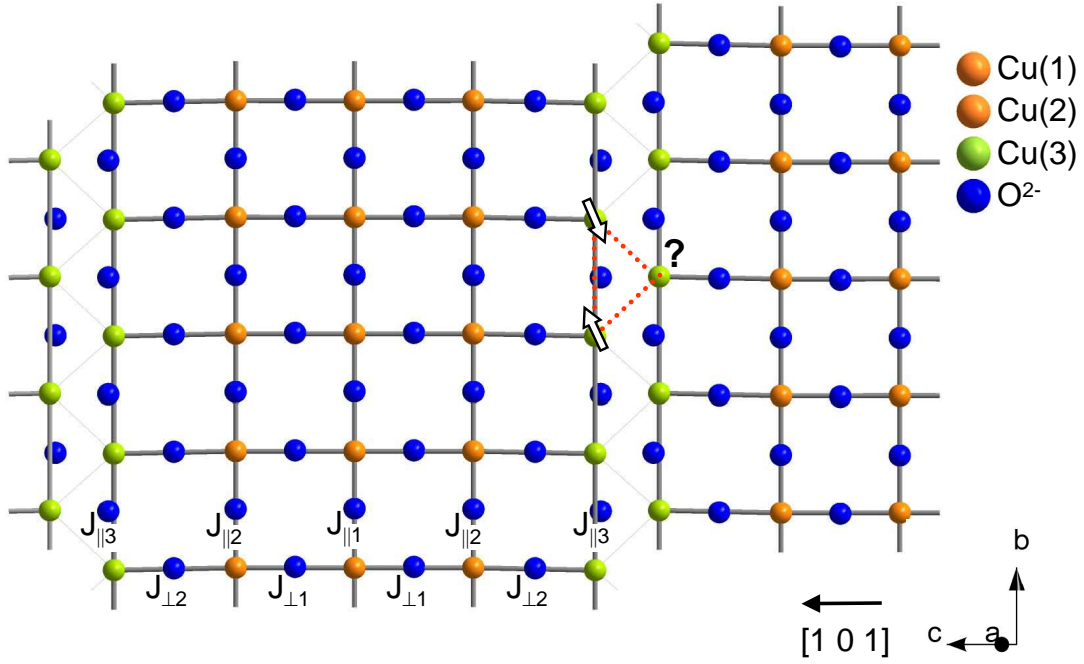
Figure 5.27.: Five-leg ladders in $La_8Cu_7O_{19}$.

Table 5.5.: Classification of the superexchange constants J_i in the 5-leg ladder substructure of $La_8Cu_7O_{19}$ on the basis of the Cu-O-Cu bond angle α and the bond length $d_{Cu-O-Cu}$ [229]. Note that for $\|1$ and $\|2$ the $d_{Cu-O-Cu}$ distance is equal, but the d_{Cu-O} distances are different.

	$\alpha(°)$	$d_{Cu-O-Cu}$ (Å)
$J_{\|1}$	180	3.76
$J_{\|2}$	180	3.76
$J_{\|3}$	158	3.83
$J_{\perp 1}$	177	3.82
$J_{\perp 2}$	179	3.92

At least at high energies/temperatures the Cu(1,2,3)-O substructure (red box in Fig. 5.26) can be understood as a realization of isolated five-leg spin ladders with legs parallel to the b direction and rungs along [1 0 1]. A top view is shown in Fig. 5.27. Considering only the exchange interactions between nearest-neighbor Cu ions, five different coupling constants $J_{\|1}$, $J_{\|2}$, $J_{\|3}$, $J_{\perp 1}$, and $J_{\perp 2}$ are expected due to the different bond angles and bond lengths [229] (see Fig. 5.27 and Tab. 5.5). According to the Goodenough-Kanamori-Anderson (GKA) rules [92, 130, 131], all of the above mentioned J_i of the 5-leg ladder substructure are expected to be antiferromagnetic ($J_i > 0$). We suggest $J_{\|1} \approx J_{\|2} > J_{\|3}$ and $J_{\perp 1} \approx J_{\perp 2}$.

5.3.2. Experimental Details

Samples of $La_8Cu_7O_{19}$

Samples of $La_8Cu_7O_{19}$ have been grown by the traveling-solvent floating zone method by M. Reuther [230].[17] The purity, stoichiometry and single-phase structure of the crystals was checked by x-ray diffraction and EDAX analysis. The obtained lattice parameters are in good agreement with previous results [229] (Tab. 5.4). Typical crystal dimensions are a few mm along all three crystallographic axes. Measurements of the susceptibility show an anisotropy for the magnetic field being aligned parallel to the b axis and perpendicular to b. The temperature dependence shows a maximum at 175 K for $H \parallel b$ and at 185 K for $H \perp b$, respectively. A Néel transition was found at $T_N = 103$ K, in agreement with previous results from neutron scattering [231].

For our measurements of the transmittance, a sample with a thickness of $(200 \pm 4)\,\mu$m has been prepared. Opposite surfaces were polished to high gloss with the standard procedure (Sec. 3.2). The orientation of the sample was ascertained with the back-reflection Laue diffraction method. The Laue picture for the x-ray beam perpendicular to the considered crystal plane is shown in Fig. 5.28. A mirror plane is clearly observed along the diagonal direction, from the upper left to the lower right corner of the picture. Because there is only one mirror plane perpendicular to b in space group $C2/c$, we conclude that the b direction must lie in the chosen plane and is perpendicular to the mirror plane. For the second in-plane direction it is difficult to distinguish between two possible solutions. This is demonstrated by the two simulations shown on the right hand side in Fig. 5.28.[18] The first possibility for the assignment of the central spot is the (1 0 0) reflex. Then the second in-plane axis is c, i.e. the [0 0 1] direction. Alternatively, the central spot is the (1 0 1) reflex. Then the assignment for the in-plane direction perpendicular to b is approximately the [23 0 1] direction.

---

[17]Institute of Physics II, University of Cologne, Germany

[18]The simulations have been performed using the 'OrientExpress V3.3' software by J. Laugier and B. Bochu (Laboratoire des Materiaux et du Génie Physique de l'Ecole Supérieure de Physique de Grenoble, France).
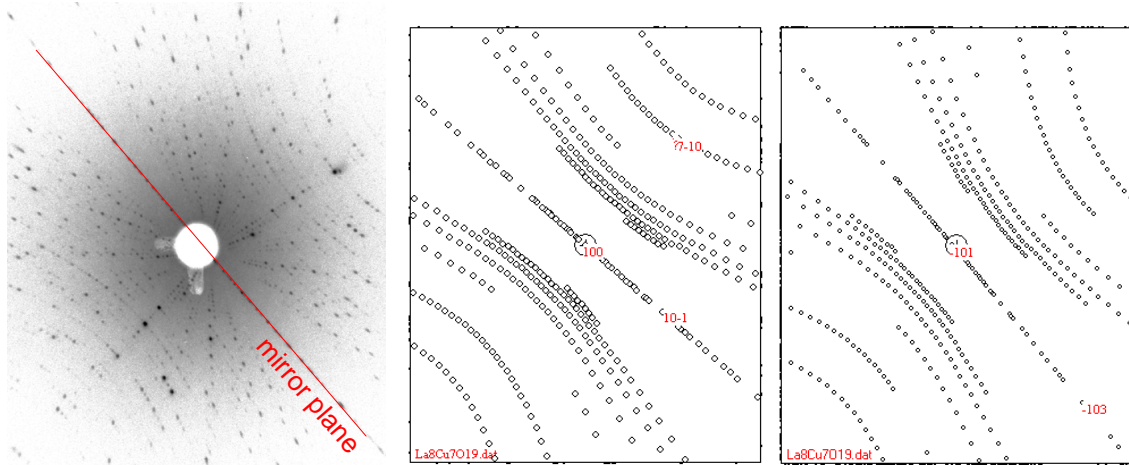
Figure 5.28.: Laue picture of the $La_8Cu_7O_{19}$ sample (left) and the simulations of two possible solutions (for details see text). Note that the simulations are shown with respect to the reciprocal axis, i.e. the reciprocal direction [1 0 0]* and [1 0 1]* are parallel to the line of sight, respectively. In the text we always refer to directions in direct space.

Transmittance of $La_8Cu_7O_{19}$

The mid-infrared transmittance of $La_8Cu_7O_{19}$ for $E \parallel b$ and $E \perp b$ in the temperature range from $10\,K$ to $300\,K$ is shown in Fig. 5.29(a). The measurement has been performed using the globar, the BaF_2 polarizer, the KBr beam splitter, and the MCT detector (see Chap. 3). For both polarization directions the transmittance is at most $50\,\%$ below $0.2\,eV$. The small sharp absorption features in this energy range are ascribed to multi-phonon absorption in comparison with other cuprates. In the range 0.2 - $0.7\,eV$ the transmittance is strongly suppressed for both polarizations, reaching values below $1\,\%$. Overall the transmittance shows a pronounced polarization dependence, in particular at low temperatures, where the spectra show a more pronounced fine structure. The data for $E \parallel b$ directly reflects ε_{yy}, since the b axis is unique in monoclinic $La_8Cu_7O_{19}$. However, we have to keep in mind that the $\hat{\varepsilon}$ tensor of a monoclinic system with monoclinic angle $\beta \approx 99°$ has finite off-diagonal entries $\varepsilon_{xz} = \varepsilon_{zx}$ [57] (see also Sec. 2.1.1). Because of the low symmetry, any direction of the dipole moments within the monoclinic ac plane is possible. To determine all entries of the sub-tensor $\hat{\varepsilon}_{ac}$, measurements of at least three polarization directions in the ac plane are required [56]. This means that our measurement with $E \perp b$ is not sufficient to specify the optical conductivity for $E \parallel a$ and c.
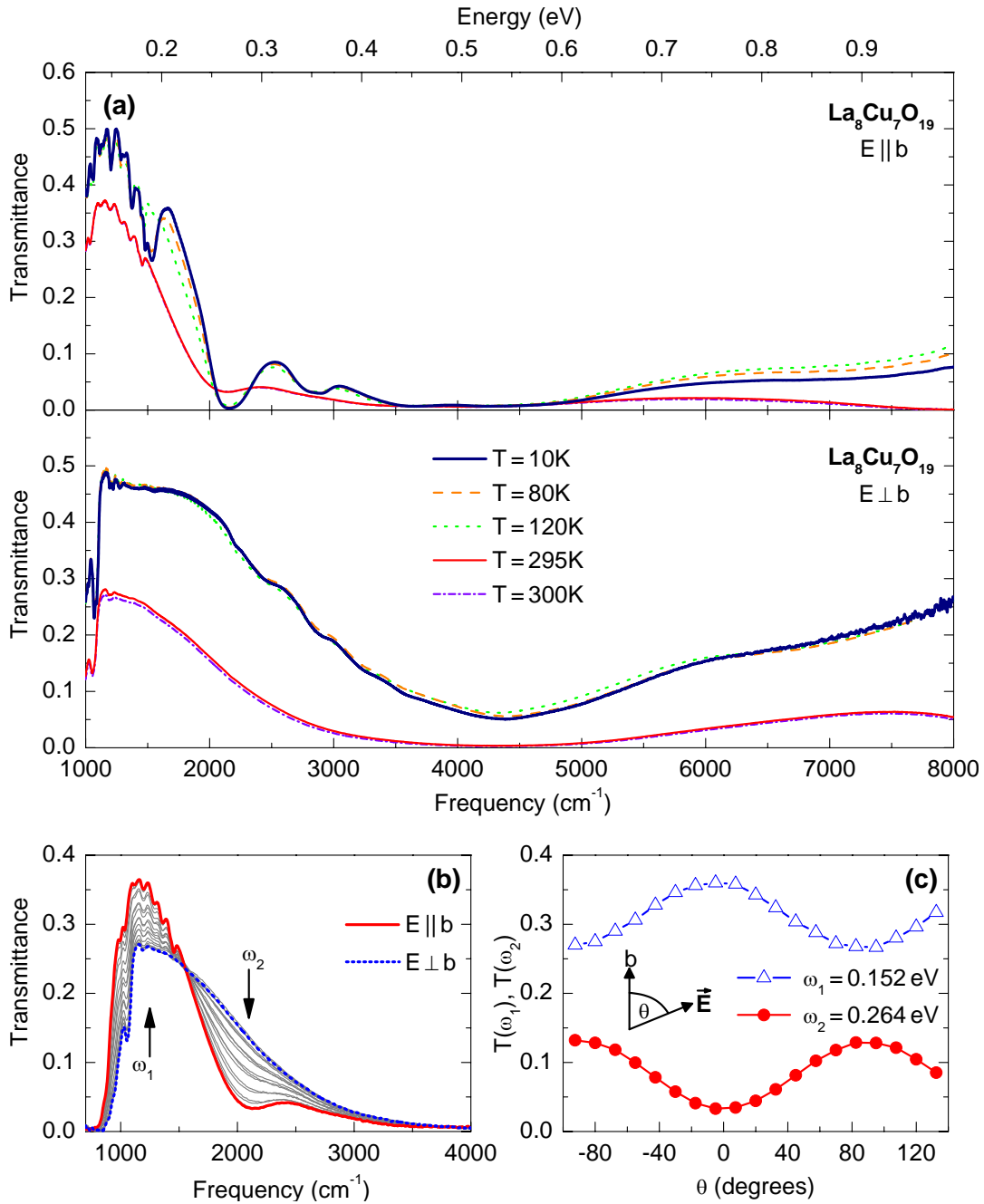
Figure 5.29.: (a) Temperature dependence of the mid-infrared transmittance of $La_8Cu_7O_{19}$ for polarization $E \parallel b$ and $E \perp b$. (b) Mid-infrared transmittance of $La_8Cu_7O_{19}$ for several polarization directions, obtained by rotating the polarizer a total of 180 degrees. (c) Transmittance at two selected frequencies ω_1 and ω_2 as a function of the polarization angle θ. As sketched in the inset, $\theta = 0$ corresponds to $E \parallel b$ (specified with the Laue camera). A second maximum (minimum) of transmittance is observed for polarization perpendicular to b, i.e. for $\theta = \pm 90°$.

5.3.3. Results: Magnetic Excitations in La₈Cu₇O₁₉

The absorption coefficient $\alpha(\omega) = -\ln(T)/d$ of $La_8Cu_7O_{19}$ for $E \parallel b$ ($\alpha_b(\omega)$) and $E \perp b$ ($\alpha_{\perp b}(\omega)$) is shown in Fig. 5.30. In the energy range from 0.2 to 0.7 eV broad absorption features are observed for both polarizations which are assigned to magnetic absorption of the five-leg ladders due to a comparison with spectra of other low-dimensional cuprates [43, 101, 106].

First we focus on $E \parallel b$ which is easily identified with the leg polarization (see Fig. 5.26). Since the dielectric response ε_b is a scalar, no admixture of contributions from other directions is expected for this polarization. While at room temperature a broad absorption feature is observed, the spectrum at 10 K shows a pronounced fine
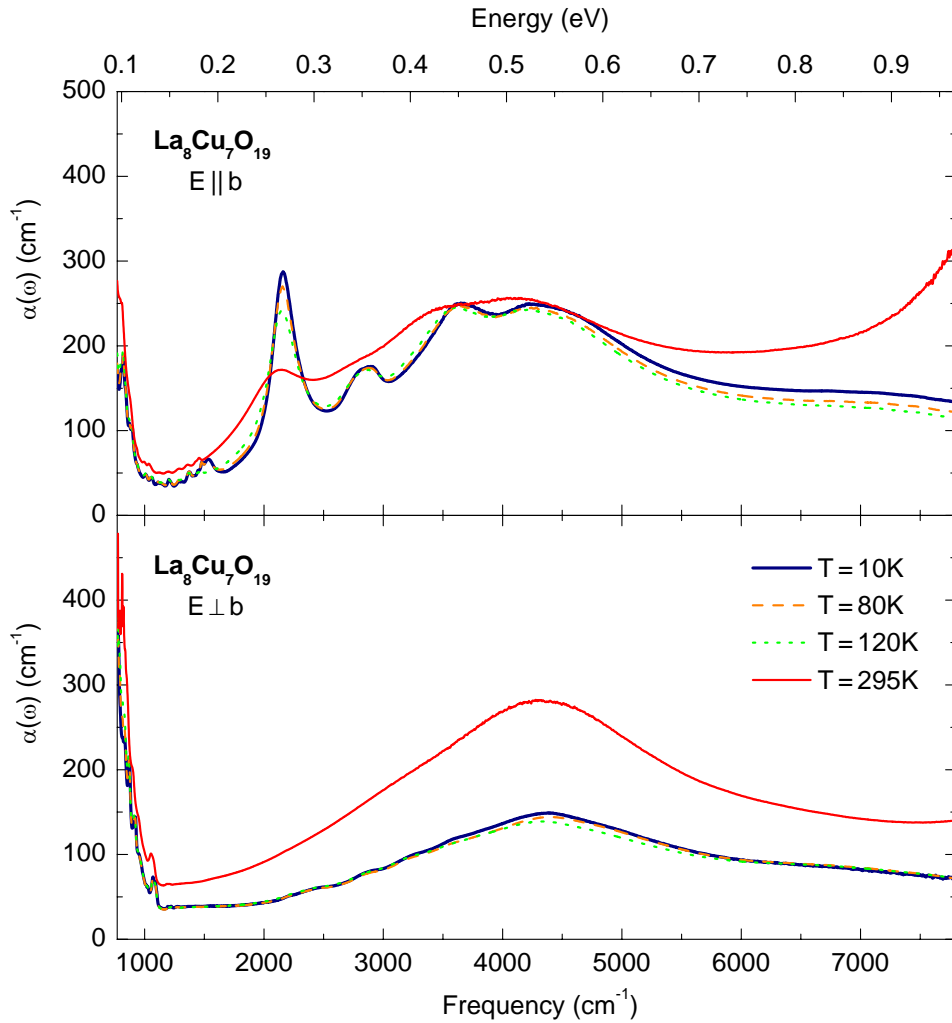
Figure 5.30.: Temperature dependence of the optical absorption coefficient $\alpha(\omega) = -\ln(T)/d$ of $La_8Cu_7O_{19}$ for polarization $E \parallel b$ and $E \perp b$, respectively.

structure. We observe up to five peaks, at 0.19, 0.27, 0.35, 0.45, and 0.55 eV. The small peak at 0.19 eV may have to be attributed to multi-phonon absorption, but its strong temperature dependence suggests a possible magnetic origin. The latter four peaks are assigned to magnetic peaks due to their energy position and due to the comparison with other low-dimensional cuprates. In particular the comparison with the magnetic contribution to σ_{leg} of the 2-leg ladders in La$_{5.2}$Ca$_{8.8}$Cu$_{24}$O$_{41}$ (LCCO) shows an intriguing resemblance (top panel in Fig. 5.31). For LCCO the magnetic contribution to the optical conductivity has been investigated in detail [106, 109, 115, 218]. By a comparison between experiment and theory two sharp peaks around 0.25 and 0.35 eV are unambiguously assigned to a bound state of two triplets [106]. In particular a detailed analysis has shown that these two peaks stem from two local extremal values of the $S = 0$ bound-state dispersion (Fig.5.31(a) and inset). The spectral weight at higher energies has been attributed to the two-triplet continuum. From a comparison with results of the density-matrix renormalization group (DMRG) [109] the following set of exchange couplings was determined for LCCO: $J_{\parallel}/J_{\perp} = 1.3$, $J_{\perp} = 124$ meV, and $J_{\text{cyc}}/J_{\perp} = 0.2$. In particular the importance of the four-spin cyclic exchange J_{cyc} for a quantitative description of the data has been demonstrated [109]. The DMRG results for the spectrum in leg and rung polarization are also shown in Fig. 5.31.

The spectrum for $E \perp b$ in the same energy range shows a broad bump around 0.55 eV which is assigned likewise to a magnetic contribution. In particular we claim that this bump reflects the magnetic contribution in rung polarization. The arguments are as follows. As mentioned above, to determine all entries of $\hat{\varepsilon}_{ac}$ at least measurements of three polarization directions in the ac plane are required. To determine the magnetic contribution in rung polarization this is not necessary. Because in the energy range of the magnetic excitation no other absorption features are expected (see e.g. σ_a for SrCuO$_2$ in Sec. 5.2.3), the dielectric response in this energy range is fully determined by the magnetic excitations of the two-dimensional Cu$_5$O$_9$ ladder subsystem. The dipole moments for the phonon-assisted magnetic excitations are parallel to the legs and rungs, respectively. No magnetic contribution to σ perpendicular to the Cu$_5$O$_9$ subsystem is expected, i.e. there is no dipole moment perpendicular to the ladders. The dipole moment from the exchange along the legs is aligned along [0 1 0], while that of the rungs is parallel to [1 0 1]. The polarization $E \parallel b$ is easily identified with $E \parallel$ legs, as mentioned above. For the perpendicular direction we have to consider the two possibilities (i) $E \parallel [0\ 0\ 1]$ and (ii) $E \parallel [23\ 0\ 1]$ (see Sec. 5.3.2). Therefore we claim that we have measured the projection of the dipole moment along [1 0 1] to [0 0 1] or [23 0 1], respectively. However, this just affects the absolute value, not the line shape of the measured magnetic contribution. Therefore we claim that the magnetic absorption for $E \parallel$ rungs is probed by the measurement with $E \perp b$ except from a possibly smaller absolute value. In fact, also for $E \perp b$ we find an intriguing resemblance with the spectrum of LCCO for $E \parallel$ rungs (bottom panel in Fig. 5.31).

The resemblance of the optical spectra of La$_8$Cu$_7$O$_{19}$ and LCCO is surprisingly.
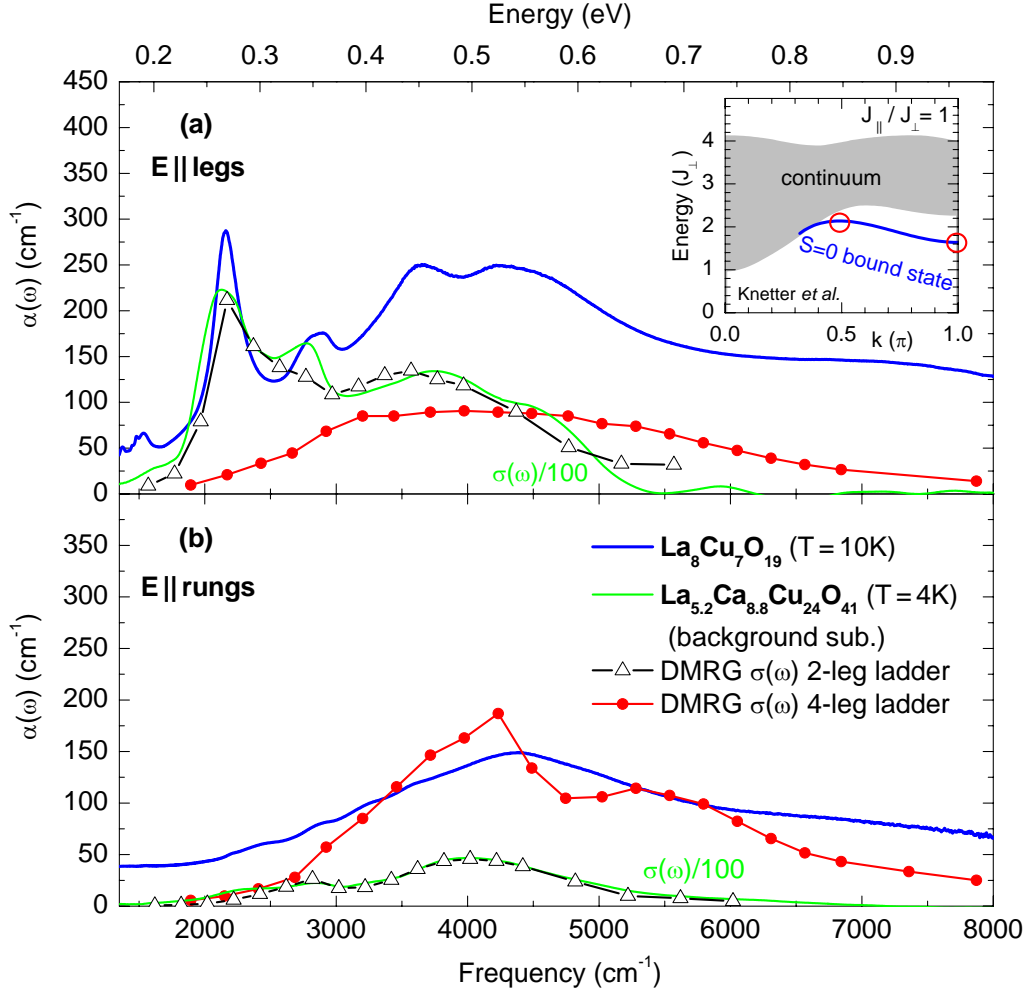
Figure 5.31.: Comparison of the magnetic contribution of $La_8Cu_7O_{19}$ with the two-triplet-plus-phonon contribution to $\sigma(\omega)$ of the two-leg ladder compound $La_{5.2}Ca_{8.8}Cu_{24}O_{41}$ (LCCO) for (a) $E \parallel$ legs and (b) $E \parallel$ rungs. Additionally the DMRG results for a 2-leg ladder with $J_\parallel = 161\,\text{meV}$, $J_\parallel/J_\perp = 1.3$, and $J_{cyc}/J_\perp = 0.2$ and for a 4-leg ladder with $J_\parallel = 161\,\text{meV}$, $J_\parallel/J_\perp = 1$, and $J_{cyc} = 0$ are plotted [109, 232]. For both DMRG results $\omega_{ph} = 74\,\text{meV}$ is assumed for the involved phonon. The inset shows the two-triplet $\Delta S = 0$ excitation spectrum of a 2-leg ladder with $J_\parallel/J_\perp = 1$ [192]. The red circles denote the two local extremal values of the bound-state dispersion from which the two peaks at 0.27 eV and 0.34 eV in LCCO stem [106]. In should be noted that the absolute values of the theoretical data are arbitrarily scaled and $\sigma(\omega)$ of LCCO have been divided by 100.

Considering the low-energy properties, the excitation spectra of $S = 1/2$ two-leg and five-leg ladders are very different. While even-leg ladders have a spin gap and show short range spin correlations, odd-leg ladders have no gap and power-law correlations

[233]. At least at low temperatures (energies) and small ratios of $J_\parallel/J_\perp$ three- and five-leg ladders can be mapped to single nearest-neighbor chains [234, 235]. However, in our optical experiment we probe excitations at high energies, which may contribute from the entire Brillouin zone due to the momentum supply of the involved phonon. In this regard theoretical predictions for the dispersion of magnetic excitations with $\Delta S = 0$ in a 5-leg ladder are highly desirable. For spin ladders with an odd number of legs and *periodic* boundary conditions in the rung direction gapped spinon-like excitations have been proposed [236].[19] In particular the possibility of bound states of spinon-like excitations near $k = \pi/2$ has been suggested [236]. Such bound states may be responsible for the observed fine structure in $\alpha_b(\omega)$.

For the four-leg ladder clear theoretical predictions concerning the line shape of the magnetic contribution to $\sigma(\omega)$ have been derived by T. Nunner using the DMRG method [232]. The result for $J_\parallel = 161\,\mathrm{meV}$, $J_\parallel/J_\perp = 1$, and $J_{cyc} = 0$ for $E \parallel$ legs and $E \parallel$ rungs is also shown in Fig. 5.31. In comparison with the 2-leg ladder the high-energy weight is enhanced and shifted to higher frequencies in the four-leg ladder, especially for the rung polarization. The bound state resonance, pronounced in leg polarization for the 2-leg ladder, is less developed in the four-leg ladder. However, the agreement of the predicted line shape with our data of five-leg ladders in La$_8$Cu$_7$O$_{19}$ is rather poor for both polarizations. As mentioned above the agreement with the spectra of the two-leg ladder is much better. Without further theoretical progress a complete understanding of the line shape of the magnetic contribution in La$_8$Cu$_7$O$_{19}$ is far from reach. A detailed assignment of the fine structure requires the knowledge of the $\Delta S = 0$ excitations spectrum, i.e. not only the dispersion of the elementary excitations but also of the interactions. The description of the line shape is even more demanding, when considering also contributions from a direct absorption, as discussed for SrCuO$_2$ in Sec. 5.2.3. In the five-leg ladder, inversion symmetry is only present on the central leg. Thus one may expect direct magnetic contributions for rung polarization, although with a considerably smaller spectral weight. Finally, the phonon-assisted contribution requires a detailed analysis of the form factor.

In summary we give an experimental view on the crossover from one to two dimensions for $S = 1/2$ systems at high energies. For this purpose we show the results from optical spectroscopy on several low-dimensional systems in Fig. 5.32. Here we have arranged the optical conductivity of the chain compound SrCuO$_2$ (Sec. 5.2), the two-leg ladder compound LCCO [106], the five-leg ladders in La$_8$Cu$_7$O$_{19}$, and the 2D square lattice in Ba$_2$Cu$_3$O$_4$Cl$_2$ [48].[20] As discussed in Sec. 5.2 the spectrum of the spin chain shows a broad peak assigned with a two-spinon-plus-phonon contribution, i.e. a contribution due to a continuum of incoherent excitations. Also the spectrum of the 2D square lattice shows a broad feature around $0.5\,\mathrm{eV}$ reflecting a continuum of two-magnon excitations. For both compounds a resonance, i.e. an

---

[19]For periodic boundary conditions the odd-leg ladders are frustrated in the rung direction and show different properties, i.e. a spin gap and an exponential decay of the spin correlations [236].

[20]The structure of Ba$_2$Cu$_3$O$_4$Cl$_2$ shows 2D Cu$_3$O$_4$ planes. However, results from optical spectroscopy suggests that Ba$_2$Cu$_3$O$_4$Cl$_2$ is a typical example of a 2D square lattice [48].
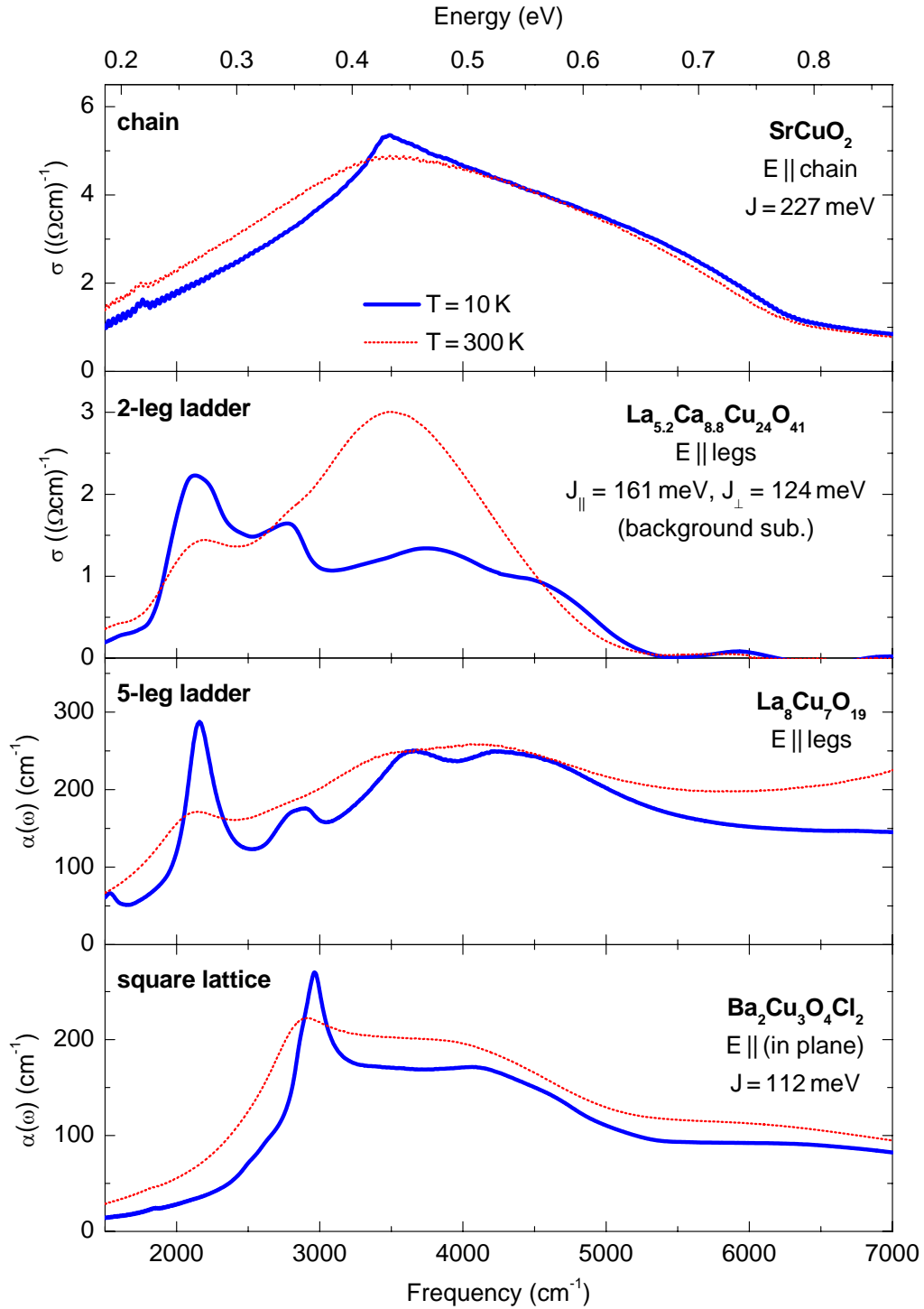
Figure 5.32.: Comparison of phonon-assisted magnetic absorption in different low-dimensional $S = 1/2$ systems: the chain compound $SrCuO_2$, the 2-leg ladder compound LCCO [106], the 5-leg ladder compound $La_8Cu_7O_{19}$, and the 2D square lattice $Ba_2Cu_3O_4Cl_2$ [48] at 10 K and 300 K, respectively.

almost bound state is observed, namely the cusp at $\sim 0.42\,\text{eV}$ in $SrCuO_2$ and the sharp peak at $0.37\,\text{eV}$ in $Ba_2Cu_3O_4Cl_2$. The two-leg ladder shows real bound states of two triplets below the high-energy continuum. Our data of the five-leg ladder strongly suggest the existence of real bound states also in this system. Furthermore, the comparison suggests that the magnetic excitations in the high-energy continua are rather similar and develop smoothly from 1D to 2D.

6. Conclusion

In this thesis the low-energy excitations of undoped Mott insulators have been investigated by means of optical spectroscopy. We have studied the orbital excitations in orbitally ordered vanadates $R\mathrm{VO}_3$ with $R = \mathrm{Y}$, Ho, and Ce, and the magnetic excitations of the low-dimensional quantum magnets $(\mathrm{Sr,Ca})\mathrm{CuO}_2$ and $\mathrm{La}_8\mathrm{Cu}_7\mathrm{O}_{10}$. Our data revealed new and unexpected absorption features for all three compounds which are clearly related to the orbital and magnetic degrees of freedom. In particular, the following results have been obtained:

Orbital Excitations in Orbitally Ordered Vanadates
To study the orbital excitations we have determined the optical conductivity $\sigma(\omega)$ of $R\mathrm{VO}_3$ with $R = \mathrm{Y}$, Ho, and Ce as a function of temperature T and polarization of the incident light. For this purpose we have measured the transmittance and reflectance using a Fourier transform spectrometer. We considered the mid- and near-infrared range, i.e. the energy range $0.12\text{-}1.60\,\mathrm{eV}$. While the reflectance in this energy range, well above phonon absorption and below electronic excitations is nearly constant and featureless, the transmittance of thin samples is very sensitive to small absorption features and shows a pronounced temperature and polarization dependence. Likewise we have considered the compounds VOCl and $\mathrm{Dy}(\mathrm{Sc,V})\mathrm{O}_3$ which ought to demonstrate the local crystal-field transitions of V^{3+} ($3d^2$) in a predominantly octahedral environment. From this comparison we have shown that the absorption features around 0.2 and $1.1\,\mathrm{eV}$ in $R\mathrm{VO}_3$ in principle can be explained in terms of local crystal-field excitations of the V^{3+} ions.

Our main experimental result is the observation of two absorption features in $R\mathrm{VO}_3$ at $0.55\,\mathrm{eV}$ for $E \parallel a$ and $0.4\,\mathrm{eV}$ for $E \parallel c$. As follows from the comparison with the reference materials and the results of a cluster calculation, the energies of both peaks are hard to reconcile with a local crystal-field scenario. The same holds true for the strong polarization and temperature dependence of both features, which is entirely unexpected for phonon-assisted crystal-field excitations. We suggest that the feature at $0.4\,\mathrm{eV}$ for $E \parallel c$ gives evidence for collective orbital excitations, i.e. orbital excitations that are based on the orbital exchange coupling between neighboring V sites, in contrast to the single-site physics of local crystal-field excitations. The absorption feature at $0.4\,\mathrm{eV}$ is solely observed in the monoclinic phase with G-type orbital and C-type spin order. We have demonstrated that the exchange of two neighboring orbitals is directly infrared active for $E \parallel c$ in this phase. In particular, the spectral weight has been estimated to be of an adequate size. In terms of k space, the optical conductivity is restricted to the observation of two-orbiton

absorption processes with $k_{\text{total}} = k_1 + k_2 \approx 0$. This means that the two orbitons have opposite momenta $k_1 = \text{-}k_2$ with arbitrary k_1. Thus the two-orbiton continuum is probed throughout the entire Brillouin zone.

The feature at $0.55\,\text{eV}$ observed for $E \,\|\, a$ is less clear up to now. In particular the pronounced anisotropy within the ab plane puts severe constraints on the interpretation in terms of a two-orbiton excitation. Here theoretical efforts are highly desirable.

Altogether our results strongly suggest that in $R\text{VO}_3$ with $R = \text{Y}$, Ho, and Ce the orbital exchange interactions play a decisive role.

Magnetic Excitations of the Spin 1/2 Double Chain (Sr,Ca)CuO$_2$

To study the magnetic excitations of a 1D $S = 1/2$ system we determined the optical conductivity $\sigma(\omega)$ of $(\text{Sr,Ca})\text{CuO}_2$ from measurements of the transmittance and reflectance for polarization parallel to all three orthorhombic axes. We have considered a wide energy range from $12\,\text{meV}$ up to $2\,\text{eV}$. Up to $100\,\text{meV}$ excitations of optical phonons were observed. We have demonstrated that the energy, polarization dependence, and number of modes are in good agreement with group-theoretical predictions and previous experimental results. Our high-energy data enabled the very precise determination of the polarization and temperature dependence of the onset of electronic excitations across the charge-transfer gap in SrCuO_2. In the intermediate energy range we have identified two absorption features around $0.4\,\text{eV}$ for $E \,\|\, c$ (chain direction) and $E \,\|\, b$ (inter-chain direction) as magnetic contributions to $\sigma(\omega)$.

Our analysis of the two-spinon-plus-phonon contribution to $\sigma(\omega)$ for $E \,\|$ chains has shown that SrCuO_2 is a good realization of a 1D $S = 1/2$ chain. The excitations are well described by spinons, even at low temperatures. From a comparison with the theoretically predicted line shape we obtained $J_c = (227 \pm 4)\,\text{meV}$ for the nearest-neighbor exchange coupling between spins along the chain, in good agreement with results from inelastic neutron scattering. For the involved phonon we obtained $\omega_{ph} = (78 \pm 5)\,\text{meV}$. Furthermore we ascertained that the theoretically predicted two-spinon-plus-phonon contribution describes roughly $74\text{-}97\,\%$ of the observed spectral weight. We suggest that the remaining weight has to be ascribed to multi-spinon excitations, presumably four-spinon contributions. From the analysis of the temperature dependence we derived a temperature dependent value of the exchange coupling, which is attributed to changes in the Cu-Cu distance due to the thermal expansion of the lattice.

The optical conductivity for polarization perpendicular to the chains $(E \,\|\, b)$ gives evidence for a small magnetic contribution. Such a contribution is highly unexpected because the inter-chain coupling is very small and frustrated. So far, such a contribution only has been observed in the related compound CaCu_2O_3, investigated earlier in our group. To explain such small magnetic absorption features in $\sigma(\omega)$ we have sketched a new mechanism which gives rise to a dipole moment *perpendicular* to the chains when to spins are exchanged *along* the chain. For a more quantitative

analysis theoretical calculations are in progress.

Our investigations of the compound $Sr_{0.9}Ca_{0.1}CuO_2$ have shown that the value of J_c is not affected upon Ca-substitution of 10 %. The change of the line shape of the two-spinon-plus-phonon contribution suggests that the character of the excitations is somewhat different.

Magnetic Excitations of $S = 1/2$ Five-Leg Spin Ladders

Our data of $La_8Cu_7O_{19}$ are the first experimental result on the magnetic excitations of n-leg ladders ($n > 2$) at high energies. We have observed magnetic contributions to $\sigma(\omega)$ for both polarizations, $E \parallel$ legs and $E \parallel$ rungs. Up to now, no theoretical prediction for the line shape of the magnetic contribution to $\sigma(\omega)$ for a five-leg ladder are available. Amongst others we compared our data with the well-investigated spectrum of a two-leg ladder and found a surprising resemblance. Although a detailed understanding of the observed line shape is missing up to now, our data of the five-leg ladder strongly suggest the existence of bound states also in this system. The comparison of different low-dimensional $S = 1/2$ systems suggests that the magnetic excitations in the high-energy continua are rather similar and develop smoothly from 1D to 2D.

A. Appendix

A.1. Cluster Calculation

To obtain a reliable estimate of the crystal-field levels for the $R\mathrm{VO_3}$ series and the reference system VOCl, we performed cluster calculations of a octahedral cluster ML_6, consisting of a transition-metal ion M and six ligands L embedded in a crystal field. For the electron hopping between ions within the ML_6 cluster a tight-binding approximation is made, i.e. eigenfunctions of the Hamiltonian of a single atom are assumed to be very small at distances exceeding the lattice constant. The many-body interactions are treated in a mean-field approximation. The cluster calculation for VOCl has been performed by R. Rückamp[1] analog to TiOCl (for details see [15]). The calculations for both compounds have been performed using the code XTLS8 written by A. Tanaka.[2] For the input file of the program a set of parameters for $R\mathrm{VO_3}$ is required, which are briefly summarized in the following (for details see [168]).

(i) For the radial integrals, the Slater integrals, and the spin-orbit constants we used values, which were obtained by Hartree-Fock calculations in [168] and are summarized in Tab. A.1.[3] To calculate the (ligand p)-(metal d) transfer integrals we used the formulas reported in [237]:

$$pd\sigma = \left(-\frac{3\sqrt{15}}{2\pi}\frac{\hbar^2}{m}\sqrt{r_O r_V^3} \right) / d^4$$

$$pd\pi = -\frac{\sqrt{5}}{\sqrt{15}}\ pd\sigma,$$

where d is the distance between the transition metal and the corresponding ligand, r_V and r_O are the ionic radii, and m is the electron rest mass. For the ionic radius of oxygen we used $r_O = 4.41\,\text{Å}$ [238]. For the ionic radii of vanadium two values are reported in [238]: $r_V = 0.934\,\text{Å}$ and $1.060\,\text{Å}$. Because the energy values of the lowest states do not drastically change (see Fig. A.2(d)) we used $r_V = 0.934\,\text{Å}$, unless otherwise noted. For the ligand p-p transfer

---

[1] Institute of Physics II, University of Cologne, Germany
[2] Hiroshima University, Japan
[3] For the Slater integrals F^2 and F^4 we used values of $80\,\%$ of the atomic Hartree-Fock values listed in Tab. A.1 [170].

integrals the relations

$$pp\sigma = \frac{1}{\pi}\left(\frac{\hbar^2}{m}r_O\right)/d^2$$

$$pd\pi = -0.5$$

are used [237].

(ii) To describe the local crystal field, the potential of all other charges, the Madelung potential $\mathcal{V}(r, \theta, \phi)$, at the corresponding position of the transition-metal ion M is needed. This can be expressed by an expansion on spherical harmonic Y_k^m

$$\mathcal{V}(r, \theta, \phi) = \sum_{k=0}^{\infty} \sum_{m=-k}^{k} A_{k,m} r^k \sqrt{\frac{4\pi}{2k+1}} Y_k^m(\theta, \phi), \tag{A.1}$$

with quantum numbers k, m and coefficients $A_{k,m}$, related to the derivative of $\mathcal{V}(r, \theta, \phi)$, for which $A_{k,m} = (-1)^m A_{k,-m}^*$ apply [168]. Equation A.1 can be solved using the Ewald summation method by assuming point charges (for details see e.g. [239]). To calculate the coefficients $A_{k,m}$ we used the code $A_{k,m}$ by M. Haverkort [168]. The positions of the atoms within one unit cell were taken from the structure data of $R\text{VO}_3$ and VOCl reported in [26, 29, 76, 148, 149].

(iii) The *M-O* bond lengths within the octahedra are needed. To be precise as possible we preferred to use structural data from neutron scattering because the position of the oxygen ions is determined more accurately compared to x-ray diffraction. The calculations for YVO_3 were performed by the use of structural data at several temperatures in the low, intermediate, and high temperature phase reported in [76] and [29], respectively. For VOCl we used x-ray diffraction data reported in [149].

(iv) Unfortunately, experimental and theoretically obtained values for the Coulomb repulsion U_{dd} and the charge-transfer energy Δ vary within a few eV. Two sets of values, one from Hartree-Fock band-structure calculations [170] and another from core-level photoemission spectra [240] are summarized in Tab. A.2.

The temperature dependence of the nine lowest levels of YVO_3 are shown in Fig. A.1 (the values are also summarized in Tab. 4.6 in Sec. 4.3). For the monoclinic phase of YVO_3 we considered two VO_6 cluster, one for each vanadium ion V(1) and V(2), respectively. To overcome the inaccuracy of U_{dd}, Δ, U_{pp}, and r_V mentioned above, we calculated the level energies as a function of these values (see Fig. A.2(a)-(d)). Although we considered a large range of values, the influence of these parameter is rather small, in particular for the lowest triplet states. Furthermore we examined the effect of spin-orbit coupling on the energy values (Fig. A.2(e)&(f)). The spin-orbit coupling yields a splitting of the level in the region of $10\,\text{meV}$ and is therefore irrelevant for our discussion.

Table A.1.: Radial integrals, Slater integrals (unreduced), and spin-orbit constants (in eV) of V^{3+}, V^{2+}, and V^{1+} obtained by atomic Hartree-Fock calculations [168].

	R2	R4	ζ	F^2	F^4
$2p^6\ 3d^4\ 4s^0$	0.829	1.786	0.018	7.599	4.674
$2p^6\ 3d^3\ 4s^0$	0.595	0.793	0.022	8.961	5.576
$2p^6\ 3d^2\ 4s^0$	0.470	0.456	0.027	10.126	6.353

Table A.2.: Values for the charge-transfer energy Δ, the on-site Coulomb repulsion U_{dd}, and the (ligand p)-(metal d) transfer integral $pd\sigma$ [170, 240] (all values in eV).

	Δ	U_{dd}	$pd\sigma$	Ref.
RVO_3	6.0	4.5	2.2	[170]
$LaVO_3$	4.0	4.0	2.0	[240]
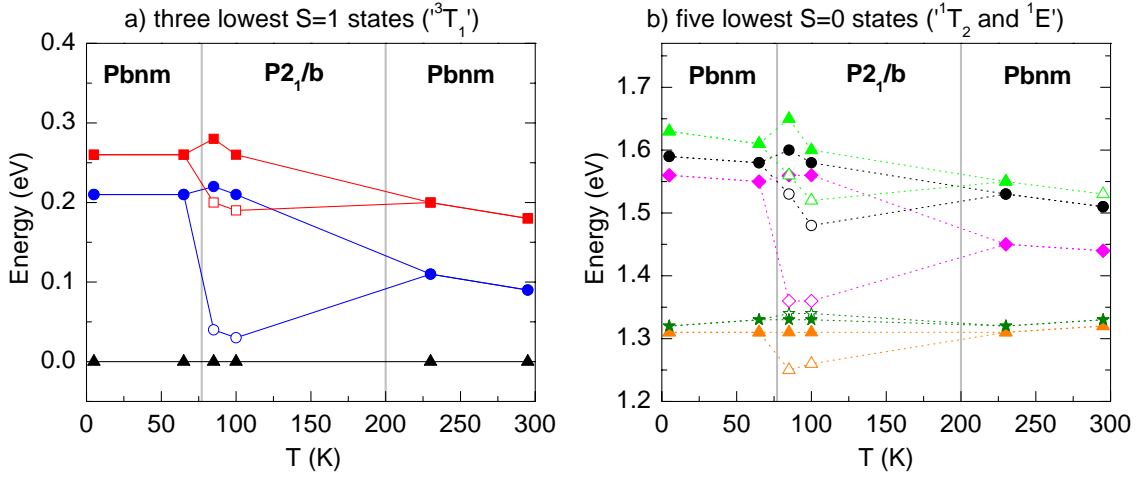
Figure A.1.: Temperature dependence of the three lowest triplet states (left panel) and the five lowest singlet states (right panel) obtained by cluster calculations for YVO_3 using $U_{dd} = 4.5\,\text{eV}$, $\Delta = 4\,\text{eV}$ and $U_{pp} = 5\,\text{eV}$. The exact values are given in Tab. 4.6 in Sec. 4.3.
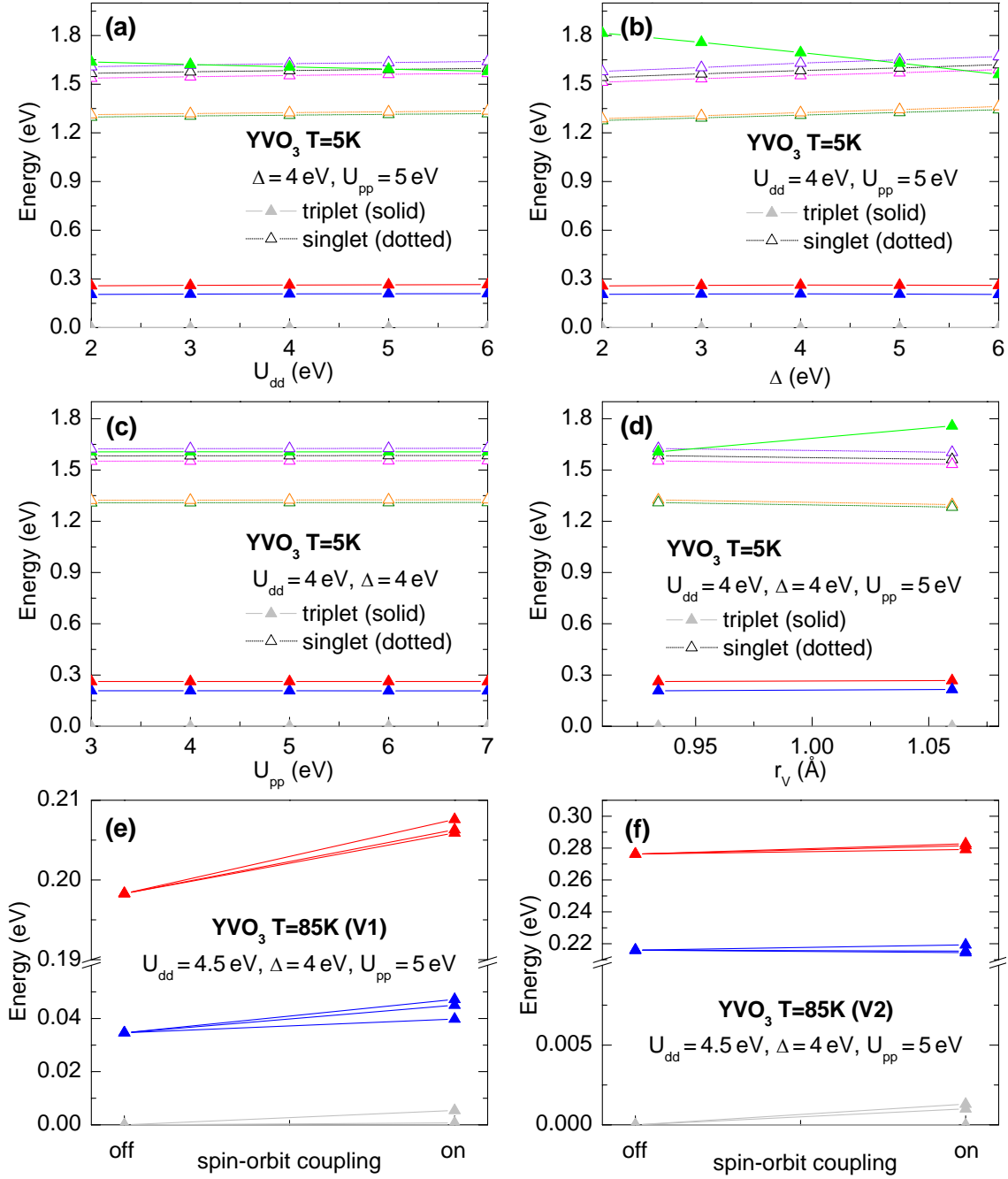
Figure A.2.: Energies of the first nine crystal-field levels of YVO_3 at $T = 5\,K$ as a function of (a) U_{dd}, (b) Δ, (c) U_{pp}, and (d) r_V. (e) & (f): crystal-field levels of YVO_3 at $85\,K$ for V(1) and V(2) with and without taking spin-orbit coupling (ζ, Tab. A.1) into account.

A.2. Configuration Mixing of the ^{3}T$_1$ Ground State

To estimate the configuration mixing of the $^3T_1$ state for a d^2 system in a cubic crystal field, one has to diagonalize the following matrix in the basis of the single-electron states $\{t_{2g}^2, t_{2g}^1 e_g^1\}$ [77]:

$$\begin{pmatrix} -5B - 8Dq & 6B \\ 6B & 4B + 2Dq \end{pmatrix}. \tag{A.2}$$

Here B is one of the Racah parameters, which describe the Coulomb interaction. Compared with the matrix for the free ion with d^2 electron configuration [77], the corresponding energy shifts for the cubic crystal field in fractions of $10\,Dq$ has been added on the diagonal entries of Eq. A.2. While the energy of the t_{2g}^2 state is lowered by -8 Dq, the energy is raised by $2\,Dq$ for the $t_{2g}^1 e_g^1$ state (see Fig. A.3). For a rough estimate of the configuration mixing of the $^3T_1$ ground state in $R\mathrm{VO_3}$ we used the free ion value $B = 0.11\,\mathrm{eV}$ for $\mathrm{V^{3+}}$ given in [77] and $10\,Dq = 2\,\mathrm{eV}$ ([166, 167] and this work Sec. 4.3.5). Then the eigenvector to the lowest eigenvalue in the basis $\{t_{2g}^2, t_{2g}^1 e_g^1\}$ is $\{0.98, -0.21\}$. From this follows a mixing of about $96\,\%$ t_{2g}^2 and $4\,\%$ $t_{2g}^1 e_g^1$. Without consideration of the crystal-field splitting the result reads: $80\,\%$ t_{2g}^2 and $20\,\%$ $t_{2g}^1 e_g^1$.
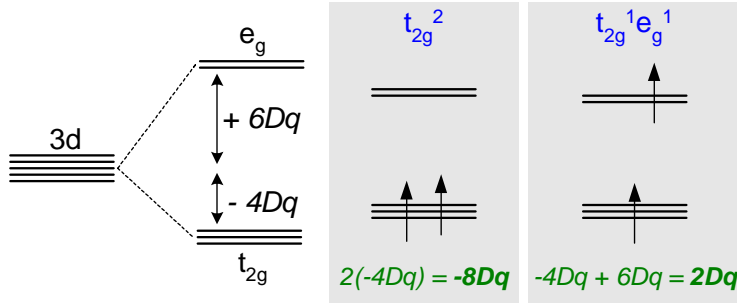
Figure A.3.:
Energy splitting of $10\,Dq$ between the single-electron basis states t_{2g}^2 and $t_{2g}^1 e_g^1$ contributing to the configuration mixing for the $^3T_1$ level of a d^2 system. Thus, the t_{2g}^2 state is shifted by -8 Dq and the $t_{2g}^1 e_g^1$ by $+2\,Dq$ state with regard to the balance point.

A.3. Assignment of the Dy^{3+} *f*-*f* Transitions in DyScO$_3$

The $\mathrm{Dy^{3+}}$ ion in $\mathrm{DyScO_3}$ exhibits 9 electrons occupying the open $4f$ shell. This state is $\binom{14}{9} = 2002$-fold degenerate. The influence of the crystal field on the f electrons is comparatively small because they are more localized compared with d electrons. Therefore, the first term in perturbation theory is the electron-electron interaction, followed by spin-orbit coupling. The latter yields a further removal of the degeneracy of the levels with J being a good quantum number (Fig. A.4). For $\mathrm{Dy^{3+}}$ the ground
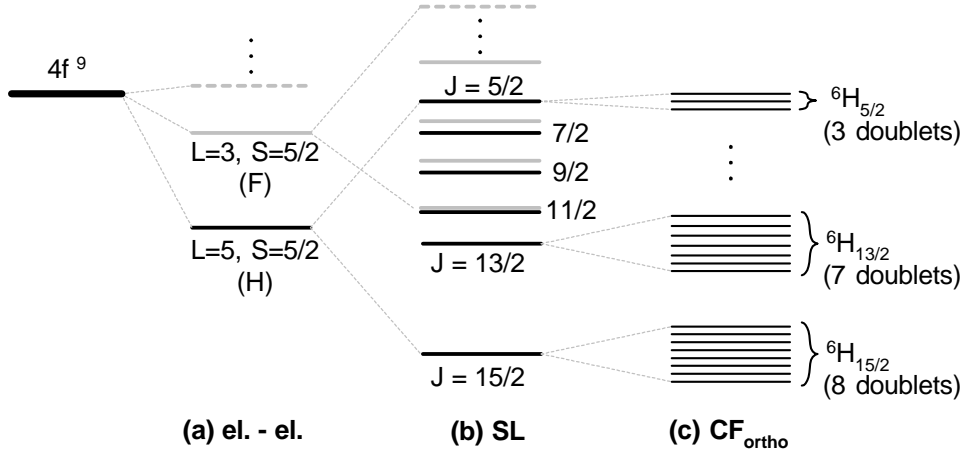
Figure A.4.: Qualitative energy-level diagram for the nine $4f$ electrons of Dy^{3+} in $DyScO_3$. (a) Due to the electron-electron interaction, the degeneracy of the 2002-fold degenerate $4f^9$ state is lifted, where the ($L=5$, $S=5/2$) state is lowest in energy. (b) The next relevant term is the spin-orbit coupling which yields a splitting of the $L=5$, $S=5/2$ state into six multiplets ($J=15/2$, ..., $5/2$) with the $J=15/2$ level is the ground state. (c) At last the crystal field is taken into account. For a crystal field of tetragonal symmetry or lower, the $J=15/2$ multiplet splits into 8 Kramers doublets.

state is the $J=15/2$ multiplet which is $(2J+1)=16$-fold degenerate [241]. In a crystal field of tetragonal symmetry or lower, e.g. orthorhombic symmetry, the $J=15/2$ multiplet splits into 8 Kramers doublets [242].

In optical spectra electric-dipole transitions between f states are forbidden due to the parity selections rule (Tab. 2.1). However, due to a lack of inversion symmetry on the rare-earth metal ion site, a mixing of the $4f^{n-1}5d$ configuration with opposite parity into the $4f^n$ states can occur, which gives rise to a (small) electric-dipole moment [50]. Since the f electrons couple only weakly to the lattice, f-f transitions are usually observed as sharp lines [50].

A rough assignment of the f-f transitions observed in the optical spectrum of $DyScO_3$ was performed on the basis of a comparison with the absorption spectrum of $DyCl_3$ [175] (see Fig. A.5). We find a good agreement for several observed bands, except for the transition $^6H_{15/2} \rightarrow^6 H_{5/2}$ which is specified by 1.26 eV in Ref. [175]. However, the intensities of the lines are not examined in [175], therefore, the $^6H_{15/2} \rightarrow^6 H_{5/2}$ absorption band may be less intense. Because the spectrum of $DyScO_3$ is obtained at room temperature, probably additional lines appear, which are due to transitions from higher Stark components of the ground state level, i.e. from the six higher lying doublets of the $^6H_{15}$ level ($300\,\mathrm{K} \sim 26\,\mathrm{meV} \sim 210\,\mathrm{cm}^{-1}$).
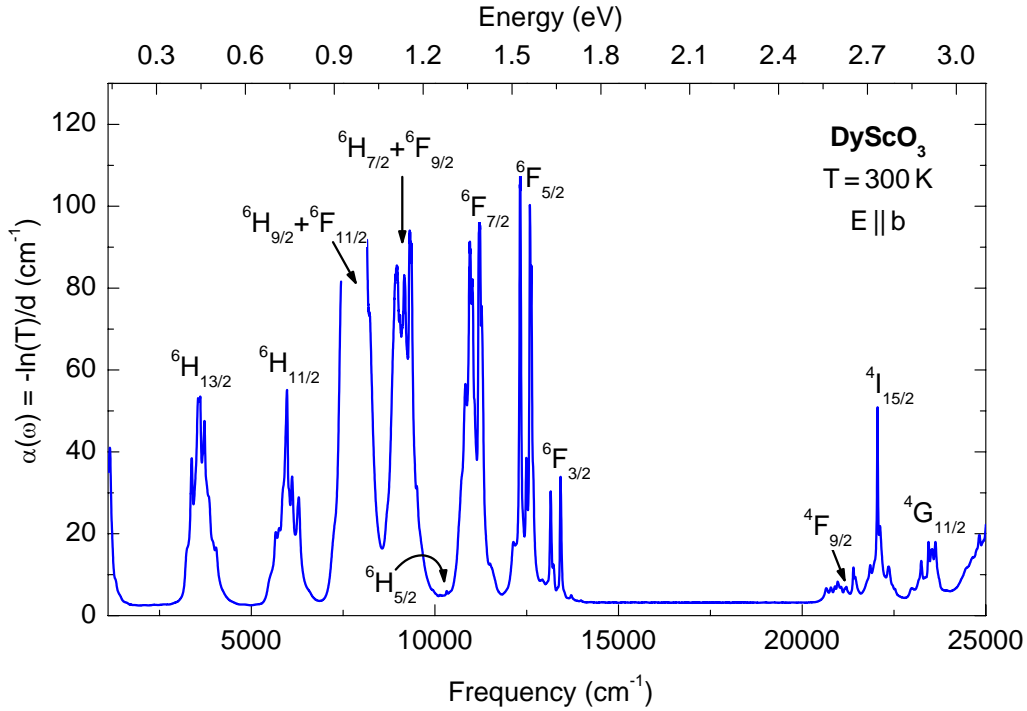
Figure A.5.: Assignment of the f-f transition bands observed in the optical absorption spectrum of DyScO$_3$. For details see text.

A.4. Assignment of the Ce^{3+} *f-f* Transitions in CeVO$_3$

The absorption band at ~ 0.3 eV observed in the optical absorption spectrum of CeVO$_3$ can be assigned to f-f transitions of the single electron occupying the Ce^{3+} $4f$ shell. Taking spin-orbit coupling into account, the configuration of the free cerium ion consists of two ^2F levels separated by 0.28 eV [243]. The further splitting of the ^2F levels due to the crystal field in CeVO$_3$ should not change this free-ion value very much, but it explains the fine structure of the spectrum. For a comparison we take the infrared absorption spectra of CeF$_3$ obtained by [244] (see Fig. A.7). There six absorption lines between 0.24 and 0.36 eV have been assigned to transitions between the 3-fold Kramers-degenerate $^2F_{5/2}$ ground state and the 4-fold Kramers-degenerate Stark levels of the $^2F_{7/2}$ multiplet (see Fig. A.6). The degeneracy of these levels is fully removed by a crystal field of tetragonal symmetry or lower, certainly except for the Kramers degeneracy [242]. Due to the relatively large thickness of the CeVO$_3$, sample $T(\omega) \approx 0$ in the energy range of the f-f band and the fine structure could not be fully resolved (regions cut out in Fig. A.7). However, the absorption feature around 0.5 eV observed for $E \parallel \tilde{c}$ belongs definitely not to the f-f band.
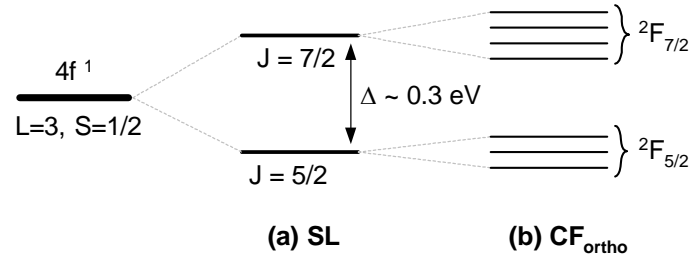
Figure A.6.: Qualitative energy-level diagram for the single $4f$ electron of Ce^{3+} in $CeVO_3$.
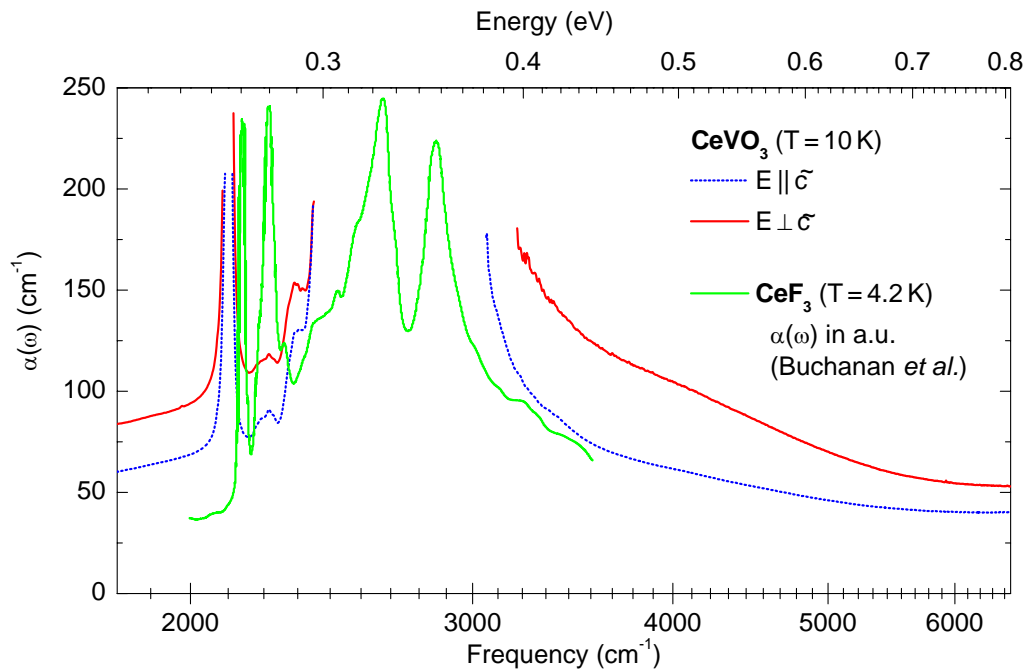
Figure A.7.: Assignment of the f-f transition band observed in the optical absorption spectrum of $CeVO_3$. For comparison the absorption spectrum of CeF_3, taken from [244] is shown. For details see text.

A.5. Assignment of the Ho^{3+} *f-f* Transitions in HoVO$_3$

The Ho^{3+} ion in HoVO$_3$ exhibits 10 electrons occupying the open $4f$ shell. This state is $\binom{14}{10} = 1001$-fold degenerate. The electron-electron interaction, followed by spin-orbit coupling yields a splitting of these levels as shown in Fig. A.8. The ground state is the 17-fold degenerated $^5I_8$ level. In a cubic crystal field the $^5I_8$ level split into 1 singlet (sg) + 2 doublets (db) + 4 triplets (tr), for a tetragonal crystal field into 9 sg + 4 db, and for a crystal field still lower in symmetry the degeneracy is fully lifted, i.e. 17 sg are expected [242].

From a comparison with the energy levels observed from Ho^{3+} centers in hexagonal LaCl$_3$ [245] and LaF$_3$ [245], we identify the absorption band around 0.65 eV in HoVO$_3$ with the transition $^5I_8 \rightarrow {}^5I_7$ (Fig. A.9). The fine structure is due to transitions between different Stark components. In the $T = 10$ K spectrum up to 12 lines ($2J + 1 = 15$ are expected) are observed, reflecting a low site symmetry (C_S) for the Ho^{3+} ion in HoVO$_3$. In the room-temperature spectrum additional lines appear at lower energies, which may are due to transitions from higher Stark components of the ground state level, i.e. ~ 26 meV above [246]. The polarization of the incident light mainly affects the intensity of the observed lines.
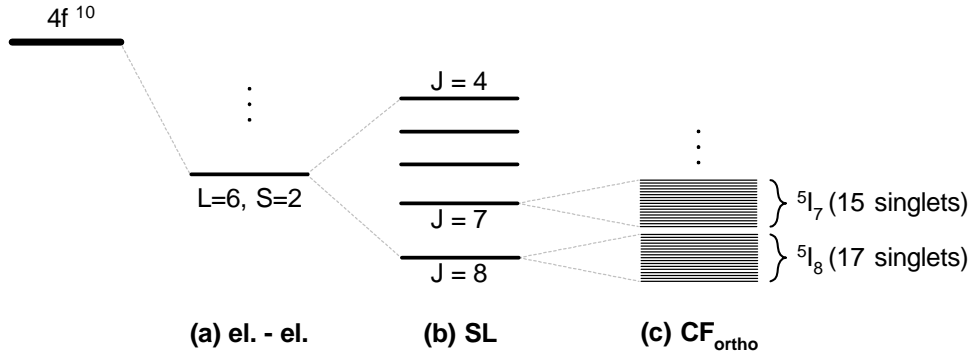
Figure A.8.: Qualitative energy-level diagram for the $4f^{10}$ electron configurations of Ho^{3+} in HoVO$_3$.
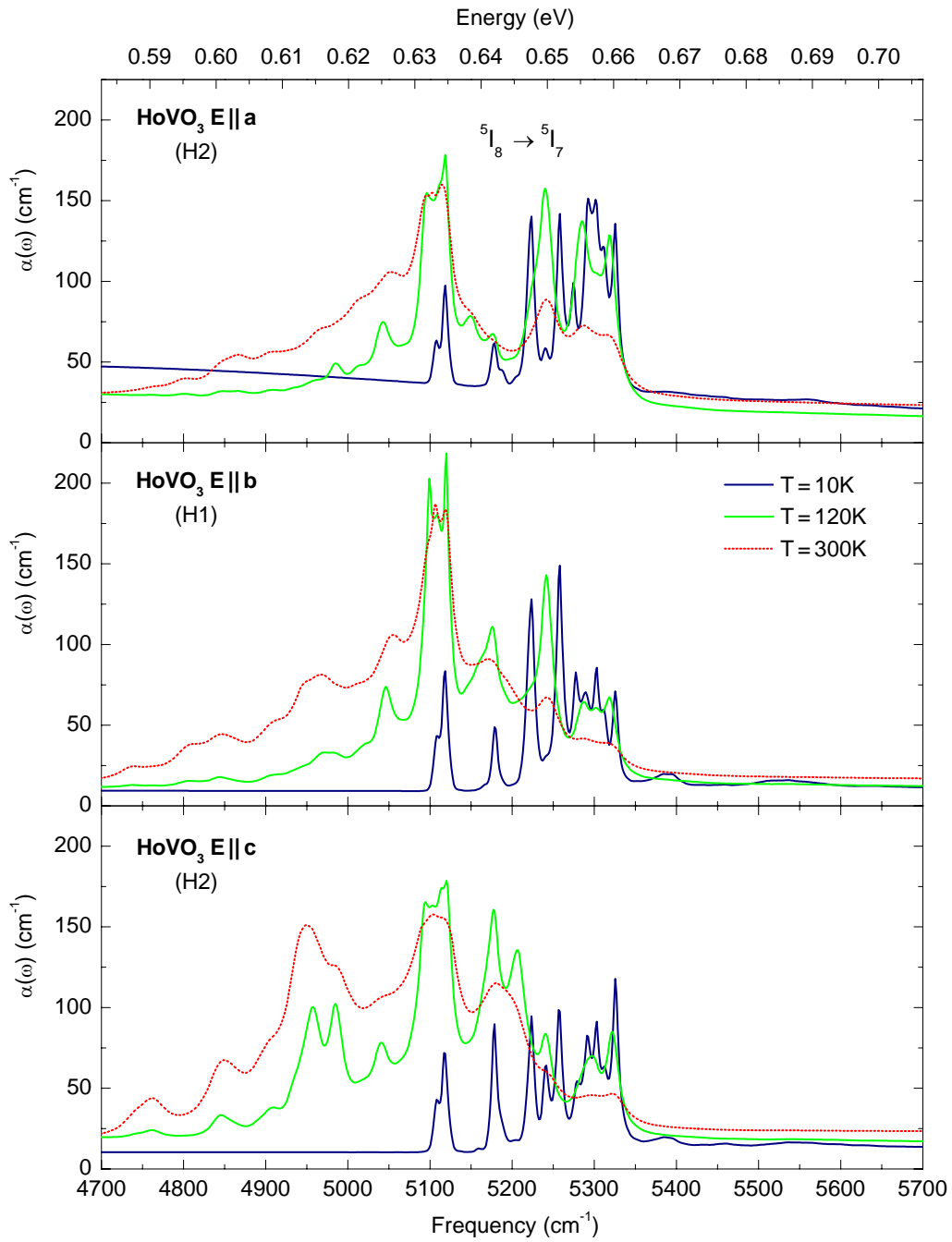
Figure A.9.: *f-f* transition band observed in the optical absorption spectrum of HoVO₃. Exemplarily the spectra for $E \parallel a$ (top panel), $E \parallel b$ (middle panel), and $E \parallel c$ (bottom panel) at 10, 120, and 300 K are shown.

A.6. Near-Infrared Photoinduced Absorption in SrCuO₂

In the near-infrared (NIR) spectra of SrCuO$_2$ for $E \parallel c$ we have observed an unusual absorption feature at temperatures below $200\,\mathrm{K}$ (top panel in Fig. A.10). In particular, this absorption feature around $0.9\,\mathrm{eV}$ is solely present in spectra which have been measured with the NIR setup (tungsten lamp, VIS beam splitter, etc.; see Chap. 3). In the spectra obtained with the MIR setup (globar, KBr beam split-
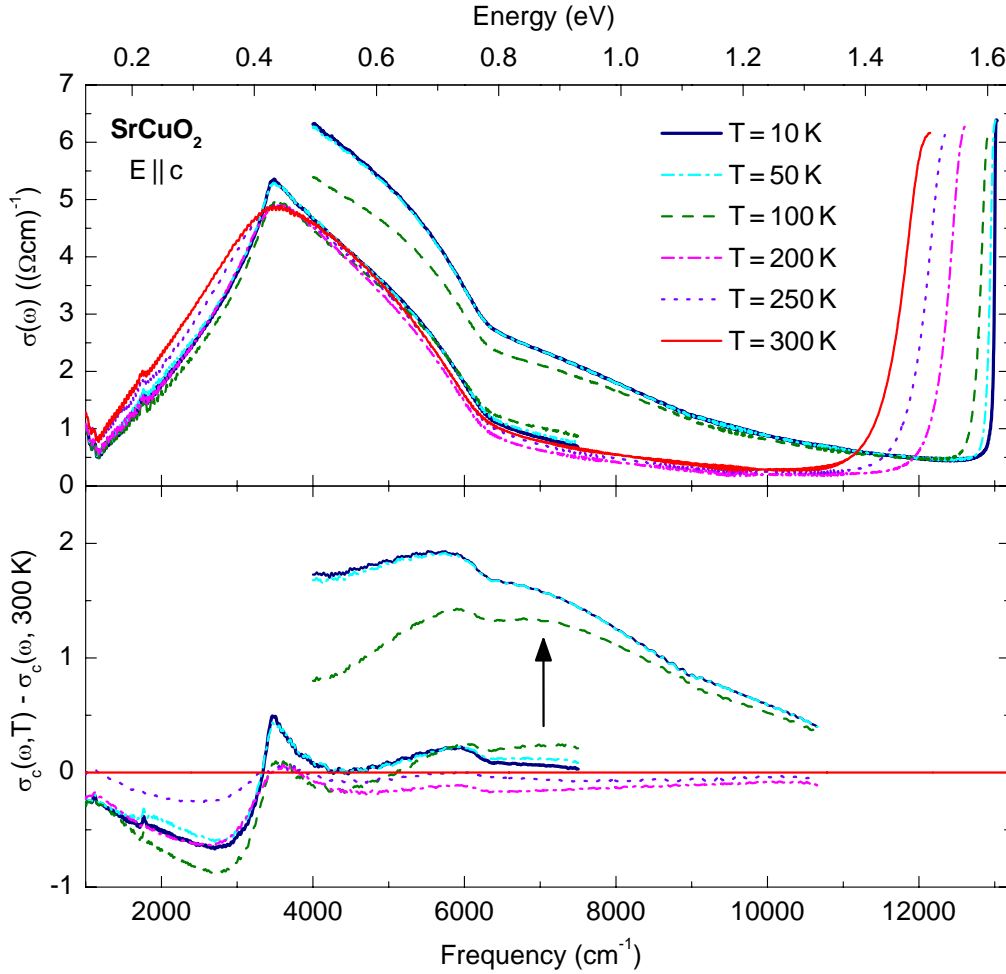
Figure A.10.: Mid- and near-infrared spectra of the optical conductivity ($\sigma_c(\omega)$) of SrCuO$_2$ for $E \parallel c$ obtained with the Fourier spectrometer. Below $200\,\mathrm{K}$ the NIR spectra show additional spectral weight compared to the MIR spectra (top panel). In the bottom panel the difference spectra of $\sigma_c(\omega, T)$ at several temperatures T and $\sigma_c(\omega, T = 300\,\mathrm{K})$ at room temperature is shown.

ter, etc.) this feature is not observed, although both data sets show a significant overlap. While at 200 K, 250 K, and 300 K the MIR and NIR spectra merge nicely, below 200 K the NIR spectra clearly deviates from those in the MIR. This is more clearly seen from the difference spectra, i.e. $\sigma_c(\omega, T)$ at several temperatures T minus $\sigma_c(\omega, T = 300\,\text{K})$ at room temperature (bottom panel of Fig. A.10). A major difference between both setups is that there is almost no intensity at frequencies above 1 eV with the MIR setup, while there is large intensity up to 2.2 eV with the NIR setup. Because of this very unusual dependency on the used lamp, we have also performed transmittance measurements from 0.6 up to 1.65 eV using a grating spectrometer with monochromator. Here we observe *no* significant changes in transmittance around 0.9 eV with decreasing temperature. In contrast, the transmittance at 0.9 eV changes from 35 % at 300 K to 13 % at 10 K in the Fourier spectrometer measurement. Note that the same sample S1b (see Tab. 5.2) has been used for both measurements. As a result of our observations we claim that the feature around 0.9 eV is a photoinduced absorption excited with visible light. Very recently, similar observations have been reported in LaSrAlO$_4$ [247]. Here, extremely long-lived (up to hours) photoinduced excitations excited with visible light have been observed at temperatures below 200 K. The photoinduced absorption spectrum of LaSrAlO$_4$ at 4 K is peaked at 0.7 eV with a spectral width of about 0.5 eV. In [247] it is argued that photoexcited carriers are trapped in the vicinity of oxygen vacancies in annealed LaSrAlO$_4$ samples. The trapping induces local lattice distortions which relax very slowly. When a NIR photon is absorbed the trapped charge carriers get efficiently retrapped at low temperatures, giving rise to a long-lived photoinduced absorption feature in LaSrAlO$_4$. However, for a more detailed analysis of the photoinduced absorption feature in SrCuO$_2$ further experimental research is required. In particular, the dependency on the sample quality and a detailed analysis of the line shape is of interest.

A.7. Madelung Potentials at O(1) and O(2) in SrCuO$_2$

To calculate the Madelung potential $\mathcal{V}$ at O(1) and O(2) in SrCuO$_2$ the formula given in Eq. A.1 has been used. By assuming point charges, the coefficients $A_{k,m}$ were calculated with the program $A_{k,m}$ by M. Haverkort [168]. The positions of the charges were taken from the structural data reported in [195]. The coefficients $A_{k,m}$ are listed in Tab. A.3. The Madelung potential is given by the coefficients $A_{0,0}$. Higher coefficients allow for the crystal field splitting, which are an order of magnitude smaller. For the difference/ratio in Madelung potential at site O(1) and O(2) we obtain

$$\mathcal{V}(\text{O}(2)) - \mathcal{V}(\text{O}(1)) = 3.43\,eV; \quad \frac{\mathcal{V}(\text{O}(2))}{\mathcal{V}(\text{O}(1))} \approx 85\,\%.$$

In should be noted, that the values of the Madelung potential are somehow overestimated here, because no screening effects have been considered.

Table A.3.: Coefficients $A_{k,m}$ (in eV) for SrCuO$_2$ at the position of O(1) and O(2), respectively. For details on the programm $A_{k,m}$ see [168].

$A_{k,m}$	at O(1)	at O(2)
$A_{0,0}$	(-23.26566596,0.00000000)	(-19.83867354, 0.00000000)
$A_{1,0}$	(0.00000000, 0.00000000)	(0.00000000, 0.00000000)
$A_{1,1}$	(0.00000000, -1.56216763)	(0.00000000, 2.11159166)
$A_{2,0}$	(-2.78780746, 0.00000000)	(1.53440186, 0.00000000)
$A_{2,1}$	(0.00000000, 0.00000000)	(0.00000000, 0.00000000)
$A_{2,2}$	(1.22058922, 0.00000000)	(1.47931652, 0.00000000)
$A_{3,0}$	(0.00000000, 0.00000000)	(0.00000000, 0.00000000)
$A_{3,1}$	(0.00000000, 0.94889504)	(0.00000000, -0.71393334)
$A_{3,2}$	(0.00000000, 0.00000000)	(0.00000000, 0.00000000)
$A_{3,3}$	(0.00000000, 1.58616819)	(0.00000000, -0.36563827)
$A_{4,0}$	(-2.79442174, 0.00000000)	(-0.32567102, 0.00000000)
$A_{4,1}$	(0.00000000, 0.00000000)	(0.00000000, 0.00000000)
$A_{4,2}$	(-0.82440761, 0.00000000)	(-1.12746533, 0.00000000)
$A_{4,3}$	(0.00000000, 0.00000000)	(0.00000000, 0.00000000)
$A_{4,4}$	(-0.20441176, 0.00000000)	(-0.73513734, 0.00000000)
$A_{5,0}$	(0.00000000, 0.00000000)	(0.00000000, 0.00000000)
$A_{5,1}$	(0.00000000, -0.03632117)	(0.00000000, 0.15253430)
$A_{5,2}$	(0.00000000, 0.00000000)	(0.00000000, 0.00000000)
$A_{5,3}$	(0.00000000, -0.27845561)	(0.00000000, 0.25679957)
$A_{5,4}$	(0.00000000, 0.00000000)	(0.00000000, 0.00000000)
$A_{5,5}$	(0.00000000, -0.36747860)	(0.00000000, 0.20142354)
$A_{6,0}$	(-0.40545137, 0.00000000)	(0.13678756, 0.00000000)
$A_{6,1}$	(0.00000000, 0.00000000)	(0.00000000, 0.00000000)
$A_{6,2}$	(0.10071370, 0.00000000)	(0.09251705, 0.00000000)
$A_{6,3}$	(0.00000000, 0.00000000)	(0.00000000, 0.00000000)
$A_{6,4}$	(0.11611438, 0.00000000)	(0.08180927, 0.00000000)
$A_{6,5}$	(0.00000000, 0.00000000)	(0.00000000, 0.00000000)
$A_{6,6}$	(0.14198364, 0.00000000)	(0.15817324, 0.00000000)

References

[1] P. W. Anderson, Science **177**, 393 (1972). v

[2] M. Imada, A. Fujimori, and Y. Tokura, Rev. Mod. Phys. **70**, 1039 (1998). 1

[3] N. F. Mott, Proc. Phys. Soc. A **62**, 416 (1949). 1, 13

[4] J. Hubbard, Proc. Roy. Soc. London A **276**, 238 (1963). 1, 13

[5] Y. Tokura and N. Nagaosa, Science **288**, 462 (2000). 1, 14, 21

[6] H. A. Jahn and E. Teller, Proc. Roy. Soc. London A **161**, 220 (1937). 1, 20

[7] K. I. Kugel and D. I. Khomskii, Sov. Phys. JETP **37**, 725 (1973). 1, 21

[8] G. Khaliullin and S. Maekawa, Phys. Rev. Lett. **85**, 3950 (2000). 1, 21

[9] P. Horsch, G. Khaliullin, and A. M. Olés, Phys. Rev. Lett. **91**, 257203 (2003). 1, 21

[10] S. Miyasaka, S. Onoda, Y. Okimoto, J. Fujioka, M. Iwama, N. Nagaosa, and Y. Tokura, Phys. Rev. Lett. **94**, 076405 (2005). 1, 2, 39, 48, 49, 50

[11] E. Saitoh, S. Okamoto, K. T. Kakahashi, K. Tobe, K. Yamamoto, T. Kimura, S. Ishihara, S. Maekawa, and Y. Tokura, Nature **410**, 180 (2001). 2, 20, 21, 50

[12] E. Saitoh, S. Okamoto, K. Tobe, K. Yamamoto, T. Kimura, S. Ishihara, S. Maekawa, and Y. Tokura, Nature **418**, 40 (2002). 2, 50

[13] C. Ulrich, A. Gössling, M. Grüninger, M. Guennou, H. Roth, M. Cwik, T. Lorenz, G. Khaliullin, and B. Keimer, Phys. Rev. Lett. **97**, 157401 (2006). 2, 21

[14] C. Ulrich, G. Ghiringhelli, A. Piazzalunga, L. Braicovich, N. B. Brookes, H. Roth, T. Lorenz, and B. Keimer, Phys. Rev. B **77**, 113102 (2008). 2, 21

[15] R. Rückamp, E. Benckiser, M. W. Haverkort, H. Roth, T. Lorenz, A. Freimuth, L. Jongen, A. Möller, G. Meyer, P. Reutler, et al., New J. Phys. **7**, 144 (2005). 2, 18, 21, 51, 77, 145

[16] G. Khaliullin, P. Horsch, and A. M. Olés, Phys. Rev. Lett. **86**, 3879 (2001). 2, 21, 47, 48, 95

[17] S. Ishihara, Phys. Rev. B **69**, 075118 (2004). 2, 20, 21, 47, 48, 50, 95

[18] H. Sawada, N. Hamada, K. Terakura, and T. Asada, Phys. Rev. B **53**, 12742 (1996). 2, 39, 41, 75

[19] T. Mizokawa, D. I. Khomskii, and G. A. Sawatzky, Phys. Rev. B **60**, 7309 (1999). 2, 35, 36, 38

[20] Y. Ren, T. T. M. Palstra, D. I. Khomskii, E. Pellegrin, A. A. Nugroho, A. A. Menovsky, and G. A. Sawatzky, Nature **396**, 441 (1998). 2, 35, 39, 40, 41, 45, 46

[21] G. R. Blake, T. T. M. Palstra, Y. Ren, A. A. Nugroho, and A. A. Menovsky, Phys. Rev. Lett. **87**, 245501 (2001). 2, 39, 40, 41, 42, 49

[22] Y. Ren, A. A. Nugroho, A. A. Menovsky, J. Strempfer, U. Rütt, F. Iga, T. Takabatake, and C. W. Kimball, Phys. Rev. B **67**, 014107 (2003). 2, 35, 39, 51

[23] S. Miyasaka, Y. Okimoto, M. Iwama, and Y. Tokura, Phys. Rev. B **68**, 100406(R) (2003). 2, 35, 38, 39

[24] Z. Fang and N. Nagaosa, Phys. Rev. Lett. **93**, 176404 (2004). 2, 35, 36, 47

[25] P. Bordet, C. Chaillout, M. Marezio, Q. Huang, A. Santoro, S.-W. Cheong, H. Takagi, C. S. Oglesby, and B. Batlogg, J. Sol. State Chem. **106**, 253 (1993). 2, 36

[26] A. Muñoz, J. A. Alonso, M. T. Casáis, M. J. Martínez-Lope, J. L. Martínez, and M. T. Fernández-Díaz, Phys. Rev. B **68**, 144429 (2003). 2, 35, 36, 50, 51, 87, 146

[27] A. Muñoz, J. A. Alonso, M. T. Casáis, M. J. Martínez-Lope, J. L. Martínez, and M. T. Fernández-Díaz, J. Mat. Chem. **13**, 1234 (2003). 2, 35, 36, 39

[28] C. Ulrich, G. Khaliullin, J. Sirker, M. Reehuis, M. Ohl, S. Miyasaka, Y. Tokura, and B. Keimer, Phys. Rev. Lett. **91**, 257202 (2003). 2, 21, 35, 36, 39, 41, 43, 45, 46, 47, 49, 73, 92

[29] M. Reehuis, C. Ulrich, P. Pattison, B. Ouladdiaf, M. C. Rheinstädter, M. Ohl, L. P. Regnault, M. Miyasaka, Y. Tokura, and B. Keimer, Phys. Rev. B **73**, 094440 (2006). 2, 16, 35, 36, 39, 40, 41, 42, 43, 45, 46, 60, 75, 84, 146

[30] F. Wang, J. Zhang, P. Yuan, Q. Yan, and P. Zhang, J. Phys.: Cond. Mat. **12**, 3037 (2000). 2, 35, 36

[31] J. Pickardt, T. Schendler, and M. Kolm, Z. Allg. Anorg. Chem. **560**, 153 (1988). 2, 35, 36

[32] S. Sugai and K. Hirota, Phys. Rev. B **73**, 020409(R) (2006). 2, 35, 36, 39, 48, 49, 50, 73

[33] S. Miyasaka, J. Fujioka, M. Iwama, Y. Okimoto, and Y. Tokura, Phys. Rev. B **73**, 224436 (2006). 2, 39, 48, 49, 50, 73

[34] S. Ishihara, Y. Murakami, T. Inami, K. Ishii, J. Mizuki, K. Hirota, S. Maekawa, and Y. Endoh, New J. Phys. **7**, 119 (2005). 2, 20, 21, 22, 82

[35] J. G. Bednorz and K. A. Müller, Z. Phys. B **64**, 189 (1986). 3, 97

[36] P. W. Anderson, Science **235**, 1196 (1987). 3, 97, 98

[37] H. Bethe, Z. Physik **71**, 205 (1931). 3, 99

[38] L. D. Faddeev and L. A. Takhtajan, Phys. Lett. **85A**, 375 (1981). 3, 99

[39] E. Dagotto and T. M. Rice, Science **271**, 618 (1996). 3, 100, 101

[40] E. Dagotto and A. Moreo, Phys. Rev. B **38**, 5087 (1988). 3, 101

[41] E. Dagotto, J. Riera, and D. J. Scalapino, Phys. Rev. B **45**, 5744 (1992). 3, 101

[42] S. Notbohm, P. Ribeiro, B. Lake, D. A. Tennant, K. P. Schmidt, G. S. Uhrig, C. Hess, R. Klingeler, G. Behr, B. Büchner, et al., Phys. Rev. Lett. **98**, 027403 (2007). 3, 101

[43] M. Grüninger, M. Windt, E. Benckiser, T. Nunner, K. P. Schmidt, G. S. Uhrig, and T. Kopp, Advances in Solid State Physics **43**, Springer-Verlag Berlin Heidelberg (2003). 3, 4, 98, 107, 119, 120, 123, 134

[44] J. Lorenzana and G. A. Sawatzky, Phys. Rev. Lett. **74**, 1867 (1995). 3, 22, 23, 24, 79, 82, 119

[45] J. Lorenzana and G. A. Sawatzky, Phys. Rev. B **52**, 9576 (1995). 3, 22, 23, 25, 79, 82, 124

[46] H. Suzuura, H. Yasuhara, A. Furusaki, N. Nagaosa, and Y. Tokura, Phys. Rev. Lett. **76**, 2579 (1996). 4, 22, 25, 99, 107, 117, 119, 120

[47] N. Motoyama, H. Eisaki, and S. Uchida, Phys. Rev. Lett. **76**, 3212 (1996). 4, 25, 106

[48] E. Benckiser, Master's thesis, University of Cologne, Germany (2003). 4, 107, 123, 137, 138

[49] P. Ribeiro, C. Hess, P. Reutler, G. Roth, and B. Büchner, J. Magn. and Magn. Mat. **290-291**, 334 (2005). 4, 107, 108, 126

[50] B. Henderson and G. F. Imbusch, *Optical Spectroscopy of Inorganic Solids* (Oxford University Press, 2006). 4, 7, 150

[51] F. Wooten, *Optical properties of solids* (Academic Press INC New York and London, 1972). 7

[52] T. Mayer-Kuckuk, *Atomphysik* (Teubner Studienbücher Physik, 1997). 7

[53] K. M. Aggarwal and F. P. Keenan, Astronomy and Astrophysics **427**, 763 (2004). 7

[54] H. Kuzmany, *Solid-State Spectroscopy* (Springer-Verlag Berlin Heidelberg, 1998). 8, 10, 19

[55] M. Grüninger, M. Windt, T. Nunner, C. Knetter, K. P. Schmidt, G. S. Uhrig, T. Kopp, A. Freimuth, U. Ammerahl, B. Büchner, et al., J. Phys. Chem. Sol. **63**, 2167 (2002). 8

[56] A. B. Kuz'menko, E. A. Tishchenko, and V. G. Orlov, J. Phys.: Cond. Mat. **8**, 6199 (1996). 9, 10, 132

[57] A. B. Kuz'menko, D. van der Marel, P. J. M. van Bentum, E. A. Tishchenko, C. Presura, and A. A. Bush, Phys. Rev. B **63**, 094303 (2001). 9, 132

[58] A. Gößling, T. Möller, W.-D. Stein, P. Becker, L. Bohatý, and M. Grüninger, Physica Stat. Sol. (B), Appl. Res. **242**, R85 (2005). 9

[59] W. C. Martin and W. L. Wiese, *Atomic, Molecular, and Optical Physics Handbook* (G. W. F. Drake (Ed.), AIP Press, Woodbury, NY, 1996), chap. 10. 10, 11

[60] G. Y. Lyubarskii, *The Application of Group Theory in Physics* (Pergamon Press Ltd., London, 1960). 11

[61] H.-W. Streitwolf, *Gruppentheorie in der Festkörperphysik* (Akademische Verlagsgesellschaft Geest & Portig K.-G., Leipzig, 1966). 11

[62] D. L. Rousseau, R. P. Bauman, and S. P. S. Porto, J. Raman Spec. **10**, 253 (1981). 12, 13, 15, 109

[63] E. Kroumova, M. I. Aroyo, J. M. Perez-Mato, A. Kirov, C. Capillas, S. Ivantchev, and H. Wondratschek, Phase Trans.: A Multinat. J. **76**, 155 (2003). 12, 15, 16

[64] A. Gelessus, W. Thiel, and W. Weber, J. Chem. Edu. **72**, 505 (1995). 12, 15

[65] L. H. Gade, *Koordinationschemie* (Wiley-VCH, Weinheim, 1998). 12, 37

[66] R. L. Carter, J. Chem. Edu. **48**, 297 (1971). 13, 15

[67] P. Fazekas, *Lecture Notes on Electron Correlation and Magnetism* (World Scientific Publishing Co. Pte. Ltd., 1999). 13, 97

[68] J. Zaanen, G. Sawatzky, and J. Allen, Phys. Rev. Lett. **55**, 418 (1985). 14

[69] V. J. Emery, Phys. Rev. Lett. **58**, 2794 (1987). 14

[70] Y. Ōno, M. Potthoff, and R. Bulla, Phys. Rev. B **67**, 035119 (2003). 14

[71] J. S. Lee, M. W. Kim, and T. W. Noh, New J. Phys. **7**, 147 (2005). 14

[72] C. Buhler and A. Moreo, Phys. Rev. B **59**, 9882 (1999). 14

[73] D. van der Marel, *Optical Signatures of Electron Correlations in the Cuprates* (D. Baeriswyl and L. Degiorgi (Ed.), Kluwer Academic Publishers; cond-mat/0301506, 2004), vol. 25. 14

[74] D. M. Roessler, Brit. J. Appl. Phys. **16**, 1119 (1965). 15

[75] A. A. Tsvetkov, F. P. Mena, P. H. M. van Loosdrecht, D. van der Marel, Y. Ren, A. A. Nugroho, A. A. Menovsky, I. S. Elfimov, and G. A. Sawatzky, Phys. Rev. B **69**, 075110 (2004). 15, 16, 35, 37, 39, 43, 44, 45, 46, 50, 66, 68, 69, 70, 73

[76] G. R. Blake, T. T. M. Palstra, Y. Ren, A. A. Nugroho, and A. A. Menovsky, Phys. Rev. B **65**, 174112 (2002). 16, 39, 40, 41, 42, 46, 49, 60, 75, 146

[77] S. Sugano, Y. Tanabe, and H. Kamimura, *Multiplets of Transition-Metal Ions in Crystals* (Academic Press, INC., New York and London, 1970). 17, 73, 74, 75, 76, 149

[78] M. Gerloch and E. C. Constable, *Transition Metal Chemistry* (VCH Weinheim, 1994). 17, 18, 19, 20, 92

[79] R. Rückamp, Ph.D. thesis, University of Cologne, Germany (2006). 18, 51, 53, 55

[80] J. Franck, Trans. Faraday Soc. **21**, 536 (1926). 18, 19

[81] E. Condon, Phys. Rev. **28**, 1182 (1926). 18, 19

[82] E. Condon, Phys. Rev. **32**, 858 (1928). 18, 19

[83] A. S. Coolidge, H. M. James, and R. D. Present, The J. Chem. Phys. **4**, 193 (1936). 18, 19

[84] R. L. Greene, D. D. Sell, W. M. Yen, and A. L. Schawlow, Phys. Rev. Lett. **15**, 656 (1965). 20

[85] J. Woods-Halley and I. Silvera, Phys. Rev. Lett. **15**, 654 (1965). 20

[86] R. Bhandari and L. M. Falicov, J. Phys. C: Sol. State Phys. **5**, 1445 (1972). 20

[87] S. Ishihara, J. Inoue, and S. Maekawa, Phys. Rev. B **55**, 8280 (1997). 20, 21

[88] G. Khaliullin and S. Okamoto, Phys. Rev. Lett. **89**, 167201 (2002). 20, 21

[89] G. Khaliullin and S. Okamoto, Phys. Rev. B **68**, 205109 (2003). 20, 21

[90] D. I. Khomskii, Physica Scripta **72**, CC8 (2005). 20, 21, 22

[91] P. W. Anderson, *Basic Notions of Condensed Matter Physics* (Benjamin-Cummings, London, 1984). 20

[92] J. Kananmori, J. Phys. Chem. Sol. **10**, 87 (1959). 21, 38, 131

[93] S. Ishihara, M. Yamanaka, and N. Nagaosa, Phys. Rev. B **56**, 686 (1997). 21

[94] L. F. Feiner, A. M. Olés, and J. Zaanen, Phys. Rev. Lett. **78**, 2799 (1997). 21

[95] J. Sirker and G. Khaliullin, Phys. Rev. B **67**, 100408(R) (2003). 21

[96] D. I. Khomskii and T. Mizokawa, Phys. Rev. Lett. **94**, 156402 (2005). 21

[97] K. P. Schmidt, M. Grüninger, and G. S. Uhrig, Phys. Rev. B **76**, 075108 (2007). 21

[98] J. van den Brink, New J. Phys. **6**, 201 (2004). 21

[99] G. Khaliullin, Prog. Theo. Phys. Suppl. **160**, 155 (2005). 21

[100] D. D. Sell, R. L. Greene, and R. M. White, Phys. Rev. **158**, 489 (1967). 21

[101] J. D. Perkins, J. M. Graybeal, M. A. Kastner, R. J. Birgeneau, J. P. Falck, and M. Greven, Phys. Rev. Lett. **71**, 1621 (1993). 22, 134

[102] J. D. Perkins, R. J. Birgeneau, J. M. Graybeal, M. A. Kastner, and D. S. Kleinberg, Phys. Rev. B **58**, 9390 (1998). 22

[103] J. Lorenzana and R. Eder, Phys. Rev. B **55**, R3358 (1997). 22, 107, 117, 118, 119, 121, 126, 127, 128

[104] M. A. Kastner, R. J. Birgeneau, G. Shirane, and Y. Endoh, Rev. Mod. Phys. **70**, 897 (1998). 22, 25

[105] J. Lorenzana, J. Eroles, and S. Sorella, Phys. Rev. Lett. **83**, 5122 (1999). 22

[106] M. Windt, M. Grüninger, T. Nunner, C. Knetter, K. P. Schmidt, G. S. Uhrig, T. Kopp, A. Freimuth, U. Ammerahl, B. Büchner, et al., Phys. Rev. Lett. **87**, 127002 (2001). 22, 101, 119, 120, 124, 134, 135, 136, 137, 138

[107] C.-M. Ho, V. N. Muthukumar, M. Ogata, and P. W. Anderson, Phys. Rev. Lett. **86**, 1626 (2001). 22

[108] E. Gagliano, F. Lema, S. Bacci, J. J. V. Alvarez, and J. Lorenzana, Phys. Rev. B **62**, 1218 (2000). 22, 120, 121

[109] T. S. Nunner, P. Brune, T. Kopp, M. Windt, and M. Grüninger, Phys. Rev. B **66**, 180404 (2002). 22, 101, 135, 136

[110] J. Lorenzana, Physica B: Cond. Mat. **384**, 181 (2006). 22

[111] E. Müller-Hartmann, *Theoretische Festkörperphysik II* (lecture notes, University of Cologne, 2006). 25, 124

[112] M. Grüninger, Ph.D. thesis, Rijksuniversiteit Groningen, The Netherlands (1999). 25

[113] D. Garcia, J. Eroles, and J. Lorenzana, Phys. Rev. B **58**, 13574 (1998). 25, 124

[114] W. Herres and J. Gronholz, *Understanding FT-IR Data Processing* (Dr. Alfred Huethig Publishers; Bruker Analytische Messtechnik, Karlsruhe, 1985). 29, 30

[115] M. Windt, Ph.D. thesis, University of Cologne, Germany (2002). 30, 31, 101, 135

[116] N. Ockman, Advan. Phys. **7**, 199 (1958). 32, 33

[117] M. M. Maldoni, R. G. Smith, G. Robinson, and V. L. Rookyard, Mon. Not. R. Astron. Soc. **298**, 251 (1998). 32, 33

[118] W. M. Irvine and J. B. Pollack, Icarus **8**, 324 (1968). 32

[119] P. V. Hobbs, *Ice Physics* (Oxford University Press, 1974). 32, 33

[120] M. Wutz, H. Adam, W. Walcher, and K. Jousten, *Handbuch Vakuumtechnik* (7. Auflage, Vieweg, 2000). 33

[121] B. D. Cullity, *Elements of X-Ray Diffraction* (Addison Wesley Publishing Company, 1978). 34

[122] Y. Ren, T. T. M. Palstra, D. I. Khomskii, A. A. Nugroho, A. A. Menovsky, and G. A. Sawatzky, Phys. Rev. B **62**, 6577 (2000). 35, 39, 40, 45, 46

[123] L. D. Tung, M. R. Lees, G. Balakrishnan, and D. M. Paul, Phys. Rev. B **75**, 104404 (2007). 35, 45, 55

[124] J. B. Goodenough and M. Longo, Solid-State Spec., Landolt-Börnstein III Cond. Mat. **4a**, 126 (1970). 36

[125] V. M. Goldschmidt, Die Naturwissenschaften **14**, 477 (1926). 36

[126] R. D. Shannon, Acta Cryst. **A32**, 751 (1976). 36

[127] U. Müller, *Anorganische Strukturchemie* (B. G. Teubner Stuttgart, 1996). 36

[128] G. F. Dionne, Phys. Rev. **137**, A743 (1965). 37

[129] K. Nakamoto, *Infrared and Raman Spectra of Inorganic and Coordination Compounds* (3. edition, Wiley, New York, 1978). 37

[130] P. W. Anderson, Phys. Rev. **79**, 350 (1950). 38, 105, 131

[131] J. B. Goodenough, Phys. Rev. **100**, 564 (1955). 38, 105, 131

[132] G. V. Bazuev, I. I. Matveenko, and G. P. Shveikin, Sov. Phys. Sol. State (English Trans.) **16**, 155 (1974). 39

[133] M. Noguchi, A. Nakazawa, S. Oka, T. Arima, Y. Wakabayashi, H. Nakao, and Y. Murakami, Phys. Rev. B **62**, R9271 (2000). 39, 40, 75

[134] H. Sawada and K. Terakura, Phys. Rev. B **58**, 6831 (1998). 39, 41, 75

[135] S. Miyasaka, Y. Okimoto, and Y. Tokura, J. Phys. Soc. Japan **71**, 2086 (2002). 39, 43, 44, 49

[136] J. Rodríguez-Carvajal, M. Hennion, F. Moussa, A. H. Moudden, L. Pinsard, and A. Revcolevschi, Phys. Rev. B **57**, R3189 (1998). 42

[137] W. Massa, *Kristallstrukturbestimmung* ((3. Auflage) Teubner, 2002). 42

[138] N. N. Kovaleva, A. V. Boris, C. Bernhard, A. Kulakov, A. Pimenov, A. M. Balbashov, G. Khaliullin, and B. Keimer, Phys. Rev. Lett. **93**, 147204 (2004). 45

[139] A. Gößling, Ph.D. thesis, University of Cologne, Germany (2007). 45, 118

[140] Y. Otsuka and M. Imada, J. Phys. Soc. Japan **75**, 124707 (2006). 45, 70

[141] Y. Kimishima, M. Uehara, and T. Saitoh, Solid State Comm. **133**, 559 (2002). 45

[142] Y. Motome, H. Seo, Z. Fang, and N. Nagaosa, Phys. Rev. Lett. **90**, 146602 (2003). 47, 48

[143] M. Grüninger, R. Rückamp, M. Windt, P. Reutler, C. Zobel, T. Lorenz, A. Freimuth, and A. Revcolevschi, Nature **418**, 39 (2002). 50

[144] A. Bombik, B. Leśniewska, and A. Oleś, Phys. Stat. Sol. A **50**, K17 (1978). 50

[145] V. G. Zubkov, G. V. Bazuev, and G. P. Shveikin, Sov. Phys. Sol. State (English Trans.) **18**, 1165 (1976). 50, 51

[146] A. A. Nugroho, private communication. 50, 87, 92

[147] R. Rückamp, J. Baier, M. Kriener, M. W. Haverkort, T. Lorenz, G. S. Uhrig, L. Jongen, A. Möller, G. Meyer, and M. Grüninger, Phys. Rev. Lett. **95**, 097203 (2005). 51

[148] P. Ehrlich and H.-J. Seifert, Z. Allg. Anorg. Chem. **301**, 282 (1959). 55, 56, 146

[149] A. Haase and G. Brauer, Acta. Cryst. B **31**, 2521 (1975). 55, 56, 146

[150] J. P. Vénien, P. Palvadeau, D. Schleich, and J. Rouxel, Mat. Res. Bull. **14**, 891 (1979). 55

[151] T. Möller, Ph.D. thesis, University of Cologne, Germany (2008). 55

[152] R. Thomas, P. Ehrhart, M. Luysberg, M. Boese, R. Waser, M. Roeckerath, E. Rije, J. Schubert, S. van Elshocht, and M. Caymax, App. Phys. Lett. **89**, 232902 (2006). 55

[153] H. L. Frisch, E. Sonnenblick, V. A. Vyssotsky, and J. M. Hammersley, Phys. Rev. **124**, 1021 (1961). 56, 92

[154] M. F. Sykes and J. W. Essam, Phys. Rev. **133**, A310 (1964). 56, 92

[155] R. P. Liferovich and R. H. Mitchell, J. Sol. State Chem. **177**, 2188 (2004). 56, 57

[156] M. Kasuya, Y. Tokura, T. Arima, H. Eisaki, and S. Uchida, Phys. Rev. B **47**, 6197 (1993). 56, 60

[157] I. Klassen, Master's thesis, University of Cologne, Germany (2006). 57

[158] J. Strohmenger, Master's thesis, University of Cologne, Germany (2000). 57

[159] N. F. Mott, J. Non-Cryst. Solids **1**, 1 (1968). 58

References

[160] A. L. Efros and B. I. Shklovskii, J. Phys. C: Sol. State Phys. **8**, L49 (1974). 58

[161] T. Holstein, Annals of Physics **8**, 343 (1959). 58, 60

[162] I. G. Austin and N. F. Mott, Advances in Physics **18**, 41 (1969). 58

[163] D. C. Worledge, G. J. Snyder, M. R. Beasley, and T. H. Geballe, J. Appl. Phys. **80**, 5158 (1996). 60

[164] D. Emin and T. Holstein, Annals of Physics **53**, 439 (1969). 60

[165] P. Y. Yu and M. Cardona, *Fundamentals of Semiconductors: Physics and Materials Properties (Third Edition)* (Springer, 2005). 70

[166] G. Oversluizen and R. Metselaar, J. Phys. C: Sol. State Phys. **15**, 4869 (1982). 74, 92, 149

[167] T. Ishii, K. Ogasawara, and H. Adachi, J. Chem. Phys. **116**, 471 (2002). 74, 75, 89, 92, 149

[168] M. W. Haverkort, Ph.D. thesis, University of Cologne, Germany (2005). 73, 76, 145, 146, 147, 156, 157

[169] A. Wiedenmann, J. P. Vénien, P. Palvadeau, and J. Rossat-Mignod, J. Phys. C: Sol. State Phys. **16**, 5339 (1983). 75

[170] T. Mizokawa and A. Fujimori, Phys. Rev. B **54**, 5368 (1996). 76, 145, 146, 147

[171] I. V. Solovyev, Phys. Rev. B **74**, 054412 (2006). 77, 89

[172] M. D. Raychaudhury, E. Pavarini, and O. K. Anderson, Phys. Rev. Lett. **99**, 126402 (2007). 77, 89

[173] E. Benckiser, R. Rückamp, T. Möller, T. Taetz, A. Möller, A. A. Nugroho, T. T. M. Palstra, G. S. Uhrig, and M. Grüninger, New J. Phys. **10**, 053027 (2008). 80, 81

[174] C. Marquina, M. Sikora, M. R. Ibarra, A. A. Nugroho, and T. T. M. Palstra, J. Magn. and Magn. Mat. **290-291**, 428 (2004). 82, 92

[175] H. M. Crosswhite and G. H. Dieke, The J. Chem. Phys. **35**, 1535 (1961). 92, 150

[176] M. Yin, J.-C. Krupa, E. Antic-Fidancev, and A. Lorriaux-Rubbens, Phys. Rev. B **61**, 8073 (2000). 93

[177] S. Chakravarty, B. I. Halperin, and D. R. Nelson, Phys. Rev. B **39**, 2344 (1989). 97, 100

[178] E. Manousakis, Rev. Mod. Phys. **63**, 1 (1991). 97, 100

[179] N. D. Mermin and H. Wagner, Phys. Rev. Lett. **17**, 1133 (1966). 97, 98, 100

[180] S. Liang, B. Doucot, and P. W. Anderson, Phys. Rev. Lett. **61**, 365 (1988). 98

[181] G. S. Uhrig, *Niedrigdimensionale Spinsysteme und Spin-Phonon-Kopplung* (Habilitationsschrift, University of Cologne, Germany, 1999). 98, 99

[182] L. Capriotti, A. E. Trumper, and S. Sorella, Phys. Rev. Lett. **82**, 3899 (1999). 98

[183] M. Boninsegni, Phys. Rev. B **52**, 15304 (1995). 98

[184] M. B. Hastings, Phys. Rev. B **63**, 014413 (2000). 98

[185] P. Lecheminant, B. Bernu, C. Lhuillier, L. Pierre, and P. Sindzingre, Phys. Rev. B **56**, 2521 (1997). 98

[186] C. Waldtmann, H.-U. Everts, B. Bernu, C. Lhuillier, P. Sindzingre, P. Lecheminant, and L. Pierre, Eur. Phys. J. B **2**, 501 (1998). 98

[187] M. Grüninger, *Magnetische Anregungen in niedrigdimensionalen Spinflüssigkeiten* (Habilitationsschrift, University of Cologne, Germany, 2004). 98

[188] M. Karbach, G. Müller, A. H. Bougourzi, A. Fledderjohann, and K.-H. Mütter, Phys. Rev. B **55**, 12510 (1997). 99, 120

[189] I. A. Zaliznyak, H. Woo, T. G. Perring, C. L. Broholm, C. D. Frost, and H. Takagi, Phys. Rev. Lett. **93**, 087202 (2004). 99, 104, 106, 119

[190] G. S. Uhrig and M. Grüninger, Physik Journal **2**, 41 (2003). 100

[191] J. des Cloizeaux and J. Pearson, Phys. Rev. **128**, 2131 (1962). 99, 126

[192] C. Knetter, K. P. Schmidt, M. Grüninger, and G. S. Uhrig, Phys. Rev. Lett. **87**, 167204 (2001). 100, 101, 136

[193] C. Jurecka and W. Brenig, Phys. Rev. B **61**, 14307 (2000). 100

[194] C. L. Teske and H. K. Müller-Buschbaum, Z. Allg. Anorg. Chem. **379**, 234 (1970). 102, 109

[195] M. T. Weller and D. R. Lines, J. Sol. State Chem. **82**, 21 (1989). 102, 103, 156

References

[196] M. Knupfer, R. Neudert, M. Kielwein, S. Haffner, M. S. Golden, J. Fink, C. Kim, Z.-X. Shen, M. Merz, N. Nücker, et al., Phys. Rev. B **55**, R7291 (1997). 103, 104, 118, 124

[197] Z. V. Popović, V. A. Ivanov, M. J. Konstantinović, A. Cantarero, J. Martínez-Pastor, D. Olguín, M. I. Alonso, M. Garriga, O. P. Khuong, A. Vietkin, et al., Phys. Rev. B **63**, 165105 (2001). 103, 117, 118

[198] J. Voit, Rep. Prog. Phys. **57**, 977 (1994). 104

[199] S. Tomonaga, Prog. Theor. Phys. **5**, 544 (1950). 104

[200] J. M. Luttinger, J. Math. Phys. **4**, 1154 (1963). 104

[201] E. H. Lieb and F. Y. Wu, Phys. Rev. Lett. **20**, 1445 (1968). 104

[202] A. Koitzsch, S. V. Borisenko, J. Geck, V. B. Zabolotnyy, M. Knupfer, J. Fink, P. Ribeiro, B. Büchner, and R. Follath, Phys. Rev. B **73**, 201101 (2006). 104, 106

[203] B. J. Kim, H. Koh, E. Rotenberg, S.-J. Oh, H. Eisaki, N. Motoyama, S. Uchida, T. Tohyama, S. Maekawa, Z.-X. Shen, et al., Nature Phys. **2**, 397 (2006). 104

[204] C. Kim, Z.-X. Shen, N. Motoyama, H. Eisaki, S. Uchida, T. Tohyama, and S. Maekawa, Phys. Rev. B **56**, 15589 (1997). 104

[205] C. Kim, , A. Y. Matsuura, Z.-X. Shen, N. Motoyama, H. Eisaki, S. Uchida, T. Tohyama, and S. Maekawa, Phys. Rev. Lett. **77**, 4054 (1996). 104

[206] M. Z. Hasan, P. A. Montano, E. D. Isaacs, Z.-X. Shen, H. Eisaki, S. K. Sinha, Z. Islam, N. Motoyama, and S. Uchida, Phys. Rev. Lett. **88**, 177403 (2002). 104

[207] F. H. L. Essler, F. Gebhard, and E. Jeckelmann, Phys. Rev. B **64**, 125119 (2001). 105

[208] E. Jeckelmann, Phys. Rev. B **67**, 075106 (2003). 105

[209] Y.-J. Kim, J. P. Hill, H. Benthien, F. H. L. Essler, E. Jeckelmann, H. S. Choi, T. W. Noh, N. Motoyama, K. M. Kojima, S. Uchida, et al., Phys. Rev. Lett. **92**, 137402 (2004). 105

[210] M. Matsuda, K. Katsumata, K. M. Kojima, M. Larkin, G. M. Luke, J. Merrin, B. Nachumi, Y. J. Uemura, H. Eisaki, N. Motoyama, et al., Phys. Rev. B **55**, R11953 (1997). 106

[211] I. A. Zaliznyak, C. Broholm, M. Kibune, M. Nohara, and H. Takagi, Phys. Rev. Lett. **83**, 5370 (1999). 106

[212] A. Revcolevschi, U. Ammerahl, and G. Dhalenne, J. Cryst. Growth **198/199**, 593 (1999). 108, 109

[213] C. T. Lin, W. Zhou, A. P. Mackenzie, F. Gauthier, and W. Y. Liang, J. Cryst. Growth **140**, 72 (1994). 108

[214] M. V. Abrashev, A. P. Litvinchuk, C. Thomsen, and V. N. Popov, Phys. Rev. B **55**, 9136 (1997). 111, 117

[215] Y. S. Lee, T. W. Noh, H. S. Choi, E. J. Choi, H. Eisaki, and S. Uchida, Phys. Rev. B **62**, 5285 (2000). 111

[216] A. R. Pico, C. S. Houk, T. J. R. Weakley, and C. J. Page, Inorg. Chim. Acta **258**, 155 (1997). 115

[217] O. V. Misochko, S. Tajima, C. Urano, H. Eisaki, and S. Uchida, Phys. Rev. B **53**, R14733 (1996). 117

[218] T. S. Nunner, P. Brune, T. Kopp, M. Windt, and M. Grüninger, Acta Phys. Polonica B **34**, 1545 (2003). 119, 124, 135

[219] J.-S. Caux and R. Hagemans, J. Stat. Mech.: Theory and Experiment **12**, P12013 (2006). 120, 126

[220] S. T. Bramwell, J. Phys.: Cond. Mat. **2**, 7527 (1990). 122

[221] L. J. de Jongh and R. Block, Physica B **79**, 568 (1975). 122

[222] J. B. Torrance, A. Bezinge, A. I. Nazzal, T. C. Huang, S. S. P. Parkin, D. T. Keane, S. J. LaPlaca, P. M. Horn, and G. A. Held, Phys. Rev. B **40**, 8872 (1989). 122

[223] E. Benckiser, T. Nunner, T. Kopp, C. Sekar, G. Krabbes, and M. Grüninger, in preparation. 123

[224] P. Bordet, C. Chaillout, M. Marezio, Q. Huang, A. Santoro, S.-W. Cheong, H. Takagi, C. S. Oglesby, and B. Batlogg, Theo. Chem. Acc. **116**, 535 (2006). 123

[225] F. C. Zhang and T. M. Rice, Phys. Rev. B **37**, 3759 (1988). 124, 125

[226] E. Müller-Hartmann and A. Reischl, Eur. Phys. J. B **28(2)**, 173 (2002). 124

[227] A. V. Sologubenko, K. Giannò, and H. R. Ott, Phys. Rev. B **64**, 054412 (2001). 126

[228] C. Sekar, T. Watanabe, A. Matsuda, and H. Shibata, J. Sol. State Chem. **156**, 422 (2001). 129

References

[229] B. Schüpp, C. Sekar, W. Gruner, G. Auffermann, C. Bähtz, and G. Krabbes, Z. Allg. Anorg. Chem. **630**, 663 (2004). 129, 130, 131

[230] M. Reuther, Master's thesis, University of Cologne, Germany (2004). 130, 131

[231] I. A. Zobkalo, V. A. Polyakov, O. P. Smirnov, S. V. Gavrilov, S. N. Barilo, D. I. Zhigunov, and M. Bonnet, Physica B: Cond. Mat. **234-236**, 734 (1997). 131

[232] T. S. Nunner, Ph.D. thesis, University of Augsburg, Germany / Cuvellier Verlag Goettingen (2003). 136, 137

[233] S. R. White, R. M. Noack, and D. J. Scalapino, Phys. Rev. Lett. **73**, 886 (1994). 137

[234] M. Azzouz and K. A. Asante, Phys. Rev. B **72**, 094433 (2005). 137

[235] B. Frischmuth, B. Ammon, and M. Troyer, Phys. Rev. B **54**, R3714 (1996). 137

[236] H.-T. Wang, Phys. Rev. B **64**, 174410 (2001). 137

[237] W. A. Harrison and G. K. Straub, Phys. Rev. B **36**, 2695 (1987). 145, 146

[238] W. A. Harrison, *Elementary Electronic Structure* (World Scientific Publishing Co. Pte. Ltd., 1999). 145

[239] E. Müller-Hartmann, *Theoretische Festkörperphysik I* (lecture notes, University of Cologne, 1998). 146

[240] A. E. Bocquet, T. Mizokawa, K. Morikawa, A. Fujimori, S. R. Barman, K. Maiti, D. D. Sarma, Y. Tokura, and M. Onoda, Phys. Rev. B **53**, 1161 (1996). 146, 147

[241] N. W. Ashcroft and N. D. Mermin, *Solid State Physics* (Brooks/Cole; Thomson Learning, 1976). 150

[242] U. Walter, J. Phys. Chem. Sol. **45**, 401 (1984). 150, 151, 153

[243] R. J. Lang, Can. J. Res. A **14**, 127 (1936). 151

[244] R. A. Buchanan, H. E. Rast, and H. H. Caspers, J. Chem. Phys. **44**, 4063 (1966). 151, 152

[245] H. H. Caspers, H. E. Rast, and J. L. Fry, The J. Chem. Phys. **53**, 3208 (1970). 153

[246] G. H. Dieke and B. Pandey, The J. Chem. Phys. **41**, 1952 (1964). 153

[247] J. Demsar, A. Gozar, V. K. Thorsmølle, A. J. Taylor, and I. Bozovic, Phys. Rev. B **76**, 054304 (2007). 156

List of Publications

1. **Collective orbital excitations in orbitally ordered YVO$_3$ and HoVO$_3$**

   E. Benckiser, R. Rückamp, T. Möller, T. Taetz, A. Möller, A. A. Nugroho, T. T. M. Palstra, G. S. Uhrig, and M. Grüninger
   New Journal of Physics, **10**, 053027 (2008)

2. **Optical study of orbital excitations in transition-metal oxides**

   R. Rückamp, E. Benckiser, M. W. Haverkort, H. Roth, T. Lorenz, A. Freimuth, L. Jongen, A. Möller, G. Meyer, P. Reutler, B. Büchner, A. Revcolevschi, S-W. Cheong, C. Sekar, G. Krabbes, and M. Grüninger
   New Journal of Physics, **7**, 144 (2005)

3. **Optical Spectroscopy of Low-Dimensional Quantum Spin Systems**

   M. Grüninger, M. Windt, E. Benckiser, T. S. Nunner, K. P. Schmidt, G. S. Uhrig, and T. Kopp
   Advances in Solid State Physics, ed. by B. Kramer, Springer, Vol. **43**, 95-112, (2003)

4. **Magnetic Excitations in SrCuO$_2$**

   E. Benckiser, P. Ribero, C. Hess, B. Büchner, A. Revcolevschi, U. Ammerahl, G. Dhalenne, E. Müller-Hartmann, and M. Grüninger
   in preparation

5. **Magnetic Excitations in the Five-Leg Spin 1/2 Ladder La$_8$Cu$_7$O$_{19}$**

   E. Benckiser, M. Reuter, T. Lorenz, A. Freimuth and M. Grüninger
   in preparation

6. **Magnetic Excitations in CaCu$_2$O$_3$**

   E. Benckiser, T. Nunner, T. Kopp, C. Sekar, G. Krabbes, and M. Grüninger
   in preparation

7. **Conference contributions**

   - *Spring meeting of the German Physical Society (DPG)*, division condensed matter, Dresden, 2003, Regensburg, 2004, Berlin, 2005
   - *International workshop on Strongly Correlated Transition Metal Compounds of SFB 608*, Cologne, 2003

- *21st General Conference of the Condensed Matter Division of the European Physical Society* (EPS) & DPG-*Spring meeting*, Dresden, 2006

- *International Workshop on Highly Correlated Transition Metal Compounds II* of SFB 608, Cologne, 2006

Acknowledgements

$\sim$

Supplement

Offizielle Erklärung

Ich versichere, dass ich die von mir vorgelegte Dissertation selbstständig angefertigt, die benutzten Quellen und Hilfsmittel vollständig angegeben und die Stellen der Arbeit - einschließlich Tabellen, Karten und Abbildungen -, die anderen Werken im Wortlaut oder dem Sinn nach entnommen sind, in jedem Einzelfall als Entlehnung kenntlich gemacht habe, dass diese Dissertation noch in keiner anderen Fakultät oder Universität zur Prüfung vorgelegen hat, dass sie - abgesehen von den in der Publikationsliste angegebenen Teilpublikationen - noch nicht veröffentlicht worden ist sowie, dass ich eine solche Veröffentlichung vor Abschluss des Promotionsverfahrens nicht vornehmen werde. Die Bestimmungen dieser Promotionsordnung sind mir bekannt. Die von mir vorgelegte Dissertation ist von Prof. Dr. M. Grüninger betreut worden.

Köln, den 10. Oktober 2007

Eva Benckiser

Abstract

Within the scope of this thesis, the low-energy excitations of undoped Mott insulators RVO_3 with $R = $ Y, Ho, and Ce, (Sr,Ca)CuO$_2$ and La$_8$Cu$_7$O$_{19}$ have been investigated by means of optical spectroscopy. The compounds RVO_3 with $R = $ rare-earth ion recently have attracted a lot of interest because of their unusual structural, orbital, and magnetic properties. The compounds undergo a series of temperature-induced phase transitions accompanied by a change of orbital and magnetic order. Furthermore, it has been proposed that YVO$_3$ represents the first realization of a one-dimensional orbital liquid and an orbital Peierls phase, with a transition to an orbitally ordered phase at lower temperatures. In this thesis, we present the optical conductivity $\sigma(\omega)$ of RVO_3 with $R = $ Y, Ho, and Ce for energies from 0.1 to 1.6 eV as a function of temperature (10–300 K) and polarization of the incident light parallel to the crystallographic axes ($\sigma_a, \sigma_b, \sigma_c$). Our main experimental result is the observation of two absorption features at 0.55 eV in $\sigma_a(\omega)$ and 0.4 eV in $\sigma_c(\omega)$ which are assigned to collective orbital excitations, in contrast to conventional local crystal-field transitions. Altogether, our results strongly suggest that in RVO_3 with $R = $ Y, Ho, and Ce the orbital exchange interactions play a decisive role.

In a second study, we have investigated the magnetic excitations of low-dimensional quantum magnets, namely the spin chain (Sr,Ca)CuO$_2$ and the five-leg ladder La$_8$Cu$_7$O$_{19}$. For (Sr,Ca)CuO$_2$, two absorption features around 0.4 eV in $\sigma_c(\omega)$ (chain direction) and $\sigma_b(\omega)$ (inter-chain direction) are identified as magnetic contributions to the optical conductivity. The analysis of $\sigma_c(\omega)$ enables the very precise determination of the nearest-neighbor exchange coupling J_c as a function of temperature and Ca substitution. We have found $J_c = (227 \pm 4)$ meV for SrCuO$_2$ at low temperatures and no effect on J_c upon Ca-substitution of 10 %. Furthermore, we ascertained that the theoretically predicted two-spinon-plus-phonon contribution describes roughly 74–97 % of the observed spectral weight. We suggest that the remaining weight has to be ascribed to multi-spinon excitations. To explain the small magnetic absorption features in $\sigma_b(\omega)$, we sketch a new mechanism which gives rise to a dipole moment *perpendicular* to the chains when holes are virtually exchanged *along* the chain. In particular, we point out the possible relevance of this contribution to the optical conductivity of many quasi-1D quantum spin systems.

Our data of La$_8$Cu$_7$O$_{19}$ are the first experimental result on the magnetic excitations of n-leg ladders ($n > 2$) at high energies. Amongst others, we compared our data with the well-investigated spectrum of the two-leg ladder and found a surprising resemblance. Although a detailed understanding of the observed line shape of the 5-leg ladder is missing up to now, our data strongly suggest the existence of bound states of magnetic excitations also in this system. The comparison of different low-dimensional $S = 1/2$ systems suggests that the magnetic excitations in the high-energy continua are similar and develop smoothly from 1D to 2D.

Kurzzusammenfassung

Im Rahmen der vorliegenden Doktorarbeit wurden die niederenergetischen Anregungen in den Mott-Isolatoren $R\text{VO}_3$ mit $R = \text{Y}$, Ho und Ce, $(\text{Sr,Ca})\text{CuO}_2$ und $\text{La}_8\text{Cu}_7\text{O}_{19}$ mittels optischer Spektroskopie untersucht.

Aufgrund ihrer ungewöhnlichen strukturellen, orbitalen und magnetischen Eigenschaften haben die Verbindungen $R\text{VO}_3$ mit $R = \text{Seltenerd-Ion}$ erst kürzlich viel Aufmerksamkeit erregt. Die Verbindungen zeigen eine Reihe von temperaturinduzierten Phasenübergängen, die mit einer Änderung der orbitalen und magnetischen Ordnung verbunden sind. Des Weiteren ist YVO_3 als erstes orbitales Peierls-System mit einem Übergang zu einer orbital geordneten Phase bei tiefen Temperaturen vorgeschlagen worden. In dieser Doktorarbeit präsentieren wir die optische Leitfähigkeit $\sigma(\omega)$ von $R\text{VO}_3$ mit $R = \text{Y}$, Ho und Ce im Energiebereich von 0.1 bis 1.6 eV als Funktion der Temperatur (10–300 K) und Polarisation des einfallenden Lichtes parallel zu den kristallographischen Achsen ($\sigma_a, \sigma_b, \sigma_c$). Unser Hauptergebnis ist die Beobachtung von zwei Absorptionsbanden bei etwa 0.55 eV in $\sigma_a(\omega)$ und 0.4 eV in $\sigma_c(\omega)$, die wir, im Gegensatz zu herkömmlichen lokalen Kristallfeldübergängen, kollektiven orbitalen Anregungen zuordnen. Insgesamt deuten unsere Ergebnisse stark darauf hin, dass in $R\text{VO}_3$ mit $R = \text{Y}$, Ho, und Ce die orbitale Austauschwechselwirkung eine entscheidende Rolle spielt.

In einer zweiten Studie haben wir die magnetischen Anregungen niedrigdimensionaler Quantenspinsysteme, die der Spinkette $(\text{Sr,Ca})\text{CuO}_2$ und die der fünfbeinigen Spinleiter $\text{La}_8\text{Cu}_7\text{O}_{19}$, untersucht. Für $(\text{Sr,Ca})\text{CuO}_2$ wurden zwei Absorptionsbanden bei etwa 0.4 eV in $\sigma_c(\omega)$ (Kettenrichtung) und $\sigma_b(\omega)$ (Zwischenkettenrichtung) als magnetische Beiträge zur optischen Leitfähigkeit identifiziert. Die Analyse von $\sigma_c(\omega)$ erlaubt eine sehr genaue Bestimmung der Nächsten-Nachbar-Austauschkopplung J_c als Funktion der Temperatur und der Ca-Substitution. Für SrCuO_2 haben wir $J_c = (227 \pm 4)\,\text{meV}$ bei tiefen Temperaturen bestimmt und bis zu 10 % Ca-Substitution keinen Einfluss auf J_c feststellen können. Ferner haben wir festgestellt, dass der von der Theorie vorhergesagte Zwei-Spinon-Plus-Phonon-Beitrag nur etwa 74–97 % des beobachteten spektralen Gewichts beschreibt. Wir behaupten, dass das verbleibende Gewicht Multi-Spinon-Anregungen zugeschrieben werden muss. Zur Erklärung der kleinen magnetischen Absorptionsbande in $\sigma_b(\omega)$ skizzieren wir einen neuen Mechanismus, der beschreibt, wie durch den virtuellen Austausch von Löchern *parallel* zu den Ketten ein Dipolmoment *senkrecht* zu den Ketten entsteht. Insbesondere weisen wir auf die mögliche Relevanz eines solchen Beitrages zur optischen Leitfähigkeit in vielen quasi-1D Quantenspinsystemen hin.

Unsere Daten für $\text{La}_8\text{Cu}_7\text{O}_{19}$ stellen das erste experimentelle Ergebnis für die magnetischen Anregungen einer n-beinigen Leiter ($n > 2$) bei hohen Energien dar. Unter anderem haben wir unsere Daten mit dem gut untersuchten Spektrum der 2-beinigen Leiter verglichen und eine überraschende Übereinstimmung gefunden. Obwohl bis zum jetzigen Zeitpunkt ein detailliertes Verständnis der beobachteten Linienform der 5-beinigen Leiter fehlt, deuten unsere Daten stark darauf hin, dass

auch hier gebundene Zustände magnetischer Anregungen existieren. Der Vergleich verschiedener niedrig-dimensionaler $S = 1/2$ Systeme zeigt einen deutlichen Hinweis, dass die magnetischen Anregungen im Bereich der Hochenergie-Kontinua ähnlich sind und von 1D nach 2D ineinander übergehen.